Charge and spin transport in topological insulator heterojunctions

Dissertation zur Erlangung des naturwissenschaftlichen Doktorgrades der Bayerischen Julius-Maximilians-Universität Würzburg

vorgelegt von
Rolf Walter Reinthaler
aus Ansbach

Würzburg 2015

Eingereicht am 06.10.2015 .....
bei der Fakultät für Physik und Astronomie

1. Gutachter: Prof. Dr. Ewelina M. Hankiewicz .....

2. Gutachter: Prof. Dr. Giorgio Sangiovanni .....

3. Gutachter: Prof. Dr. Jürgen König .....

der Dissertation.

1. Prüfer: Prof. Dr. Ewelina M. Hankiewicz .....

2. Prüfer: Prof. Dr. Giorgio Sangiovanni .....

3. Prüfer: Prof. Dr. Hartmut Buhmann .....

im Promotionskolloquium.

Tag des Promotionskolloquium: 24.06.2016 .....

Doktorurkunde ausgehändigt am: .....

To my parents

Zusammenfassung

Während des letzten Jahrzehnts haben sich topologische Isolatoren zu einem der aktivsten Bereiche der Festkörperphysik entwickelt. Diese neuartige Materialklasse charakterisiert sich durch einen isolierenden Volumenzustand, welcher, in zweidimensionalen und zeitumkehrinvarianten Systemen, durch helikale Randkanäle ergänzt wird. Diese Randkanäle machen topologische Isolatoren zu vielversprechenden Kandidaten für Anwendungen in den Bereichen der präzisen Spintronik und der topologischen Quantencomputer. Diese Doktorarbeit trägt zu der Realisierung dieser faszinierenden Konzepte bei, indem sie den Transport durch Heterostrukturen aus zweidimensionalen topologischen Isolatoren und Metallen oder Supraleitern analysiert. Hierfür werden analytische und numerische Methoden angewandt. Im Besonderen wird eine generalisierte Methode zum Wellenfunktionsanpassung an Grenzflächen verwendet, um Rand- und Volumenzustände simultan beschreiben zu können.

Für die numerische Untersuchung nicht-supraleitender Systeme werden topologische Isolatoren als Tunnelbarrieren zwischen metallischen Kontakten betrachtet. Unerwarteterweise sind die Leitfähigkeiten von Rand- und Volumenzuständen nicht additiv. In langen und breiten Tunnelbarrieren wird der Transport ausschließlich durch die Randkanäle bestimmt. In kurzen Tunnelbarrieren hingegen ergibt sich die Leitfähigkeit aus einem Gemisch von Rand- und Volumenzuständen, welches von der Breite der Probe abhängt. In kurzen Tunnelbarrieren zeigt die Leitfähigkeit als Funktion der Probenlänge außerdem ein Maximum, welches das topologisch nicht-triviale Regime von dem topologisch trivialen Regime unterscheidet. Diese nicht-monotone Leitfähigkeit basiert auf der Formation einer effektiv propagierenden Mode, welche gegen Streuung durch nicht-magnetische Störstellen geschützt ist.

Die Analyse des Zusammenspiels von Rand- und Volumenzuständen wird auf supraleitende Tunnelbarrieren zwischen zwei topologischen Isolatoren ausgeweitet. Wenn die räumlichen Dimensionen der Tunnelbarriere klein genug sind, können die entgegenlaufenden Randkanäle an gegenüberliegenden Rändern des topologischen Isolators durch die evaneszenten Volumenzustände des Supraleiters gekoppelt werden. Hierdurch kann eine nicht-lokale Andreev-Reflexion generiert und kontrolliert werden. In Experimenten wird dieser Prozess normalerweise durch simultane Elektrontransmission überlagert. Für einzelne Kramers-Partner jedoch forciert die Helizität der Randkanäle die räumliche Trennung beider Prozesse, was eine rein elektrische Messung der nicht-lokalen Andreev-Reflexion ermöglicht.

Im Weiteren wird eine Studie über Hybridsysteme aus helikalen Randkanälen und konventionellen Supraleitern im magnetischen Feld, welches in der Ebene des zweidimensionalen topologischen Isolators liegt, präsentiert. Die Studie beschreibt den neuartigen supraleitenden Quanten-Spin-Hall-Effekt. Die hierfür charakteristischen Randkanäle bleiben selbst in endlichen Magnetfeldern helikal und gegen nicht-magnetische Störstellen geschützt. Gleichzeitig führt die Kombination von helikalen Randkanälen und Supraleitung zu einem riesigen Landé-Faktor, wodurch die supraleitende Bandlücke und der Magnetotransport dieser Systeme mit kleinen Magnetfeldern manipuliert werden kann. Dies kann durch einen nicht-monotonen supraleitenden Überschussstrom und ein aufgespaltenes Maximum der $\mathrm{d}I/\mathrm{d}V$-Charakteristik als Funktion des Magnetfeldes gemessen werden. In der Folge stellt der supraleitende Quanten-Spin-Hall-Effekt einen effektiven Generator und Detektor für Spinströme dar.

Die hier präsentierte Forschung vertieft das Verständnis des Zusammenspiels von Rand- und Volumentransport in Heterostrukturen aus toplogischen Isolatoren. Außerdem werden realisierbare Experimente beschrieben, mit welchen die nicht-lokale Andreev-Reflexion rein elektrisch gemessen und die Spinpolarisierung der helikalen Randkanäle getestet werden können.

Summary

Over the last decade, the field of topological insulators has become one of the most vivid areas in solid state physics. This novel class of materials is characterized by an insulating bulk gap, which, in two-dimensional, time-reversal symmetric systems, is closed by helical edge states. The latter make topological insulators promising candidates for applications in high fidelity spintronics and topological quantum computing. This thesis contributes to bringing these fascinating concepts to life by analyzing transport through heterostructures formed by two-dimensional topological insulators in contact with metals or superconductors. To this end, analytical and numerical calculations are employed. Especially, a generalized wave matching approach is used to describe the edge and bulk states in finite size tunneling junctions on the same footing.

The numerical study of non-superconducting systems focuses on two-terminal metal/topological insulator/metal junctions. Unexpectedly, the conductance signals originating from the bulk and the edge contributions are not additive. While for a long junction, the transport is determined purely by edge states, for a short junction, the conductance signal is built from both bulk and edge states in a ratio, which depends on the width of the sample. Further, short junctions show a non-monotonic conductance as a function of the sample length, which distinguishes the topologically non-trivial regime from the trivial one. Surprisingly, the non-monotonic conductance of the topological insulator can be traced to the formation of an effectively propagating solution, which is robust against scalar disorder.

The analysis of the competition of edge and bulk contributions in nanostructures is extended to transport through topological insulator/superconductor/topological insulator tunneling junctions. If the dimensions of the superconductor are small enough, its evanescent bulk modes can couple edge states at opposite sample borders, generating significant and tunable crossed Andreev reflection. In experiments, the latter process is normally disguised by simultaneous electron transmission. However, the helical edge states enforce a spatial separation of both competing processes for each Kramers' partner, allowing to propose an all-electrical measurement of crossed Andreev reflection.

Further, an analytical study of the hybrid system of helical edge states and conventional superconductors in finite magnetic fields leads to the novel superconducting quantum spin Hall effect. It is characterized by edge states. Both the helicity and the protection against scalar disorder of these edge states are unaffected by an in-plane magnetic field. At the same time its superconducting gap and its magnetotransport signals can be tuned in weak magnetic fields, because the combination of helical edge states and superconductivity results in a giant g-factor. This is manifested in a non-monotonic excess current and peak splitting of the $\mathrm{d}I/\mathrm{d}V$ characteristics as a function of the magnetic field. In consequence, the superconducting quantum spin Hall effect is an effective generator and detector for spin currents.

The research presented here deepens the understanding of the competition of bulk and edge transport in heterostructures based on topological insulators. Moreover it proposes feasible experiments to all-electrically measure crossed Andreev reflection and to test the spin polarization of helical edge states.

Contents

1. Introduction

Computer chips are an indispensable part of our everyday life. The basic component of a computer is the transistor [Bardeen48], which works as a logical unit by switching currents ON or OFF. The actual power of a chip depends on the number of integrated transistors which was predicted by Moore [Moore65] to double every 18 months, because progress in technology allows to build smaller and smaller transistors. Despite the advances in building transistors [Tan10] and data storage [Loth12] on an atomic level, Moore's law is prone to face its end, when fundamental physical barriers [Lloyd00], like the Heisenberg uncertainty, or thermal fluctuations [Kish02] prevent further miniaturization. Populating chips with even more and faster logical circuits, causes heating problem and energy losses. The reduction of dissipation could lead to substantial speed-up and energy savings, making it one of the biggest goals of modern solid state physics [Awschalom07].
In the field of classical computing, the possible paths to reduce dissipative losses are twofold: Firstly, new materials with high mobilities can outperform silicon devices, like it was shown for transistors based on carbon nanotubes [Franklin12] or graphene naonoribbons [Han14]. Secondly, spintronics focuses on switching from charge to spin based information processing [Wolf01, Awschalom07], where switching times are not limited by capacitance but by the much shorter spin precession time. This requires to generate, store and manipulate spins and spin currents. Moreover, a conceptually new way of information processing is provided by quantum computing [Bennett00, Nielsen05]. In this case, the quantum of information (qubit) is stored in a two level quantum system. Since long coherence times of the qubit are one of the key criterion for successful calculations [DiVincenzo00], it is advantageous to perform the latter on protected, anyonic states [Kitaev03, Nayak08]. The most prominent proposal to find non-abelian statistics [Ivanov01] involves Majorana bound states, which are supposed to exist in p-wave superconductors [Kitaev01, Oreg10, Mourik12].
With the discovery of time-reversal invariant two-dimensional topological insulators [Kane05a, Bernevig06, König07, Hasan10, Qi11], solid state physics has advanced in all three previously mentioned aspects: The helical edge states of two-dimensional topological insulators generate quasi dissipation-less charge and spin currents [Roth09, Brüne12] and, when combined with superconductors, open the possibility to host [Fu08] as well as braid [Mi13] Majorana bound states.
The research field of topological states of matter was born with the discovery of the quantum Hall effect [Klitzing80]. Unlike all previously known states of matter, it is not characterized by symmetry arguments, but by a topological quantum number [Kohmoto85]. This introduces a new and unexpected variety of different phases, which can be categorized by different topological indices [Schnyder08]. Although the topological characterization is a bulk property, it reveals itself by the existence of protected boundary modes through the bulk-boundary correspondence, underlining the experimental and application-technical relevance of these systems. The most prominent examples are topological insulators, which combine a band insulator in the bulk with metallic edge states. The knowledge and understanding of the building blocks of topological states of matters has led to a large number of proposals for topological band insulators in two [Kane05a, Bernevig06, Liu08, Hu12] and three [Fu07b, Fu07a, Zhang09] dimensions, which often have been verified experimentally [König07, Hsieh08, Xia09, Chen09, Brüne11, Knez11]. Further,

these concepts have been expanded to gapless phases [Matsuura13, Baum15a] and interaction driven systems in form of topological superconductors [Fu08, Qi09], Mott insulators [Raghu08] as well as Kondo insulators [Dzero10].
An apt tool to find new topological states of matter is to combine topological insulators with other types of materials. A very prominent example for this procedure is the prediction [Fu08] of topological superconductors, which arise in hybrid structures of topological insulators and ordinary (s-wave) superconductors. On the experimental side, superconductivity has been successfully induced into the helical edge states of two-dimensional topological insulators [Knez12, Hart14, Pribiag15] as well as into the surface states of three-dimensional insulators [Maier12, Sochnikov15]. Hosting zero energy bound states, topological superconductors are believed to show a fractional, i.e., 4π-periodic Josephson effect [Kitaev01, Fu09]. However, the experimental detection of the latter effect [Rokhinson12, Wiedenmann16] might be disguised by quasi-particle poisoning [Houzet13].

About this thesis

Potential applications of topological insulators in spintronic devices would need the fabrication of integrated circuits of topological insulators, which are finite in size and contacted by leads. This thesis advances the understanding of transport effects in heterostructures of topological insulators and introduces the novel superconducting quantum spin Hall effect. Moreover, it addresses two outstanding problems in the field: the measurement of crossed Andreev reflection and the detection of spin polarization in helical edge states.
Part I illustrates the physical background and methods needed to describe topological insulator heterojunctions. To be specific, chapter 2 introduces the concept of time-reversal symmetric topological insulators in terms of the Berry phase. Additionally, HgTe/CdTe quantum wells are introduced as an explicit and prominent example of two-dimensional topological insulators. Chapter 3 deals with the hybrid system of topological insulators and superconductors. The second building block, conventional superconductors, is recapitulated in section 3.1. The proximity effect, which induces superconductivity in normally conducting thin films, is presented in section 3.2, where we also demonstrate, that inducing conventional superconductivity into the helical boundary modes of a topological insulator gives rise to non-trivial triplet pairing terms. Depending on the cleanliness of the interface, the induced superconductivity is accompanied by a large (clean limit) or zero (dirty limit) doping of the thin film. Therefore, both limits will lead to different effective pairing terms, because they induce superconductivity in the bulk (cf. chapter 6) or the helical edge states (cf. chapter 7). Possible detection schemes for and applications of topological states of matter involve their unique transport properties. Therefore, chapter 4 describes phase coherent transport in mesoscopic systems. In particular, we introduce a generalized wave matching approach, the numerical solution of which allows to treat the scattering of bulk and edge modes on the same footing.
Part II presents the scientific results. First, chapter 5 focuses on the non-superconducting case and describes heterojunctions between two-dimensional topological insulators and highly doped metals. The physics of these devices is significantly enriched by finite size effects. For example, a single interface between a topological insulator and a metal cannot introduce backscattering of the helical edge states, unless the latter are directly coupled in narrow samples. This insight helps to interpret more sophisticated structures. Specifically, we analyze a topological insulator tunneling junction coupled to two metallic leads. This geometry has been found to support a conductance maximum in the tunneling bulk modes, providing a hallmark of the topologically non-trivial regime [Novik10, Recher10]. This thesis completes the characterization of the con-

ductance maximum by introducing hard wall boundary conditions. The presence of protected edge states does not alter the bulk mode transport, unless both species of modes are coupled by finite size effects. In chapter 6, similar arguments are used to introduce the coupling of helical edge states across a superconducting tunneling junction. This allows to generate and tune crossed Andreev reflection, a process which is conceptually forbidden for a single pair of helical edge states [Adroguer10]. Crossed Andreev reflection is connected with the non-local splitting of singlet Cooper pairs, which is a possible source of spin-entangled electrons. The measurement of this process is often disguised by simultaneously happening electron tunneling processes. However, when the leads are in the quantum spin Hall insulator regime, crossed Andreev reflection and electron tunneling are spatially separated for each Kramers' partner due to the helicity of the edge states. Based on this, we propose a feasible setup, which selects one Kramers' partner, and describe an all-electrical measurement scheme for the crossed Andreev reflection. In chapter 7, we describe the hybrid system of helical edge states in proximity to an ordinary superconductor in magnetic fields. We dub this phenomenon the superconducting quantum spin Hall effect, because its edge states remain spin-polarized and protected against elastic backscattering, even in finite in-plane magnetic fields. The interplay of helical states with $U(1)$-symmetry breaking superconductivity generates a giant g-factor. The latter allows to characterize the superconducting quantum spin Hall effect by tuning the edge state spectrum in weak magnetic fields, paving the way to possibly apply this novel effect as generator and detector of spin currents.
Chapter 8 concludes our results and gives some interesting prospects for future research.

Of course this thesis can only present a small part of the world-wide scientific struggle to understand and engineer new phases of matter. Further research is needed to deepen the understanding of the underlying physics and to bring these concepts to life in novel devices. Moreover, this thesis potentially triggers future experiments aiming to confirm the proposed effects and measurement schemes. Therefore, it is written in the spirit, that its research can be understood, reproduced and, most importantly, continued by students, who bring the knowledge of advanced quantum mechanics and basic solid state lectures but otherwise are new to the field. Especially the theory part should serve as a self-contained and detailed introduction to the physical background. Often further reading is suggested, especially when details are left out for the sake of brevity or readability.
The research presented in the chapters 5, 6 and 7 is based on the publications [Reinthaler12][1], [Reinthaler13][2] and [Reinthaler15][3], which are copyrighted by the corresponding publisher. These chapters adapt the text of the mentioned publications in parts word by word.

[1] ©2012 American Physical Society. All rights reserved.
[2] ©2013 American Physical Society. All rights reserved.
[3] ©2015 American Physical Society. All rights reserved.

Part I.

Theory and Methods

2. Two-dimensional topological insulators

In this chapter, we provide the reader with a notion of topologically protected states of matter. Specifically, we will be concerned with topological phases of matter which emerge in the presence of time-reversal symmetry. The latter is discussed in section 2.1. Section 2.2 classifies topological phases of matter by evaluating the time-reversal polarization in terms of the system's Berry phase. The experimental relevance of topological states of matter becomes clear in section 2.2.3, where we introduce the bulk-boundary correspondence. Finally, in section 2.3, we discuss HgTe quantum wells, in which the two-dimensional topological insulator phase has been experimentally realized for the first time.

2.1. Time-reversal symmetry

Our introduction to time-reversal symmetry (TRS) follows the classical textbook by Sakurai [Sakurai94], if not cited differently.

2.1.1. Time-reversal operator and Kramers' theorem

TRS is a discrete symmetry connected with the inversion of motion. The propagation of a wave function is dominated by the Schrödinger equation

$$\mathrm{i}\hbar\partial_t\psi(t) = H\psi(t), \tag{2.1}$$

where $\psi(t)$ is a solution to the time dependent problem. Since obviously $\partial_t \to -\partial_t$ under time-reversal, $\psi(-t)$ cannot be another valid solution, but $\psi^*(-t)$ is, provided that the system is spinless. Hence, we demand that complex conjugation is an integral part of time-reversal. Further, we would like to impose that the inner product of two states ($\langle\alpha|\beta\rangle$) remains unaltered under time-reversal. This is true for any unitary symmetry operator, like, e.g., rotations. Concerning TRS, however, this is in contradiction with the associated complex conjugation. Let us define the time-reversal operator ($\hat{\Theta}$) as the product of a unitary operator ($\hat{U}$) and the complex conjugation operator ($\hat{K}$):

$$\hat{\Theta} = \hat{U}\hat{K}. \tag{2.2}$$

In order to describe the action of time-reversal (TR) on a state $|\alpha\rangle$, let us define $\{|a\rangle\}$ to be an orthonormal basis of the Hilbert space. Assuming that $\hat{K}$ does not change the basis kets $|a\rangle$[1],

[1] This is a valid assumption, if this basis has an explicit, real representation, e.g., $\{|a\rangle\} = \{(1,0,\ldots)^T,(0,1,0,\ldots)^T,\ldots\}$. Note, however, that the general action of $\hat{K}$ on the basis ket might change upon basis transformation. In this sense, one has to additionally readjust the unitary operator $\hat{U}$ according to the chosen basis, see [Sakurai94] for details.

we can write the time-reversed state $\left|\hat{\Theta}\alpha\right\rangle$ as

$$\left|\hat{\Theta}\alpha\right\rangle := \hat{\Theta}\left|\alpha\right\rangle = \hat{\Theta}\left(\sum_a \left|a\right\rangle\left\langle a|\alpha\right\rangle\right) = \sum_a \left\langle a|\alpha\right\rangle^* \hat{U}\hat{K}\left|a\right\rangle = \sum_a \left\langle\alpha|a\right\rangle \hat{U}\left|a\right\rangle, \tag{2.3}$$

where we used the completeness relation $\sum_a \left|a\right\rangle\left\langle a\right| = \mathbb{I}$. The inner product hence transforms as

$$\begin{aligned}\left\langle\hat{\Theta}\beta|\hat{\Theta}\alpha\right\rangle &= \left(\sum_b \left\langle b|\beta\right\rangle \left\langle\hat{U}b\right|\right)\left(\sum_a \left\langle\alpha|a\right\rangle \hat{U}\left|a\right\rangle\right) \\ &= \sum_{a,b} \left\langle\alpha|a\right\rangle\left\langle b|\beta\right\rangle \underbrace{\left\langle\hat{U}b|\hat{U}a\right\rangle}_{=\langle b|a\rangle=\delta_{ba}} = \sum_a \left\langle\alpha|a\right\rangle\left\langle a|\beta\right\rangle = \left\langle\alpha|\beta\right\rangle,\end{aligned} \tag{2.4}$$

i.e., TRS is an anti-unitary operation conserving the absolute value of the inner product. A simple corollary of Eq. (2.4) is

$$\left\langle\hat{\Theta}\alpha\right|\hat{\Theta}\hat{A}\hat{\Theta}^{-1}\left|\hat{\Theta}\beta\right\rangle = \left\langle\hat{A}\beta|\alpha\right\rangle = \left\langle\beta\right|\hat{A}^\dagger\left|\alpha\right\rangle \tag{2.5}$$

for any linear operator $\hat{A}$.
As mentioned before, TRS can be seen as inversion of motion. Consequently, we expect TRS to invert the expectation value of the momentum operator $\hat{\boldsymbol{p}}$:

$$\left\langle\hat{\Theta}\alpha\right|\hat{\boldsymbol{p}}\left|\hat{\Theta}\alpha\right\rangle = -\left\langle\alpha\right|\hat{\boldsymbol{p}}\left|\alpha\right\rangle \Rightarrow \hat{\Theta}\hat{\boldsymbol{p}}\hat{\Theta}^{-1} = -\hat{\boldsymbol{p}}, \tag{2.6}$$

that is the momentum operator is odd under time-reversal. From this we can infer that $\hat{\boldsymbol{p}}\hat{\Theta}\left|\boldsymbol{p}'\right\rangle = -\hat{\Theta}\hat{\boldsymbol{p}}\hat{\Theta}^{-1}\hat{\Theta}\left|\boldsymbol{p}'\right\rangle = -\hat{\Theta}\boldsymbol{p}'\left|\boldsymbol{p}'\right\rangle = (-\boldsymbol{p}')\hat{\Theta}\left|\boldsymbol{p}'\right\rangle$, i.e., time-reversal inverses the momentum state

$$\hat{\Theta}\left|\boldsymbol{p}\right\rangle = \left|-\boldsymbol{p}\right\rangle. \tag{2.7}$$

In contrast, inversion of motion should not change the position. The position operator $\hat{\boldsymbol{x}}$ is even under time-reversal, which can also be deduced from the invariance of the fundamental commutation relation $[\hat{x}_i, \hat{p}_j] = \mathrm{i}\hbar\delta_{ij}$.
The commutation relation for angular momentum transforms according to

$$\begin{aligned}\hat{\Theta}\left[\hat{J}_i, \hat{J}_j\right]\left|\alpha\right\rangle &= \hat{\Theta}\mathrm{i}\hbar\epsilon_{ijk}\hat{J}_k\left|\alpha\right\rangle \\ \Leftrightarrow \left[\hat{\Theta}\hat{J}_i\hat{\Theta}^{-1}, \hat{\Theta}\hat{J}_j\hat{\Theta}^{-1}\right]\hat{\Theta}\left|\alpha\right\rangle &= -\mathrm{i}\hbar\epsilon_{ijk}\hat{\Theta}\hat{J}_z\hat{\Theta}^{-1}\hat{\Theta}\left|\alpha\right\rangle,\end{aligned} \tag{2.8}$$

and consequently remains unaltered for $\hat{\boldsymbol{J}}$ being odd: $\hat{\Theta}\hat{\boldsymbol{J}}\hat{\Theta}^{-1} = -\hat{\boldsymbol{J}}$.
In the following, we will restrict our discussion to spin-1/2 systems. We choose the real S_z eigenbasis representation, in which the spin operator is given by $\hat{S}_i = \hbar\sigma_i/2$, with σ_i being the Pauli matrices in spin space. In this basis

$$\hat{\Theta} = \hat{U}\hat{K} = -\mathrm{i}\frac{2}{\hbar}\hat{S}_y\hat{K} = -\mathrm{i}\sigma_y\hat{K} \tag{2.9}$$

is a suitable choice for the time-reversal operator. The action of TRS on the eigenstates $\sigma_z |\pm\rangle = \pm |\pm\rangle$ is to flip the spin

$$\hat{\Theta} |\pm\rangle = \pm |\mp\rangle . \tag{2.10}$$

From Eq. (2.9), one finds

$$\hat{\Theta}^2 = -\mathbb{I}. \tag{2.11}$$

This is in general true for all half-integer angular momentum states and has two striking consequences: Kramers' degeneracy and protection of the states against backscattering by any TR symmetric perturbation.

Kramers' degeneracy

Let $|\alpha\rangle$ be an eigenstate of H with energy E_α. In case H preserves TRS, i.e., $\left[H, \hat{\Theta}\right] = 0$, the time-reversed state $\hat{\Theta} |\alpha\rangle$ has the same energy eigenvalue, because

$$H\hat{\Theta} |\alpha\rangle = \hat{\Theta} H |\alpha\rangle = E_\alpha \hat{\Theta} |\alpha\rangle . \tag{2.12}$$

Assuming that $|\alpha\rangle$ and $\hat{\Theta} |\alpha\rangle$ represent the same physical state, they may only differ by a phase ϕ_α. In this case,

$$-\mathbb{I} |\alpha\rangle = \hat{\Theta}(\hat{\Theta} |\alpha\rangle) = \hat{\Theta}(\exp[\mathrm{i}\phi_\alpha] |\alpha\rangle) = \exp[-\mathrm{i}\phi_\alpha]\hat{\Theta} |\alpha\rangle = |\alpha\rangle \tag{2.13}$$

violates Eq. (2.11). In consequence, $|\alpha\rangle$ and $\hat{\Theta} |\alpha\rangle$ are enegetically degenerate but distinct states, called Kramers' partners.
In the above argument, we did not make any assumption about H except from that the system conserves TRS. This means that any TRS conserving interaction or potential cannot lift Kramers' degeneracy. This is especially true for electric potentials. However, TRS can be broken, for example, by applying a magnetic field.

Protection against backscattering

Let the Hamiltonian contain a TRS preserving scattering potential V, like it would, e.g., arise from non-magnetic impurities. Can this potential elastically scatter the state $|\alpha\rangle$ into its time-reversed partner $\hat{\Theta} |\alpha\rangle$? We follow an argument by Xu and Moore [Xu06] and calculate the matrix element of the scattering potential using Eqs. (2.4) and (2.11)

$$\left\langle \hat{\Theta}\alpha \middle| V \middle| \alpha \right\rangle = \left\langle \hat{\Theta} V \alpha | \hat{\Theta}^2 \alpha \right\rangle \overset{[V,\hat{\Theta}]=0}{=} - \left\langle \hat{\Theta}\alpha \middle| V^\dagger \middle| \alpha \right\rangle \overset{V=V^\dagger}{=} - \left\langle \hat{\Theta}\alpha \middle| V \middle| \alpha \right\rangle = 0. \tag{2.14}$$

Thus, direct, elastic backscattering between Kramers' partners is forbidden. This is at the heart of the transport phenomena analyzed in this thesis, i.e., ballistic charge and spin transport connected with the time-reversal symmetry protected, helical edge states in the quantum spin Hall (QSH) effect.
In the previous argument, we neglected inelastic effects from electron-electron interaction [Xu06, Wu06, Ström10, Crépin12] or electron-phonon interaction [Budich12b], which are expected to induce backscattering without breaking TRS.

2.1.2. Time-reversal symmetry for Bloch states

For the later use, let us analyze the effect of TR on Bloch waves. Bloch found that in a lattice periodic system the solutions of $\mathcal{H}\left|\psi_{n\boldsymbol{k}}\right\rangle = E_n(\boldsymbol{k})\left|\psi_{n\boldsymbol{k}}\right\rangle$ take the form

$$\left|\psi_{n\boldsymbol{k}}\right\rangle = \exp[\mathrm{i}\boldsymbol{k}\cdot\boldsymbol{x}]\left|u_n(\boldsymbol{k})\right\rangle, \tag{2.15}$$

where the index n stands for different degrees of freedom, like sub-bands or spins, and $\boldsymbol{k}$ is a conserved lattice momentum, spanning the Brillouin zone (BZ). For example, in a one-dimensional system with lattice constant a, the first BZ spans from $-\pi/a$ to π/a. The states $\left|u_n(\boldsymbol{k})\right\rangle$ have the same periodicity as the lattice and are eigenfunctions to the Bloch Hamiltonian $H(\boldsymbol{k})$. We want to find the action of TRS on the Bloch Hamiltonian

$$\begin{aligned}\hat{\Theta}\mathcal{H}\hat{\Theta}^{-1} &= \hat{\Theta}\int_{BZ}\mathrm{d}\boldsymbol{k}\ \left|\boldsymbol{k}\right\rangle H(\boldsymbol{k})\left\langle\boldsymbol{k}\right|\hat{\Theta}^{-1} \overset{(2.7)}{=} \int_{BZ}\mathrm{d}\boldsymbol{k}\ \left|-k\right\rangle\hat{\Theta}H(\boldsymbol{k})\hat{\Theta}^{-1}\left\langle -k\right| \\ &= \int_{BZ}\mathrm{d}\boldsymbol{k}\ \left|\boldsymbol{k}\right\rangle\hat{\Theta}H(-\boldsymbol{k})\hat{\Theta}^{-1}\left\langle\boldsymbol{k}\right|. \end{aligned}\tag{2.16}$$

In order to find $\mathcal{H}$ which preserves TRS, we need to impose

$$H(\boldsymbol{k}) = \hat{\Theta}H(-\boldsymbol{k})\hat{\Theta}^{-1} = \hat{U}H^*(-\boldsymbol{k})\hat{U}^{-1} \tag{2.17}$$

on the Bloch Hamiltonian. For Bloch states with spin-1/2, we find

$$\left|u_{\alpha\uparrow}(\boldsymbol{k})\right\rangle \quad \text{and} \quad \left|u_{\alpha\downarrow}(-\boldsymbol{k})\right\rangle \tag{2.18}$$

to be Kramers' partners. Here, $\uparrow$ and $\downarrow$ symbolize the Kramers' partners, which do not necessarily have to be perfect spin up or down states, and α is an additional degree of freedom, like, e.g., a sub-band. They are related by TRS via

$$\hat{\Theta}\left|u_{\alpha\uparrow}(\boldsymbol{k})\right\rangle = \exp[-\mathrm{i}\chi_\alpha(\boldsymbol{k})]\left|u_{\alpha\downarrow}(-\boldsymbol{k})\right\rangle, \quad \hat{\Theta}\left|u_{\alpha\downarrow}(\boldsymbol{k})\right\rangle = -\exp[-\mathrm{i}\chi_\alpha(-\boldsymbol{k})]\left|u_{\alpha\uparrow}(-\boldsymbol{k})\right\rangle, \tag{2.19}$$

where the relative sign comes from the opposite spin in Eq. (2.10) and the phase $\chi_\alpha(\boldsymbol{k})$ stems from the fact, that there is not necessarily a one-to-one correspondence between Kramers' partners and spin-z eigenstates.
The periodicity of the system demands that $\boldsymbol{k}$-points, which are connected by a vector $\boldsymbol{K} = l\frac{2\pi}{a}\hat{e}_{k_x} + m\frac{2\pi}{a}\hat{e}_{k_y}$, $l, m \in \mathbb{Z}$, are equivalent. Therefore, in the two-dimensional (2D) BZ there exist four momenta which, upon TRS ($\boldsymbol{k} \xrightarrow{\hat{\Theta}} -\boldsymbol{k}$), are mapped onto themselves or an equivalent momentum. These time-reversal invariant momenta (TRIM) Λ_i are explicitly shown in Fig. 2.1a. At these points we have $\hat{\Theta}\left|\Lambda_i\uparrow\right\rangle = \left|\Lambda_i\downarrow\right\rangle$. Thus, the two Kramers' partners must be degenerate at the TRIM. Fig. 2.1b shows the band structure of two pairs of Kramers' partners along one k-direction in the first BZ. At the two TRIM $k = \Lambda_0$ and $k = \Lambda_j = -\Lambda_j$, the branches for $\uparrow$ and $\downarrow$ cross. These degeneracies cannot be lifted as long as TRS is conserved.
At the end of this section, let us discuss the properties of a convenient matrix representation of $\hat{\Theta}$ using the Bloch wave basis [Ando13]. It will proof useful in writing down the topological invariant of a TR symmetric system in an elegant way. We define

$$w_{\alpha\beta}(\boldsymbol{k}) := \left\langle u_\alpha(-\boldsymbol{k})\right|\hat{\Theta}\left|u_\beta(\boldsymbol{k})\right\rangle, \tag{2.20}$$

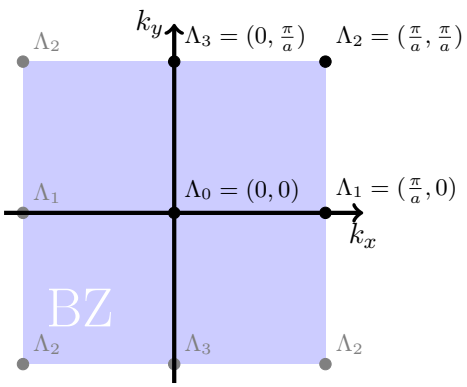

(a) 4 time-reversal invariant momenta (TRIM) in the first BZ

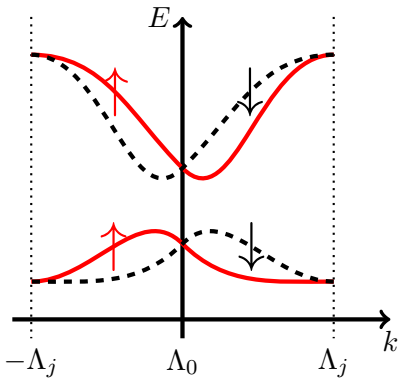

(b) Schematic of the bandstructure in presence of TRS. $\Lambda_j = -\Lambda_j$, $j = 1, 2, 3$ is a TRIM at the BZ border.

Figure 2.1.: The 4 TRIM of a 2D square lattice. At these Λ_i the two Kramers' partner branches meet. This degeneracy cannot be lifted unless TRS is broken.

which is unitary, because

$$\begin{aligned}\sum_\alpha w^\dagger_{\gamma\alpha}(\boldsymbol{k}) w_{\alpha\beta}(\boldsymbol{k}) &= \sum_\alpha \left\langle \hat{\Theta} u_\gamma(\boldsymbol{k}) | u_\alpha(-\boldsymbol{k}) \right\rangle \left\langle u_\alpha(-\boldsymbol{k}) | \hat{\Theta} u_\beta(\boldsymbol{k}) \right\rangle \\ &= \left\langle \hat{\Theta} u_\gamma(\boldsymbol{k}) | \hat{\Theta} u_\beta(\boldsymbol{k}) \right\rangle = \langle u_\beta(\boldsymbol{k}) | u_\gamma(\boldsymbol{k}) \rangle = \delta_{\beta\gamma}. \end{aligned} \tag{2.21}$$

Further with Eq. (2.4), on can show show that

$$w_{\beta\alpha}(-\boldsymbol{k}) = -w_{\alpha\beta}(\boldsymbol{k}), \tag{2.22}$$

making the matrix antisymmetric at the TRIM: $w_{\beta\alpha}(\Lambda_i) = -w_{\alpha\beta}(\Lambda_i)$. The matrix w connects two Bloch states at opposite $\boldsymbol{k}$ by

$$|u_\alpha(-\boldsymbol{k})\rangle = \sum_\beta \left\langle \hat{\Theta} u_\beta(\boldsymbol{k}) | u_\alpha(-\boldsymbol{k}) \right\rangle \left| \hat{\Theta} u_\beta(\boldsymbol{k}) \right\rangle = \sum_\beta w^*_{\alpha\beta}(\boldsymbol{k}) \hat{\Theta} \left| u_\beta(\boldsymbol{k}) \right\rangle . \tag{2.23}$$

As an example imagine $2N$ states, coupled in Kramers' pairs according to Eq. (2.19). In this case, the matrix w is given by

$$w(\boldsymbol{k}) = \begin{pmatrix} 0 & e^{-\mathrm{i}\chi_1(\boldsymbol{k})} & 0 & 0 & \cdots \\ -e^{-\mathrm{i}\chi_1(-\boldsymbol{k})} & 0 & 0 & 0 & \cdots \\ 0 & 0 & 0 & e^{-\mathrm{i}\chi_2(\boldsymbol{k})} & \cdots \\ 0 & 0 & -e^{-\mathrm{i}\chi_2(-\boldsymbol{k})} & 0 & \cdots \\ \vdots & \vdots & \vdots & \vdots & \ddots \end{pmatrix} . \tag{2.24}$$

2.2. Topological states of matter

In this section, we want to present an intuitive picture of topological states of matter from the point of view of the Berry phase, following, if not cited differently, the review by Ando [Ando13]. We will not dive deep into differential geometry and topology. For more details, the interested reader may consult, for example, the textbook by Nakahara [Nakahara03].

2.2.1. Adiabatic transport and Berry phase

Imagine a system, whose Hamiltonian is a function of a set of time dependent parameters $\boldsymbol{R}(t) = (R_1(t), R_2(t), \ldots)^T$. At each time t, we find a set of instantaneous eigenstates

$$\mathcal{H}[\boldsymbol{R}(t)]\,|\alpha, \boldsymbol{R}(t)\rangle = E_\alpha(t)\,|\alpha, \boldsymbol{R}(t)\rangle\,. \tag{2.25}$$

We want to calculate the time evolution of an arbitrary state by

$$\mathcal{H}[\boldsymbol{R}(t)]\,|\psi(t)\rangle = \mathrm{i}\hbar\frac{\mathrm{d}}{\mathrm{d}t}\,|\psi(t)\rangle\,. \tag{2.26}$$

When the initial state at $t = t_0$ is of the form $|\psi(t = t_0)\rangle = |\beta, \boldsymbol{R}(t_0)\rangle$, then the general solution is given by

$$|\psi(t)\rangle = \sum_\alpha c_\alpha(t)\,|\alpha, \boldsymbol{R}(t)\rangle\, e^{-\mathrm{i}\phi^D_\alpha(t)}, \tag{2.27}$$

where we defined the dynamical phase $\phi^D_\alpha(t) = \frac{1}{\hbar}\int_{t_0}^t \mathrm{d}t'\, E_\alpha(t')$. Plugging Eq. (2.27) into (2.26) one finds a differential equation for the coefficients

$$\dot{c}_\beta = -c_\beta\,\langle\beta, \boldsymbol{R}(t)|\,\frac{\mathrm{d}}{\mathrm{d}t}\,|\beta, \boldsymbol{R}(t)\rangle - \sum_{\alpha\neq\beta} e^{\mathrm{i}(\phi^D_\alpha(t)-\phi^D_\beta(t))} c_\alpha(t)\,\langle\alpha, \boldsymbol{R}(t)|\,\frac{\mathrm{d}}{\mathrm{d}t}\,|\beta, \boldsymbol{R}(t)\rangle\,. \tag{2.28}$$

If the initial state $|\beta, \boldsymbol{R}(t_0)\rangle$ is separated from the rest of the spectrum by an energy gap, which is larger than Δ at all times t, then we can rescale the time dependence as $t = s\mathcal{T}$, where $\hbar/s$ is of the order of Δ and $\mathcal{T}$ is called the adiabatic time scale. Born and Fock [Born28] proved that for slowly varying Hamiltonians, meaning $\mathcal{T} \to \infty$, the second term of Eq. (2.28) vanishes, resulting in

$$c_\beta(t) = c_\beta(t_0)\exp\left[-\int_{t_0}^t \mathrm{d}t'\,\langle\beta, \boldsymbol{R}(t')|\,\frac{\mathrm{d}}{\mathrm{d}t'}\,|\beta, \boldsymbol{R}(t')\rangle\right]. \tag{2.29}$$

The exponential is a pure phase factor, because

$$\begin{aligned} 0 = \frac{\mathrm{d}}{\mathrm{d}t}\,\langle\beta, \boldsymbol{R}(t)|\beta, \boldsymbol{R}(t)\rangle &= \langle\beta, \boldsymbol{R}(t)|\,\frac{\mathrm{d}}{\mathrm{d}t}\,|\beta, \boldsymbol{R}(t)\rangle + \left(\frac{\mathrm{d}}{\mathrm{d}t}\,\langle\beta, \boldsymbol{R}(t)|\right)|\beta, \boldsymbol{R}(t)\rangle \\ &= \langle\beta, \boldsymbol{R}(t)|\,\frac{\mathrm{d}}{\mathrm{d}t}\,|\beta, \boldsymbol{R}(t)\rangle + \langle\beta, \boldsymbol{R}(t)|\,\frac{\mathrm{d}}{\mathrm{d}t}\,|\beta, \boldsymbol{R}(t)\rangle^* \end{aligned} \tag{2.30}$$

and, consequently, $\langle\beta, \boldsymbol{R}(t)|\,\frac{\mathrm{d}}{\mathrm{d}t}\,|\beta, \boldsymbol{R}(t)\rangle$ is imaginary. Later on, the proof has been generalized to systems with degeneracies [Kato50]. Eq. (2.29) means that, when the system is evolving slowly on the scale of Δ, $|\psi(t)\rangle$ will not leave the eigenspace associated with the initial state $|\beta, \boldsymbol{R}(t_0)\rangle$. This is called the adiabatic theorem of quantum mechanics. For a long time, it was believed

that the phase in Eq. (2.29) can simply be gauged away and has no physical relevance. However, Berry [Berry84] realized that the phase arising by performing a closed loop $\mathcal{C}$ in the parameter space is gauge invariant and has physically observable consequences. When $\mathcal{C}$ is parametrized to start at $t = 0$ and to return to the starting position in parameter space at $t = T$, i.e., $\boldsymbol{R}(0) = \boldsymbol{R}(T)$, then the Berry phase associated with the loop is

$$\begin{aligned}\gamma_\alpha[\mathcal{C}] :=& \mathrm{i}\int_0^T \mathrm{d}t' \, \langle \alpha, \boldsymbol{R}(t')| \frac{\mathrm{d}}{\mathrm{d}t'} |\alpha, \boldsymbol{R}(t')\rangle = \mathrm{i}\int_0^T \mathrm{d}t' \, \langle \alpha, \boldsymbol{R}| \nabla_{\boldsymbol{R}} |\alpha, \boldsymbol{R}\rangle \cdot \dot{\boldsymbol{R}}(t') \\ =& \mathrm{i}\oint_{\mathcal{C}} \mathrm{d}\boldsymbol{R} \cdot \langle \alpha, \boldsymbol{R}| \nabla_{\boldsymbol{R}} |\alpha, \boldsymbol{R}\rangle = -\oint_{\mathcal{C}} \mathrm{d}\boldsymbol{R} \cdot \boldsymbol{A}_\alpha(\boldsymbol{R}). \end{aligned} \tag{2.31}$$

The hereby defined Berry connection

$$\boldsymbol{A}_\alpha(\boldsymbol{R}) = -\mathrm{i} \langle \alpha, \boldsymbol{R}| \nabla_{\boldsymbol{R}} |\alpha, \boldsymbol{R}\rangle \tag{2.32}$$

acts as a gauge potential on the parameter space R, because a gauge transformation $|\alpha, \boldsymbol{R}\rangle \to \exp[\mathrm{i}\phi(\boldsymbol{R})] |\alpha, \boldsymbol{R}\rangle$ results in

$$\boldsymbol{A}_\alpha(\boldsymbol{R}) \to -\mathrm{i} \langle \alpha, \boldsymbol{R}| \exp[-\mathrm{i}\phi(\boldsymbol{R})] \nabla_{\boldsymbol{R}} (\exp[\mathrm{i}\phi(\boldsymbol{R})] |\alpha, \boldsymbol{R}\rangle) = \boldsymbol{A}_\alpha(\boldsymbol{R}) + \nabla_{\boldsymbol{R}}\phi(\boldsymbol{R}). \tag{2.33}$$

The algebraic similarity to the magnetic vector potential allows to define the Berry curvature

$$\boldsymbol{B}_\alpha(\boldsymbol{R}) = \nabla_{\boldsymbol{R}} \times \boldsymbol{A}_\alpha(\boldsymbol{R}), \tag{2.34}$$

which, analogously to the magnetic field, is gauge invariant. Let S be the surface encircled by $\mathcal{C}$. Stokes theorem allows to rewrite the Berry phase as

$$\gamma_\alpha[\mathcal{C}] = -\int_S \mathrm{d}\boldsymbol{S} \cdot \boldsymbol{B}_\alpha(\boldsymbol{R}), \tag{2.35}$$

showing that $\gamma_\alpha[\mathcal{C}]$ is a gauge invariant quantity.
As a first example for the significance of the Berry phase, we calculate the Hall conductance in the quantum Hall (QH) effect in appendix A. We find that it is quantized and given by summing up the Berry phase associated with the BZ of the occupied bands

$$\sigma_{xy} = \frac{e^2}{h} \sum_{\alpha,\mathrm{occ}} \left(-\frac{\gamma_\alpha[\partial BZ]}{2\pi} \right) = \frac{e^2}{h} \sum_{\alpha,\mathrm{occ}} n_\alpha. \tag{2.36}$$

In this case, the Berry phase counts the number of flux quanta in the magnetic unit cell and is defined for a system in which TRS is broken. This also defines an integer topological invariant n_α, the so-called Chern number or TKNN invariant.
In the following, we will mainly concentrate on systems which conserve TRS. Therefore, we define the Berry connection matrix

$$\boldsymbol{a}_{\alpha\beta}(\boldsymbol{k}) = -\mathrm{i} \langle u_\alpha(\boldsymbol{k})| \nabla_{\boldsymbol{k}} |u_\beta(\boldsymbol{k})\rangle = \boldsymbol{a}^*_{\beta\alpha}(\boldsymbol{k}) \tag{2.37}$$

in the Bloch basis, where we identified $\boldsymbol{R}$ with the lattice momentum $\boldsymbol{k}$. In a system of d spatial dimensions, $\boldsymbol{a}$ thus is a d-dimensional vector of matrices. In presence of TRS, we can relate the

matrix entries at the points $\boldsymbol{k}$ and $-\boldsymbol{k}$ via ($\nabla_{\boldsymbol{k}} = -\nabla_{-\boldsymbol{k}} = -\hat{\Theta}\nabla_{\boldsymbol{k}}\hat{\Theta}^{-1}$)

$$\begin{aligned}
\boldsymbol{a}_{\alpha\beta}(-\boldsymbol{k}) &= -\,\mathrm{i}\,\langle u_\alpha(-\boldsymbol{k})|\,\nabla_{\boldsymbol{k}}\,|u_\beta(-\boldsymbol{k})\rangle \overset{(2.23)}{=} -\mathrm{i}\sum_{\gamma\delta} w_{\alpha\delta}(\boldsymbol{k})\left\langle\hat{\Theta}u_\delta(\boldsymbol{k})\right|\nabla_{\boldsymbol{k}}\left(\left|\hat{\Theta}u_\gamma(\boldsymbol{k})\right\rangle w^*_{\beta\gamma}(\boldsymbol{k})\right)\\
&= +\,\mathrm{i}\sum_{\gamma\delta} w_{\alpha\delta}(\boldsymbol{k})\underbrace{\left\langle\hat{\Theta}u_\delta(\boldsymbol{k})\right|\hat{\Theta}\nabla_{\boldsymbol{k}}\hat{\Theta}^{-1}\left|\hat{\Theta}u_\gamma(\boldsymbol{k})\right\rangle}_{\overset{(2.5)}{=}-\langle u_\gamma(\boldsymbol{k})|\nabla_{\boldsymbol{k}}|u_\delta(\boldsymbol{k})\rangle\overset{(2.37)}{=}-\mathrm{i}\boldsymbol{a}^*_{\delta\gamma}(\boldsymbol{k})} w^*_{\beta\gamma}(\boldsymbol{k}) - \mathrm{i}\sum_{\gamma\delta} w_{\alpha\delta}(\boldsymbol{k})\nabla_{\boldsymbol{k}} w^*_{\beta\gamma}(\boldsymbol{k})\delta_{\gamma\delta}\\
&= \sum_{\gamma\delta}\left[w_{\alpha\delta}(\boldsymbol{k})\boldsymbol{a}^*_{\delta\gamma}(\boldsymbol{k})w^\dagger_{\gamma\beta}(\boldsymbol{k}) - \mathrm{i}w_{\alpha\delta}(\boldsymbol{k})\nabla_{\boldsymbol{k}} w^\dagger_{\gamma\beta}(\boldsymbol{k})\delta_{\gamma\delta}\right].
\end{aligned} \tag{2.38}$$

Summing up the Berry connections of all bands corresponds to the trace

$$\begin{aligned}
\mathrm{Tr}\,\boldsymbol{a}(-\boldsymbol{k}) &= \mathrm{Tr}\left[w(\boldsymbol{k})\boldsymbol{a}^*(\boldsymbol{k})w^\dagger(\boldsymbol{k})\right] - \mathrm{i}\,\mathrm{Tr}\left[w(\boldsymbol{k})\nabla_{\boldsymbol{k}} w^\dagger(\boldsymbol{k})\right]\\
&= \mathrm{Tr}\,\boldsymbol{a}(\boldsymbol{k}) + \mathrm{i}\,\mathrm{Tr}\left[w^\dagger(\boldsymbol{k})\nabla_{\boldsymbol{k}} w(\boldsymbol{k})\right].
\end{aligned} \tag{2.39}$$

In the last step, the term has been simplified by the cyclic invariance of the trace together with Eqs. (2.21) and (2.37). For the second summand, we additionally employed $w(\boldsymbol{k})\nabla_{\boldsymbol{k}} w^\dagger(\boldsymbol{k}) = -[\nabla_{\boldsymbol{k}} w(\boldsymbol{k})]w^\dagger(\boldsymbol{k})$, which follows from the unitary of $w(\boldsymbol{k})$. Finally, we arrive at

$$\mathrm{Tr}\,\boldsymbol{a}(\boldsymbol{k}) = \mathrm{Tr}\,\boldsymbol{a}(-\boldsymbol{k}) - \mathrm{i}\,\mathrm{Tr}\left[w^\dagger(\boldsymbol{k})\nabla_{\boldsymbol{k}} w(\boldsymbol{k})\right]. \tag{2.40}$$

2.2.2. Time-reversal polarization and Z_2 invariant

TR symmetric systems are not characterized by an integer invariant, like the TKNN invariant derived in appendix A, but by a topological invariant which is defined as an integer modulo 2 (Z_2 invariant). We want to motivate the Z_2 invariant for a 2D system by looking at the pumping of a time-reversal polarization in a one dimensional system [Fu06]. For the pumping process, we assume the system to evolve in time with periodicity T:

$$H(t+T) = H(t). \tag{2.41}$$

Hence, the system must be TR symmetric at times $t = 0$ and $t = T/2$. We consider a state $|\alpha s\rangle$, where α labels the energy band and $s = \uparrow, \downarrow$ is the Kramers' partner. Its charge polarization is related to the Berry connection [King-Smith93]

$$P_{\alpha s} = -\frac{1}{2\pi}\int_{-\pi}^{\pi} \mathrm{d}k\, A_{\alpha s}(k). \tag{2.42}$$

Here for the 1D system, we do not use the vector notation and the 1D BZ spans from $-\pi$ to π, because the lattice constant $a = 1$ has been chosen. Let us motivate the above form of the charge polarization by introducing the Wannier states, which are localized at the lattice vector R

$$|W_{\alpha s}(R)\rangle = \frac{1}{\sqrt{2\pi}}\int_{\mathrm{BZ}} \mathrm{d}k\, \exp[-\mathrm{i}kR]\,|\psi_{\alpha sk}\rangle\,, \tag{2.43}$$

as the Fourier transformation of the Bloch states (2.15). The polarization can be calculated as the dipole moment of the Wannier charge density [Bohm03]

$$P_{\alpha s} \propto \langle W_{\alpha s}(R=0)|\,\hat{r}\,|W_{\alpha s}(R=0)\rangle = \frac{1}{2\pi}\int \mathrm{d}k \int \mathrm{d}k'\, \exp[-\mathrm{i}(k-k')R]\,\langle \psi_{\alpha s k}|\,\hat{r}\,|\psi_{\alpha s k'}\rangle\,. \quad (2.44)$$

The connection to Eq. (2.42) can be seen by the matrix element of the Bloch states with the position operator, which is [Bohm03]

$$\langle \psi_{\alpha s k}|\,\hat{r}\,|\psi_{\alpha s k'}\rangle = -\mathrm{i}\partial_k \delta(k-k') + \delta(k-k')\,\langle u_{\alpha s}(k)|\,\mathrm{i}\partial_k\,|u_{\alpha s}(k)\rangle\,. \quad (2.45)$$

The first term is antisymmetric and vanishes upon integration in Eq. (2.44) for $R=0$. We define the total charge polarization for each Kramers' partner flavor s

$$P_s = \sum_{\alpha=1}^{N} P_{\alpha s}. \quad (2.46)$$

The total charge polarization P and the time-reversal polarization P_Θ are thus given to by

$$P = P_\uparrow + P_\downarrow, \quad P_\Theta = P_\uparrow - P_\downarrow = 2P_\uparrow - P. \quad (2.47)$$

We assume $2N$ states to be occupied, of which always two have the same energy index α and - due to Kramers' degeneracy - are related by Eq. (2.19) at $t = 0, T/2$. The matrix representation of $\hat{\Theta}$ is given by Eq. (2.24). With this, we derive a useful relation for the Berry connection matrix

$$\begin{aligned} a_{(\alpha\uparrow)(\alpha\uparrow)}(-k) &\overset{(2.38)}{=} \sum_{\beta\beta' ss'} w_{(\alpha\uparrow)(\beta s)}(k) a^*_{(\beta s)(\beta' s')}(k) w^\dagger_{(\beta' s')(\alpha\uparrow)}(k) - \mathrm{i}\sum_{\beta s} w_{(\alpha\uparrow)(\beta s)}(k)\partial_k w^\dagger_{(\beta s)(\alpha\uparrow)}(k) \\ &\overset{(2.24)}{=} w_{(\alpha\uparrow)(\alpha\downarrow)}(k) a_{(\alpha\downarrow)(\alpha\downarrow)}(k) w^*_{(\alpha\uparrow)(\alpha\downarrow)}(k) - \mathrm{i} w_{(\alpha\uparrow)(\alpha\downarrow)}(k)\partial_k w^\dagger_{(\alpha\downarrow)(\alpha\uparrow)}(k) \\ &= a_{(\alpha\downarrow)(\alpha\downarrow)}(k) + \partial_k \chi_\alpha(k). \end{aligned} \quad (2.48)$$

By splitting the integral into two parts, we can simplify

$$\begin{aligned} P_\uparrow &= -\frac{1}{2\pi}\sum_{\alpha=1}^{N}\left(\int_0^\pi \mathrm{d}k\, a_{(\alpha\uparrow)(\alpha\uparrow)}(k) + \int_{-\pi}^0 \mathrm{d}k\, a_{(\alpha\uparrow)(\alpha\uparrow)}(k)\right) \\ &= -\frac{1}{2\pi}\int_0^\pi \mathrm{d}k \underbrace{\sum_\alpha \left(a_{(\alpha\uparrow)(\alpha\uparrow)}(k) + a_{(\alpha\downarrow)(\alpha\downarrow)}(k)\right)}_{=\mathrm{Tr}[a(k)]} - \frac{1}{2\pi}\sum_\alpha \underbrace{\int_0^\pi \mathrm{d}k\,\partial_k \chi_\alpha(k)}_{=\chi_\alpha(\pi)-\chi_\alpha(0)} \\ &\overset{(2.24)}{=} -\frac{1}{2\pi}\int_0^\pi \mathrm{d}k\ \mathrm{Tr}[a(k)] - \frac{\mathrm{i}}{2\pi}\log\left[\frac{\prod_\alpha w_{(\alpha\uparrow)(\alpha\downarrow)}(\pi)}{\prod_\alpha w_{(\alpha\uparrow)(\alpha\downarrow)}(0)}\right] \\ &= -\frac{1}{2\pi}\int_0^\pi \mathrm{d}k\ \mathrm{Tr}[a(k)] - \frac{\mathrm{i}}{2\pi}\log\left[\frac{\mathrm{Pf}[w(\pi)]}{\mathrm{Pf}[w(0)]}\right]. \end{aligned} \quad (2.49)$$

At the TRIM, where $-k = k$, w takes the simple form $w_{(\alpha\uparrow)(\alpha\downarrow)} = -w_{(\alpha\downarrow)(\alpha\uparrow)}$, cf. Eq. (2.24). With this, its determinant is given by $\det[w] = \left[\prod_\alpha w_{(\alpha\uparrow)(\alpha\downarrow)}\right]^2$, so that we could introduce the Pfaffian into Eq. (2.49). The Pfaffian is defined as $\mathrm{Pf}[M]^2 = \det[M]$ for any skew symmetric

matrix M. The time-reversal polarization becomes

$$\begin{aligned} P_\Theta = \; & 2P_\uparrow - P = \frac{1}{2\pi}\left(-\int_0^\pi \mathrm{d}k\, 2Tr[a(k)] + \int_{-\pi}^{\pi} \mathrm{d}k\ \mathrm{Tr}[a(k)]\right) - \frac{\mathrm{i}}{\pi}\log\left[\frac{\mathrm{Pf}[w(\pi)]}{\mathrm{Pf}[w(0)]}\right] \\ = \; & \frac{1}{2\pi}\int_0^\pi \mathrm{d}k\ (-\mathrm{Tr}[a(k)] + \mathrm{Tr}[a(-k)]) - \frac{\mathrm{i}}{\pi}\log\left[\frac{\mathrm{Pf}[w(\pi)]}{\mathrm{Pf}[w(0)]}\right] \\ \overset{(2.40)}{=} \; & \frac{\mathrm{i}}{2\pi}\int_0^\pi \mathrm{d}k\ \mathrm{Tr}\left[w^\dagger(k)\partial_k w(k)\right] - \frac{\mathrm{i}}{\pi}\log\left[\frac{\mathrm{Pf}[w(\pi)]}{\mathrm{Pf}[w(0)]}\right] \\ = \; & \frac{\mathrm{i}}{2\pi}\int_0^\pi \mathrm{d}k\, \partial_k \log\det[w(k)] - \frac{\mathrm{i}}{\pi}\log\left[\frac{\mathrm{Pf}[w(\pi)]}{\mathrm{Pf}[w(0)]}\right] \\ = \; & \frac{1}{\mathrm{i}\pi}\log\left[\frac{\sqrt{\det[w(0)]}}{\mathrm{Pf}[w(0)]}\cdot\frac{\mathrm{Pf}[w(\pi)]}{\sqrt{\det[w(\pi)]}}\right]. \end{aligned} \tag{2.50}$$

Again, we have made use of the explicit form of w, cf. Eq. (2.24), and evaluated the trace

$$\begin{aligned} \mathrm{Tr}[w^\dagger(k)\partial_k w(k)] &= \partial_k \sum_\alpha (-\mathrm{i})\left[\chi_\alpha(k) + \chi_\alpha(-k)\right] \\ &= \partial_k \log\prod_\alpha \exp\left[-\mathrm{i}\left(\chi_\alpha(k) + \chi_\alpha(-k)\right)\right] = \partial_k \log\det[w(k)]. \end{aligned} \tag{2.51}$$

The argument of the logarithm in Eq. (2.50) can only have the values 1 or -1. The angle in the complex plane is 2π-periodic and, hence, the polarization at the TR symmetric times can only describe two different states: $P_\Theta \mod 2 = 0$ or 1, corresponding to the log[1] and log[-1] solution, respectively. The difference in polarization at the two time-reversal invariant times

$$\nu = P_\Theta\left(\frac{T}{2}\right) - P_\Theta(0) \tag{2.52}$$

is only defined up to modulo 2. Thus, it is apt to define a topological invariant which is defined as an integer modulo 2 (Z_2 invariant). It casts the Hilbert space in two different groups: $\nu = 0$ describes the trivial case, whereas $\nu = 1$ means that a topological charge has been pumped during the half circle from $t = 0$ to $t = T/2$. The last describes the topologically non-trivial case.

The Z_2 invariant defined for pumping a time-reversal charge in a 1D system is equivalent to that of a 2D topological insulator (TI), as was argued by Fu and Kane [Fu06]. This is analogous to the Laughlin argument [Laughlin81] for the quantization of the Hall conductance in the QH effect. The equivalence can be understood by identifying the phase space (k, t) with (k_x, k_y), because both have the same periodicity for $T = 2\pi$. The Z_2 invariant then is given in terms of

the TRIM of the 2D BZ, which are specified in Fig. 2.1a:

$$\begin{aligned} & \nu \mathrm{i}\pi = \log\left[\frac{\sqrt{\det[w(\Lambda_0)]}}{\mathrm{Pf}[w(\Lambda_0)]}\cdot\frac{\mathrm{Pf}[w(\Lambda_1)]}{\sqrt{\det[w(\Lambda_1)]}}\right] - \log\left[\frac{\sqrt{\det[w(\Lambda_2)]}}{\mathrm{Pf}[w(\Lambda_2)]}\cdot\frac{\mathrm{Pf}[w(\Lambda_3)]}{\sqrt{\det[w(\Lambda_3)]}}\right] \\ \Leftrightarrow \quad & \nu \mathrm{i}\pi = \log\left[\prod_{i=0}^{4}\frac{\mathrm{Pf}[w(\Lambda_i)]}{\sqrt{\det[w(\Lambda_i)]}}\right] \\ \Leftrightarrow \quad & (-1)^{\nu} = \prod_{i=1}^{4}\frac{\mathrm{Pf}[w(\Lambda_i)]}{\sqrt{\det[w(\Lambda_i)]}}. \end{aligned} \tag{2.53}$$

Topological insulators with inversion symmetry

Spatial inversion is described by the parity operator ($\hat{\Pi}$) acting according to

$$\hat{\Pi}\,|\boldsymbol{r},\alpha,s\rangle = |-\boldsymbol{r},\alpha,s\rangle\,, \tag{2.54}$$

where $\boldsymbol{r}$ is the spatial position vector and s stands for the Kramers' partner. Letting $\hat{\Pi}$ act twice on the same state, we find $\hat{\Pi}^2 = \mathbb{I}$ and thus the parity operator can only have the eigenvalues 1 or -1. Fu and Kane [Fu07a] showed that the Z_2 invariant of a system which preserves TRS can be expressed in the parity eigenvalues $\xi_{\alpha s}(\Lambda_i)$ of the Bloch states $|u_{\alpha s}(\Lambda_i)\rangle$ at the TRIM of the BZ. Since the parity for the two Kramers' partners is the same, $\xi_{\alpha\uparrow} = \xi_{\alpha\downarrow} = \xi_\alpha$, one finds for $2N$ occupied states [Fu07a]

$$(-1)^{\nu} = \prod_{i=1}^{4}\prod_{\alpha=1}^{N}\xi_\alpha(\Lambda_i). \tag{2.55}$$

In section 2.3.2, we will use this simple formula to classify the topology of the effective model for HgTe quantum wells (QWs).

Three-dimensional topological insulators

Although this work focuses on 2D TIs, we would like to mention that the above formalism for 2D systems can be generalized to three-dimensional (3D) TIs [Fu07b]. In this case, the BZ has 8 TRIM and six sides, each of which is equivalent to a 2D BZ, cf. Fig. 2.2. These systems are characterized by four Z_2 invariants $(\nu_0;\nu_x,\nu_y,\nu_z)$. The first one involves all 8 TRIM in Fig. 2.2

$$(-1)^{\nu_0} = \prod_{k_x=0,\pi}\prod_{k_y=0,\pi}\prod_{k_z=0,\pi}\frac{\mathrm{Pf}[w(\Lambda_{k_x,k_y,k_z})]}{\sqrt{\det[(\Lambda_{k_x,k_y,k_z})]}}. \tag{2.56}$$

It characterizes the system to be a "strong" ($\nu_0 = 1$) or weak ($\nu_0 = 0$) topological insulator. The remaining indices correspond to a certain direction in the reciprocal space and are given by

$$(-1)^{\nu_i} = \prod_{j\neq i}\prod_{k_{j\neq i}=0,\pi;k_i=0}\frac{\mathrm{Pf}[w(\Lambda_{k_x,k_y,k_z})]}{\sqrt{\det[(\Lambda_{k_x,k_y,k_z})]}}, \quad i = x,y,z. \tag{2.57}$$

In the case of $\nu_0 = 0$ and $\nu_i \neq 0,\ i = x,y,z$, the system can be interpreted as 2D TIs stacked in the $\boldsymbol{G} = \sum_{i=x,y,z}\nu_i\hat{e}_i$ direction. These are characterized by unprotected surface states on the

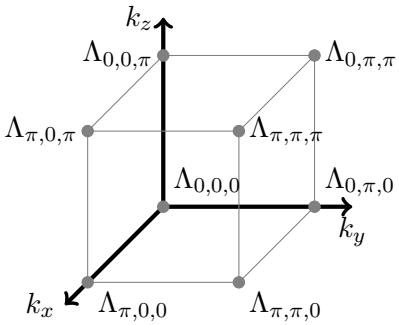

Figure 2.2.: The 3D BZ has 8 TRIM, from which we can calculate 4 independent topological indices.

side planes, i.e., the planes parallel to $\boldsymbol{G}$.
A vast variety of different realizations of 3D TI phases has been predicted and measured, e.g., in $Bi_{1-x}Sb_x$ [Fu07b, Hsieh08], in Bi_2X_3, where X=Se,Te, [Zhang09, Xia09, Chen09] and in strained HgTe [Fu07a, Brüne11].
Moreover, each possible 3D TI is also a promising candidate for supporting a 2D TI phase. In thin films of 3D TIs, the surface states of the top and bottom surface hybridize and open a gap. This gap closes as the energetically lowest lying states, which have opposite parity, cross at certain thicknesses d_z of the thin film. The parity changes at each crossing, leading to the oscillations between topologically trivial and non-trivial insulators as a function of the film thickness [Shan10, Lu10, Liu10b]. Around the band crossing points, a folding of the Hamiltonian of the 3D TI [Zhang09, Liu10a] to the energetically lowest sub-bands reproduces the 2D model of a 2D TI. In chapters 5 and 7 we will use a 3D TI thin film as a concrete realization of a 2D TI.

2.2.3. Topological protection and bulk-boundary correspondence

The time-reversal polarization in Eq. (2.50) can only have the two values 0 or 1. The two polarization states are not adiabatically connected. This implies that the $2N$ occupied bands, which we assumed in the derivation of Eq. (2.50), are always separated from the unoccupied states by a finite energy gap, i.e., the system is an insulator. In other words: a continuous deformation of the bands that does not close the gap is not able to flip the polarization state from 0 to 1 or vice versa. In a QH insulator, the bands are Landau levels and the gap between them is induced by a magnetic field. In a TRS conserving TI, the gap opening is induced by spin-orbit interaction [Kane05a] or possibly by interactions [Raghu08, Dzero10].
A topological phase transition, that is the transition from the state with one polarization to the other, can hence only occur upon gap closing. In consequence, a spatial transition from a topologically non-trivial insulator to a topologically trivial one (e.g. vacuum) is accompanied by a spatially local gap closure. This means that a topological insulator, although being an insulator, is always associated with metallic states at its boundary. This is referred to as the *bulk-boundary correspondence* which connects the topological invariant, which is defined as a bulk property, with the existence of metallic states. In the case of the integer QH effect, Halperin [Halperin82] found that the corresponding invariant (TKNN invariant) gives the number of localized edge states surrounding the QH insulator. Since these states are chiral, i.e., they

(a) $\nu = 0$, trivial

(b) $\nu = 1$, non-trivial

Figure 2.3.: Electronic dispersion of a 2D TR symmetric insulator for half of the BZ. The bulk gap between the valence (blue) and conduction (green) bands is closed at the boundary of the system (black lines). In the trivial case (a), an even number of edge modes crosses the Fermi energy E_F. The non-trivial case (b) shows an odd number of edge channels at E_F. At the neighboring TRIMs, Λ_a and Λ_b, the modes are degenerate.

propagate only in one direction, the absence of counter-propagating states leads to protection against backscattering.

In the case of a TRS preserving TI, the situation is a bit different. The Z_2 invariant (2.53) is only defined modulo 2. It is thus not directly connected to the number of boundary modes crossing the Fermi energy E_F, but to the number of crossings in half of the BZ modulo 2. To illustrate this better, we follow the argumentation in [Fu07a, Hasan10] and show the dispersion of a TR symmetric insulator between two neighboring TRIM (Λ_a and Λ_b) in Fig. 2.3. For the following argument, it is crucial to restrict the discussion to half the BZ, because the second half of the BZ ($-\Lambda_b$ to Λ_a) is determined by TRS. Therefore, looking at the whole BZ, there is always an even number of modes at all energies[2]. At the TRIM, Kramers' theorem dictates twofold degeneracy. There are two possibilities to connect these degenerate states: pairwise, as in Fig. 2.3a, or by a single branch, as in Fig. 2.3b. For the first case, where an even number of modes crosses E_F, the pair of edge states can simply be shifted out of the gap, corresponding to a topologically trivial state with $\nu = 0$. On the other hand, the single branch in Fig. 2.3b cannot be shifted out of the band gap. This situation is identified by an odd number of crossings, describing the topologically non-trivial insulator with $\nu = 1$.

Kramers' degeneracy dictates that for each mode at lattice momentum $\boldsymbol{k}$ there will always be an additional mode at $-\boldsymbol{k}$, cf. Fig. 2.1b. However, scattering into this mode is forbidden according to Eq. (2.14). The protected edge states are helical, i.e., the momentum is locked to the Kramers' partner polarization. Therefore, these systems are often referred to as quantum spin Hall insulator (QSHI) in accordance to the QH effect. Additionally to quantized charge transport, the QSH effect allows for quantized spin currents [Kane05a].

In the discussion of Eq. (2.14), we already mentioned that there are corrections to the topological protection against backscattering due to many-particle effects. An additional single-particle backscattering process can be induced by the overlap of edge modes at opposite boundaries. States at different boundaries do not belong to the same Kramers' pair and hybridize, when

[2]Equivalently, we could have considered the full BZ and restrict the discussion to one Kramers' partner.

they are not sufficiently separated by the gapped bulk material. Such finite size effects have first been reported in [Zhou08] and are of one of the central topics of chapters 5 and 6.

2.3. HgTe quantum wells as two-dimensional topological insulators

Graphene was the first material, for which a TR symmetric 2D TI phase has been predicted [Kane05a]. Undoped graphene shows the linear dispersion of massless relativistic electrons, so-called Dirac cones [Castro Neto09]. Kane and Mele found a TRS preserving spin-orbit interaction (SOI), which opens a topologically non-trivial gap at the Dirac points. First principle calculations, however, revealed that this gap is too small to be observed experimentally [Min06, Yao07]. Heavy elements, which have strong SOI, became possible candidates for 2D TIs. Indeed the first proposal using a HgTe/CdTe quantum well (QW) [Bernevig06] was soon confirmed experimentally [König07] to show the QSH effect.
Following the course of using heavy elements, 2D TI phases have been proposed, e.g., in 2D bismuth [Murakami06], in inverted type-II semiconductors [Liu08] and even in graphene, provided SOI is enhanced by heavy ad-atoms [Hu12]. However, the QSH effect has so far only been observed in inverted HgTe/CdTe [König07] and InAs/GaSb [Knez11] QWs. Since the latter has a very small and indirect band gap, HgTe/CdTe QWs remain the prime material for 2D TIs.
Here, we introduce an effective low-energy Hamiltonian to describe HgTe/CdTe QWs in section 2.3.1. In section 2.3.2, we calculate the topological classification as a bulk property of the effective model, while in section 2.3.3, we use the tight binding (TB) formalism to analyze the resulting edge states.

2.3.1. Effective low-energy model

The compound HgTe was one of the first candidates for 2D [Bernevig06] and 3D [Fu07a] TIs, because of its strong SOI . In the 2D case, a thin layer of HgTe is embedded in a CdTe barrier. Both materials crystallize in the Zinc blende structure with roughly the same lattice constant. Their bulk dispersions are plotted in Fig. 2.4. CdTe is a normal semiconductor, which has a large energy gap at the Γ-point between the s-type Γ_6 band and the p-type Γ_8 bands[3]. HgTe exhibits an inverted band structure, where the Γ_6 band lies below the Γ_8 bands. This is quantified by a negative gap value of $E_{\text{gap}} = E_{\Gamma_6} - E_{\Gamma_8} = -0.303$ eV [Pfeuffer-Jeschke00]. The band inversion is the result of the interplay of relativistic mass-velocity correction terms and strong SOI in the system [Brüne13]. The Fermi energy lies between the light- and heavy hole branch of the Γ_8 band which touch each other, i.e., bulk HgTe behaves like a semi-metal. The gap can be opened by strain in case of a 3D TI [Fu07a] or, for a 2D TI, by confining the system in a QW, e.g., by sandwiching HgTe within CdTe layers [Bernevig06].
HgTe/CdTe QWs can be described in an 8×8-Kane Hamiltonian [Pfeuffer-Jeschke00, Novik05]. We assume the quantum well to be grown in z-direction. The well width, meaning the thickness of the central HgTe layer, is d_{QW}. Neglecting the spin split-off bands Γ_7, Bernevig et al. [Bernevig06] found the sub-band structure at $k_x = k_y = 0$, which is presented in Fig. 2.5 as a function of d_{QW}. One finds that the lowest lying states around the Fermi energy are an electron like (E1) and heavy-hole like (H1) sub-band, which originate mainly from the Γ_6 and Γ_8 bands, respectively. At large d_{QW}, we observe the inverted band ordering of bulk HgTe. The heuristic reason is that in a thick HgTe layer its bulk band structure survives. Going to very small d_{QW}, the quantum confinement increases and pushes the E1 band above the H1, restoring normal

[3] An explanation of the characterization of the bands can be found in [Winkler03].

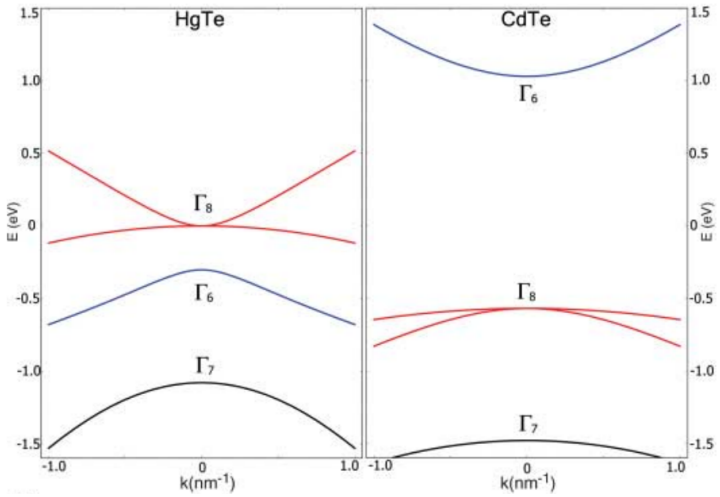

Figure 2.4.: The bulk dispersions of HgTe and CdTe. In HgTe, the Γ_8 band is above the Γ_6 band, resulting in an inverted band structure. Taken from [Bernevig06]. Reprinted with permission from AAAS.

band ordering. In the intermediate region the gap closes at a critical thickness $d_c \approx 6.4$ nm. As we will explore in the following section, the gap closure from the normal to the inverted regime is connected with a topological phase transition.
Around the gap closing at d_c, all sub-bands except E1 and H1 are energetically far separated from the Fermi energy. Consequently, it is advantageous to describe the composite system in an effective low-energy Hamiltonian considering only E1 and H1. To this end, one integrates out the z-dependence and performs a Löwdin partitioning. Here, we will only state the results. A very detailed description of the procedure can, for example, be found in [Winkler03, Rothe09]. The effective Hamiltonian is written in the basis

$$\left(|\mathrm{E1},\uparrow\rangle, |\mathrm{H1},\uparrow\rangle, |\mathrm{E1},\downarrow\rangle, |\mathrm{H1},\downarrow\rangle\right). \tag{2.58}$$

It is named after Bernevig, Hughes, and Zhang (BHZ) and reads [Bernevig06]:

$$H_{\mathrm{BHZ}}(k_x,k_y) = \begin{pmatrix} h(k_x,k_y) & 0 \\ 0 & h^*(-k_x,-k_y) \end{pmatrix}. \tag{2.59}$$

It is block-diagonal in the Kramers' partner polarizations. For each Kramers' partner the behavior is governed by

$$h(k_x,k_y) = \epsilon(k_x,k_y)\tau_0 + d_i(k_x,k_y)\tau_i \tag{2.60}$$

with the Pauli matrices in sub-band space (τ_i), $\tau_0 = \mathbb{I}_{2\times 2}$ and

$$\epsilon(k_x,k_y) = C - D(k_x^2+k_y^2), \quad d_1 = Ak_x, \quad d_2 = -Ak_y, \quad d_3 = M - B(k_x^2+k_y^2). \tag{2.61}$$

Since all z-dependence has been integrated out, H_{BHZ} only depends on the in-plane momentum $\boldsymbol{k}_\parallel = (k_x,k_y)^T$. The material parameters C, M, A, B and D depend on the well width d_{QW}. The band off-set of the sub-bands at the Γ-point is given by $C + M\tau_z$. C is a shift in energy and

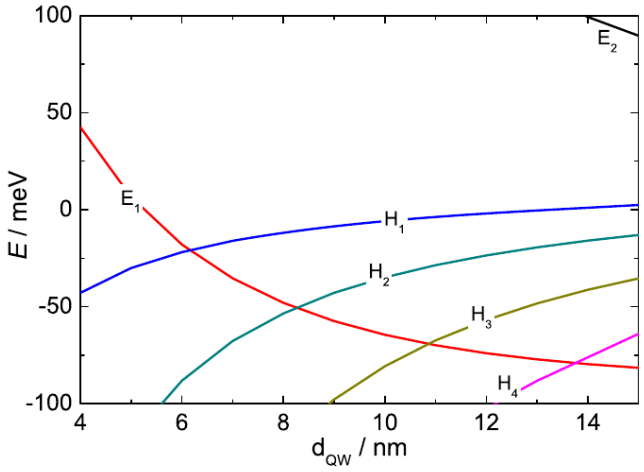

Figure 2.5.: The sub-bands of a HgTe/CdTe QW show a well width (d_{QW}) dependent energy gap, which changes sign at a critical thickness $d_c \approx 6.4$ nm. Taken from [König08]. Reprinted with permission from JPSJ.

will be mostly chosen to be $C = 0$, which means the energy zero point is in the middle of the band gap. In contrast, M denotes the energy gap $E_{\mathrm{gap}} = E_{\mathrm{E1}} - E_{\mathrm{H1}} = 2M$. From comparison with Fig. 2.5, one finds that the sign of M is positive (negative) in the normal (inverted) regime. For finite $\boldsymbol{k}_\parallel$ we have two competing terms: the diagonals of $h(\boldsymbol{k}_\parallel)$ give rise to a quadratic dispersion with effective masses $m^*_{\mathrm{E1}} = \hbar/2(-B - D)$ and $m^*_{\mathrm{H1}} = \hbar/2(B - D)$, where the asymmetry of the bands is induced by D. On the other hand, the coupling of the E1 and H1 band on the off-diagonal of $h(\boldsymbol{k}_\parallel)$ induces a Dirac-like linear dispersion with A being its Fermi velocity. This makes HgTe/CdTe QWs a model system in which the interplay of linear and quadratic terms can be analysed. For example, at low doping, quadratic terms in k can be neglected [Schmidt09] and the carriers behave like relativistic electrons, giving rise to a Pauli term, which has been predicted to alter spin transport significantly [Rothe10].
In the basis (2.58), the TRS operator is

$$\hat{\Theta} = -\mathrm{i}\sigma_y \otimes \mathbb{I}_{2\times 2}\hat{K}, \tag{2.62}$$

where σ_i are the Pauli matrices in spin space. With Eq. (2.17), one can to check that H_{BHZ} indeed preserves TRS.
In the following, we discuss two corrections to the Hamiltonian (2.59), which are allowed by the symmetries of the system: the bulk- and structure inversion asymmetry.

Bulk inversion asymmetry

Having two different atoms in the unit cell, the Zinc blende structure is not inversion symmetric, which is referred to as bulk inversion asymmetry (BIA). This induces a spin-orbit term, which,

A [nm eV]	$365 \cdot 10^{-3}$
B [nm^2 eV]	$-706 \cdot 10^{-3}$
D [nm^2 eV]	$-532 \cdot 10^{-3}$
M [eV]	$-10.09 \cdot 10^{-3}$

Table 2.1.: Material parameters for $n = 10^{-2}$ nm^{-2} and $d_{\mathrm{QW}} = 7.0$ nm taken from [Rothe10].

in the basis (2.58), takes the form [König08]

$$H_{\mathrm{BIA}} = \Delta_{\mathrm{BIA}} \begin{pmatrix} 0 & 0 & 0 & -1 \\ 0 & 0 & 1 & 0 \\ 0 & 1 & 0 & 0 \\ -1 & 0 & 0 & 0 \end{pmatrix}. \tag{2.63}$$

The strength of the BIA has been estimated to be $\Delta_{\mathrm{BIA}} \approx 1.6$ meV [König08]. To the best of our knowledge, detailed theoretical and experimental studies of the dependence of the BIA coupling on the well width have not yet been performed, so that the real strength of BIA is still unknown. Since Δ_{BIA} is anyway much smaller than the rest of the energy scales in this model, cf. [Novik05] and also Tab. 2.1, we will neglect BIA terms in the following. Only in section 6.2.1, we will comment on the influence of BIA on the separation of the two Kramers' partners' contribution to transport.

Structure inversion asymmetry

Inversion symmetry breaking can also be induced by the structure of the quantum well. On the one hand, the growth of the QW will in general be asymmetric. On the other hand, the asymmetry can be artificially imposed by a gate potential. In both cases, this so-called structure inversion asymmetry (SIA) leads to an asymmetric well potential accompanied by an electric field. In [Rothe10], the derivation of H_{BHZ} has been generalized to the presence of a linearly varying potential, i.e., $\boldsymbol{\mathcal{E}} = \mathcal{E}_z \hat{e}_z = \mathrm{const}$. With $k_\pm = k_x \pm \mathrm{i}k_y$, the resulting correction was found to be

$$H_{\mathrm{R}} = \begin{pmatrix} 0 & 0 & -\mathrm{i}R_0 k_- & -S_0 k_-^2 \\ 0 & 0 & S_0 k_-^2 & \mathrm{i}T_0 k_-^3 \\ \mathrm{i}R_0 k_+ & S_0 k_+^2 & 0 & 0 \\ -S_0 k_+^2 & -\mathrm{i}T_0 k_+^3 & 0 & 0 \end{pmatrix}. \tag{2.64}$$

The interaction scales with the electric field ($R_0,\ T_0,\ S_0 \propto \mathcal{E}_z$) and corresponds to the linear, cubic and quadratic Rashba terms for electrons, heavy holes and the coupling of electrons and heavy holes, respectively. In contrast to the BIA term, the Rashba interaction can be controlled by QW growth and/or applied gates. In the following, we will thus assume the Rashba interaction to be "switched off" and disregard H_{R}.

At the end of this section, let us give exemplary material parameters, which have been derived at $d_{\mathrm{QW}} = 7$ nm, i.e., in the inverted regime, cf. Tab. 2.1. Although we concentrate on HgTe QWs here, let us mention that the same effective model is valid for inverted type-II semiconductors like InAs/GaSb QWs [Liu08].

i	$\Lambda_i = (k_x, k_y)$	$d_3(\Lambda_i)$ for $B < 0$
0	$(0,0)$	M
1	$\left(\frac{\pi}{a}, 0\right)$	$M + \frac{4\lvert B\rvert}{a^2}$
2	$\left(0, \frac{\pi}{a}\right)$	$M + \frac{4\lvert B\rvert}{a^2}$
3	$\left(\frac{\pi}{a}, \frac{\pi}{a}\right)$	$M + \frac{8\lvert B\rvert}{a^2}$

Table 2.2.: The four TRIM in the 2D BZ together with their parities, cf. Eq. (2.71).

2.3.2. Topological classification of the HgTe quantum wells

Here, we want to calculate the Z_2 invariant of the BHZ model (2.59). Since, in the employed basis, the $|E1\rangle$ and $|H1\rangle$ sub-bands have parity -1 and 1, respectively, the parity operator $\hat{\Pi}$ can be written as [Rothe10][4]

$$\hat{\Pi} = -\sigma_0 \otimes \tau_z. \tag{2.65}$$

Neglecting inversion breaking terms in the off-diagonal blocks of H_{BHZ}, we find $\hat{\Pi} H_{\mathrm{BHZ}}(-\boldsymbol{k})\hat{\Pi}^{-1} = H_{\mathrm{BHZ}}(\boldsymbol{k})$. This is the condition for parity conservation, because space inversion leads to $\boldsymbol{k} \to -\boldsymbol{k}$ in the Bloch basis. Therefore, it is possible to use Eq. (2.55) and restrict our considerations to one of the Kramers partners. To evaluate the parity at the time-reversal invariant momenta (TRIM), we need to impose the periodicity of the BZ onto the model. Analogously to [König08], we can do this by a lattice regularization

$$k_i \to \frac{\sin[k_i a]}{2a}, \quad k_i^2 \to \frac{2 - 2\cos[k_i a]}{a^2}, \tag{2.66}$$

where a is the lattice constant in real space (see appendix B for more details). The Hamiltonian for one of the Kramers' partner then takes the form

$$h(\boldsymbol{k}) = d_0\tau_0 + d_i\tau_i, \tag{2.67}$$

$$\begin{aligned}
\text{with: } d_0 &= C - \frac{4D}{a^2} + \frac{2D}{a^2}(\cos[k_x a] + \cos[k_y a]) \\
d_1 &= \frac{A}{2a}\sin[k_x a] \\
d_2 &= -\frac{A}{2a}\sin[k_y a] \\
d_3 &= M - \frac{4B}{a^2} + \frac{2B}{a^2}(\cos[k_x a] + \cos[k_y a]).
\end{aligned} \tag{2.68}$$

At the four TRIM in the Brillouin zone (see Tab. 2.2 and Fig. 2.1a), the Hamiltonian takes the simple form

$$h(\Lambda_i) = d_0\tau_0 + d_3\tau_3. \tag{2.69}$$

[4] Again we use the convention, that the σ_i (τ_i) act on the Kramers' partner (sub-band) degree of freedom.

This can also be seen from the fact that only τ_3 is even under the parity operator. The eigenvalues of $h(\Lambda_i)$ are

$$E_{\mathrm{E1}} = d_0 + d_3 \quad \text{and} \quad E_{\mathrm{H1}} = d_0 - d_3 \tag{2.70}$$

and have E1 and H1 character, respectively. At half filling, i.e., the Fermi energy is in the band gap, this means that $\xi(\Lambda_i)$, which is the parity eigenvalue at the TRIM Λ_i and which has been introduced in Eq. (2.55), is equal to $\mathrm{sign}\,[d_3(\Lambda_i)]$, because

$$\begin{aligned} & \mathrm{sign}\,[d_3(\Lambda_i)] = 1 \quad && \Rightarrow E_{\mathrm{E1}} > E_{\mathrm{H1}} && \Rightarrow |\mathrm{H1}\rangle \text{ is occupied} && \Rightarrow \xi(\Lambda_i) = 1 \\ \text{and} \quad & \mathrm{sign}\,[d_3(\Lambda_i)] = -1 \quad && \Rightarrow E_{\mathrm{E1}} < E_{\mathrm{H1}} && \Rightarrow |\mathrm{E1}\rangle \text{ is occupied} && \Rightarrow \xi(\Lambda_i) = -1. \end{aligned} \tag{2.71}$$

With this, we find the topological index

$$(-1)^{\nu} = \prod_{i=1}^{4} \mathrm{sign}\,[d_3(\Lambda_i)]\,. \tag{2.72}$$

For fixed $B < 0$, we can read off the parities from Tab. 2.2, yielding

$$\begin{aligned} M > 0 \Rightarrow & \qquad \xi(\Lambda_{0123}) > 0 \Rightarrow & \nu = 0 \\ M < 0 \;\&\; M > -\frac{4|B|}{a^2} \Rightarrow & \qquad \xi(\Lambda_0) < 0,\ \xi(\Lambda_{123}) > 0 \Rightarrow & \nu = 1 \\ M < -\frac{4|B|}{a^2} \;\&\; M > -\frac{8|B|}{a^2} \Rightarrow & \qquad \xi(\Lambda_{012}) < 0,\ \xi(\Lambda_3) > 0 \Rightarrow & \nu = 1 \end{aligned} \tag{2.73}$$

This means that a change in $\mathrm{sign}\,[M]$ triggers a phase transition from the topologically trivial ($M > 0$) to the topologically non-trivial regime ($M < 0$). The parameter M is related to the bulk gap in the system. Hence, the phase transition is connected with a change of band ordering, which first occurs at the Γ-point. The topologically non-trivial regime is consequently also referred to as the *inverted regime*.

One might wonder, if there is a second topological phase transition when $M < -8|B|/a^2$. Indeed the formal evaluation results in $\nu = 0$. However, this is an artifact of the TB formalism. In a 2D system, the TB bandwidth is 4 times the hopping energy. Neglecting the linear terms at large energies, one finds the hopping energy $t_{\mathrm{E1,H1}} = 4(B \pm D)/a^2$. Therefore, choosing $M < -8|B|/a^2$ causes an artificial band inversion, which does not occur in the physical system.

The topological invariant and its physically measurable analogues are properties of the whole BZ. Here, we calculated the Z_2 invariant by evaluating an effective low-energy model, which is valid around the Γ-point, at the border of the BZ. However, it was shown [Budich12a], that low-energy models give the correct topological invariants, provided that the topological defect is sufficiently localized around $\boldsymbol{k} = 0$. This is true in the above case, because the topological phase transition occurs around the Γ-point in Eq. (2.73), where the parity $\xi(\Lambda_0)$ changes sign. Let us note that the topological defect is not localized at the center of the BZ, if we would fix M and tune B, see [Budich12a] for more details.

Another way to understand the Z_2 invariant is to calculate the spin Chern number [Kane05b]. The Chern number or TKNN invariant, which is presented in appendix A, usually describes the quantized conductance of the QH effect, i.e., in the absence of TRS. In the presence of TRS, one can calculate the first Chern number n_s for each Kramers' partner individually, provided that S_z is conserved. TRS enforces that $n_\uparrow + n_\downarrow = 0$. However, it is possible to define a spin Chern

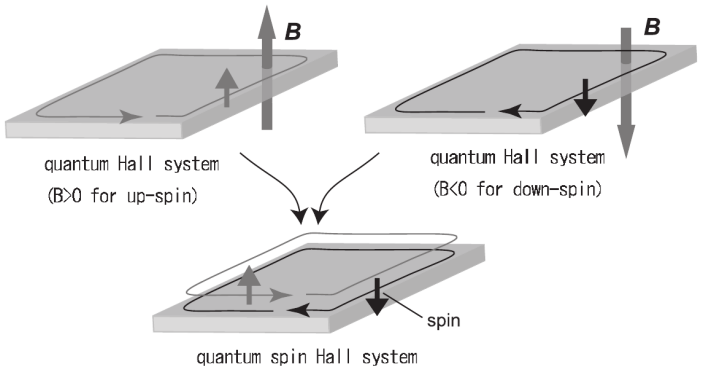

Figure 2.6.: The QSH effect can be understood as a superposition of two opposite copies of the QH effect. Taken from [Murakami07]. ©IOP Publishing & Deutsche Physikalische Gesellschaft. CC BY-NC-SA.

number by $n_\uparrow - n_\downarrow$ which is related to the Z_2 invariant by [Kane05b]

$$\nu = (n_\uparrow - n_\downarrow) \mathrm{mod} 2. \tag{2.74}$$

In this sense, one can interpret the QSH effect as two copies of the QH effect, like it is schematically demonstrated in Fig. 2.6. Each Kramers' partner corresponds to one of the copies and gives rise to a quantized charge polarization at the edges. Further, the two copies are related by TRS, so that the associated magnetic fields/magnetic polarizations cancel, which is reflected by a vanishing total charge polarization. However, this reinstalls TRS and leads to a finite time-reversal polarization of the Kramers' partners at the edges of the sample, as defined in Eq. (2.52).

2.3.3. Tight binding dispersion and edge states

In this section, we analyze the model (2.59) within the TB formalism, introduced in appendix B. To this end, we have chosen the lattice constant $a = 1$ nm. In Fig. 2.7, we plot the TB dispersion of a 2D TI in the quasi 1D ribbon geometry, which extents infinitely in x-direction, cf. Fig. B.1. Its width in y-direction (L_y) is discretized by $N_y = 100$ lattice points. Whereas the gap parameter M changes strongly with the quantum well thickness d_{QW}, we will neglect the smaller changes of the other parameters and stick to the values presented in Tab. 2.1. However, M changes sign at $d_{\mathrm{QW}} = d_c$, triggering a topological phase transition. We therefore compare the topologically trivial regime ($M = 10.09$ meV > 0) in Fig. 2.7a with the non-trivial regime ($M = -10.09$ meV < 0) in Fig. 2.7b. In both regimes, the conduction- and valence band are separated by a gap, which exceeds its continuum value $2M$ due to finite size effects. The band character is color encoded, ranging from blue (H1 like) to red (E1 like). While, in the trivial regime, the conduction and valence band have E1 and H1 character, respectively, we find that $M < 0$ induces the band inversion, which characterizes bulk HgTe. It manifests itself in an inverse band character at the band edges around the Γ-point.
The most striking difference between the two regimes, however, is the gap closing by a pair of states for $M < 0$. In good approximation, these states disperse linearly with the Fermi velocity $v_{\mathrm{F}} = A/\hbar$ inside the gap. To analyze these states further, we plot their spatial density

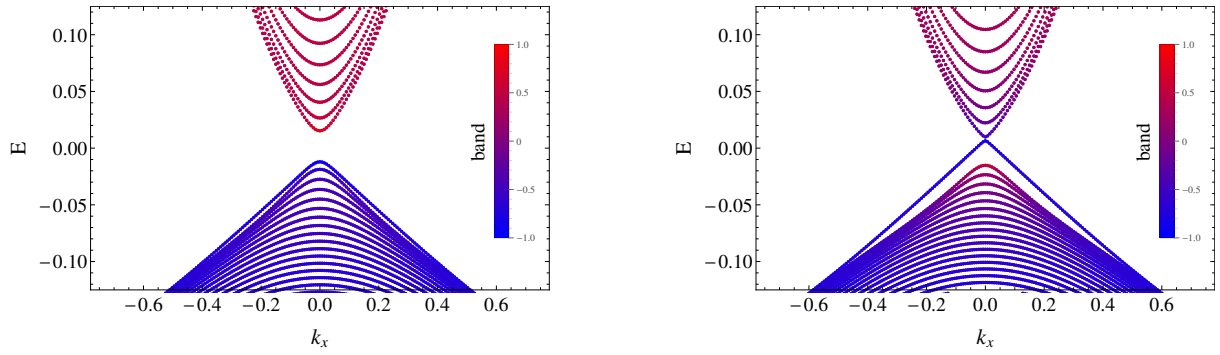

(a) $M > 0$, trivial regime

(b) $M < 0$, non-trivial regime

Figure 2.7.: The TB dispersion of a HgTe QW in the trivial (a) and non-trivial (b) regime. We used $a = 1$ nm and $N_y = 100$. The color code indicates the band character to be E1 like (1, red) or H1 like (-1, blue).

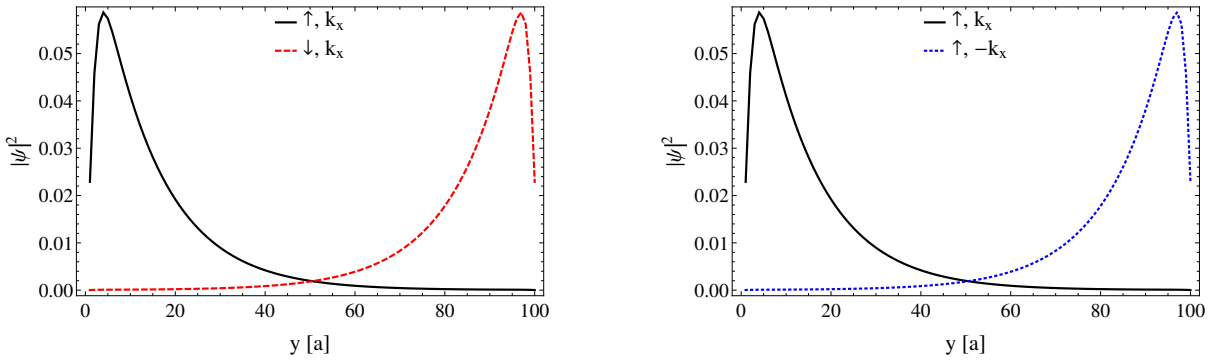

(a) $k_x = 0.025$ nm^{-1}, different pseudo-spin

(b) $k_x = \pm 0.025$ nm^{-1}, same pseudo-spin

Figure 2.8.: The density of states of the edge states.

of states (DOS) in Fig. 2.8. At fixed $k_x = 0.025$ nm^{-1} (Fig. 2.8a), we find two states, which propagate in the same direction. The helicity of the system dictates that such states are localized at opposite edges of the system, which we find to be fulfilled. These states, hence, are the previously discussed edge states and – according to the bulk-boundary correspondence – a direct consequence of the non-trivial topology in the inverted regime. Since we evaluated the DOS at a fixed k_x, the two states shown in Fig. 2.8a are not Kramers' partners, which in turn would counter-propagate along the same edge. It was experimentally demonstrated by Brüne et al. [Brüne12] that these states indeed carry opposite Karmers' partner polarization, i.e., ↑ or ↓, which strongly corresponds to the real electron spin in inverted HgTe QWs.

Elastic backscattering between the Kramers' partner is forbidden. However, there are counter-propagating states with the same pseudo-spin and opposite k_x localized at the opposite edge of the system, cf. Fig. 2.8b. The spatial separation between these states suppresses backscattering in the limit of large L_y. For the narrow ribbon analyzed here, we find significant spatial overlap, which introduces hybridization and backscattering between these states.

As a direct consequence of the hybridization, a small gap opens in the edge state spectrum at

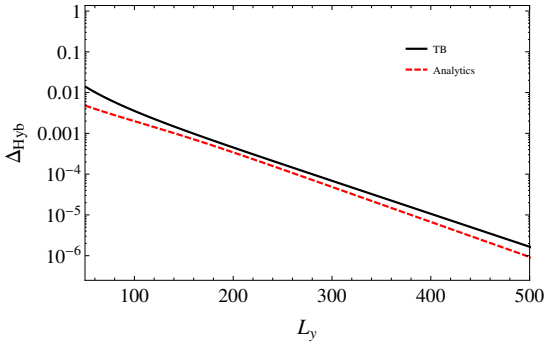

Figure 2.9.: The hybridization gap Δ_{Hyb} of the edge states in a HgTe QW as a function of the ribbon width L_y. We compare the TB solution (black, solid) with the analytical approximation (red, dashed).

the Γ-point in Fig. 2.7b. This so-called mini-gap Δ_{Hyb} can be approximated by [Zhou08]:

$$\Delta_{\mathrm{Hyb}} \approx \frac{4|A(B^2-D^2)M|}{\sqrt{B^3(A^2B-4(B^2-D^2)M)}} \exp\left[-\lambda_2 L_y\right]. \tag{2.75}$$

To do so, Zhou et al. considered an exponentially decaying ansatz for the edge states

$$\psi_{\mathrm{edge}} = \exp[\mathrm{i}k_x x]\left(c_1^+ \exp[\lambda_1 y] + c_1^- \exp[-\lambda_1 y] + c_2^+ \exp[\lambda_2 y] + c_2^- \exp[-\lambda_2 y]\right) \tag{2.76}$$

with decay lengths

$$\lambda_{1,2}^2(k_x, E) = k_x^2 + F \pm \sqrt{F^2 - \frac{M^2-E^2}{B^2-D^2}}, \quad F = \frac{A^2-2(MB+ED)}{2(B^2-D^2)}. \tag{2.77}$$

Eq. (2.75) shows the typical exponential decay of a finite-size effect. In order to evaluate it, one has to plug the ansatz (2.76) into H_{BHZ} and solve for the energy at a fixed k_x. Since this involves transcendental equations, it is impossible to give a closed analytical form of Δ_{Hyb} as a function of only k_x or E.
Fig. 2.9 compares the analytical approximation (red, dashed line) with Δ_{Hyb} obtained from TB calculations (black, solid line). We find that Eq. (2.75) slightly underestimates the hybridization gap. But there are only small corrections to the exponential decay at small L_y. This suggest that hybridization and backscattering of the edge states can be neglected for very wide ribbons. However, finite size effects can give rise to rich physics, which will be analyzed further in chapters 5 and 6.

3. Superconducting topological insulators

In this chapter, the reader will be equipped with the basics of superconductivity which is needed in the course of this thesis. We give a quick introduction to the microscopic theory of a conventional superconductivity in section 3.1 before we turn to the mechanism of induced superconductivity in 3.2. The combination of a topological insulator (TI) with a conventional superconductor (SC) gives rise to unconventional superconducting phases, like p-wave pairing. The last section, 3.3, deals with Andreev reflection, a unique transport process, which will be used to characterize the exotic transport features in superconducting TIs.

3.1. Intrinsic superconductivity

In presenting the essential basics of the superconducting state, we follow mainly the classic textbooks by de Gennes [Gennes99] and Tinkham [Tinkham04].

3.1.1. The pairing mechanism

The research area of superconductivity was born in 1911, when Onnes discovered the breakdown of electrical resistance in mercury at low temperatures [Onnes11]. The reason for the breakdown is that the Fermi sea is unstable in the presence of an arbitrarily small attractive interaction V [Cooper56]. To achieve an attraction between two electrons, the interaction has to be indirect. In the case of ordinary SCs, it was found that the interaction is mediated by phonons. The physical picture is that an electron attracts the positively charged atom cores along its path. Being much faster than the heavy cores, the electron leaves a positive polarization cloud behind, which by itself attracts another electron. In the case that this effective, retarded attraction outweighs the screened Coulomb repulsion of two electrons with lattice momentum $\boldsymbol{k}$ and $\boldsymbol{k'}$, it can be approximated by

$$V_{\boldsymbol{k},\boldsymbol{k'}} = \begin{cases} -V & \text{if } E(\boldsymbol{k}) \text{ and } E(\boldsymbol{k'}) \leq \hbar\omega_{\boldsymbol{q}} \\ 0 & \text{else} \end{cases} . \tag{3.1}$$

Here, V is a positive constant and $\hbar\omega_{\boldsymbol{q}}$ is the energy scale of a phonon with wave vector $\boldsymbol{q} = \boldsymbol{k} - \boldsymbol{k'}$. In the following, we will consider the weak coupling limit $D(E_f)V \ll 1$, where $D(E_f)$ is the density of states (DOS) at the Fermi energy E_f. For a pair of electrons with opposite momentum ($\boldsymbol{k'} = -\boldsymbol{k}$) and opposite spin, the effective interaction (3.1) leads to a decrease in energy

$$\delta E = E - 2E_f \approx -2\hbar\omega_{\boldsymbol{q}} \exp\left[-\frac{2}{D(E_f)V}\right] . \tag{3.2}$$

In their ground breaking paper, Bardeen, Cooper, and Schriefer (BCS) [Bardeen57] used so-called *Cooper pairs*, that are pairs of electrons with opposite spin and momentum, to form the

trial wave function

$$|\psi\rangle_{\mathrm{BCS}} = \prod_{\boldsymbol{k}} \left(u_{\boldsymbol{k}} + v_{\boldsymbol{k}} c^\dagger_{\boldsymbol{k}\uparrow} c^\dagger_{-\boldsymbol{k}\downarrow} \right) |\mathrm{VAC}\rangle \,. \tag{3.3}$$

Here, we introduced the annihilation ($c_{\boldsymbol{k}\sigma}$) and creation ($c^\dagger_{\boldsymbol{k}\sigma}$) operators for electrons with momentum $\boldsymbol{k}$ and spin σ. They obey the fermionic anticommutation relations ($[a,b]_+ = ab + ba$)

$$[c_{\boldsymbol{k}\sigma}, c_{\boldsymbol{k}'\sigma'}]_+ = \left[c^\dagger_{\boldsymbol{k}\sigma}, c^\dagger_{\boldsymbol{k}'\sigma'}\right]_+ = 0, \quad \left[c^\dagger_{\boldsymbol{k}\sigma}, c_{\boldsymbol{k}'\sigma'}\right]_+ = \delta_{\sigma\sigma'}\delta_{\boldsymbol{k}\boldsymbol{k}'}. \tag{3.4}$$

Here, the operators act on the vacuum state $|\mathrm{VAC}\rangle$. The combination $c^\dagger_{\boldsymbol{k}\uparrow} c^\dagger_{-\boldsymbol{k}\downarrow}$ creates Cooper pairs. Hence, $|\psi\rangle_{\mathrm{BCS}}$ does not have a fixed particle number. However, the simple form of Eq. (3.3) is justified in the limit of many particles, where the relative fluctuations of the total particle number are negligible. It can be interpreted as a *condensate* of Cooper pairs ($\boldsymbol{k}\uparrow, -\boldsymbol{k}\downarrow$), which are occupied or empty with the probability $|v_{\boldsymbol{k}}|^2$ and $|u_{\boldsymbol{k}}|^2$, respectively. The condition

$$|u_{\boldsymbol{k}}|^2 + |v_{\boldsymbol{k}}|^2 = 1 \tag{3.5}$$

ensures the normalization of $|\psi\rangle_{\mathrm{BCS}}$.
The general Hamiltonian of two interacting electrons is given by

$$\mathcal{H} = \sum_{\boldsymbol{k}} \sum_{\sigma\sigma'} H_{\sigma\sigma'}(\boldsymbol{k}) c^\dagger_{\boldsymbol{k}\sigma} c_{\boldsymbol{k}\sigma'} - \frac{V}{2} \sum_{\boldsymbol{k}\boldsymbol{l}\boldsymbol{q}} \sum_{\sigma\sigma'} c^\dagger_{(\boldsymbol{k}+\boldsymbol{q})\sigma} c^\dagger_{(\boldsymbol{l}-\boldsymbol{q})\sigma'} c_{\boldsymbol{l}\sigma'} c_{\boldsymbol{k}\sigma}, \tag{3.6}$$

where $H_{\sigma\sigma'}(\boldsymbol{k})$ is the matrix element of the single-particle Bloch Hamiltonian. The Hamiltonian (3.6) is in general not solvable. Bardeen, Cooper, and Schriefer, however, found a mean-field description, the so-called pairing Hamiltonian H_Δ, which has the ground state $|\psi\rangle_{\mathrm{BCS}}$ of Eq. (3.3). The amplitudes $u_{\boldsymbol{k}}$ and $v_{\boldsymbol{k}}$ as well as the ground state energy can then be determined by minimizing the expectation value ${}_{\mathrm{BCS}}\langle\psi| \mathcal{H}_\Delta |\psi\rangle_{\mathrm{BCS}}$. This microscopic theory of SCs, called BCS theory, was awarded with the Nobel prize in 1972. It was derived for superconductivity which is mediated by phonons. However, understanding the superconducting ground state as a condensate of electron pairs is the building block for all kinds of SCs. Hence, we will focus on conventional SCs and present a generalization of the BCS theory in the following.

3.1.2. The pairing Hamiltonian

Here, we present a generalized BCS theory, allowing for spatially varying potentials $\mathcal{U}(\boldsymbol{r})$ and magnetic vector potentials $\boldsymbol{\mathcal{A}}(\boldsymbol{r})$. To this end, we introduce the field operators

$$\hat{\psi}_\sigma(\boldsymbol{r}) = \sum_{\boldsymbol{k}} \exp\left[\mathrm{i}\boldsymbol{k}\boldsymbol{r}\right] c_{\boldsymbol{k}\sigma}, \quad \hat{\psi}^\dagger_\sigma(\boldsymbol{r}) = \sum_{\boldsymbol{k}} \exp\left[-\mathrm{i}\boldsymbol{k}\boldsymbol{r}\right] c^\dagger_{\boldsymbol{k}\sigma}, \tag{3.7}$$

which annihilate and create electrons of spin σ at position $\boldsymbol{r}$. They obey the Fermion statistics and hence analogous anticommutation relations to Eq. (3.4)

$$\left[\hat{\psi}_\sigma(\boldsymbol{r}), \hat{\psi}_{\sigma'}(\boldsymbol{r}')\right]_+ = \left[\hat{\psi}^\dagger_\sigma(\boldsymbol{r}), \hat{\psi}^\dagger_{\sigma'}(\boldsymbol{r}')\right]_+ = 0, \quad \left[\hat{\psi}^\dagger_\sigma(\boldsymbol{r}), \hat{\psi}_{\sigma'}(\boldsymbol{r}')\right]_+ = \delta(\boldsymbol{r}-\boldsymbol{r}')\delta_{\sigma\sigma'}. \tag{3.8}$$

In this basis, the Hamiltonian (3.6) becomes

$$\mathcal{H} = \int \mathrm{d}\boldsymbol{r} \sum_{\sigma\sigma'} \hat{\psi}^\dagger_\sigma(\boldsymbol{r}) H_{\sigma\sigma'}(\hat{\boldsymbol{p}}, \boldsymbol{r}) \hat{\psi}_{\sigma'}(\boldsymbol{r}) - \frac{V}{2} \int \mathrm{d}\boldsymbol{r} \sum_{\sigma\sigma'} \hat{\psi}^\dagger_\sigma(\boldsymbol{r}) \hat{\psi}^\dagger_{\sigma'}(\boldsymbol{r}) \hat{\psi}_{\sigma'}(\boldsymbol{r}) \hat{\psi}_\sigma(\boldsymbol{r}). \tag{3.9}$$

The single-particle Hamiltonian $H_{\sigma\sigma'}(\hat{\boldsymbol{p}}, \boldsymbol{r})$ may now depend on the potentials $\boldsymbol{\mathcal{A}}$ and $\mathcal{U}$. In its general form, $\mathcal{H}$ is unsolvable. We will therefore treat it in mean-field theory. Since the effective attraction creates singlet pairs, we will first approximate the interaction part by putting $\sigma' = -\sigma$,[1] which yields:

$$-\frac{V}{2} \int \mathrm{d}\boldsymbol{r} \sum_{\sigma\sigma'} \hat{\psi}^\dagger_\sigma(\boldsymbol{r}) \hat{\psi}^\dagger_{\sigma'}(\boldsymbol{r}) \hat{\psi}_{\sigma'}(\boldsymbol{r}) \hat{\psi}_\sigma(\boldsymbol{r}) \to -\frac{V}{2} \int \mathrm{d}\boldsymbol{r} \sum_{\sigma} \hat{\psi}^\dagger_\sigma(\boldsymbol{r}) \hat{\psi}^\dagger_{-\sigma}(\boldsymbol{r}) \hat{\psi}_{-\sigma}(\boldsymbol{r}) \hat{\psi}_\sigma(\boldsymbol{r}). \tag{3.10}$$

The derivation of the mean-field Hamiltonian, in which the free energy has to be minimized by the use of Wick's theorem [Gennes99], results in an effective pair potential and a Hartree potential. Since the latter can be incorporated into the single-particle Hamiltonian $H_{\sigma\sigma'}(\hat{\boldsymbol{p}}, \boldsymbol{r})$, we will neglect it hereafter. The pure pairing Hamiltonian, H_Δ, can then be motivated following a simple reasoning presented in [Tinkham04]. The idea is to rewrite pairs of operators by their mean value

$$\hat{\psi}_\sigma(\boldsymbol{r}) \hat{\psi}_{-\sigma}(\boldsymbol{r}) = \left\langle \hat{\psi}_\sigma(\boldsymbol{r}) \hat{\psi}_{-\sigma}(\boldsymbol{r}) \right\rangle + \underbrace{\left(\hat{\psi}_\sigma(\boldsymbol{r}) \hat{\psi}_{-\sigma}(\boldsymbol{r}) - \left\langle \hat{\psi}_\sigma(\boldsymbol{r}) \hat{\psi}_{-\sigma}(\boldsymbol{r}) \right\rangle \right)}_{=\delta} \tag{3.11}$$

$$\hat{\psi}^\dagger_\sigma(\boldsymbol{r}) \hat{\psi}^\dagger_{-\sigma}(\boldsymbol{r}) = \left\langle \hat{\psi}^\dagger_\sigma(\boldsymbol{r}) \hat{\psi}^\dagger_{-\sigma}(\boldsymbol{r}) \right\rangle + \left(\hat{\psi}^\dagger_\sigma(\boldsymbol{r}) \hat{\psi}^\dagger_{-\sigma}(\boldsymbol{r}) - \left\langle \hat{\psi}^\dagger_\sigma(\boldsymbol{r}) \hat{\psi}^\dagger_{-\sigma}(\boldsymbol{r}) \right\rangle \right) \tag{3.12}$$

and to consider the fluctuations δ around the mean value to be small. Plugging this into Eq. (3.9) and neglecting terms quadratic in δ gives the effective pairing Hamiltonian

$$\begin{aligned} \mathcal{H} &\approx \int \mathrm{d}\boldsymbol{r} \sum_{\sigma\sigma'} \hat{\psi}^\dagger_\sigma(\boldsymbol{r}) H_{\sigma\sigma'}(\hat{\boldsymbol{p}}, \boldsymbol{r}) \hat{\psi}_{\sigma'}(\boldsymbol{r}) - \frac{V}{2} \int \mathrm{d}\boldsymbol{r} \sum_{\sigma} \left(\left\langle \hat{\psi}^\dagger_\sigma \hat{\psi}^\dagger_{-\sigma} \right\rangle \hat{\psi}_{-\sigma} \hat{\psi}_\sigma + \left\langle \hat{\psi}_{-\sigma} \hat{\psi}_\sigma \right\rangle \hat{\psi}^\dagger_\sigma \hat{\psi}^\dagger_{-\sigma} \right) \\ &= \int \mathrm{d}\boldsymbol{r} \sum_{\sigma\sigma'} \hat{\psi}^\dagger_\sigma(\boldsymbol{r}) H_{\sigma\sigma'}(\hat{\boldsymbol{p}}, \boldsymbol{r}) \hat{\psi}_{\sigma'}(\boldsymbol{r}) + \int \mathrm{d}\boldsymbol{r} \left(\Delta^*(\boldsymbol{r}) \hat{\psi}_\downarrow(\boldsymbol{r}) \hat{\psi}_\uparrow(\boldsymbol{r}) + \Delta(\boldsymbol{r}) \hat{\psi}^\dagger_\uparrow(\boldsymbol{r}) \hat{\psi}^\dagger_\downarrow(\boldsymbol{r}) \right) =: \mathcal{H}_\Delta. \end{aligned} \tag{3.13}$$

In the last line, we evaluate the sum over the different spin directions and used $\hat{\psi}_\uparrow \hat{\psi}_\downarrow = -\hat{\psi}_\downarrow \hat{\psi}_\uparrow$. Additionally, we defined the *pair potential*

$$\Delta(\boldsymbol{r}) = -V \left\langle \hat{\psi}_\downarrow(\boldsymbol{r}) \hat{\psi}_\uparrow(\boldsymbol{r}) \right\rangle = V \left\langle \hat{\psi}_\uparrow(\boldsymbol{r}) \hat{\psi}_\downarrow(\boldsymbol{r}) \right\rangle, \tag{3.14}$$

which has to be determined self-consistently.

[1] In this notation we assume that $-\sigma$ indicates the opposite spin as σ.

3.1.3. The Bogoliubov-de Gennes formalism

To solve the pairing Hamiltonian (3.13), we perform the Bogoliubov-Valatin transformation

$$\begin{aligned}\hat{\psi}_\sigma(\boldsymbol{r}) &= \sum_n \left(u_{\sigma n}(\boldsymbol{r})\gamma_n + v^*_{\sigma n}(\boldsymbol{r})\gamma_n^\dagger \right), \\ \hat{\psi}^\dagger_\sigma(\boldsymbol{r}) &= \sum_n \left(u^*_{\sigma n}(\boldsymbol{r})\gamma_n^\dagger + v_{\sigma n}(\boldsymbol{r})\gamma_n \right).\end{aligned} \tag{3.15}$$

The sum runs over a discrete or continuous set of quasi-particle states, which are created and annihilated by the operators $\gamma_n^\dagger$ and γ_n, respectively. The operators again obey the fermionic anticommutation relations (3.4). The dependence of the field operators on spin and on position has been shifted to the coefficients $u_{\sigma n}(\boldsymbol{r})$ and $v_{\sigma n}(\boldsymbol{r})$, which will be identified as the wave functions of the elementary excitations in the system. We want to determine the coefficients so that Eq. (3.15) diagonalizes the pairing Hamiltonian:

$$\mathcal{H}_\Delta = E_\mathrm{G} + \sum_n \epsilon_n \gamma_n^\dagger \gamma_n. \tag{3.16}$$

First, we will use the identity

$$[AB, C]_- = A\,[B, C]_+ - B\,[A, C]_+ \tag{3.17}$$

together with Eq. (3.8) to calculate

$$\left[\hat{\psi}_\sigma(\boldsymbol{r}), \mathcal{H}_\Delta\right]_- = \sum_{\sigma'} H_{\sigma'\sigma}(\hat{\boldsymbol{p}}, \boldsymbol{r})\hat{\psi}_{\sigma'}(\boldsymbol{r}) + \mathrm{sign}\,[\sigma]\,\Delta(\boldsymbol{r})\hat{\psi}^\dagger_{-\sigma}(\boldsymbol{r}). \tag{3.18}$$

Here, we defined $\mathrm{sign}\,[\uparrow] = 1$ and $\mathrm{sign}\,[\downarrow] = -1$. Replacing the field operators with Eq. (3.15) and using

$$[\gamma_n, \mathcal{H}_\Delta]_- = \epsilon_n \gamma_n, \quad \left[\gamma_n^\dagger, \mathcal{H}_\Delta\right]_- = -\epsilon_n \gamma_n^\dagger, \tag{3.19}$$

one finds

$$\begin{aligned}&\sum_n \left(\epsilon_n u_{\sigma n}(\boldsymbol{r}) - \sum_{\sigma'} H_{\sigma'\sigma}(\hat{\boldsymbol{p}}, \boldsymbol{r}) u_{\sigma' n}(\boldsymbol{r}) + \mathrm{sign}\,[\sigma]\,\Delta(\boldsymbol{r}) v_{-\sigma n}(\boldsymbol{r}) \right) \gamma_n \\ &\quad = \sum_n \left(\epsilon_n v^*_{\sigma n}(\boldsymbol{r}) + \sum_{\sigma'} H_{\sigma'\sigma}(\hat{\boldsymbol{p}}, \boldsymbol{r}) v^*_{\sigma' n}(\boldsymbol{r}) - \mathrm{sign}\,[\sigma]\,\Delta(\boldsymbol{r}) u^*_{-\sigma n}(\boldsymbol{r}) \right) \gamma_n^\dagger.\end{aligned} \tag{3.20}$$

Setting the prefactors of γ_n and $\gamma_n^\dagger$ individually to zero for $\sigma = \uparrow, \downarrow$ results in a coupled system of linear equations for the coefficients. In this process, one has to conjugate the prefactors of either γ_n or $\gamma_n^\dagger$, of which we choose the latter here. We define the spinors

$$u_n(\boldsymbol{r}) = (u_{\uparrow n}(\boldsymbol{r}), u_{\downarrow n}(\boldsymbol{r}))^T, \quad v_n(\boldsymbol{r}) = (v_{\uparrow n}(\boldsymbol{r}), v_{\downarrow n}(\boldsymbol{r}))^T \tag{3.21}$$

to write the so-called Bogoliubov-de Gennes (BdG) equations in matrix form

$$\underbrace{\begin{pmatrix} H(\hat{\boldsymbol{p}},\boldsymbol{r}) & \mathrm{i}\sigma_y\Delta(\boldsymbol{r}) \\ -\mathrm{i}\sigma_y\Delta^*(\boldsymbol{r}) & -H^*(\hat{\boldsymbol{p}},\boldsymbol{r}) \end{pmatrix}}_{=:H_{\mathrm{BdG}}} \begin{pmatrix} u_n(\boldsymbol{r}) \\ v_n(\boldsymbol{r}) \end{pmatrix} = \epsilon_n \begin{pmatrix} u_n(\boldsymbol{r}) \\ v_n(\boldsymbol{r}) \end{pmatrix} \tag{3.22}$$

and to define the BdG Hamiltonian H_{BdG}. The paring potential becomes a matrix, whose structure $\mathrm{i}\sigma_y = \begin{pmatrix} 0 & 1 \\ -1 & 0 \end{pmatrix}$ reflects the spin-singlets formed in BCS theory. The BdG equations are the first quantization analog to the pairing Hamiltonian $\mathcal{H}_\Delta$. In this sense, $u_n(\boldsymbol{r})$ and $v_n(\boldsymbol{r})$ are the wave functions of the quasi-particle excitations of energy ϵ_n above the superconducting condensate, which has the ground state energy E_{G}.

Nambu basis

The SC's ground state (3.3) is a condensate of Cooper pairs with total energy E_{G}. The number of pairs is not fixed, meaning that adding or removing a Cooper pair does not change E_{G}. The elementary excitations are described by *quasi-particles* γ_n. From the Bogoliubov-Valatin transformation (3.15), one finds that $\hat{\psi}_\sigma$ and $\hat{\psi}_\sigma^\dagger$ consist of combinations of γ_n and $\gamma_n^\dagger$. Creating and annihilating an electron, hence, has the same effect, i.e., creating an excitation in the SC. Both leaves an un-paired electron behind and thus is also referred to as *Cooper pair breaking*. The structure of the elementary excitations is reflected in the so-called Nambu basis, which we introduced in writing down Eq. (3.22). In terms of the field operators, it takes the form

$$\hat{\Psi}(\boldsymbol{r}) = \left(\hat{\psi}_\uparrow(\boldsymbol{r}), \hat{\psi}_\downarrow(\boldsymbol{r}), \hat{\psi}_\uparrow^\dagger(\boldsymbol{r}), \hat{\psi}_\downarrow^\dagger(\boldsymbol{r})\right)^T. \tag{3.23}$$

It combines creation and annihilation operators. This resembles a doubling of the Hilbert space by introducing sub-spaces connected with the creation and annihilation of an electron. In the following, we will refer to these as the electron-like and the hole-like sub-spaces, where we have identified an annihilated (missing) electron with a hole-like excitation[2].
The pairing Hamiltonian becomes diagonal in the basis of the Nambu operators $\hat{\Psi}(\boldsymbol{r})$: $\mathcal{H}_\Delta = \int \mathrm{d}\boldsymbol{r}\, \hat{\Psi}^\dagger(\boldsymbol{r}) H_{\mathrm{BdG}} \hat{\Psi}(\boldsymbol{r})$, allowing to obtain the excitation spectrum by solving the BdG equations (3.22). Comparing Eq. (3.23) with the BdG equations, we find that the coefficients $u_{\sigma n}$ and $v_{\sigma n}$ describe the weights of electron- and hole-like excitations, respectively.
Another frequently used basis can be obtained by the unitary transformation [Tkachov15]

$$U = \begin{pmatrix} \sigma_0 & 0 \\ 0 & \mathrm{i}\sigma_y \end{pmatrix}, \tag{3.24}$$

where σ_0 is the identity in spin-space. The explicit transformations are

$$U\hat{\Psi} = \left(\hat{\psi}_\uparrow(\boldsymbol{r}), \hat{\psi}_\downarrow(\boldsymbol{r}), \hat{\psi}_\downarrow^\dagger(\boldsymbol{r}), -\hat{\psi}_\uparrow^\dagger(\boldsymbol{r})\right)^T \tag{3.25}$$

[2] There is a subtle difference between a missing electron and a hole-like excitation, which does not touch the physics discussed in this chapter. The exact relation between a missing electron and a hole is elaborated in appendix D.

and

$$UH_{\mathrm{BdG}}U^\dagger = \begin{pmatrix} H(\hat{\boldsymbol{p}},\boldsymbol{r}) & \sigma_0\Delta(\boldsymbol{r}) \\ \sigma_0\Delta^*(\boldsymbol{r}) & -(\mathrm{i}\sigma_y)H^*(\hat{\boldsymbol{p}},\boldsymbol{r})(-\mathrm{i}\sigma_y) \end{pmatrix} = \begin{pmatrix} H(\hat{\boldsymbol{p}},\boldsymbol{r}) & \sigma_0\Delta(\boldsymbol{r}) \\ \sigma_0\Delta^*(\boldsymbol{r}) & -\hat{\Theta}H(\hat{\boldsymbol{p}},\boldsymbol{r})\hat{\Theta}^{-1} \end{pmatrix}, \tag{3.26}$$

where we used the definition of the time-reversal operator for spin-1/2 systems $\hat{\Theta} = -\mathrm{i}\sigma_y\hat{K}$, cf. Eq. (2.9).

Particle-hole symmetry

In deriving the BdG equations from Eq. (3.20), we have arbitrarily chosen to conjugate the prefactor of $\gamma_n^\dagger$. If we instead conjugate the prefactor of γ_n, we arrive at the equivalent equation

$$H_{\mathrm{BdG}} \begin{pmatrix} v_n^*(\boldsymbol{r}) \\ u_n^*(\boldsymbol{r}) \end{pmatrix} = -\epsilon_n \begin{pmatrix} v_n^*(\boldsymbol{r}) \\ u_n^*(\boldsymbol{r}) \end{pmatrix}. \tag{3.27}$$

Hence, each solution $(u_n(\boldsymbol{r}), v_n(\boldsymbol{r}))^T$ with excitation energy ϵ_n is accompanied by a second solution $(v_n^*(\boldsymbol{r}), u_n^*(\boldsymbol{r}))^T$ at $-\epsilon_n$. This is a direct consequence of the particle-hole symmetry (PHS) in superconductors. We already encountered it, when we realized that the creation and annihilation of an electron has the same effect on the superconducting condensate. The transformation connected with this symmetry is *particle-hole* or *charge conjugation*. It can be written in terms of the Pauli matrices in particle-hole space (π_i) as

$$\hat{C} = \begin{pmatrix} 0 & \sigma_0 \\ \sigma_0 & 0 \end{pmatrix} \hat{K} = \pi_x \otimes \sigma_0 \hat{K}, \tag{3.28}$$

which can be directly seen from comparing Eqs. (3.22) and (3.27). Since PHS contains the complex conjugation operator ($\hat{K}$), it is anti-unitary.
The BdG equations determine the excitation spectrum of $\mathcal{H}_\Delta$ in Eq. (3.16). Therefore, we can restrict the further discussion to positive energies and the BdG equations in Eq. (3.22). As a consequence of PHS, H_{BdG} has two eigenenergy branches

$$\epsilon_\pm = \pm\sqrt{|H(\hat{\boldsymbol{p}},\boldsymbol{r})|^2 + |\Delta|^2}. \tag{3.29}$$

When we will plot the excitation energy spectrum later, we will always show all solutions. The reader should, however, keep in mind that the positive and negative branch are redundant and each one can be chosen to describe all physical solutions. The second branch emerges from the doubling of the space by introducing the Nambu spinors.

3.1.4. Self-consistent pair potential

Having solved the mean-field Hamiltonian, one has to solve the self-consistency equation for $\Delta(\boldsymbol{r})$ (3.14). With Eq. (3.15), it becomes

$$\Delta(\boldsymbol{r}) = V\left\langle \hat{\psi}_\uparrow(\boldsymbol{r})\hat{\psi}_\downarrow(\boldsymbol{r})\right\rangle = V\sum_{nm}\left\langle u_{\uparrow n}(\boldsymbol{r})v_{\downarrow m}^*(\boldsymbol{r})\gamma_n\gamma_m^\dagger + v_{\uparrow n}^*(\boldsymbol{r})u_{\downarrow m}\gamma_n^\dagger\gamma_m\right\rangle, \tag{3.30}$$

where all terms $\left\langle\gamma_n^\dagger\gamma_m^\dagger\right\rangle$ and $\langle\gamma_n\gamma_m\rangle$ do not contribute to averages, because the number of quasi-particles is conserved. At zero temperature, where no excitations are present, we use

$\gamma_n\gamma_m^\dagger = \delta_{mn} - \gamma_m^\dagger\gamma_n$ and simplify

$$\Delta(\boldsymbol{r}) = V\sum_n u_{\uparrow n}(\boldsymbol{r})v_{\downarrow n}^*(\boldsymbol{r}). \tag{3.31}$$

For the solution, we make three assumptions, which correspond to the original BCS scenario [Bardeen57]: 1. The system should be translational invariant, so that we can drop all $\boldsymbol{r}$-dependences. 2. The single-particle Hamiltonian is spin independent and thus real. It will now only depend on the state n and we write H_n, where n could, for example, be a momentum eigenstate, like in the original BCS theory. 3. Also Δ is real, which can always be chosen for an isolated conventional SC. With these conditions met, we can restrict the analysis to a reduced system of BdG-equations

$$\epsilon_n \begin{pmatrix} u_{\uparrow n} \\ v_{\downarrow n} \end{pmatrix} = \begin{pmatrix} H_n & \Delta \\ \Delta & -H_n \end{pmatrix} \begin{pmatrix} u_{\uparrow n} \\ v_{\downarrow n} \end{pmatrix} \tag{3.32}$$

with eigenenergies $\epsilon_n = \pm\sqrt{H_n^2 + \Delta^2}$. The normalized eigenvector of the positive energy branch is

$$\frac{1}{\sqrt{2\epsilon_n}\sqrt{\epsilon_n + H_n}} \begin{pmatrix} H_n + \epsilon_n \\ \Delta \end{pmatrix}. \tag{3.33}$$

Now

$$\Delta = \frac{V}{2}\sum_n \frac{\Delta}{\sqrt{\Delta^2 + H_n^2}} \tag{3.34}$$

can be evaluated by dividing by Δ and replacing

$$\sum_n = \int_{-\hbar\omega_{\boldsymbol{q}}}^{\hbar\omega_{\boldsymbol{q}}} \mathrm{d}\xi\, D(\xi) \approx D(Ef) \int_{-\hbar\omega_{\boldsymbol{q}}}^{\hbar\omega_{\boldsymbol{q}}} \mathrm{d}\xi. \tag{3.35}$$

Here, ξ is the single-particle energy of H_n and we made use of the range of the attraction potential V in Eq. (3.1). Finally, we obtain

$$\begin{aligned} 1 = D(E_f)V \int_0^{\hbar\omega_{\boldsymbol{q}}} \mathrm{d}\xi\, \frac{1}{\sqrt{\Delta^2 + \xi^2}} &= VD(E_f)\sinh^{-1}\left[\frac{\hbar\omega_{\boldsymbol{q}}}{\Delta}\right] \\ \Leftrightarrow \quad \Delta = \hbar\omega_{\boldsymbol{q}}\sinh\left[\frac{1}{VD(E_f)}\right] &\overset{VD(E_f)\ll 1}{\approx} 2\hbar\omega_{\boldsymbol{q}}\exp\left[\frac{1}{VD(E_f)}\right]. \end{aligned} \tag{3.36}$$

Condensation energy

Knowing Δ, it is possible to calculate the expectation value of the interaction Hamiltonian (3.6) with the ground state of the superconductor (3.3). Subtracting the expectation value for a normal, non-superconducting state, one obtains the condensation energy at zero temperature [Gennes99]

$$E_\mathrm{G} - D(E_f)E_f \overset{E_f \gg \hbar\omega_{\boldsymbol{q}}}{\approx} -\frac{1}{2}D(E_f)\Delta^2. \tag{3.37}$$

This shows the same functional dependency as the simple evaluation for only two electrons by Cooper [Cooper56], cf. Eq. (3.2).

Excitation gap

From Eq. (3.29), we find that Δ is the minimum energy of an excitation, i.e., Δ is the minimum energy one has to pay to add (remove) an un-paired electron to (from) the SC. Additionally to "pair potential", Δ is hence often referred to as *superconducting gap* or *quasi-particle gap*.
In the case of a finite magnetic field $\boldsymbol{\mathcal{B}}$, the spin branches split in energy, leading to a shift of the excitation gap for each spin flavor. When this change in energy exceeds Δ, the SC becomes gapless. In chapter 7, we study superconducting 2D TIs and find gapless superconductivity at very small magnetic fields. Throughout this thesis, we stick to the name pair potential to avoid confusion between the parameter Δ and the $\boldsymbol{\mathcal{B}}$-dependent, effective quasi-particle gap.

Gauge invariance

In the derivation of the BdG Eqs. (3.22), the single-particle Hamiltonian $H(\hat{\boldsymbol{p}}, \boldsymbol{r})$ may incorporate a magnetic field via a vector potential $\boldsymbol{\mathcal{A}}(\boldsymbol{r})$. A gauge transformation

$$\boldsymbol{\mathcal{A}}'(\boldsymbol{r}) = \boldsymbol{\mathcal{A}}(\boldsymbol{r}) + \boldsymbol{\nabla}\chi(\boldsymbol{r}), \tag{3.38}$$

where $\chi(\boldsymbol{r})$ is an arbitrary, two times differentiable function, does not change the magnetic field and, hence, must not have any effect on physical observables. Suppose $(u_n(\boldsymbol{r}), v_n(\boldsymbol{r}))^T$ to be a solution to H_{BdG} in the gauge $\boldsymbol{\mathcal{A}}(\boldsymbol{r})$. In order to ensure that the excitation energies ϵ_n are gauge invariant, the solutions for the transformed vector potential $\boldsymbol{\mathcal{A}}'(\boldsymbol{r})$ must fulfill

$$\begin{pmatrix} u_n'(\boldsymbol{r}) \\ v_n'(\boldsymbol{r}) \end{pmatrix} = \begin{pmatrix} u_n(\boldsymbol{r}) \exp\left[\mathrm{i}\frac{e}{\hbar}\chi(\boldsymbol{r})\right] \\ v_n(\boldsymbol{r}) \exp\left[-\mathrm{i}\frac{e}{\hbar}\chi(\boldsymbol{r})\right] \end{pmatrix}. \tag{3.39}$$

From Eq. (3.31), we find that the pair potential has to accordingly change by

$$\Delta'(\boldsymbol{r}) = \Delta(\boldsymbol{r}) \exp\left[\mathrm{i}\frac{2e}{\hbar}\chi(\boldsymbol{r})\right]. \tag{3.40}$$

A complex superconducting gap can be written as $\Delta(\boldsymbol{r}) = |\Delta(\boldsymbol{r})| \exp[\mathrm{i}\phi(\boldsymbol{r})]$. Choosing the so-called *London gauge*

$$\chi(\boldsymbol{r}) = -\frac{\hbar}{2e}\phi(\boldsymbol{r}) \tag{3.41}$$

ensures a real pair potential $\Delta'(\boldsymbol{r}) = |\Delta(\boldsymbol{r})|$. In a single, homogeneous SC, this is equivalent to the *Coulomb gauge* [Gennes99]

$$\boldsymbol{\nabla} \cdot \boldsymbol{\mathcal{A}}(\boldsymbol{r}) = 0. \tag{3.42}$$

Let us shortly remark that the phase of the pair potential may have striking physical consequences. For example, when two SCs with different phases ϕ_1 and ϕ_2 are coupled by a tunneling junction, the phase difference $\Delta\phi = \phi_1 - \phi_2$ cannot be gauged away. In contrast, $\Delta\phi$ drives the tunneling of Cooper pairs from one SC to the other, even in the absence of an electric voltage.

This is the so-called *DC Josephson effect* [Josephson62], which carries the current

$$I_\mathrm{J} \propto \sin \Delta\phi. \tag{3.43}$$

3.1.5. Macroscopic wave function

The superconducting condensate was very successfully described in a phenomenological theory by Ginzburg and Landau. It assumes the superconducting condensate to be described by a macroscopic, complex wave function

$$\psi(\boldsymbol{r}) = |\psi(\boldsymbol{r})| \exp[\mathrm{i}\phi(\boldsymbol{r})], \tag{3.44}$$

in which the phase factor is inherited from the complex pair potential, with the same gauge dependence (3.40). It gives the local density of superconducting electrons

$$n_\mathrm{SC}(\boldsymbol{r}) = |\psi(\boldsymbol{r})|^2, \tag{3.45}$$

which, at zero temperature, is equal to the total density of electrons. Since $n_\mathrm{SC} = 0$ corresponds to a non-superconducting metal, ψ takes the role of an *order parameter* of the SC. Writing the free energy in terms of ψ allows the description of the electro- and thermodynamics of the SC. Here, we will just state two results of this theory, which are needed in the further course of the thesis:

Coherence length

The explicit position dependence of the macroscopic wave function allows to describe the boundaries of a SC and in particular the coexistence of superconducting and normal regions, like, e.g., in the presence of a magnetic field. Imagine the SC to be broken at a point $\boldsymbol{r}_0$. The length scale on which the superconducting order parameter changes around such an inhomogeneity is given by the *coherence length*. At zero temperature, it reads

$$\xi_\mathrm{SC} = \frac{\hbar v_\mathrm{F}}{\pi\Delta}, \tag{3.46}$$

where v_F is the Fermi velocity of the electrons. ξ_SC is of the order of the spacial extension of a Cooper pair, which is much larger than the average interparticle distance. Its value usually ranges from 10 to 100 nm [Kittel96]. For example, one finds $\xi_\mathrm{SC} \approx 40$ nm for clean Nb.

London equations

The electrodynamics of SCs can be phenomenologically described by the London equations [London35]. They can be motivated from the macroscopic wave function by considering the current density of superconducting electrons

$$\boldsymbol{j}_\mathrm{SC} = -e\langle\hat{\boldsymbol{v}}\rangle_\psi = -e\frac{\langle\hat{\boldsymbol{p}}\rangle_\psi}{m^*} = -e\frac{n_\mathrm{SC}}{m^*}\left[\hbar(\boldsymbol{\nabla}_{\boldsymbol{r}}\phi) + e\boldsymbol{\mathcal{A}}\right], \tag{3.47}$$

where the canonical momentum $\hat{\boldsymbol{p}} = -\mathrm{i}\hbar\boldsymbol{\nabla}_{\boldsymbol{r}} + e\boldsymbol{\mathcal{A}}$ with $e > 0$ was used. Again, we observe the physical relevance of the phase, whose gradient adds to the supercurrent. For a constant phase,

we obtain the *London equation*

$$\boldsymbol{j}_{\mathrm{SC}} = -\frac{e^2 n_{\mathrm{SC}}}{m^*}\boldsymbol{\mathcal{A}}. \tag{3.48}$$

This simple picture is enough to explain the two fundamental properties of SCs:
Perfect conductivity: The time derivative of Eq. (3.48) is

$$\partial_t \boldsymbol{j}_{\mathrm{SC}} = -\frac{e^2 n_{\mathrm{SC}}}{m^*}\partial_t \boldsymbol{\mathcal{A}} = \frac{e^2 n_{\mathrm{SC}}}{m^*}\boldsymbol{\mathcal{E}}. \tag{3.49}$$

In Ohmic conductors this acceleration would be balanced by a damping term, $-m^* v/\tau_s$, which originates from the scattering from impurities after a scattering time τ_s. For the heuristic (and not rigorous) motivation here, we assume $\tau_s \to \infty$ for SCs, resulting in an unlimited growth of the supercurrent in presence of a constant electric field $\boldsymbol{\mathcal{E}}$.
The Meissner effect: Taking the curl of Eq. (3.48) and using Ampère's law, we get a differential equation for the magnetic field

$$\boldsymbol{\nabla} \times \boldsymbol{j}_{\mathrm{SC}} = \boldsymbol{\nabla} \times \boldsymbol{\nabla} \times \boldsymbol{\mathcal{B}} = -\nabla^2 \boldsymbol{\mathcal{B}} = -\mu_0 \frac{e^2 n_{\mathrm{SC}}}{m^*}\boldsymbol{\mathcal{B}} = -\frac{1}{\lambda_{\mathrm{L}}^2}\boldsymbol{\mathcal{B}}, \tag{3.50}$$

whose characteristic scale is the *London length*

$$\lambda_{\mathrm{L}} = \sqrt{\frac{m^*}{e^2 \mu_0 n_{\mathrm{SC}}}}. \tag{3.51}$$

In a simple one-dimensional model, where the SC covers the half space $x > 0$, we find the solution $\boldsymbol{\mathcal{B}}(x) = \boldsymbol{\mathcal{B}}(x=0)\exp[-\lambda_{\mathrm{L}} x]$. The SC screens the magnetic field on a length scale of λ_{L} which is of the order of 10 nm and which usually is smaller than the coherence length [Kittel96].

3.2. Proximity effect

Bringing SCs in contact with thin films of normal conductors, Meissner [Meissner58, Meissner60] realized that the latter become superconducting, provided that the films' thickness is small enough. In contrast, if the superconducting film itself is too thin, it looses its superconducting properties. Therefore, it was suggested that this so-called *proximity effect* is mediated by electrons tunneling from the SC to the normal conductor and vice versa, which was described in a microscopic theory [McMillan68]. The effective or *induced* pair potential $\tilde{\Delta}$ inherits some of the features of the band structure of the normal conductor, allowing for the generation of exotic states. For example, combining conventional SCs with TIs leads to an induced pairing with p-wave components [Fu08]. Hence, the proximity effect allows to engineer *unconventional* SCs using conventional ones.
Here, we will first give some introductory remarks on unconventional superconductivity in section 3.2.1. Then, we describe the induced superconductivity in TIs in detail by presenting the full tunneling model in section 3.2.2, deriving the reduced model for the superconducting TI in section 3.2.3 and finally analyzing the induced pair potential in section 3.2.4.

3.2.1. Unconventional superconductivity

In general, the minimal excitation energy above the superconducting condensate can depend on the direction of the momentum within the BZ. In analogy to atomic orbitals, which are eigenstates of the angular momentum l, the pair potentials are characterized by their functional dependence on the momentum direction $\hat{\boldsymbol{p}}$ as l-wave pairing. So far, we have considered conventional superconductivity, which has an isometric ($l = 0$) pair potential and hence is referred to as *s-wave* pairing. The term *unconventional superconductivity* collects the phenomena of all pair potentials with $l > 0$ [Norman11]. For example, the high temperature superconductivity, which is realized in cuprates, has been shown to have d-wave symmetry [Norman11]. While the pairing mechanism is known to be mediated by phonons in case of conventional SCs, it is still an open question how the superconducting condensate is formed in unconventional SCs.
Unconventional superconductivity allows for exotic states with non-trivial topology. The BdG Hamiltonian (3.22) is analogous to a Hamiltonian describing a band insulator, where Δ takes the role of the band gap. Hence, it is possible to assign topological invariants to superconducting systems [Qi11]. These states are referred to as *topological superconductors*.
Here, we focus on p-wave pairing ($l = 1$) which is linear in the momentum $\boldsymbol{p}$. In contrast to isotropic s-wave SCs, which pair electrons to spin singlets, the p-wave pairing leads to an antisymmetric wave function. Consequently, p-wave SCs pair electrons in spin triplets and even allow for the condensation of spinless fermions [Qi11].
In the case of spinless fermions, the p-wave pairing breaks TRS ($\boldsymbol{p} \to -\boldsymbol{p}$) and the topology is described by an integer $\mathcal{N}$, analogously to the TKNN invariant in appendix A. In accordance with the bulk-boundary correspondence, the SC with topological index $\mathcal{N}$ is accompanied by $\mathcal{N}$ protected edge modes at zero energy. Since SCs are inherently particle-hole symmetric, states at zero energy are realizations of Majorana fermions, which are their own anti-particle. Indeed, it was shown, that the pair potential $\Delta(\boldsymbol{p}) \propto p_x + \mathrm{i}p_y$ supports Majorana zero energy bound states at its borders and vortices, see, e.g., [Alicea12]. Having a second copy of the system with pairing $p_x - \mathrm{i}p_y$ allows to form a spin-full system which conserves TRS. This is analogous to understanding the QSH effect as two copies of the QH effect, cf. Fig. 2.6 and its discussion in section 2.3.2. The spin-full models are characterized by a Z_2 invariant, which indicates the presence or absence of a pair of helical Majorana fermions [Qi11]. Due to their non-abelian statistics [Ivanov01], Majorana fermions are possible building blocks for topological quantum computing [Nayak08]. Unfortunately, the only currently known candidate for intrinsic p-wave pairing is Sr_2RuO_4, whose exact pairing structure is still on debate [Norman11]. However, in 2008, Fu and Kane [Fu08] realized that the p-wave pairing could be engineered by the combination of an s-wave SC with the helical spin structure in TIs by the proximity effect.

3.2.2. The tunneling model

The microscopic description of the proximity effect was introduced by McMillan [McMillan68]. Here, we follow Tkachov [Tkachov13, Tkachov15], who applied the tunneling model to (3D) TIs. A schematic of the system in question is shown on Fig. 3.1. It consists of an ordinary (s-wave) SC, which is coupled to a TI via an interface in the $x - y$ plane. At the interface, the superconducting order parameter changes on the length scale of the superconducting coherence length ξ_{SC} in Eq. (3.46). Since this is also the spatial extension of a Cooper pair, we can assume, that it is also the range, in which electrons from the SC will tunnel and induce superconductivity into a normal conductor. For example $\xi_{\mathrm{SC}} \approx 40$ nm for Nb [Kittel96], which has a rather small coherence length.

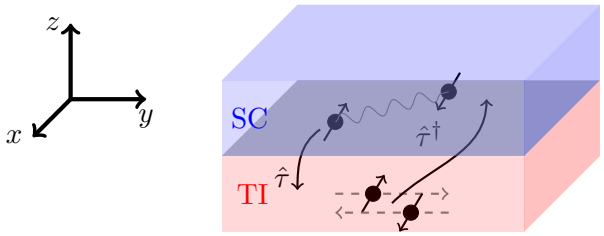

Figure 3.1.: A SC (blue) is brought in contact with a TI (red) via a planar interface in the $x-y$ plane. Electrons can tunnel from the SC into the TI and vice versa, inducing a superconducting pairing inside the TI.

Here, we assume the normal conductor to be either the surface state of a 3D TI, like it was calculated in [Tkachov13], or a 2D TI. In case of the 3D TI surface, the effective thickness is given by the penetration depth of the surface states, which ranges from about 4 nm (2-3 quintuple layers) for Bi-based compounds [Zhang10b] to about 20 nm in strained HgTe [Brüne14]. For typical 2D TIs, we find thicknesses of $d_{\mathrm{QW}} \approx 7$ nm in HgTe QWs [Bernevig06] and of about 4 quintuple layers for Bi-compound thin films [Shan10, Liu10b]. Altogether, we can conclude that the layer, into which superconductivity should be induced is much smaller than the tunneling range ξ_{SC}. Therefore, we will neglect any z-dependence in the tunneling strength in the following. Without space dependencies, the tunneling Hamiltonian can be written in the basis of the in-plane momentum $\boldsymbol{k} = (k_x, k_y)^T$

$$\mathcal{H} = \frac{1}{2}\sum_{\boldsymbol{k},\boldsymbol{k}'} \left(A_{\boldsymbol{k}}^\dagger, B_{\boldsymbol{k}}^\dagger\right) \underbrace{\begin{pmatrix} H_{\boldsymbol{k}}^{\mathrm{SC}}\delta_{\boldsymbol{k}\boldsymbol{k}'} & \hat{\tau}_{\boldsymbol{k}\boldsymbol{k}'} \\ \hat{\tau}_{\boldsymbol{k}\boldsymbol{k}'}^\dagger & H_{\boldsymbol{k}}^{\mathrm{TI}}\delta_{\boldsymbol{k}\boldsymbol{k}'} \end{pmatrix}}_{=:H_{\boldsymbol{k}\boldsymbol{k}'}} \begin{pmatrix} A_{\boldsymbol{k}'} \\ B_{\boldsymbol{k}'} \end{pmatrix}. \tag{3.52}$$

Here, $A_{\boldsymbol{k}}$ and $B_{\boldsymbol{k}}$ are the Nambu spinors of the SC and the TI in momentum space:

$$A_{\boldsymbol{k}} = \left(a_{\boldsymbol{k}\uparrow}, a_{\boldsymbol{k}\downarrow}, a_{-\boldsymbol{k}\uparrow}^\dagger, a_{-\boldsymbol{k}\downarrow}^\dagger\right)^T, \quad B_{\boldsymbol{k}} = \left(b_{\boldsymbol{k}\uparrow}, b_{\boldsymbol{k}\downarrow}, b_{-\boldsymbol{k}\uparrow}^\dagger, b_{-\boldsymbol{k}\downarrow}^\dagger\right)^T. \tag{3.53}$$

Since all the $a_{\boldsymbol{k}\sigma}$ and $b_{\boldsymbol{k}\sigma}$ ($a_{\boldsymbol{k}\sigma}^\dagger$ and $b_{\boldsymbol{k}\sigma}^\dagger$) are annihilation (creation) operators, also the full operator

$$C_{\boldsymbol{k}} = (A_{\boldsymbol{k}}, B_{\boldsymbol{k}})^T \tag{3.54}$$

fulfills the fermionic anticommutation relations (3.4), with $\left[C_{\boldsymbol{k}}, C_{\boldsymbol{k}'}^\dagger\right]_+ = 8\delta_{\boldsymbol{k}\boldsymbol{k}'}$. The Hamiltonian in the superconducting part is the singlet pairing BdG Hamiltonian (3.22) in momentum basis

$$H_{\boldsymbol{k}}^{\mathrm{SC}} = \begin{pmatrix} (\xi_{\boldsymbol{k}} - \mu^{\mathrm{SC}})\sigma_0 & \mathrm{i}\sigma_y\Delta\exp[\mathrm{i}\phi] \\ -\mathrm{i}\sigma_y\Delta\exp[-\mathrm{i}\phi] & -(\xi_{\boldsymbol{k}} - \mu^{\mathrm{SC}})\sigma_0 \end{pmatrix} \tag{3.55}$$

where we assume that the SC's dispersion $\xi_{\boldsymbol{k}}$ is diagonal in spin-space and the chemical potential $\mu^{\mathrm{SC}} \gg \Delta$. Here, we have written the phase of the pair potential ϕ explicitly and assume $\Delta \in \mathbb{R}$.

The BdG Hamiltonian for the TI

$$H_{\boldsymbol{k}}^{\mathrm{TI}} = \begin{pmatrix} h_{\boldsymbol{k}} & 0 \\ 0 & -h_{-\boldsymbol{k}}^{*} \end{pmatrix} \tag{3.56}$$

is diagonal in electron-hole space. $h_{\boldsymbol{k}}$ has an arbitrary spin-structure and will be specified later. The tunneling matrix is assumed not to couple electron- and hole-like states or different spin polarizations, but might mix different $\boldsymbol{k}$ values. It takes the general form

$$\hat{\tau}_{\boldsymbol{k}\boldsymbol{k}'} = \begin{pmatrix} \sigma_0 t_{\boldsymbol{k}\boldsymbol{k}'} & 0 \\ 0 & -\sigma_0 t_{-\boldsymbol{k}-\boldsymbol{k}'}^{*} \end{pmatrix}. \tag{3.57}$$

In the next section, we will use the Green's function formalism to reduce the hybrid system (3.52) to an effective description of the TI layer alone.

3.2.3. The superconductor's self-energy

The time-ordered Green's function for the bilayer system in terms of the time-dependent operators (3.54) is defined by

$$\begin{aligned} G(\boldsymbol{k},t;\boldsymbol{k}',t') &= \frac{1}{\mathrm{i}\hbar}\left\langle \hat{T} C_{\boldsymbol{k}}(t) \otimes C_{\boldsymbol{k}'}^{\dagger}(t') \right\rangle \\ &= \frac{1}{\mathrm{i}\hbar}\left\langle \hat{T} \begin{pmatrix} A_{\boldsymbol{k}}(t) \\ B_{\boldsymbol{k}}(t) \end{pmatrix} \otimes \left(A_{\boldsymbol{k}'}^{\dagger}(t'), B_{\boldsymbol{k}'}^{\dagger}(t') \right) \right\rangle = \begin{pmatrix} G^{\mathrm{SC}}(\boldsymbol{k},t;\boldsymbol{k}',t') & G^{\hat{\tau}}(\boldsymbol{k},t;\boldsymbol{k}',t') \\ G^{\hat{\tau}^{\dagger}}(\boldsymbol{k},t;\boldsymbol{k}',t') & G^{\mathrm{TI}}(\boldsymbol{k},t;\boldsymbol{k}',t') \end{pmatrix}. \end{aligned} \tag{3.58}$$

On the right hand side, we introduced the Green's functions of the respective subsystems G^{SC}, G^{TI}, $G^{\hat{\tau}}$ and $G^{\hat{\tau}^{\dagger}}$. Time ordering is enforced by the operator $\hat{T}$, which acts on two time dependent operators $a(t)$ and $b(t')$ according to

$$\hat{T} a(t) b(t') = \begin{cases} a(t)b(t') & , t > t' \\ -b(t')a(t) & , t < t' \end{cases}. \tag{3.59}$$

With this, one can reformulate the time-ordered Green's function in terms of step functions $\Theta(t)$:

$$G(\boldsymbol{k},t;\boldsymbol{k}',t') = \frac{\Theta(t-t')}{\mathrm{i}\hbar}\left\langle C_{\boldsymbol{k}}(t) \otimes C_{\boldsymbol{k}'}^{\dagger}(t') \right\rangle - \frac{\Theta(t'-t)}{\mathrm{i}\hbar}\left\langle C_{\boldsymbol{k}'}^{\dagger}(t') \otimes C_{\boldsymbol{k}}(t) \right\rangle. \tag{3.60}$$

The dynamics of the Green's function is determined by the dynamics of the operators which in turn is given by the Heisenberg equation of motion together with Eq. (3.52)

$$\mathrm{i}\hbar \partial_t C_{\boldsymbol{k}} = [C_{\boldsymbol{k}}, \mathcal{H}]_{-} = \sum_{\boldsymbol{k}'} H_{\boldsymbol{k}\boldsymbol{k}'} C_{\boldsymbol{k}'}. \tag{3.61}$$

Calculating the time derivative of Eq. (3.60) with $\partial_t \Theta(t-t') = \delta(t-t')$ leads to

$$\mathrm{i}\hbar \partial_t G(\boldsymbol{k},t;\boldsymbol{k}',t') - \sum_{\boldsymbol{l}} H_{\boldsymbol{k}\boldsymbol{l}} G(\boldsymbol{l},t;\boldsymbol{k}',t') = \delta(t-t')\delta_{\boldsymbol{k}\boldsymbol{k}'}. \tag{3.62}$$

For time independent systems, the Green's function only depends on the time difference $t - t'$ and it is convenient to use the energy representation

$$G(\boldsymbol{k}, \boldsymbol{k}', t - t') = \int \frac{\mathrm{d}E}{h} G(\boldsymbol{k}, \boldsymbol{k}', E) \exp\left[-\frac{\mathrm{i}}{\hbar} E(t - t')\right], \tag{3.63}$$

because its dynamics ($\mathbb{I}$ is the unit matrix)

$$\begin{aligned} \mathbb{I}\, \delta_{\boldsymbol{k}\boldsymbol{k}'} &= \sum_{\boldsymbol{l}} \left[E\delta_{\boldsymbol{l}\boldsymbol{k}} - H_{\boldsymbol{k}\boldsymbol{l}}\right] G(\boldsymbol{l}, \boldsymbol{k}', E) \\ &= \sum_{\boldsymbol{l}} \begin{pmatrix} (E - H^{\mathrm{SC}}_{\boldsymbol{k}})\delta_{\boldsymbol{k}\boldsymbol{l}} & -\hat{\tau}_{\boldsymbol{k}\boldsymbol{l}} \\ -\hat{\tau}^{\dagger}_{\boldsymbol{k}\boldsymbol{l}} & (E - H^{\mathrm{TI}}_{\boldsymbol{k}})\delta_{\boldsymbol{k}\boldsymbol{l}} \end{pmatrix} \begin{pmatrix} G^{\mathrm{SC}}(\boldsymbol{l}, \boldsymbol{k}', E) & G^{\hat{\tau}}(\boldsymbol{l}, \boldsymbol{k}', E) \\ G^{\hat{\tau}^{\dagger}}(\boldsymbol{l}, \boldsymbol{k}', E) & G^{\mathrm{TI}}(\boldsymbol{l}, \boldsymbol{k}', E) \end{pmatrix} \end{aligned} \tag{3.64}$$

can be solved by matrix inversion.
We assume that the SC's Fermi surface is much larger than that of the TI: $k_{\mathrm{F}}^{\mathrm{SC}} \gg k_{\mathrm{F}}^{\mathrm{TI}}$, where k_{F} is the Fermi momentum. In this case, we can neglect the influence of the electrons tunneling into the SC and solve $G^{\mathrm{SC}}(\boldsymbol{k}, \boldsymbol{k}', E)$ independently of the TI layer. To determine $G^{\mathrm{TI}}(\boldsymbol{k}, \boldsymbol{k}', E)$, we reformulate the second column of Eq. (3.64) into a system of coupled equations

$$0 = \left[E - H^{\mathrm{SC}}_{\boldsymbol{k}}\right] G^{\hat{\tau}}(\boldsymbol{k}, \boldsymbol{k}', E) - \sum_{\boldsymbol{l}} \hat{\tau}_{\boldsymbol{k}\boldsymbol{l}} G^{\mathrm{TI}}(\boldsymbol{l}, \boldsymbol{k}', E) \tag{3.65a}$$

$$\delta_{\boldsymbol{k}\boldsymbol{k}'} = \left[E - H^{\mathrm{TI}}_{\boldsymbol{k}}\right] G^{\mathrm{TI}}(\boldsymbol{k}, \boldsymbol{k}', E) - \sum_{\boldsymbol{l}} \hat{\tau}^{\dagger}_{\boldsymbol{k}\boldsymbol{l}} G^{\hat{\tau}}(\boldsymbol{l}, \boldsymbol{k}', E). \tag{3.65b}$$

Eliminating $G^{\hat{\tau}}(\boldsymbol{k}, \boldsymbol{k}', E)$ in the second equation gives *Dyson's equation* for the Green's function of the TI

$$\left[E - H^{\mathrm{TI}}_{\boldsymbol{k}}\right] G^{\mathrm{TI}}(\boldsymbol{k}, \boldsymbol{k}', E) - \sum_{\boldsymbol{l}\boldsymbol{l}'} \hat{\tau}^{\dagger}_{\boldsymbol{k}\boldsymbol{l}} G^{\mathrm{SC}}_0(\boldsymbol{l}, E) \hat{\tau}_{\boldsymbol{l}\boldsymbol{l}'} G^{\mathrm{TI}}(\boldsymbol{l}', \boldsymbol{k}', E) = \delta_{\boldsymbol{k}\boldsymbol{k}'}. \tag{3.66}$$

Since we assumed that the SC can be solved independently,

$$\begin{aligned} G^{\mathrm{SC}}_0(\boldsymbol{k}, E) &= \left[E - H^{\mathrm{SC}}_{\boldsymbol{k}}\right]^{-1} \\ &= \frac{1}{E^2 - \Delta^2 - (\xi_{\boldsymbol{k}} - \mu^{\mathrm{SC}})^2} \begin{pmatrix} E - \mu^{\mathrm{SC}} + \xi_{\boldsymbol{k}} & \mathrm{i}\sigma_y \Delta \exp[\mathrm{i}\phi] \\ -\mathrm{i}\sigma_y \Delta \exp[-\mathrm{i}\phi] & E + \mu^{\mathrm{SC}} - \xi_{\boldsymbol{k}} \end{pmatrix} \end{aligned} \tag{3.67}$$

is the SC's free Green's function. The solution of Eq. (3.66) is non-trivial and requires expansions in orders of the tunneling strength. To get an intuitive picture of the proximity effect let us start with the analytically solvable model of a clean interface.

Clean interface

In the simplest model, we treat a clean interface. In this case, the tunneling process conserves $\boldsymbol{k}$ and is assumed to be of constant strength τ. The tunneling matrix (3.57) thus is diagonal in k-space

$$t_{\boldsymbol{k}\boldsymbol{k}'} = \tau \delta_{\boldsymbol{k}\boldsymbol{k}'}, \tag{3.68}$$

and the Dyson equation takes the form

$$\left[E - H_{\boldsymbol{k}}^{\mathrm{TI}} - \Sigma_{\boldsymbol{k}}^{\mathrm{SC}}(E)\right] G^{\mathrm{TI}}(\boldsymbol{k}, \boldsymbol{k}', E) = \delta_{\boldsymbol{k}\boldsymbol{k}'}. \tag{3.69}$$

We have arrived at an effective model within the sub-space of the TI. The proximity coupled SC appears in form of the self-energy, which can be found from Eqs. (3.66) and (3.67)

$$\Sigma_{\boldsymbol{k}}^{\mathrm{SC}}(E) = \hat{\tau}^\dagger G_0^{\mathrm{SC}}(\boldsymbol{k}, E)\hat{\tau} = \frac{\tau^2}{E^2 - \Delta^2 - (\xi_{\boldsymbol{k}} - \mu^{\mathrm{SC}})^2} \begin{pmatrix} E - \mu^{\mathrm{SC}} + \xi_{\boldsymbol{k}} & -\mathrm{i}\sigma_y\Delta \exp[\mathrm{i}\phi] \\ \mathrm{i}\sigma_y\Delta \exp[-\mathrm{i}\phi] & E + \mu^{\mathrm{SC}} - \xi_{\boldsymbol{k}} \end{pmatrix}. \tag{3.70}$$

Comparing with the dynamics of the Green's function $\left[\tilde{E} - H_{\mathrm{BdG}}^{\mathrm{TI}}\right] G^{\mathrm{TI}}(\boldsymbol{k}, \boldsymbol{k}', E) = \delta_{\boldsymbol{k}\boldsymbol{k}'}$, we find the effective BdG Hamiltonian for the superconducting TI

$$H_{\mathrm{BdG}}^{\mathrm{TI}}(\boldsymbol{k}) = H_{\boldsymbol{k}}^{\mathrm{TI}} + \Sigma_{\boldsymbol{k}}^{\mathrm{SC}}(E) = \begin{pmatrix} h_{\boldsymbol{k}} - \tilde{\mu} & \mathrm{i}\sigma_y\tilde{\Delta} \exp[\mathrm{i}\phi] \\ -\mathrm{i}\sigma_y\tilde{\Delta} \exp[-\mathrm{i}\phi] & -h_{-\boldsymbol{k}}^* + \tilde{\mu} \end{pmatrix}. \tag{3.71}$$

The spectral shift $\tilde{E} - E = \Gamma E$, the doping $\tilde{\mu} = \Gamma(\xi_{\boldsymbol{k}} - \mu^{\mathrm{SC}})$ as well as the induced gap $\tilde{\Delta} = \Gamma\Delta$ are given in terms of the effective tunneling energy scale

$$\Gamma = \frac{\tau^2}{(\xi_{\boldsymbol{k}} - \mu^{\mathrm{SC}})^2 + \Delta^2 - E^2} \approx \frac{\tau^2}{(\xi_{\boldsymbol{k}=0} - \mu^{\mathrm{SC}})^2 + \Delta^2 - E^2}. \tag{3.72}$$

The approximation to neglect the $\boldsymbol{k}$ dependence is valid, again because $k_{\mathrm{F}}^{\mathrm{SC}} \gg k_{\mathrm{F}}^{\mathrm{TI}}$.

Dirty interface

A more sophisticated modelling of the bilayer takes into account that the interface in general is dirty [McMillan68, Tkachov13]. This breaks translational symmetry and the tunneling cannot conserve $\boldsymbol{k}$ anymore. When the contact area is large, the tunneling strength can be assumed to fluctuate randomly. The tunneling matrix (3.57) becomes a random matrix, whose correlation function

$$\left\langle t_{\boldsymbol{k}\boldsymbol{k}'} t_{\tilde{\boldsymbol{k}}\tilde{\boldsymbol{k}}'} \right\rangle = \frac{\tau^2}{a} \delta_{\boldsymbol{k}-\boldsymbol{k}', \tilde{\boldsymbol{k}}'-\tilde{\boldsymbol{k}}} \tag{3.73}$$

is given by the tunneling strength τ and the contact area a. Now, one cannot find an analytical solution of the Dyson equation (3.66) anymore. In the approximation, in which the SC is not affected by the TI, one can keep the mean value of the tunneling strength to be τ and assume that the dirty interface simply randomizes the momenta of the electrons which tunnel from the SC into the TI. In this case, we approximate Eq. (3.66) by

$$\left[E - H_{\boldsymbol{k}}^{\mathrm{TI}} - \tau^2(\pi_z \otimes \sigma_0)\mathcal{G}_0^{SC}(E)(\pi_z \otimes \sigma_0)\right] G^{\mathrm{TI}}(\boldsymbol{k}, \boldsymbol{k}', E) = \delta_{\boldsymbol{k}\boldsymbol{k}'}, \tag{3.74}$$

where we used the Pauli matrices in particle-hole space (π_i) and we have replaced the SC's Green's function in Eq. (3.70) by its momentum integrated version [Tkachov13]

$$\mathcal{G}_0^{SC}(E) = \int \frac{\mathrm{d}\boldsymbol{k}}{(2\pi)^2} G_0^{\mathrm{SC}}(\boldsymbol{k}, E) = -\mathrm{i}\frac{\pi D(\mu^{\mathrm{SC}})}{\sqrt{E^2 - \Delta^2}} \begin{pmatrix} E & \mathrm{i}\sigma_y\Delta \exp[\mathrm{i}\phi] \\ -\mathrm{i}\sigma_y\Delta \exp[-\mathrm{i}\phi] & E \end{pmatrix}. \tag{3.75}$$

Here $D(\mu^{\mathrm{SC}})$ is the DOS at the Fermi energy of the SC. Surprisingly, a rigorous calculation within second order self-consistent Born approximation confirms this simple picture [Tkachov13]. Comparing with the clean case, we find that the effective Hamiltonian for the superconducting TI (3.71) remains unchanged, except of the induced doping $\tilde{\mu}$, which becomes zero upon averaging over all $\boldsymbol{k}$. The effective tunneling strength now is $\boldsymbol{k}$ independent

$$\Gamma = \frac{\pi\tau^2 D(\mu^{\mathrm{SC}})}{\sqrt{\Delta^2 - E^2}}. \tag{3.76}$$

The effective tunneling strength Γ becomes imaginary, when $E^2 > \Delta^2$. This leads to an non-hermitian part in the spectral shift $\tilde{E} - E = \Gamma E$, describing the finite life-time of electrons which escape into the SC at energies above the excitation gap [Datta05].

In conclusion, we have found that the effective BdG Hamiltonian of a TI, into which superconductivity is induced by the proximity effect, can be written in Nambu basis as[3]

$$H_{\mathrm{BdG}}^{\mathrm{TI}}(\boldsymbol{k}) = \begin{pmatrix} h_{\boldsymbol{k}} & \mathrm{i}\sigma_y\tilde{\Delta}\exp[\mathrm{i}\phi] \\ -\mathrm{i}\sigma_y\tilde{\Delta}\exp[-\mathrm{i}\phi] & -h^*_{-\boldsymbol{k}} \end{pmatrix}. \tag{3.77}$$

Here and in the following, we will neglect the excitation energy dependence of the effective tunneling strength and treat the induced pair potential as constant. The induced doping $\tilde{\mu}$ has been absorbed into $h_{\boldsymbol{k}}$ and can only be non-zero, when the interface is sufficiently clean, an assumption we will use in chapter 6.
On the experimental side, induced superconductivity has been measured in the surface states of the 3D TI strained HgTe in contact with Niobium, resulting in an induced gap ranging from $\tilde{\Delta} \approx 50$ μeV [Maier12] up to $\tilde{\Delta} \lessapprox 190$ μeV [Sochnikov15]. Studies on 2D TIs using inverted InAs/GaSb QWs found $\tilde{\Delta} \lesssim 125$ μeV [Knez12, Pribiag15]. For HgTe/CdTe QWs $\tilde{\Delta} \approx 20$ μeV has been measured [Hart14]. The last value is smaller in comparison with the induced pairing measured in InAs/GaSb QWs, because Hart et al. used aluminum instead of niobium for the superconducting layer.

3.2.4. p-wave pairing contribution

In the previous section, we have derived the effective BdG Hamiltonian $H_{\mathrm{BdG}}^{\mathrm{TI}}$, cf. Eq. (3.77), for the superconducting TI layer. On the level of the Hamiltonian, the pairing term keeps the singlet symmetry $\mathrm{i}\sigma_y\Delta$ of the ordinary SC in contact with the TI, cf. Fig. 3.1. Here, we will analyze the structure of the pair potential in detail. To do so, we evaluate the Green's function of the normal system explicitly by inversion of

$$[E - H_{\mathrm{BdG}}^{\mathrm{TI}}(\boldsymbol{k})]G^{\mathrm{TI}}(\boldsymbol{k}, \boldsymbol{k}', E) = \delta_{\boldsymbol{k}\boldsymbol{k}'}. \tag{3.78}$$

Since all terms only depend on $\boldsymbol{k}$, we seek the solution in terms of $G^{\mathrm{TI}}(\boldsymbol{k}, E) = G^{\mathrm{TI}}(\boldsymbol{k}, \boldsymbol{k}', E)\delta_{\boldsymbol{k}\boldsymbol{k}'}$. In order to see the connection of the pair potential with the Green's function, we will go back to its time-ordered formulation in the Nambu basis (3.53)

$$G^{\mathrm{TI}}(\boldsymbol{k}, t, t') = \frac{1}{\mathrm{i}\hbar}\left\langle \hat{T}B_k(t) \otimes B_k^\dagger(t')\right\rangle = \begin{pmatrix} G_e^{\mathrm{TI}}(t,t') & G_{eh}^{\mathrm{TI}}(t,t') \\ G_{he}^{\mathrm{TI}}(t,t') & G_h^{\mathrm{TI}}(t,t') \end{pmatrix}. \tag{3.79}$$

[3] The derived effective Hamiltonian is also valid for other systems than TIs. Since we did not make any assumption about the normal system, $h_{\boldsymbol{k}}$ could indeed describe any 2D system which preserves momentum.

It consists of parts describing the electron- (G_e^{TI}) and hole-like (G_h^{TI}) excitations as well as their coupling (G_{eh}^{TI}). At $t = t'$, we find that

$$G_{eh}^{\mathrm{TI}}(\boldsymbol{k}, t, t) = \frac{1}{\mathrm{i}\hbar} \begin{pmatrix} \langle b_{\boldsymbol{k}\uparrow} b_{-\boldsymbol{k}\uparrow} \rangle & \langle b_{\boldsymbol{k}\uparrow} b_{-\boldsymbol{k}\downarrow} \rangle \\ \langle b_{\boldsymbol{k}\downarrow} b_{-\boldsymbol{k}\uparrow} \rangle & \langle b_{\boldsymbol{k}\downarrow} b_{-\boldsymbol{k}\downarrow} \rangle \end{pmatrix} \tag{3.80}$$

resembles the $\boldsymbol{k}$ space equivalent to the pair correlation function, which defines the pair potential in mean field theory. Using Pauli matrices in spin space (σ_i), the Green's function can be written as

$$G_{eh}^{\mathrm{TI}}(\boldsymbol{k}, t, t) = \mathrm{i}\sigma_y \left[\Delta_{\mathrm{singlet}} + \boldsymbol{\sigma} \cdot \boldsymbol{\Delta}_{\mathrm{triplet}}\right], \tag{3.81}$$

where the first part, which is proportional to $\Delta_{\mathrm{singlet}}$, corresponds to the definition of the singlet pairing in an s-wave SC in Eq. (3.14). The remaining terms are proportional to σ_0, σ_x or σ_z and result in a triplet pairing, which is even in spin. Consequently, $\boldsymbol{\Delta}_{\mathrm{triplet}}$ must be antisymmetric in $\boldsymbol{k}$, so that the total state shows fermionic symmetry.
Here, we consider induced superconductivity on the surface of a 3D TI as well as in 2D TIs. We will find that the interplay of helical modes with singlet Cooper pairs leads to a p-wave contribution in the effective pairing terms [Fu08]. While the induced pairing in 3D TI surface states has been analyzed in literature, a detailed description in case of 2D TIs has not yet been published to the best of our knowledge. Therefore, we will present detailed calculations for the latter, while only mentioning the results for the 3D TI surface states.

Surface states of a 3D TI

The simplest model for a surface state of a 3D TI is that of massless Dirac fermions [Fu07b, Zhang09, Liu10a]

$$H_{\mathrm{surface}}(\boldsymbol{k}) = \hbar v_{\mathrm{F}}(k_x\sigma_x + k_y\sigma_y) - \mu, \tag{3.82}$$

where v_{F} and μ are the Fermi velocity and the chemical potential, respectively. Plugging this into Eq. (3.77) and inverting Eq. (3.78), leads to[4]

$$G_{eh}^{\mathrm{TI}}(\boldsymbol{k}) = \mathrm{i}\sigma_y\tilde{\Delta}\frac{E^2 - \mu^2 - \hbar^2 v_{\mathrm{F}}^2 k^2 - |\tilde{\Delta}|^2 + 2\mu\hbar v_{\mathrm{F}}(\sigma_x k_x - \sigma_y k_y)}{\left[E^2 - (\hbar v_{\mathrm{F}} k - \mu)^2 - |\tilde{\Delta}|^2\right]\left[E^2 - (\hbar v_{\mathrm{F}} k + \mu)^2 - |\tilde{\Delta}|^2\right]}, \tag{3.83}$$

where $k = \sqrt{k_x^2 + k_y^2}$. The triplet component

$$\boldsymbol{\Delta}_{\mathrm{triplet}} \propto 2\tilde{\Delta}\mu\hbar v\boldsymbol{k} \tag{3.84}$$

corresponds to the p-wave pairing mechanism [Fu08].

Two-dimensional topological insulators

The two experimentally realized 2D TIs HgTe/CdTe and InAs/GaSb QWs are described by the BHZ model (2.59). This model has an additional pseudo-spin structure, encoded in the

[4] The calculation is similar to the one for 2D TIs presented below. A detailed derivation can also be found in [Tkachov15].

Pauli matrices in sub-band space (τ_i). In this sense, the fermionic operators become pseudo-spinors in the sub-band space (E1,H1): $b_{\sigma\boldsymbol{k}} = (b_{\boldsymbol{k}\sigma\mathrm{E1}}, b_{\boldsymbol{k}\sigma\mathrm{H1}})^T$, where $\sigma = \uparrow, \downarrow$. In the basis $\left(b_{\boldsymbol{k}\uparrow}, b_{\boldsymbol{k}\downarrow}, b^\dagger_{-\boldsymbol{k}\uparrow}, b^\dagger_{-\boldsymbol{k}\downarrow}\right)^T$, the BdG Hamiltonian reads

$$H_{\mathrm{BdG}}(\boldsymbol{k}) = \begin{pmatrix} \epsilon(\boldsymbol{k}) + d_i(\boldsymbol{k})\tau_i & 0 & 0 & \tilde{\Delta} \\ 0 & \epsilon(-\boldsymbol{k}) + d_i(-\boldsymbol{k})\tau_i^* & -\tilde{\Delta} & 0 \\ 0 & -\tilde{\Delta}^* & -\epsilon(-\boldsymbol{k}) - d_i(-\boldsymbol{k})\tau_i^* & 0 \\ \tilde{\Delta}^* & 0 & 0 & -\epsilon(-\boldsymbol{k}) - d_i(\boldsymbol{k})\tau_i \end{pmatrix}, \tag{3.85}$$

where we omitted the unity matrix τ_0 for simplicity and the $d_i(\boldsymbol{k})$ are defined in Eq. (2.61). In contrast to Eq. (3.82), the linear $\boldsymbol{k}$ terms couple the pseudo-spin. Here, we assume the pair potential, $\mathrm{i}\sigma_y \otimes \tau_0\tilde{\Delta}$, to be diagonal in the sub-band space, so that electron-like E1 (H1) sub-bands with spin σ couple to the corresponding hole-like E1 (H1) states with $-\sigma$. In general, the induced pairing might couple different sub-bands. The off-diagonal contributions have been found to be important, when the bulk gap M is of the same order as the induced superconducting correlation [Khaymovich11]. However, for typical parameters of HgTe/CdTe (InAs/GaSb) QWs the bulk gap $M \approx 10$ meV (≈ 4 meV) [Ando13] is much larger than the induced pairing discussed at the end of section 3.2.3.

The Hamiltonian in Eq. (3.85) is block diagonal in the Kramers' partners and can thus be decoupled in two blocks $H^{\uparrow\downarrow}_{\mathrm{BdG}}$ and $H^{\downarrow\uparrow}_{\mathrm{BdG}}$, which describe the superconducting coupling of spin-$\uparrow$ electron-like to spin-$\downarrow$ hole-like excitations and vice versa. In order to solve $H^{\uparrow\downarrow}_{\mathrm{BdG}}$ independently, we rewrite Eq. (3.78) in two coupled equations for $G^{\mathrm{TI}}_{h,\uparrow\downarrow}$ and $G^{\mathrm{TI}}_{eh,\uparrow\downarrow}$:

$$\left[E - \epsilon(\boldsymbol{k}) - d_i(\boldsymbol{k})\tau_i\right] G^{\mathrm{TI}}_{eh,\uparrow\downarrow} - \tilde{\Delta} G^{\mathrm{TI}}_{h,\uparrow\downarrow} = 0 \tag{3.86a}$$

$$-\tilde{\Delta}^* G^{\mathrm{TI}}_{eh,\uparrow\downarrow} + \left[E + \epsilon(\boldsymbol{k}) + d_i(\boldsymbol{k})\tau_i\right] G^{\mathrm{TI}}_{h,\uparrow\downarrow} = 1. \tag{3.86b}$$

Multiplying Eq. (3.86b) from the left by $[E - \epsilon(\boldsymbol{k}) - d_i(\boldsymbol{k})\tau_i]$ allows to eliminate $G^{\mathrm{TI}}_{eh,\uparrow\downarrow}$ by virtue of Eq. (3.86a) and we obtain

$$\left[E^2 - |\tilde{\Delta}|^2 - (\epsilon(\boldsymbol{k}) + d_i(\boldsymbol{k})\tau_i)^2\right] G^{\mathrm{TI}}_{h,\uparrow\downarrow} = E - \epsilon(\boldsymbol{k}) - d_i(\boldsymbol{k})\tau_i. \tag{3.87}$$

Multiplying again from the left by

$$\left[E^2 - |\tilde{\Delta}|^2 - (\epsilon(\boldsymbol{k}) - d_i(\boldsymbol{k})\tau_i)^2\right] = \left[E + \epsilon(\boldsymbol{k}) - d_i(\boldsymbol{k})\tau_i\right]\left[E - \epsilon(\boldsymbol{k}) + d_i(\boldsymbol{k})\tau_i\right] \tag{3.88}$$

leaves the left hand side of Eq. (3.87) to be purely proportional to τ_0. Defining

$$N = \left[E^2 - |\tilde{\Delta}|^2 - (\epsilon(\boldsymbol{k}) + d(\boldsymbol{k}))^2\right]\left[E^2 - |\tilde{\Delta}|^2 - (\epsilon(\boldsymbol{k}) - d(\boldsymbol{k}))^2\right], \tag{3.89}$$

where $d(\boldsymbol{k}) = ||\boldsymbol{d}(\boldsymbol{k})||$, we arrive at

$$G^{\mathrm{TI}}_{h,\uparrow\downarrow} = \frac{1}{N}\left[\left((E - \epsilon(\boldsymbol{k}))^2 - d^2(\boldsymbol{k})\right)\left(E + \epsilon(\boldsymbol{k}) - d_i(\boldsymbol{k})\tau_i\right) - |\tilde{\Delta}|^2\left(E - \epsilon(\boldsymbol{k}) - d_i(\boldsymbol{k})\tau_i\right)\right]. \tag{3.90}$$

Inserting into Eq. (3.86a), results in

$$G^{\mathrm{TI}}_{eh,\uparrow\downarrow} = \frac{\tilde{\Delta}}{N}\left[E^2 - |\tilde{\Delta}|^2 - \epsilon^2(\boldsymbol{k}) - d^2(\boldsymbol{k}) + 2\epsilon(\boldsymbol{k})d_i(\boldsymbol{k})\tau_i\right]. \tag{3.91}$$

Here, we observe a similar structure in the pseudo-spin space like the correlation function for the surface states shows for the real spin in Eq. (3.83). Analogously, we calculate

$$G^{\mathrm{TI}}_{eh,\downarrow\uparrow} = -\frac{\tilde{\Delta}}{N}\left[E^2 - |\tilde{\Delta}|^2 - \epsilon^2(\boldsymbol{k}) - d^2(\boldsymbol{k}) + 2\epsilon(\boldsymbol{k})d_i(-\boldsymbol{k})\tau_i^*\right], \tag{3.92}$$

and combine to the closed form

$$\begin{aligned} G^{\mathrm{TI}}_{eh} = \frac{\tilde{\Delta}}{N}\Big[&\underbrace{\mathrm{i}\sigma_y \otimes \left(E^2 - |\tilde{\Delta}|^2 - \epsilon^2(\boldsymbol{k}) - d^2(\boldsymbol{k}) + 2\epsilon(\boldsymbol{k})d_3(\boldsymbol{k})\tau_z\right)}_{\text{singlet}} \\ &+ \underbrace{2\epsilon(\boldsymbol{k})A\left(k_x\sigma_x \otimes \tau_x - \mathrm{i}k_y\sigma_y \otimes \tau_y\right)}_{\text{triplet}}\Big], \end{aligned} \tag{3.93}$$

where we explicitly wrote $d_1 = Ak_x$ and $d_2 = -Ak_y$, cf. Eq. (2.61). Interestingly, despite being diagonal in the Kramers' partners, the helical coupling in pseudo-spin space leads to triplet pairing terms, which consequently are proportional to the coupling strength A. To better understand this, we define $\kappa_0 = E^2 - |\tilde{\Delta}|^2 - \epsilon^2(\boldsymbol{k}) - d^2(\boldsymbol{k})$, rewrite Eq. (3.93) in explicit matrix form and compare it with the definition of Eq. (3.80):

$$\begin{aligned} G^{\mathrm{TI}}_{eh} &= \frac{\tilde{\Delta}}{N}\begin{pmatrix} 0 & 0 & \kappa_0 + 2\epsilon(\boldsymbol{k})d_3(\boldsymbol{k}) & 2\epsilon(\boldsymbol{k})A(k_x + \mathrm{i}k_y) \\ 0 & 0 & 2\epsilon(\boldsymbol{k})A(k_x - \mathrm{i}k_y) & \kappa_0 - 2\epsilon(\boldsymbol{k})d_3(\boldsymbol{k}) \\ -\kappa_0 - 2\epsilon(\boldsymbol{k})d_3(\boldsymbol{k}) & 2\epsilon(\boldsymbol{k})A(k_x - \mathrm{i}k_y) & 0 & 0 \\ 2\epsilon(\boldsymbol{k})A(k_x + \mathrm{i}k_y) & -\kappa_0 + 2\epsilon(\boldsymbol{k})d_3(\boldsymbol{k}) & 0 & 0 \end{pmatrix} \\ &= \frac{1}{\mathrm{i}\hbar}\begin{pmatrix} & & \langle b_{\boldsymbol{k}\uparrow E1}b_{-\boldsymbol{k}\downarrow E1}\rangle & \langle b_{\boldsymbol{k}\uparrow E1}b_{-\boldsymbol{k}\downarrow H1}\rangle \\ & & \langle b_{\boldsymbol{k}\uparrow H1}b_{-\boldsymbol{k}\downarrow E1}\rangle & \langle b_{\boldsymbol{k}\uparrow H1}b_{-\boldsymbol{k}\downarrow H1}\rangle \\ \langle b_{\boldsymbol{k}\downarrow E1}b_{-\boldsymbol{k}\uparrow E1}\rangle & \langle b_{\boldsymbol{k}\downarrow E1}b_{-\boldsymbol{k}\uparrow H1}\rangle & & \\ \langle b_{\boldsymbol{k}\downarrow H1}b_{-\boldsymbol{k}\uparrow E1}\rangle & \langle b_{\boldsymbol{k}\downarrow H1}b_{-\boldsymbol{k}\uparrow H1}\rangle & & \end{pmatrix}. \end{aligned} \tag{3.94}$$

All finite pairing terms couple states of different Kramers' partner polarization $\sigma = \uparrow, \downarrow$. Therefore, it is important to look at the combination of pseudo-spin and Kramers' partner polarization to identify the correct pairing symmetry. The terms proportional to $\mathrm{i}\sigma_y \otimes \tau_0$ and $\mathrm{i}\sigma_y \otimes \tau_z$ pair states with the same pseudo-spin (τ =E1,H1). The relative sign of these terms, i.e.,

$$\langle b_{\boldsymbol{k}\sigma\tau}b_{-\boldsymbol{k}-\sigma\tau}\rangle = -\langle b_{\boldsymbol{k}-\sigma\tau}b_{-\boldsymbol{k}\sigma\tau}\rangle, \tag{3.95}$$

is odd in the spinor structure of the Nambu basis. At the same time, these entries of G^{TI}_{eh} have an even structure in $\boldsymbol{k}$, which identifies them as singlet pairing terms. In contrast, all terms proportional to $\sigma_x \otimes \tau_x$ and $\mathrm{i}\sigma_y \otimes \tau_y$ correspond to triplet symmetry:

$$\langle b_{\boldsymbol{k}\sigma\tau}b_{-\boldsymbol{k}-\sigma-\tau}\rangle = \langle b_{\boldsymbol{k}-\sigma-\tau}b_{-\boldsymbol{k}\sigma\tau}\rangle. \tag{3.96}$$

These terms couple states of different Kramers' partner and pseudo-spin flavor. Analogously to the surface of a 3D TI, the triplet pairing contribution of Eq. (3.93) is proportional to $\boldsymbol{k}$, i.e., it

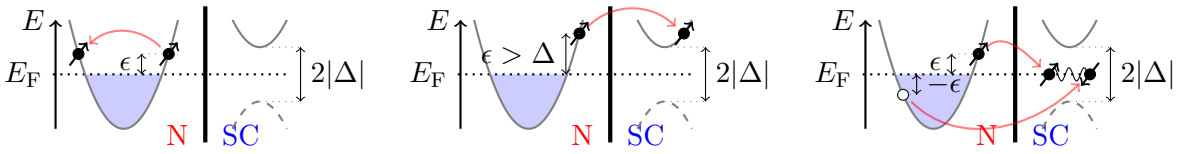

(a) electron reflection (b) electron transmission (c) Andreev reflection

Figure 3.2.: An electron, which is injected onto a junction between a normal metal (left) and a SC (right), can be reflected (a) or transmitted (b) as an electron or reflected as a hole (c).

has p-wave character.

Effective model for helical edge states

In this context, it is interesting to analyze the induced pair potential in an effective description of the helical edge states. A single pair of helical edge states along a boundary disperses linearly in k, leading to the effective Hamiltonian

$$H_{\text{edge}} = \hbar v_{\text{F}} k \sigma_z - \mu, \tag{3.97}$$

where σ_z again acts on the Kramers' partner sub-space. The pseudo-spin of the sub-bands is not explicitly contained, but its linear coupling parameter A determines the Fermi velocity v_{F} of the edge states, as discussed in section 2.3.1. In contrast, to the surface Hamiltonian (3.82), H_{edge} conserves the Kramers' partner, but the helicity of the edge states shifts the energy of the Kramers' partner branches k-dependently. Therefore, the corresponding correlation function

$$G_{eh}^{\text{edge}}(k) = \mathrm{i}\sigma_y \tilde{\Delta} \frac{E^2 - \mu^2 - \hbar^2 v_{\text{F}}^2 k^2 - |\tilde{\Delta}|^2 + 2\mu\hbar v_{\text{F}} k \sigma_z}{\left[E^2 - (\hbar v_{\text{F}} k - \mu)^2 - |\tilde{\Delta}|^2\right]\left[E^2 - (\hbar v_{\text{F}} k + \mu)^2 - |\tilde{\Delta}|^2\right]} \tag{3.98}$$

shows triplet pairing terms $\propto 2\tilde{\Delta}\mu\hbar v_{\text{F}} k$, analogously to that of a surface state in Eq. (3.83).

3.3. Andreev reflection

The exotic features of SCs in general and especially superconducting TIs can often be characterized by transport through a junction between a normal conductor and a superconductor (N-SC junction). Before we turn to transport in mesoscopic systems in chapter 4, we here introduce the transport process of Andreev reflection (AR), which is unique for N-SC junctions. An exemplary N-SC junction is depicted in Fig. 3.2. Here, the normal conducting material on the left is a metal with spin-degenerate, quadratic dispersion, which is filled with electrons up to the Fermi energy E_{F}. The SC's BdG dispersion is shown on the right side. It consist of electron like excitations with excitation energy $\epsilon > |\Delta|$ and an artificial hole-like band for $\epsilon < -|\Delta|$, which are separated by the excitation gap around E_{F}. In this configuration, the normal conductor is an (infinitely) extended contact. Thus, we consider the interface as step-like and neglect interface effects, like induced superconductivity in the normal region.
We consider a spin-↑ electron with excitation energy ϵ above E_{F} to be injected from the normal

conductor towards the junction. At the junction, it can undergo three different elastic scattering processes, which are sketched in Fig. 3.2. The electron can be reflected from the interface into the counter-propagating branch of the dispersion at excitation energy ϵ, cf. Fig. 3.2a. When $\epsilon > |\Delta|$, the incoming electron carries enough energy to enter the SC as a quasi-particle excitation. This electron transmission is shown in Fig. 3.2b. In N-SC junctions an additional scattering process can occur, which has been named Andreev reflection after its discoverer [Andreev64]. Since the number of Cooper pairs is not conserved in a SC, the incoming electron can also be absorbed into the superconducting condensate, when it pairs with an electron which has energy $-\epsilon$, spin-$\downarrow$ and momentum $-\boldsymbol{k}$. This second electron is taken out of the Fermi sea of the normal conductor and leaves behind a missing electron with spin-$\downarrow$, which is propagating away from the interface, cf. Fig. 3.2c. Since not only the incoming electron but also the second electron enters the SC, AR processes can be identified by a doubling of the charge conductance. We will describe transport in N-SC junctions in detail in the next chapter, when we discuss the BTK formalism.
To better understand AR, let us describe the scattering process in the BdG formalism of section 3.1.3, where missing electrons at energy $-\epsilon$ are incorporated as hole-like excitation at ϵ, cf. appendix D. The superconducting condensate does not enter the BdG formalism explicitly and the AR has to be seen as a conversion of an electron-like to a hole-like excitation. Both excitation branches are decoupled in the normal region, where $\Delta = 0$. The coupling happens in the SC, where the solution for $\epsilon > 0$ is given by Eq. (3.33)[5]. The Andreev reflection amplitude (R_h) must then be proportional to the relative weight of the hole-like component and its probability is given by

$$|R_h|^2 \propto \left|\frac{v_\downarrow}{u_\uparrow}\right|^2 = \left|\frac{\Delta}{H+\epsilon}\right|^2 = \left|\frac{\Delta}{\sqrt{\epsilon^2-\Delta^2}+\epsilon}\right|^2 . \tag{3.99}$$

While for $\epsilon < |\Delta|$ both branches are perfectly mixed, the hole-like component decreases for $\epsilon > |\Delta|$. This means that the states far above the quasi-particle gap behave as normal, non-superconducting electrons. In consequence, AR can only occur around the gap and will decrease at higher excitation energies, where electron transmission becomes dominant.
As we will calculate explicitly in section 7.2.4, Eq. (3.99) is correct in the absence of electron reflection. In this case, the scattering process is characterized by perfect AR for $\epsilon < |\Delta|$, making AR an apt tool to explore the superconducting gap in transport experiments. However, the interface between a normal conductor and a SC is not perfect. This situation is best described in a so-called normal-insulator-superconducting interface, in which an insulating tunneling barrier at the interface introduces backscattering.

Andreev reflection in helical edge states

In this thesis, we discuss junctions between 2D TIs as normal conductors and superconducting 2D TIs, into which superconductivity has been induced by the proximity effect. The edge states of a 2D TI are protected against backscattering and are perfectly transmitted through a possible insulating tunneling barrier at the junction, leading to perfect Andreev reflection ($|R_h|^2 = 1$) for $\epsilon < |\Delta|$ [Adroguer10]. Thus, it is sufficient to neglect the insulating layer and simply treat N-SC junctions. We discuss corrections to this simple model in chapter 6, where we deal with finite size effects in junctions between 2D TIs and SCs.

[5]This discussion is valid for any quantum number n in Eq. (3.33). Therefore, we neglect the index n here. In this case, the Hamiltonian of the normally conducting system is referred to simply by H.

(a) electron tunneling

(b) crossed Andreev reflection

Figure 3.3.: When the superconducting part has a finite length L, two new processes can occur: electron tunneling at $\epsilon < |\Delta|$ and crossed Andreev reflection.

N-SC-N junctions

Often, one is interested in transport through a superconducting junction of finite length L. Such a normal - superconducting - normal junction (N-SC-N junction) is schematically drawn in Fig. 3.3, where we assume both normally conducting regions to have the same band-structure and Fermi energy. There are two elastic transport processes, which scatter the incoming electron from the left lead into a charge carrier in the right lead: Firstly, the incoming electron can tunnel through the superconducting region even at energies $\epsilon < |\Delta|$. Secondly, the incoming spin-$\uparrow$ electron can form a Cooper pair with a spin-$\downarrow$ electron from the second lead. The last process is called crossed Andreev reflection (CAR) and ejects a hole into the right lead with probability $|T_h|^2$. Both scattering processes are non-local and decay exponentially with L.

4. Mesoscopic transport

This chapter gives a short introduction into transport in mesoscopic structures. Defining the mesoscopic regime in section 4.1, we will realize that a full quantum mechanical treatment is needed to describe transport in these systems, which is cast in the non-equilibrium Green's function formalism. For an introduction, the interested reader is referred to, e.g., [Datta05, Datta07]. In this thesis, however, we restrict our discussion to a phase coherent single-particle picture, in which the non-equilibrium Green's function formalism reduces to the S-matrix formalism presented in section 4.2. Section 4.2.4 treats the generalization to superconducting systems within the BTK formalism. The S-matrix formalism connects the transport coefficients to the scattering problem, which we solve for quasi-one dimensional systems within the wave matching approach in section 4.3. The solution is found for periodic boundary conditions as well as hard-wall boundary conditions, for which we generalize the wave matching approach in section 4.3.2.

4.1. The mesoscopic regime

The principal setup, which we analyze in this thesis, is the Hall bridge depicted in Fig. 4.1. It consists of a two-dimensional conductor of length L and width W, which is connected at each side to a contact via a lead of the same width. The whole system can be seen as a quasi one-dimensional wire, which conventionally points along x-direction.
In order to define the mesoscopic regime, we focus on the conductor. It consists of a periodic atomic lattice, in which the particles move freely with momentum $\boldsymbol{k}$ and effective mass $m^* = \hbar^2 \left[\partial^2 E/\partial \boldsymbol{k}^2\right]^{-1}$. The particles carry the charge q. In most cases, they will be electrons with $q = -e$. Their movement is characterized by three length scales:
Fermi wave length: In the nearly free electron picture, the particles move as plane waves with wave length λ. At zero temperature, all states up to the Fermi energy E_F are filled and only states close to E_F can contribute to transport. Hence, we can define a unique Fermi wavelength

$$\lambda_\mathrm{F} = \frac{2\pi}{k_\mathrm{F}}, \tag{4.1}$$

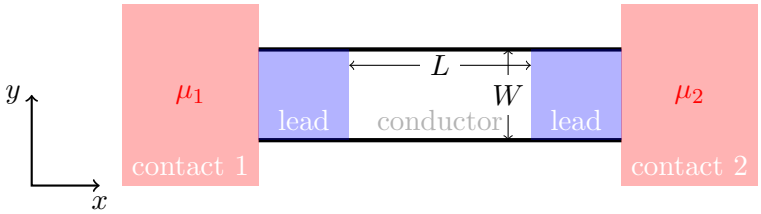

Figure 4.1.: Schematic of a mesoscopic Hall bridge of length L and width W, which is connected to contacts 1 and 2 via two leads.

by the Fermi momentum k_F. In a spin-degenerate 2D system, the Fermi momentum is given in terms of the electron density n: $k_\mathrm{F} = \sqrt{2\pi n}$. For typical HgTe/CdTe QWs n ranges from 10^{10} cm^{-2} to 10^{12} cm^{-2} [Pfeuffer-Jeschke00]. Hence, the Fermi wavelength is of the order 10 nm to 100 nm.

Mean free path: The particle can either scatter from static disorder, like impurities or vacancies in the lattice, or from dynamic degrees of freedom, like phonons or other electrons. In the single-particle picture at zero temperature, we neglect dynamic scatterers and restrict the discussion to elastic collisions. The mean free path l_m is the length scale which the carrier propagates in average before its momentum $\boldsymbol{k}$ is randomized. For HgTe/CdTe QWs $l_\mathrm{m} \approx 1\ \mu$m [König08]. The mean free path hence allows to cast the system into two regimes: the *ballistic* ($l_\mathrm{m} \gtrapprox L$) and the *diffusive* ($l_\mathrm{m} \ll L$) one.

Phase coherence length: As long as a quantum mechanical particle propagates phase coherently, the relative phases of its trajectories can interfere, leading to phase coherent phenomena like the Aharonov-Bohm effect [Aharonov59] or weak localization [Abrahams79, Gor'kov79]. The phase coherence length l_ϕ gives the length scale, on which the quantum mechanical phase of the carrier is randomized. Since static disorder without internal degrees of freedom does not change the phase of the scattered state, only dynamic scatterers contribute to phase relaxation processes. Therefore, l_ϕ and l_m can differ by several orders of magnitude and phase coherent transport can take place in the diffusive regime. For example, the phase coherence of the superconducting condensate wave function (3.44) extends to macroscopic scales.

When the dimensions of the conductor exceed these three length scales, transport can be described in terms of classical particles with independent trajectories. In this so-called Ohmic regime the conductance

$$G = \sigma_0 \frac{W}{L} \tag{4.2}$$

is described in Drude theory, in which the conductivity σ_0 is a structure independent material parameter.

In contrast, in the mesoscopic regime L and W are of the same order as the three length scales above, i.e., the sample dimensions range from several nm up to microns. For these and smaller length scales, quantum mechanical effects become important. Despite being much larger than individual atoms, mesoscopic systems hence require a full quantum mechanical treatment. In this thesis, we restrict ourselves to the single-particle picture at low temperatures, leading to phase coherent transport over the whole sample. In this case, we are able to use the Landauer-Büttiker formalism in section 4.2, to see how the conductance changes from its classical analogue.

In the case of non-interacting electrons, one often speaks of two-dimensional electron gases (2DEGs), which form in QW structures, like HgTe/CdTe QWs discussed in section 2.3.1. The layer structure of a QW allows for high mobilities, because the dopants can be separated from the electron gas itself, making 2DEGs a prime candidate to test mesoscopic physics.

The small width d_QW of the QW along the z-direction leads to the formation of discrete subbands. Integrating out the z-degrees of freedom allows a description in strictly 2D, like the BHZ model (2.59). When we assume an infinitely long sample ($L \to \infty$) with finite width W, k_x remains a good quantum number, but k_y will split into discrete sub-bands n with the energy offset E_n^0. These sub-bands are referred to as modes in equivalence to photons in wave guides. An exemplary dispersion $E(n, k_x)$ of the lowest lying modes is sketched in Fig. 4.2. In the tight binding formalism, cf. appendix B, the total number of modes scales with the number

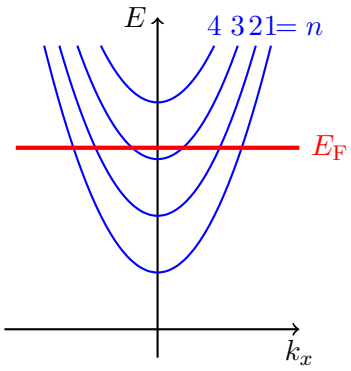

Figure 4.2.: Schematic of the dispersion of the modes $n = 1, 2, \ldots$ in a 2DEG with $L \to \infty$ but finite W.

of lattice points discretizing the sample in y-direction. In a continuum description the total number of modes is infinite. However, since only states close to the Fermi energy can contribute to transport, only the modes, which are occupied and cross E_F, are important for transport calculations. The number of occupied modes $\mathcal{M} \in \mathbb{N}$ generally depends on the details of the bulk band structure and the boundary conditions in the y-direction. Experimental knobs to change $\mathcal{M}$ are E_F and the width W, which enters the energy offset E_n^0. While the Fermi energy can be varied inside of the leads by the applied bias, it can also be shifted electrostatically by a top- or back gate.
We will provide an estimate for $\mathcal{M}$, when we discuss different boundary conditions in sections 4.3.1 and 4.3.2.

4.2. Phase coherent transport

4.2.1. Reflectionless contacts

In order to describe transport within the Landauer-Büttiker formalism, we return to the setup sketched in Fig. 4.1 and follow [Datta07], if not stated otherwise. Since the two leads and the conductor generally have a comparable width, both host a finite number of occupied modes $\mathcal{M}$, which may be different in each region. In contrast, the contacts are assumed to be macroscopically wide, so that they carry an infinite number of modes and act as thermodynamic reservoirs. Hence, the contacts are in thermal equilibrium and not affected by being attached to the conductor via the leads. This allows to assign a chemical potential μ_i to each of it. The difference in chemical potentials can be adjusted by the applied voltage $\mathcal{U}_{12} = (\mu_1 - \mu_2)/q$, which drives a current through the sample. The huge number of available modes in the contacts make it very unlikely that a particle, which approaches a contact from a lead, will be reflected back into the lead, a property often referred to as *reflection-less contacts*. In consequence, all modes in a lead, which carry current towards the conductor, are in thermal equilibrium with the contact and have the same chemical potential μ_i. The counter propagating modes might have a different chemical potential, but will always vanish into the contact. Therefore, we can neglect the contacts in the following, by replacing the hybrid system of contact and lead with the simpler picture of semi-infinite leads, provided that no backscattering takes place in the leads, i.e., the leads are ballistic.

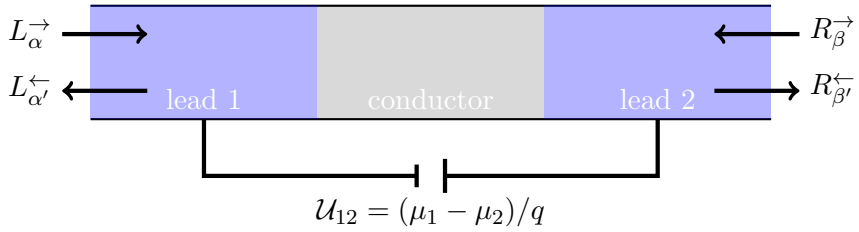

Figure 4.3.: Sketch of the in- and outgoing asymptotic modes in lead 1 and 2, which are connected by the S-matrix.

Since, in the simplified picture, the total system now has a finite number of occupied, meaning current carrying, modes, its conductance cannot rise above a limiting value G_C. This is in stark contrast to the classical expectation (4.2), which predicts $G \to \infty$ for short samples with $L \to 0$. In the next sections, we will calculate this so-called *contact resistance*[1] assuming phase coherence throughout the whole structure.

4.2.2. S-matrix formalism

In the following, we will treat the conductor as a black box and describe transport in the asymptotic states inside the two leads which are defined far away from the conductor as

$$\psi_{\alpha k_x}(y) = \frac{\exp\left[\mathrm{i}k_x^\alpha x_i\right]}{\sqrt{2\pi}} \chi_{\alpha k_x^\alpha}(y). \tag{4.3}$$

The asymptotic states consist of a plane wave along the wire and the spinor of a transversal mode α, which form a full, orthogonal set

$$\int \mathrm{d}y\, \chi^\dagger_{\alpha k_x^\alpha} \chi_{\beta k_x^\beta} = \delta_{\alpha\beta}. \tag{4.4}$$

We assume that the modes in the two leads form the same orthonormal set, because it is always possible to expand the modes in a common orthogonal basis, which we will do explicitly in section 4.3.2. The subscript α may again be a collective index, combining the mode number n and an internal degree of freedom which is conserved by the scattering process. Additionally, we introduced x_i, which describes an x-coordinate inside of lead $i = 1, 2$, cf. Fig. 4.3. In a phase coherent system, we can formulate transport in standard scattering theory, see, e.g., [Schwabl07]. The scattering state

$$\phi_{\beta\alpha}(y) = \delta_{\alpha\beta}\psi_{\alpha k^\alpha_\mathrm{in}}(y) + S_{\beta\alpha}(E)\psi_{\beta k^\beta_\mathrm{out}}(y) \tag{4.5}$$

connects the incoming asymptotic state $\psi_{\alpha k^\alpha_\mathrm{in}}(y)$ in mode α with the outgoing one $\psi_{\beta k^\beta_\mathrm{out}}(y)$ in mode β by the S-matrix $S_{\beta\alpha}$. Since the scattering state has to conserve the probability current,

[1] The name contact resistance reflects the fact that an electron, which is injected from the contact towards the lead, will most likely be reflected due to the drastic mismatch in available modes.

the S-matrix is defined to connect the in- and outgoing current amplitudes, cf. Fig. 4.3,

$$\begin{pmatrix} L_{\alpha'}^{\leftarrow} \\ R_{\beta'}^{\rightarrow} \end{pmatrix} = S(E) \begin{pmatrix} L_{\alpha}^{\rightarrow} \\ R_{\beta}^{\leftarrow} \end{pmatrix}. \tag{4.6}$$

The current amplitudes L and R are defined in the left and right lead, respectively. They carry a current in the direction indicated by the superscript $\rightarrow$ or $\leftarrow$. The current amplitudes can be defined as the product of the wave functions (4.3) with the square root of its velocity expectation value: $\sqrt{\langle \hat{v} \rangle_{\psi_{\alpha k_x}}} \psi_{\alpha k_x}$, where $\hat{v}$ is the velocity operator along the x-axis.
The S-matrix is energy dependent via the implicit energy dependence of the momentum $k_x^{\alpha}(E)$ in Eq. (4.3). We will solve the S-matrix explicitly in section 4.3. For the rest of this section, it is enough to remind ourselves of some of the key features of the S-matrix. Since evanescent modes do not contribute to transport, the S-matrix only connects occupied modes and hence is of dimension $\mathcal{M}_T(E) \times \mathcal{M}_T(E)$, with $\mathcal{M}_T(E)$ being the total number of occupied modes at energy E. It is given by $\mathcal{M}_T(E) := \sum_i \mathcal{M}_i(E)$, where $\mathcal{M}_i(E)$ is the number of propagating modes in lead i. The probability that the current is transmitted from mode α to mode β is given by

$$T_{\beta\alpha}(E) = |S_{\beta\alpha}(E)|^2, \tag{4.7}$$

with which we define the transmission function from lead i to lead j as

$$\bar{T}_{ji}(E) = \sum_{\alpha \in i} \sum_{\beta \in j} T_{\beta\alpha}(E). \tag{4.8}$$

In order to ensure the conservation of the probability current, the S-matrix has to be unitary, which can be expressed in the sum rule

$$\sum_i \sum_{\alpha \in i} T_{\beta\alpha}(E) = \sum_i \sum_{\beta \in i} T_{\beta\alpha}(E) = 1, \tag{4.9}$$

i.e., the incoming current has to be distributed completely into the outgoing modes.
From Heisenberg's equation of motion, we find the current operator

$$\hat{I} = q\hat{v} = \frac{q}{\hbar} \frac{\partial H}{\partial k}, \tag{4.10}$$

with which we calculate the current associated with the scattering state (4.5) to be

$$I_{\beta\alpha}(k_{\text{in}}^{\alpha}) = \frac{q}{2} \int \mathrm{d}y \, \left(\phi_{\beta\alpha}^{\dagger} \hat{v} \phi_{\beta\alpha} + \text{cc.} \right) = \frac{q}{2\pi\hbar} \left(\delta_{\alpha\beta} \left. \frac{\partial E_{\alpha}}{\partial k} \right|_{k=k_{\text{in}}^{\alpha}} - T_{\beta\alpha}(E) \left. \frac{\partial E_{\beta}}{\partial k} \right|_{k=k_{\text{in}}^{\beta}} \right). \tag{4.11}$$

The first and second term correspond to the incoming and transmitted mode, respectively. The mixed terms cancel, because of the symmetrization. Further, we used

$$\left. \frac{\partial E_{\beta}}{\partial k} \right|_{k=k_{\text{in}}^{\beta}} = - \left. \frac{\partial E_{\beta}}{\partial k} \right|_{k=k_{\text{out}}^{\beta}}, \tag{4.12}$$

assuming that each mode at an energy E propagates with the same velocity to the left and right at the respective k_{in}^{β} and k_{out}^{β}. Note that $k_{\text{in}}^{\beta} = -k_{\text{out}}^{\beta}$ is not generally true. For example, a finite

vector potential $\mathcal{A}_x$ shifts the zero point of the dispersion via Peierl's substitution.
Let $f_{\mu_\alpha}(E)$ be the distribution according to which the incoming mode α is occupied at energy E and chemical potential μ_α. The total current from α to β is

$$I_{\beta\alpha} = \int \mathrm{d}k_{\mathrm{in}}\, f_{\mu_\alpha}(E) I_{\beta\alpha}(k_{\mathrm{in}}) = \frac{q}{h}\int \mathrm{d}E\, f_{\mu_\alpha}(E)\left(\delta_{\alpha\beta} - T_{\beta\alpha}(E)\right). \tag{4.13}$$

In a setup with only two leads, current conservation enforces that the absolute value of the current must be the same in both leads. The total current I can then be evaluated by summing over the outgoing modes β in lead 1 as well as over all incoming modes α :

$$\begin{aligned}
I =& \sum_{\beta\in 1}\sum_{i=1,2}\sum_{\alpha\in i} I_{\beta\alpha} = \frac{q}{h}\int \mathrm{d}E \sum_{\beta\in 1}\sum_{i=1,2}\sum_{\alpha\in i}\left(\delta_{\alpha\beta} f_{\mu_\beta}(E) - T_{\beta\alpha}(E) f_{\mu_\alpha}(E)\right) \\
\overset{(4.9)}{=}& \frac{q}{h}\int \mathrm{d}E \sum_{\beta\in 1}\sum_{i=1,2}\sum_{\alpha\in i} T_{\beta\alpha}(E)\left(f_{\mu_\beta}(E) - f_{\mu_\alpha}(E)\right) \\
=& \frac{q}{h}\int \mathrm{d}E \sum_{\beta\in 1}\left[\sum_{\alpha\in 1} T_{\beta\alpha}(E)\underbrace{\left(f_{\mu_1}(E) - f_{\mu_1}(E)\right)}_{=0} + \sum_{\alpha\in 2} T_{\beta\alpha}(E)\left(f_{\mu_1}(E) - f_{\mu_2}(E)\right)\right] \\
\overset{(4.8)}{=}& \frac{q}{h}\int \mathrm{d}E\, \bar{T}_{12}(E)\left(f_{\mu_1}(E) - f_{\mu_2}(E)\right).
\end{aligned} \tag{4.14}$$

Here, we used that all incoming modes are in thermal equilibrium with the reflectionless contacts and are hence occupied with the distribution function $f_{\mu_i}(E)$ in lead $i = 1, 2$. Eq. (4.14) was generalized by Büttiker et al. [Büttiker85] to be applicable to multi terminal structures.

Transmission and reflection probabilities

The total current I in Eq. (4.14) is carried by *transmitted* modes generated in lead 2 and transmitted into lead 1 with probability $T_{\beta\alpha}$. Looking again at Eq. (4.9) we reformulate the sum rule to

$$\sum_{\alpha\in 2} T_{\beta\alpha} = 1 - \sum_{\alpha\in 1} T_{\beta\alpha} \tag{4.15}$$

When β is a mode in lead 1, the left hand side corresponds to the transmitted modes from lead 2 in Eq. (4.14). In contrast, the right hand side connects modes in the same lead, and can hence be seen as the contribution of *reflected* modes, which will often be labeled with $R_{\beta\alpha}$. With this, we can rewrite Eq. (4.14) in terms of reflected modes:

$$I = \frac{q}{h}\sum_{\beta\in 1}\sum_{\alpha\in 1}\int \mathrm{d}E\, \left(\delta_{\alpha\beta} - R_{\beta\alpha}(E)\right)\left(f_{\mu_1}(E) - f_{\mu_2}(E)\right). \tag{4.16}$$

4.2.3. Landauer formula

For the calculation of the conductance, we assume that the system is in equilibrium, so that we can identify $\mu_2 = E_{\mathrm{F}}$ and $\mu_1 = E_{\mathrm{F}} + q\mathcal{U}_{12}$ as well as use the Fermi distribution at E_{F}: $f_{E_{\mathrm{F}}}(E)$.

At low temperatures, we can simplify

$$f_{E_\mathrm{F}}(E) \approx \Theta(E_\mathrm{F} - E) \quad \text{and} \quad \frac{\partial f_{E_\mathrm{F}+q\mathcal{U}_{12}}(E)}{\partial \mathcal{U}_{12}} \approx q\delta\left(E_\mathrm{F} + q\mathcal{U}_{12} - E\right). \tag{4.17}$$

Further, we only consider the linear response for small applied bias $\mathcal{U}_{12} \ll E_\mathrm{F}$, transforming Eq. (4.14) into

$$I \approx \underbrace{I(\mathcal{U}_{12}=0)}_{=0} + [\partial_{\mathcal{U}_{12}} I]_{\mathcal{U}_{12}=0}\mathcal{U}_{12} = \frac{q^2}{h}\mathcal{U}_{12}\int \mathrm{d}E\,\delta\left(E_\mathrm{F} - E\right)\bar{T}_{12}(E) = \frac{q^2}{h}\bar{T}(E_\mathrm{F})\mathcal{U}_{12}. \tag{4.18}$$

Again, we find that only states in a range $\pm k_\mathrm{B}T$ around the Fermi energy contribute to transport. The linear conductance takes the form of Landauer's formula

$$G = \frac{I}{\mathcal{U}_{12}} = \frac{q^2}{h}\bar{T}_{12}(E_\mathrm{F}) = \frac{q^2}{h}\bar{T}\mathcal{M}(E_\mathrm{F}), \tag{4.19}$$

where we rewrote the transmission function as the product of $\bar{T}$, the average transmission probability per mode, and $\mathcal{M}(E_\mathrm{F})$, the number of propagating modes per lead at E_F. In the small bias limit, we have $\mathcal{M} = \mathcal{M}_1 = \mathcal{M}_2$. In the case where all modes are perfectly transmitted, the maximal conductance $G_C = q^2\mathcal{M}/h$ gives rise to the previously mentioned contact resistance

$$R_C = \frac{1}{G_C} = \frac{h}{q^2\mathcal{M}} \overset{q=e}{=} \frac{25.8\ \mathrm{k\Omega}}{\mathcal{M}}. \tag{4.20}$$

Such perfect transmission can for example be realized in the QH effect, cf. appendix A, or in 2D TIs, in which the edge states are protected from backscattering, cf. section 2.2.3.
In contrast to the classical conductance (4.2), G does not vary linearly with the width, but stepwise with the number of occupied modes.

4.2.4. Blonder-Tinkham-Klapwijk formalism

In order to describe the transport in superconducting hybrid systems, the Landauer-Büttiker formalism has to be generalized to the BTK formalism, named after Blonder, Tinkham, and Klapwijk [Blonder82]. The systems in question are N-SC junctions, which have been introduced in section 3.3. Such setups combine a normal (left lead) with a superconducting (right lead) region. In this case, the conductor shrinks to the interface, which is the sole source of scattering processes in this modeling of N-SC junctions.
Superconducting systems are described in the language of the BdG equations (3.22), which couple electron- and hole-like excitations, cf. appendix D. An incoming electron hence can be reflected as a hole. As we have seen in section 3.3, this so-called Andreev reflection (AR) adds to the transported charge current. The reason, why electron- and hole-like excitations contribute differently to the charge transport, is their opposite charge. Thus, we will motivate the BTK formalism by introducing a charge q_β, which depends on the particle character of the outgoing mode. Inside the SC, the current is partially carried by the superconducting condensate, which is not part of the BdG formalism. Moreover, the SC couples electron- and hole-like solutions, making it impossible to assign a unique charge to the excitations. Therefore, a complete description of the transport within the BdG framework requires to restrict the treatment on the normally conducting regions, where the electron and hole branch decouple. This breaks the equivalence of Eqs. (4.14) and (4.16). When we only consider incoming electronic modes (α_e),

the BTK current in the left lead (lead 1) reads

$$\begin{aligned} I_{\mathrm{BTK},1} =& \frac{1}{h}\sum_{\beta\in 1}\sum_{\alpha_e\in 1}\int \mathrm{d}E\ \left(-e\delta_{\alpha_e\beta} - q_\beta R_{\beta\alpha_e}(E)\right)\left(f_{\mu_1}(E) - f_{\mu_2}(E)\right) \\ =& -\frac{e}{h}\sum_{\alpha_e\in 1}\int \mathrm{d}E\ \left(1 - \sum_{\beta_e\in 1} R_{\beta_e\alpha_e}(E) + \sum_{\beta_h\in 1} R_{\beta_h\alpha_e}(E)\right)\left(f_{\mu_1}(E) - f_{\mu_2}(E)\right), \end{aligned} \tag{4.21}$$

where the sub-script 1 is used as a reminder, that the equation describes the current in the lead 1, and will later be neglected. We used $-e$ and e as the charge of electrons and holes. The indices β_e (β_h) indicates the outgoing electron-like (hole-like) modes. With this in mind, we see that the reflection probabilities $R_{\beta_h\alpha_e}$ can be identified with the AR probability $|R_h|^2$, which has been introduced in Eq. (3.99).
Note that the different charges q_β in the electric current do not influence the sum rule (4.9), because the sum rule is derived from the conservation of the probability current.

Excess current

As we have already anticipated in section 3.3, the AR increases the transported charge above the pure electronic current. The difference of the BTK current and the current arising in a non-superconducting junction is expressed by the excess current [Blonder82]

$$I_{\mathrm{ex}} = I_{\mathrm{BTK}} - I = \frac{e}{h}\sum_{\alpha_e\in 1}\int \mathrm{d}E\ \left(\sum_{\beta_h\in 1} R_{\beta_h\alpha_e}(E) - \sum_{\beta_e\in 1}\Delta R_{\beta_e\alpha_e}\right)\left(f_{\mu_1}(E) - f_{\mu_2}(E)\right), \tag{4.22}$$

where $\Delta R_{\beta_e\alpha_e}(E) = R^{\mathrm{SC}}_{\beta_e\alpha_e}(E) - R^{\mathrm{N}}_{\beta_e\alpha_e}(E)$ is the difference of the electron reflection probabilities in N-SC junctions and interfaces between two normally conducting wires. In systems, which are protected against backscattering, $\Delta R_{\beta_e\alpha_e}(E)$ is zero and the excess current is hence given by the integrated probability of AR. I_{ex} is often measured at high voltages.

$\mathrm{d}I/\mathrm{d}V$ characteristics

Since AR only gives significant contributions around the superconducting quasi-particle gap, it is an apt tool to experimentally measure the SC's spectrum, see section 3.3 for details. Since the current measurements do not resolve the spectrum at specific excitation energies E, it is advantageous to measure $\mathrm{d}I/\mathrm{d}V$ characteristics, where $V = \mathcal{U}_{12}$ is the applied bias[2]. When we again assume the system to be in quasi-equilibrium at low temperatures, the $\mathrm{d}I/\mathrm{d}V$ characteristic simply depends on $\mathcal{U}_{12}$:

$$\begin{aligned} \frac{\mathrm{d}I_{\mathrm{BTK}}}{\mathrm{d}\mathcal{U}_{12}} =& -\frac{e}{h}\sum_{\alpha_e\in 1}\int \mathrm{d}E\ \left(1 - \sum_{\beta_e\in 1} R_{\beta_e\alpha_e}(E) + \sum_{\beta_h\in 1} R_{\beta_h\alpha_e}(E)\right)\frac{\partial f_{E_{\mathrm{F}}-e\mathcal{U}_{12}}(E))}{\partial U_{12}} \\ \overset{(4.17)}{\approx}& \frac{e^2}{h}\sum_{\alpha_e\in 1}\left(1 - \sum_{\beta_e\in 1} R_{\beta_e\alpha_e}(E_{\mathrm{F}} - e\mathcal{U}_{12}) + \sum_{\beta_h\in 1} R_{\beta_h\alpha_e}(E_{\mathrm{F}} - e\mathcal{U}_{12})\right). \end{aligned} \tag{4.23}$$

[2]The applied bias in theses cases is conventionally labeled by V. We stick to this nomenclature here to avoid confusion with the literature.

N-SC-N junctions

When we consider N-SC-N junctions, the system is characterized by two normally conducting leads (N) connected by a SC. In this kind of setup, charging effects due to the formation of Cooper pairs, e.g., by Andreev processes, might shift E_F in the SC. Additionally, a self-consistent treatment of the order parameter might be needed. Both corrections can be neglected by assuming the SC to be set to ground. Additionally to Eq. (4.21), one can calculate the current in the right lead (2), which is induced by electrons injected from the left lead:

$$I_{\mathrm{BTK},2} = -\frac{e}{h}\sum_{\alpha_e\in 1}\int \mathrm{d}E \left(\sum_{\beta_e\in 2} T_{\beta_e\alpha_e}(E) - \sum_{\beta_h\in 2} T_{\beta_h\alpha_e}(E)\right)\left(f_{\mu_1}(E) - f_{\mu_2}(E)\right). \tag{4.24}$$

The first part results from electron transmission or tunneling and the second summand stems from crossed Andreev reflection (CAR). In contrast to AR, the latter diminishes the electronic current in the right lead. Here, where we only consider incoming electrons from the left lead, the currents (4.21) and (4.24) do not need to be the same, because the SC can carry a supercurrent to the ground contact.

4.3. Solution to the scattering problem

In the last section, we have seen that the transport problem can be reduced to a scattering problem in coherent systems. Here, we want to describe the solution of the S-matrix. A convenient way is to use discretized samples within the TB formalism, cf. appendix B. It can deal with arbitrary structure geometries and leads, see, for example, the implementation in [Wimmer08]. Moreover, it allows to include static disorder in form of on-site energies or spatially varying material parameters. We will use this technique in section 5.3.4, for which reason we give a short introduction to this formalism in appendix C. The rest of this thesis concentrates on quasi-one dimensional wire geometries and neglects any disorder. Therefore, scattering processes only occur at the interfaces between the leads and the conductor (cf. Fig. 4.1). This problem is solvable in a wave matching approach. In contrast to the TB formalism, for which the computational needs grow with the systems length, the complexity of the wave matching formalism only grows with the number of modes and interfaces. Moreover, it has the advantage of being a (semi-)analytical method, often providing a better understanding of the underlying processes.
Here, we will start with the discussion of the two different boundary conditions used in the later course of the thesis: periodic boundary conditions (PBC) in section 4.3.1 and hard-wall boundary conditions (HBC) in 4.3.2. The latter causes complicated mode structures, which require a generalized wave matching approach, in which we expand the system's eigenstates in an orthogonal set of Fourier modes. With this, we ensure that we can match different transversal modes independently when using the matching conditions presented in section 4.3.3.

4.3.1. Periodic boundary conditions

Like the name suggests, PBC assume the sample to be periodically continued. Here, we assume periodicity in y-direction with the width W as period length. Consequently, the eigenmodes of

the system have to fulfill

$$\psi_{\alpha k_x}(y) = \psi_{\alpha k_x}(y + W). \tag{4.25}$$

This has the advantage of a conserved quasi-momentum, which is discretized to be commensurate to that of the periodic BZ:

$$k_y^\alpha = \pm\alpha \frac{2\pi}{W}. \tag{4.26}$$

The number of propagating modes at energy E, $\mathcal{M}(E)$, can then be evaluated by counting the number of modes for which $k_y^\alpha \leq k_\mathrm{F}(E)$, resulting in

$$\mathcal{M}(E) = \mathrm{floor}\left[\frac{k_\mathrm{F}(E)W}{\pi}\right], \tag{4.27}$$

where floor$[x]$ returns the largest integer not greater than x. Having a conserved momentum k_y, the incoming modes can be associated with the angle $\theta_\alpha(E)$, under which the mode hits the interface between the lead and the conductor. The mode can then be expressed in plane waves

$$\psi_{\alpha E} \propto \exp\left[\mathrm{i}k_y^\alpha y + k_x^\alpha(E)x\right] \tag{4.28}$$

with wave vectors $k_y^\alpha = k_\mathrm{F}(E)\sin\theta_\alpha$ and $k_x^\alpha(E) = k_\mathrm{F}(E)\cos\theta_\alpha$. Since the different modes in Eq. (4.26) are only dependent on the width W, the modes in both leads as well as in the conductor are forming an equivalent orthonormal set, which allows us to match each mode independently with the appropriate matching conditions in section 4.3.3.
In Eq. (4.25), we have identified the two edges of the sample, making the edges indistinguishable from the bulk of the system. In consequence, all edge related physics is lost and phenomena like the formation of edge states in a 2D TI do not occur under these boundary conditions. In conclusion, PBC are the tool of choice to model pure bulk physics.

4.3.2. Hard wall boundary and generalized wave matching approach

A more natural boundary condition than PBC is to consider the system's edges as hard walls, which suppress the wave function [3]

$$\psi_{\alpha k_x}(y = 0) = \psi_{\alpha k_x}(y = W) = 0. \tag{4.29}$$

In case of 2D TIs, a semi-analytical solution to the effective low energy model (2.59) was provided by Zhou et al. [Zhou08], cf. Eqs. (2.76) and (2.77). This solution, however, is impractical for transport calculations. Firstly, it involves finding numerically the root of an unstable transcendental equation. Secondly, a generalization to systems with more degrees of freedom, like the superconducting 2D TI in Eq. (3.77), is cumbersome, if not impossible to solve. Even worse: the eigenmodes (2.77) are labeled by $\lambda = \mathrm{i}k_y$, which are a function of energy and of k_x. Regions of different doping, thus, are characterized by different sets of modes, which are not orthonormal to each other. In consequence, a wave matching procedure of individual modes, like in PBC, becomes impossible.

[3] The suppression of the wave function in Eq. (4.29) is only feasible, if the Hamiltonian contains terms with quadratic or higher order in k. Purely linear Hamiltonians, like Dirac systems, require different boundary conditions to enforce hard walls. We will deal with those when needed in section 7.2.1.

The *generalized wave matching approach* [Zhang10a, Reinthaler12, Reinthaler13] provides a convenient work around, which allows the treatment of normal and superconducting systems on the same footing. Its basic idea is to expand the eigenstates in a set of orthogonal Fourier modes

$$\phi_n(y) = \sqrt{\frac{2}{W}} \sin\left[\frac{n\pi y}{W}\right], \quad n \in \mathbb{N}, \tag{4.30}$$

in which the asymptotic scattering states with mode number α and conserved k_x^α become

$$\psi_\alpha(x,y) = \exp\left[\mathrm{i}k_x^\alpha x\right] \sum_{n=1}^{\infty} \chi_n^\alpha \phi_n(y). \tag{4.31}$$

The energy- and k_x-dependence are shifted to the expansion coefficients χ_n^α. The orthogonality of the W-dependent modes restores a unique identification of the modes in different parts of the setup, so that an S-matrix can be defined and solved for.
Let the Hamiltonian be of second order in $\boldsymbol{k}$, so that it can be written as

$$\mathcal{H} = \mathcal{H}^{\mathrm{const}} + \mathcal{H}^{k_x} k_x + \mathcal{H}^{k_x^2} k_x^2 + \mathcal{H}^{k_y} k_y + \mathcal{H}^{k_y^2} k_y^2 + \mathcal{H}^{k_x k_y} k_x k_y, \tag{4.32}$$

where we collected all constant terms in $\mathcal{H}^{\mathrm{const}}$ and separated the prefactors of k_x, k_x^2, $k_y = -\mathrm{i}\partial_y$, k_y^2 as well as $k_x k_y$ in $\mathcal{H}^{k_x}$, $\mathcal{H}^{k_x^2}$, $\mathcal{H}^{k_y}$, $\mathcal{H}^{k_y^2}$ and $\mathcal{H}^{k_x k_y}$, respectively. This general form of the Hamiltonian is valid for 2D TIs (2.59) as well as for superconducting 2D TIs (3.77). In doing so, the different summands in Eq. (4.32) inherit the matrix structures of the underlying Hamiltonian and the expansion coefficients χ_n^α are the corresponding spinors with components reflecting, e.g., the spin, sub-band or particle degree of freedom. Putting the Fourier ansatz (4.31) into the Schrödinger equation and multiplying from left by $\int_0^W \mathrm{d}y\, \phi_m^\dagger(y)$ leads to

$$\begin{aligned} 0 = &\left[\mathcal{H}^{\mathrm{const}} - E + \mathcal{H}^{k_x} k_x^\alpha\right] \chi_m^\alpha + \mathcal{H}^{k_x^2} k_x^\alpha \chi'^\alpha_m \\ &+ \sum_{n=1}^{\infty} \int_0^W \mathrm{d}y\, \phi_m^\dagger(y) \left(\left[\mathcal{H}^{k_y} k_y + \mathcal{H}^{k_y^2} k_y^2\right] \chi_n^\alpha + \mathcal{H}^{k_x k_y} k_y \chi'^\alpha_m\right) \phi_n(y). \end{aligned} \tag{4.33}$$

Here, we introduced the spinors $\chi'^\alpha_m = k_x^\alpha \chi_m^\alpha$. The integral can be solved straight forwardly by

$$\kappa_{nm} = -\int_0^W \mathrm{d}y\, \phi_m^\dagger(y) \partial_y^2 \phi_n(y) = \left(\frac{n\pi}{W}\right)^2 \delta_{nm} \tag{4.34}$$

$$\eta_{nm} = -\mathrm{i}\int_0^W \mathrm{d}y\, \phi_m^\dagger(y) \partial_y \phi_n(y) = \begin{cases} \frac{n\pi}{W} & , n = m \\ \frac{4\mathrm{i}}{W} \frac{nm}{m^2 - n^2} & , n + m \text{ odd} \\ 0 & , \text{ else} \end{cases}. \tag{4.35}$$

Combining the spinors into the vectors $\chi^\alpha = (\chi_{n=1}^\alpha, \chi_{n=2}^\alpha, \ldots)^T$ and $\chi'^\alpha = (\chi'^\alpha_{n=1}, \chi'^\alpha_{n=2}, \ldots)^T$ allows to rewrite Eq. (4.33) as a matrix equation

$$\begin{pmatrix} \mathbb{I} & 0 \\ 0 & \left(H^{k_x^2}\right)^{-1} \end{pmatrix} \begin{pmatrix} 0 & \mathbb{I} \\ H^{\mathrm{const}} + H^{k_y} & H^{k_x} \end{pmatrix} \begin{pmatrix} \chi^\alpha \\ \chi'^\alpha \end{pmatrix} = k_x^\alpha \begin{pmatrix} \chi^\alpha \\ \chi'^\alpha \end{pmatrix}, \tag{4.36}$$

with the sub-matrices

$$H_{nm}^{\text{const}} = \delta_{nm}\left(\mathcal{H}^{\text{const}} - E\right), \qquad H_{nm}^{k_x} = \delta_{nm}\mathcal{H}^{k_x} + \mathcal{H}^{k_x k_y}\eta_{nm},$$
$$H_{nm}^{k_x^2} = \delta_{nm}\mathcal{H}^{k_x^2}, \qquad H_{nm}^{k_y} = \mathcal{H}^{k_y}\eta_{nm} + \mathcal{H}^{k_y^2}\kappa_{nm}. \tag{4.37}$$

By introducing χ'^{α}, we have doubled the Hilbert space, allowing to reduce the problem of finding all modes with momentum k_x^α and coefficients χ_n^α at energy E to solving the linear eigenvalue problem (4.36).

Quality of the expansion

Eq. (4.35) shows that the terms proportional to k_y and k_y^2 couple an infinite number of Fourier modes. However, the coupling strength decays with the difference in mode number, allowing for a numerical approximation, which only takes a finite number of Fourier modes N into account. Here, we want to give an estimate of the approximation for one Kramers' partner block of a HgTe QW. To this end, we compare the aforementioned analytical solution from [Zhou08], which is discussed in section 2.3.3 and especially in Eq. (2.76), with its Fourier pendant. The latter is obtained by plugging Eq. (2.60) into (4.36) and solving for all k_x^α. In doing so, we truncate the series (4.31) at different N. Explicitly, we use the parameters of Tab. 2.1 and choose $W = 200$ nm. The energy zero point is set in the middle of the bulk gap ($C = 0$). In Fig. 4.4, we compare two different energies: In the upper row, $E = 0$ lies within the bulk gap, resulting in the single propagating mode of an edge state. The lower row shows the bulk states at the doping $E = 50$ meV, which corresponds to 7 propagating modes. For both configurations, we compare the Fourier approximation for $N = 20,\ 50,\ 100$. In Figs. 4.4a and 4.4d (4.4b and 4.4e) we plot the difference of k_x^α between the analytical model and the Fourier approximation for the propagating (evanescent) modes as a function of the mode number α. For all four situations we find that the error of the approximation is diminishing strongly with the number of modes considered. The deviation increases slightly with the mode number, which is due to the fact that higher modes oscillate stronger and need higher Fourier components. However, the strongest increase is observed for evanescent modes, which, for larger α, decay on very short length scales and thus play a minor role in transport.
The k_x^α of the analytical model result from a unique transcendental equation, whose solution can be sorted by the value of $\operatorname{Im} k_x^\alpha$. In contrast, the k_x solutions of the eigenvalue problem (4.36) always come in pairs, where one solution corresponds to the conduction and the other to the valence band. This can be seen, for example, for $N = 20$. While the first half of solutions coincides quite well with the analytically calculated wave vectors, the second half (corresponding to the valence band) is shifted to larger wave vectors, disregarding solutions with smaller $|k_x^\alpha|$. Especially for tunneling setups, in which evanescent modes carry the transport, it is important to take enough Fourier modes into account.
Finally, let us examine how the eigenspinors are approximated. In Fig. 4.4f, we plot the DOS of the propagating bulk mode, corresponding to the $\alpha = 7$ mode in Fig. 4.4d. While $N = 20$ again fails to give a reasonable approximation, $N = 50$ and $N = 100$ can barely be distinguished from the correct solution. The same conclusion can be drawn for the edge state at $E = 0$, whose DOS is shown in Fig. 4.4c. In this case, an insufficient approximation results in a shift of the state's weight to the edge at $y = W$. This decreases the separation of counter-propagating edge states artificially and can introduce backscattering.

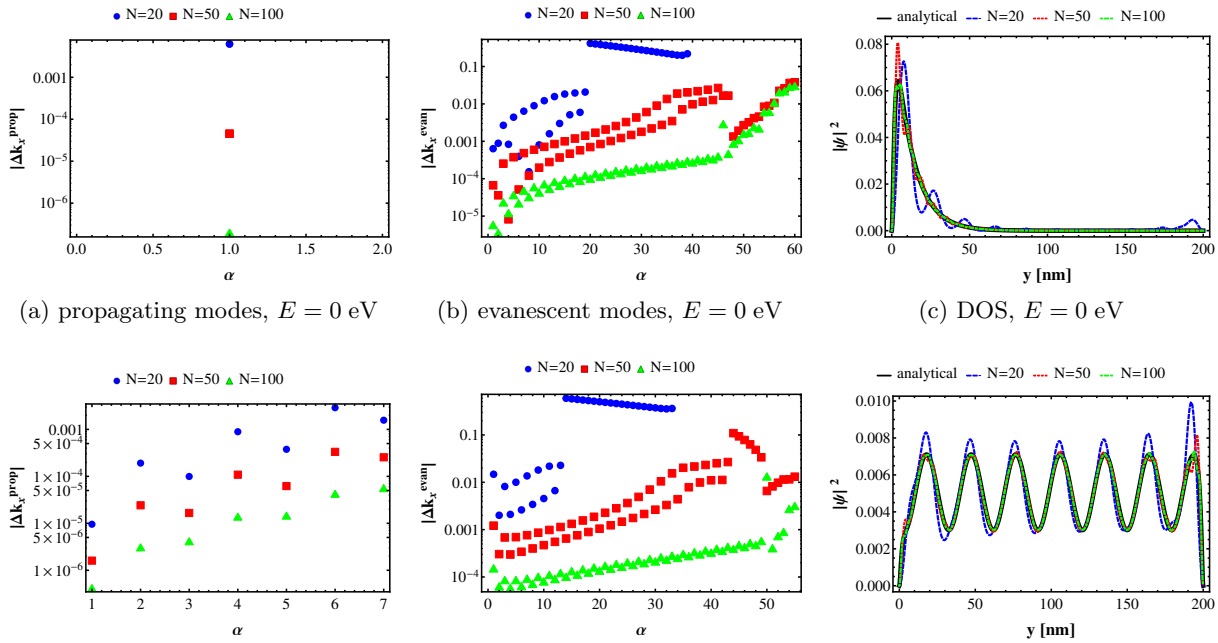

(a) propagating modes, $E = 0$ eV

(b) evanescent modes, $E = 0$ eV

(c) DOS, $E = 0$ eV

(d) propagating modes, $E = 0.05$ eV

(e) evanescent modes, $E = 0.05$ eV

(f) DOS, $E = 0.05$ eV

Figure 4.4.: The quality of the Fourier approximation in respect to the exact solution of the analytical model for different mode cut-offs N and E. $W = 200$ nm and the parameters of Tab. 2.1 have been used.

4.3.3. Matching conditions

Above, we have discussed the solutions of a quasi-one dimensional system with conserved momentum along the x-axis. In a scattering setup, like that sketched in Fig. 4.3, these states take the role of the asymptotic solutions. The solutions k_x^α can be characterized as propagating ($k_x^\alpha \in \mathbb{R}$) or evanescent ($\mathrm{Im}(k_x^\alpha) \neq 0$). For real k_x^α, the propagation direction can be determined by the sign of

$$v^\alpha = \int_0^W \mathrm{d}y\, \psi_\alpha^\dagger(x,y)\, [\partial_{k_x} \mathcal{H}(k_x)]_{k_x \to k_x^\alpha}\, \psi_\alpha(x,y). \tag{4.38}$$

Analogously, evanescent states with $\mathrm{Im}(k_x^\alpha) > 0$ ($\mathrm{Im}(k_x^\alpha) < 0$) are decaying to the right (left). In the following, the right (left) going modes will be labeled as α_R (α_L). In order to write down the full scattering state in the three parts of the setup, we will further introduce the index i, where $i = 1$ stands for the left lead stretching from $x = -\infty$ to $x = -L/2$, $i = 0$ for the conductor ($-L/2 < x < L/2$) and $i = 2$ for $x \geq L/2$.[4] In the case of an incoming electron from the left

[4]The numbering, where $i = 0$ indicates the conductor, makes it easer to compare with our previous notation, where the leads have been labeled by 1 (left) and 2 (right).

lead in mode β_R, the scattering state takes the form:

$$\Psi_{\beta_R}(x,y) = \begin{cases} \psi_{\beta_R,1}(x,y) + \sum_{\alpha_L} r_{\alpha_L,\beta_R}\psi_{\alpha_L,1}(x,y) & , \; x \leq -\frac{L}{2} \\ \sum_{\alpha_R} c_{\alpha_R,\beta_R}\psi_{\alpha_R,0}(x,y) + \sum_{\alpha_L} d_{\alpha_L,\beta_R}\psi_{\alpha_L,0}(x,y) & , \; x \in \left]-\frac{L}{2}, \frac{L}{2}\right[\\ \sum_{\alpha_R} t_{\alpha_R,\beta_R}\psi_{\alpha_R,2}(x,y), & , \; x \geq \frac{L}{2} \end{cases} \tag{4.39}$$

We used the same index α in all three parts, because all parts are built by the same set of modes. For HBC, these are the Fourier modes (4.30), while in PBC, the quantized k_y is conserved and only the mode with $k_y^\alpha = k_y^{\beta_R}$ contributes to $\Psi_{\beta_R}(x,y)$. The coefficients of the different asymptotic wave functions can be obtained by matching the wave functions at the interfaces at $x_{\text{int}} = -L/2$ and $L/2$. The interfaces might act as tunneling barriers, because of an imperfect contact between the leads and the conductor. Therefore, they are often modeled as local potentials

$$\Lambda\delta\left(x - x_{\text{int}}\right). \tag{4.40}$$

The matching conditions at an interface can be obtained by integrating the Schrödinger equation across the interface twice. Assuming the solutions $\Psi_{\beta_R}(x,y)$ to be Riemann integrable, we find the matching conditions for each interface to read

$$0 = -\mathrm{i}\hbar\left[\hat{v}\Psi_{\beta_R}(x_{\text{int}}^+, y) - \hat{v}\Psi_{\beta_R}(x_{\text{int}}^-, y)\right] + \Lambda\Psi_{\beta_R}(x_{\text{int}}, y), \tag{4.41a}$$

$$0 = \Psi_{\beta_R}(x_{\text{int}}^+, y) - \Psi_{\beta_R}(x_{\text{int}}^-, y), \tag{4.41b}$$

where $x_{\text{int}}^\pm = \lim_{\epsilon\to\pm 0}\left[x_{\text{int}} + \epsilon\right]$ addresses states right and left to the interface. In the following, we will generally set $\Lambda = 0$, neglecting the tunneling barrier at the interface. We may do so because of two reasons: Firstly, the helical edge states, with which we are concerned in this thesis, are protected against backscattering and thus are not strongly affected by the presence of a local tunneling barrier. Secondly, when we deal with N-SC junctions in chapters 6 and 7, we assume the superconducting and normally conducting part to consist of the same material, into which superconductivity has been induced locally, so that a contact area between two different materials is avoided. Neglecting the tunneling barrier means that backscattering is induced purely by the mismatch of the modes in the different parts of the wire. This mismatch can originate from different band structures or Fermi energies on both sides of the interface.
Solving Eqs. (4.41) simultaneously for both interfaces determines all coefficients and fixes the scattering states (4.39) up to normalization. The amplitudes of the reflected (transmitted) modes α_L (α_R) are given by r_{α_L,β_R} (t_{α_R,β_R}). Since these amplitudes are defined to connect the states rather than the current amplitudes, the S-matrix (4.6) can be obtained by renormalizing with the velocities of the incoming and outgoing modes:

$$S_{\alpha_R\beta_R} = t_{\alpha_R\beta_R}\sqrt{\frac{v^{\alpha_R}}{v^{\beta_R}}}, \quad S_{\alpha_L\beta_R} = r_{\alpha_L\beta_R}\sqrt{\frac{v^{\alpha_L}}{v^{\beta_R}}}. \tag{4.42}$$

Single interface

In case of a single interface, we can use the same ansatz (4.39) with $L = 0$. The matching conditions (4.41) then only have to be evaluated for a single interface at $x_{\text{int}} = 0$.

Numerical implementation

The wave matching across one or two interfaces in PBC has been solved semi-analytically in *Mathematica* [Wolfram Research12, Wolfram Research14]. The generalized wave matching approach and the corresponding wave matching routines have been implemented in *C++* using the matrix package *Eigen* [Guennebaud10] as well as the matrix solvers provided by *LAPACK* [Anderson99].
As discussed above, the advantage of the generalized wave matching approach in comparison with the TB formalism is, that the memory needed for the computation only depends on the number of modes N, but not on the length L of the conductor. Theoretically, this allows to treat arbitrarily long samples. However, a good approximation of the physical states requires to take evanescent modes with $\mathrm{Im}\, k_x^\alpha \neq 0$ into account. These modes grow or decay exponentially with increasing L. Thus, the different modes, which contribute to the scattering problem (4.41), can differ by many orders of magnitude, leading to potential instabilities in the numerical solution for large L. With our implementation, we have been able to calculate sample lengths ranging up to $L \gtrapprox 500$ nm, when wide, metallic leads are considered in chapter 5, and $L > 2000$ nm for incoming edge states in chapter 6.

Part II.

Results

5. Interplay of bulk and edge states in transport of two-dimensional topological insulators

As a first application of the generalized wave matching routine of chapter 4, we calculate the transport in two-terminal metal-quantum spin Hall insulator (QSHI)-metal junctions. This allows a novel characterization of the non-trivial topological regime by tunneling bulk modes, which we will motivate in the introductory section 5.1. In order to better understand the signals of the tunneling setups, we conclude in section 5.2 that the edge states of a QSHI are protected against the backscattering from a single interface to a metallic lead in a vast range of parameter configurations. To distinguish the signals from edge and bulk states even more clearly, we use periodic boundary conditions (PBC) as well as hard-wall boundary conditions (HBC), when we calculate the transport of the two interface setup in section 5.3.2. We demonstrate that the conductance signals originating from the bulk and the edge contributions are not additive. While for a long junction, the transport is determined by the edge states, the conductance signal of a short junction is built from both bulk and edge states in a ratio which depends on the width of the sample. Further, the conductance for short junctions shows a non-monotonic behavior as a function of the sample length in the topologically non-trivial regime. Surprisingly, the non-monotonic behavior can be traced to the formation of an effectively propagating mode, cf. section 5.3.3, which is found to be robust against scalar disorder in section 5.3.4.
Our results, which have been published in [Reinthaler12][1], pave the way to better understand hybrid structures of 2D TIs, facilitating the analysis of the superconducting junctions treated in the following chapters 6 and 7.

5.1. Introduction and model

Although the topological invariant has been introduced as a bulk property in section 2.2, this classification can be translated to the existence of topologically protected states at the edges of the system due to the bulk-boundary correspondence [Halperin82, Hasan10]. Experiments usually focus on the properties of these edge states. Indeed, the confirmation, that HgTe/CdTe quantum wells (QWs) are two-dimensional topological insulators [Bernevig06], was provided through the measurement of the quantized conductance of edge channels [König07, König08, Roth09, Brüne12].
As can be seen Fig. 2.5, HgTe/CdTe QWs allow for a direct control of the topological order by the thickness of the HgTe layer d_{QW}: below the critical thickness of $d_c \approx 6.4$ nm, the system is a trivial insulator, whereas above d_c, the system behaves as QSHI. This gives the possibility to observe the topological phase transition directly. Therefore, it is of great interest to find further experimental measurable indicators for this phase transition, which can be tested in HgTe/CdTe QWs. Since the topological invariant is a bulk property, it seems natural that the bulk conductivity could also carry information about topological properties of the system. Indeed, Novik et

[1]

al. [Novik10] proposed to measure the conductance in metal-QSHI-metal junctions, in which incoming metallic bulk states tunnel through an insulating barrier. When the tunneling barrier is in the topologically non-trivial regime, they found that the conductance becomes non-monotonic and shows a characteristic maximum as a function of the geometrical aspect ratio of the QSHI tunneling barrier. The conductance maximum is robust against scalar disorder of the order of the band gap [Recher10]. So far, this analysis was limited to PBC and neglected the existence of edge states, which can significantly modify the behavior in experimentally relevant setups. Here, we carefully analyze the properties of a single QSHI-metal interface as well as the interplay between edge states and bulk states in metal-QSHI-metal junctions.
We tackle this problem in the wave matching approach, which is described in sections 4.3.1 and 4.3.2 for PBC and HBC, respectively. The Hamiltonian under consideration is the BHZ model (2.59). Neglecting all couplings of Kramers' partner blocks, H_{BHZ} simplifies to Eq. (2.60), where the second Kramers' partner follows from TRS. Since this is a generic Hamiltonian for 2D TIs, the results presented in the following are general features of 2D TIs. Specifically, we calculate HgTe/CdTe QWs and compare them to thin films of Bi_2Se_3. For the HgTe/CdTe QWs, we use, unless specified otherwise, the parameters taken from [Novik10]: $A = 0.375$ nmeV, $B = -1.120$ nm^{2}eV, $D = -0.730$ nm^{2}eV, $M = -3.10$ meV. When we are referring to the normal regime, we put $M = +3.10$ meV. These parameters differ from that given in Tab. 2.1, because a smaller QW width d_{QW}, which is closer to the topological phase transition point d_{c}, was assumed. Remarkably, d_{QW} mainly influences M [Rothe10]. Thin films of Bi_2Se_3 map to the same Hamiltonian (2.59) with parameters $A = 0.406$ nmeV, $B = -0.250$ nm^{2}eV, $D = 0.070$ nm^{2}eV, $M = \mp 22.5$ meV [Lu10].
The single and double junctions, which we consider in this chapter, are shown in Figs. 5.1a and 5.2, respectively. The transport problem is solved by applying the matching conditions (4.41) between the lead 1 on the left and lead 2 on the right. The resulting transmission coefficients are given by Eq. (4.42) and can be summed up to give the total conductance according to Eq. (4.19):[2]

$$G = \frac{e^2}{h}\bar{T}_{21}(E_{\mathrm{F}}) = \frac{e^2}{h}\sum_{\beta_{R,1}}\sum_{\alpha_{R,2}}\left|S_{\alpha_{R,2}\beta_{R,1}}\right|^2. \tag{5.1}$$

Spinors in periodic boundary conditions

In order to apply the matching conditions (4.41), one has to solve for the asymptotic solutions in form of the eigenspinors of the system. In the case of HBC, the latter are obtained numerically from the eigensystem (4.36). Here, we present the corresponding analytical eigenspinors for PBC.
Since the lattice momentum $\boldsymbol{k}$ is conserved, we can find the eigenenergies and eigenspinors by direct diagonalization of the Hamiltonian (2.60), yielding up to normalization

$$E_{\pm}(\boldsymbol{k}) = C - Dk^2 \pm \sqrt{A^2k^2 + (M - Bk^2)^2} \tag{5.2}$$

$$\phi_{\alpha\pm}(\boldsymbol{k}) = \begin{pmatrix} \pm A(k_x + \mathrm{i}k_y) \\ g(k) \end{pmatrix}, \quad g(k) = \sqrt{A^2k^2 + (M - Bk^2)^2} - (M - Bk^2). \tag{5.3}$$

[2] Here, we assume the modes to be injected only from lead 1 (left) and sum over the outgoing modes in lead 2.

The ± sign indicates the conduction and valence band. At a fixed energy E_F, we find four solutions for k: $\pm k_\mathrm{F}^1$ and $\pm k_\mathrm{F}^2$ with [3]

$$k_\mathrm{F}^{1,2} = \sqrt{-F \pm \sqrt{F^2 - \frac{M^2 - (C - E_\mathrm{F})^2}{B^2 - D^2}}}, \quad F = \frac{A^2 - 2MB - 2(C - E_\mathrm{F})D}{2(B^2 - D^2)}. \tag{5.4}$$

In the following, we will set $E_\mathrm{F} = 0$ and define the Fermi energy solely by the doping C. For energies outside of the band gap, k_1 gives a propagating solution, while k_2 is imaginary. The asymptotic modes are labeled by a collective index (αi), where α identifies the transversal mode k_y^α of Eq. (4.26) and $i = \{1, 2\}$ refers to the Fermi wave vectors in Eq. (5.4). With the definitions of $k_y^\alpha = k_\mathrm{F}^i \sin\theta_\alpha$ and $k_x^{(\alpha i)} = k_\mathrm{F}^i \cos\theta_\alpha$, we can rewrite the spinors for the positive energy branch $\phi_{\alpha+}$ as the asymptotic wave functions

$$\psi_{(\alpha i)\pm} = \begin{pmatrix} \pm A k_\mathrm{F}^i \mathrm{e}^{\pm \mathrm{i}\theta_\alpha} \\ g(k_\mathrm{F}^i) \end{pmatrix} \exp\left[\mathrm{i} k_\mathrm{F}^i (\pm\cos\theta_\alpha + \sin\theta_\alpha)\right]. \tag{5.5}$$

The sign ± directly indicates the direction of motion of the solution. The angles θ_α are implicit functions of k_F^1, which defines the propagating incoming solution at a given Fermi energy $-C$.

5.2. Interface between a quantum spin Hall insulator and a metal

Here, we analyze the injection of the helical edge states from the QSHI on the left into a metallic lead. The latter is modeled by Eq. (2.60) with a high doping, i.e., large $|C|$. The setup is sketched in Fig. 5.1a. It consists of a single interface in a quasi-one dimensional wire of width W. On the QSHI side, the Fermi energy is chosen to be zero, while, in the metallic lead, E_F is shifted by C. In this sense C also characterizes the energetic height (strength) of the interface, where negative (positive) C indicate a QSHI/n-type metal (QSHI/p-type metal) junction. Additionally, we schematically present the corresponding band structures (see also section 2.3.3), in which the metallic bulk states (green) are connected by the helical edge states (red and dashed blue). Since we consider incoming edge states, this setup has to be solved within HBC using the generalized wave matching approach, cf. section 4.3.2. In Fig. 5.1b, we show the transmission through such an interface as a function of C for different widths of the system: $W = 250$, 1000 and 2000 nm. While, for narrow samples, strong interfaces introduce a significant backscattering due to an overlap of counter-propagating edge states, perfect transmission is observed for wide samples. The perfect transmission for wide samples can be explained analogously to that of the topologically protected edge states in graphene [Prada13], for which it was found that the counter propagating edge states for the same Kramers' partner are orthogonal. Indeed, taking into account an exponentially decaying wave function of the edge state, like it was done in Eq. (2.76), it can be confirmed that the overlap between edge states goes to zero for $W \to \infty$ in the presence of any x dependent potential:

$$\langle \psi_\mathrm{edge}(k_x) |\, V(x) \,| \psi_\mathrm{edge}(-k_x) \rangle = V(x) \int_0^W \mathrm{d}y\, \psi_\mathrm{edge}^\dagger(k_x) \psi_\mathrm{edge}(-k_x) \overset{W\to\infty}{\longrightarrow} 0. \tag{5.6}$$

In the same way, the Onsager-Casimir symmetry relation [Büttiker86, Büttiker88] ensures that electrons, which are injected from the metallic lead, perfectly populate the edge states of a very

[3] This is equivalent to Eq. (2.77) for $k_\mathrm{F} = \mathrm{i}\lambda$.

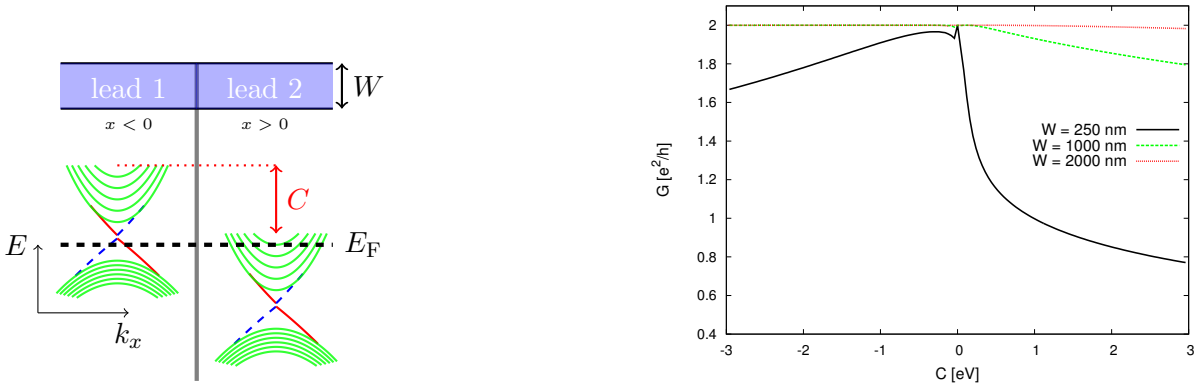

(a) Schematic of the single interface.

(b) G as a function of the doping C in the metallic region.

Figure 5.1.: The single interface between a QSHI and a metal is sketched in (a) together with the respective dispersions. (b) shows the conductance as a function of C, the energetic height of the interface for different lead widths W. Perfect transmission is observed in wide samples where counter-propagating edge states with the same Kramers' partner polarization do not couple. Adapted from [Reinthaler12].

wide QSHI. Let us mention for completeness, that a linear Rashba coupling [Rothe10] does not increase the backscattering, because there are still two orthogonal eigenstates at the same edge, although the direction of the spin polarization is rotated.

5.3. Quantum spin Hall insulator as a tunneling barrier between two metallic leads

In this section, we consider the setup of Fig. 5.2, in which the QSHI acts as a tunneling barrier of length L in between two metallic leads. For the latter, we fix the n-type doping to be $C = -2.5$eV. In [Novik10, Recher10], such junctions have been analyzed using only PBC which neglect the topological edge states. In particular, it was found that such junctions allow for the distinction of different topological phases purely due to evanescent bulk modes. While the conductance rises monotonically with decreasing L in the topologically trivial regime ($M > 0$), the topologically non-trivial regime ($M < 0$) is characterized by a conductance maximum at $L_{\max}$. The purpose of this section is to better understand the formation of the conductance maximum in the topologically non-trivial regime as well as to study the interplay of the bulk and edge contributions by comparing results obtained within PBC and HBC.

5.3.1. Analytical approach to the conductance maximum

The matching conditions (4.41) together with the spinors in PBC (5.5) allow for an analytical solution of the scattering problem. However, the resulting coefficients are in general lengthy expressions, so that no additional insight can be drawn from them. In order to get a better idea of the conductance maximum, we follow the supplementary material of [Novik10] and use the limiting parameters $D = 0$ and $BC \gg A^2 \gg BM$ ($C < 0$), which facilitate the analytical

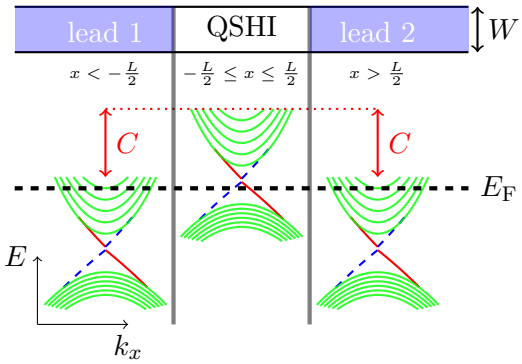

Figure 5.2.: Sketch of a QSH insulator which acts as a tunneling junction of length L and width W in between two metallic leads. The doping of the leads was fixed to $C = -2.5$ eV. Adapted from [Reinthaler12]. ©2012 American Physical Society. All rights reserved.

expressions significantly. In these limits, the Fermi energy offset C is the dominating energy scale in the metallic leads, approximating Eqs. (5.3) and (5.4) by

$$k_{\mathrm{F}}^1 \approx \sqrt{\frac{C}{B}} =: k_1, \quad g(k_1) \approx -\frac{A^2}{2B}, \quad k_{\mathrm{F}}^2 \approx \mathrm{i}\sqrt{\frac{C}{B}} =: k_2, \quad g(k_2) \approx -2C. \tag{5.7}$$

In the QSHI with $C = 0$, we analogously define

$$k_{\mathrm{F}}^1 \approx \mathrm{i}\frac{|M|}{A} =: k_3, \quad g(k_3) = -M, \quad k_{\mathrm{F}}^2 \approx -\mathrm{i}\frac{A}{B} =: k_4, \quad g(k_4) = -\frac{A^2}{B}. \tag{5.8}$$

As we will also find in the numerical results, especially in Fig. 5.3b, the conductance maximum is mainly built by the lowest mode, which in PBC is $k_y^0 = \theta_0 = 0$. In this case, the velocity operator $\hat{v}$ acting on a mode $\psi_{(0i)\pm}$ can be replaced by multiplying the mode with $k_{\mathrm{F}}^i \cdot \psi_{(0i)\pm}$. Since $\mathrm{Im}\, k_4 \gg \mathrm{Im}\, k_3$, we further set $\exp[\mathrm{i}k_4 L] = 0$. With these simplifications, one finds (lengthy) analytical solutions to all the coefficients of the scattering state (4.39). There are two transmitted modes labeled by k_1 and k_2, respectively. Due to the evanescent character of the latter, only k_1 has to be taken into account to calculate the conductance in the lowest mode $G_0 = \frac{e^2}{h}|t_{k_1 k_1}|^2$ with [4]

$$\begin{aligned} |t_{k_1 k_1}|^2 &= \frac{16BC(A^3 + 4ABC)^2 \exp\left[2\frac{LM}{A}\right]}{64A^4B^2C^2(1 + 2\exp\left[2\frac{LM}{A}\right]) + (A^4 + 16B^2C^2)^2\left[4\frac{LM}{A}\right]} \\ &\approx \frac{4A^2BC\exp\left[2\frac{LM}{A}\right]}{A^2\left(1 + 2\exp\left[2\frac{LM}{A}\right]\right) + 4B^2C^2\exp\left[4\frac{LM}{A}\right]}. \end{aligned} \tag{5.9}$$

The approximation in the second line is valid in the approximation $BC \gg A^2 \gg |M|B$. While for $M > 0$, in the topologically trivial regime, this describes an exponential decay, $M < 0$ causes

[4] For the calculation here, we shifted the x coordinate by $L/2$, so that the interfaces lie at $x = 0$ and $x = L$, respectively.

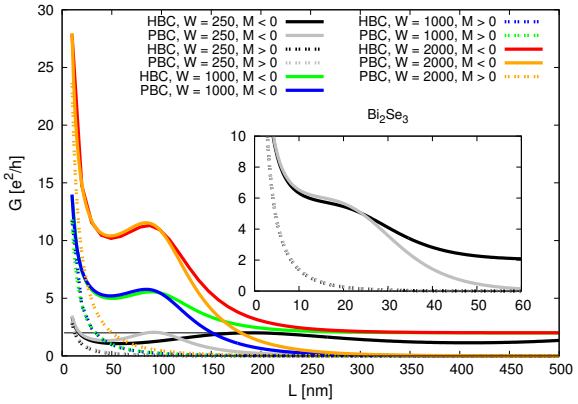

(a) Total conductance for HgTe/CdTe QWs and Bi_2Se_3 thin films (inset) for different widths. We compare the signals for PBC and HBC.

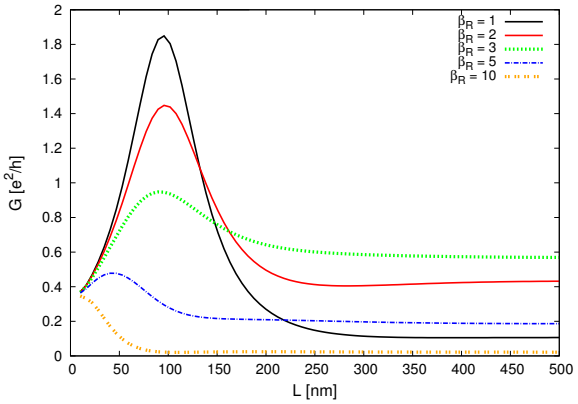

(b) Conductance corresponding to a single incoming mode β_R at $W = 1000$ nm. Here, we restrict the results to HgTe/CdTe QWs in the topologically non-trivial regime ($M < 0$) in HBC.

Figure 5.3.: Conductance through a metal-QSHI-metal junction as a function of the length L. The metallic leads are treated as highly doped QSHIs. In accordance with the definition of the bulk gap M, the topologically trivial (non-trivial) regime is indicated by $M > 0$ ($M < 0$). Adapted from [Reinthaler12].

a distinct conductance maximum, the position of which is found by setting $\partial_L |t_{k_1 k_1}|^2 = 0$:

$$L_{\max} \approx \frac{A}{2|M|} \ln\left(\frac{2BC}{A^2}\right). \tag{5.10}$$

5.3.2. Conductance and local density of states

In Fig. 5.3a, we present the total conductance (5.1) as a function of the sample length L. Looking at the dotted lines for the topologically trivial regime (indicated by $M > 0$), we observe that the conductance decreases exponentially with the increase of L, independent of the boundary conditions. Indeed, in this regime, we expect only evanescent solutions and therefore the same results for PBC and HBC.

We now focus on the topological insulator regime with inverted gap $M < 0$, which is presented by solid lines. For HBC, both, evanescent and edge states contributions to the conductance, are present and the signal depends on the length and the width of the sample. The red and orange lines represent the conductance of a very wide tunneling junction of $W = 2000$ nm for HBC and PBC, respectively. For wide and long QSHIs, G is dominated by the edge states contribution and equals $2e^2/h$. This means that the two different boundary conditions give very different results up to medium lengths L. In contrast, the conductance through a short and wide QSHI is almost independent of the applied boundary condition. This indicates that in this regime, the transport is dominated by tunneling evanescent modes[5]. This is a very interesting result, because naively one would expect that the edge state conductance of $2e^2/h$ simply adds to the

[5]Please note, that the position of the maximum in Fig. 5.3 cannot be predicted by Eq. (5.10) even for PBC, since we included a finite D parameter in the numerical calculations.

transport of the tunneling bulk states, when the width W is large enough to prevent scattering of the edge states from the interfaces. The same behavior is found for an intermediate width of 1000 nm, cf. the green and blue solid lines in Fig. 5.3a.
The signal changes for very narrow QSHIs with $W = 250$ nm. For HBC (black line), we find Fabry-Pérot like oscillations in the transmission of the edge states. At large L, the distance between two oscillation maxima is given by π/k_{edge}, where k_{edge} is the real wave vector of the edge states. The Fabry-Pérot oscillations are caused by scattering of the edge states at the interfaces and thus can only be present for narrow tunneling barriers with finite overlap between counter-propagating edge states, as we elaborated in section 5.2. In this case, the existence of edge states has a dramatic effect on the behavior of the conductance as a function of L. The quantum confinement in narrow wires shifts the bulk states to higher energies. This increases the corresponding imaginary k_x values, which in turn leads to a faster decay of the contribution of evanescent modes. The combination of the edge states with the bulk modes alters the position and the shape of the conductance maximum, which does not coincide with the maximum generated by either the evanescent bulk states or the Fabry-Pérot oscillations alone. In consequence, the conductance maximum in HBC differs significantly from that in PBC (gray line). For the latter, the position of conductance maximum is independent of the width.
For comparison, we show the conductance for a 250 nm wide ribbon of a Bi_2Se_3 thin film in the inset of Fig. 5.3a. Instead of a maximum, we observe a conductance plateau in the inverted regime.[6] Despite the narrow width, the signals of HBC and PBC coincide around the plateau. This can be explained by the larger bulk gap in Bi_2Se_3, which decreases the overlap of the edge states [Zhou08].
In Fig. 5.3b, we focus on a 1000 nm wide HgTe/CdTe QW in the topologically non-trivial regime in HBC and plot the conductance as a function of L for different incoming modes β_R. Only incoming modes with small $\beta_R \lessapprox 5$ contribute to the conductance maximum, while higher modes show the typical decaying transport signal of evanescent modes. Therefore, it is justified to restrict the further analysis to $\beta_R = 1$.
Since we have shown in the last section that the transmission through a sufficiently wide metal/QSHI junction is perfectly quantized, the scattering from the interfaces cannot cause the suppression of the edge state contribution in Fig. 5.3a. To better understand the non-additive behavior of bulk and edge contributions and the formation of the conductance maximum, we plot the local DOS for different sample lengths L in Fig. 5.4. The local DOS of the lowest incoming mode can be calculated from Eq. (4.39) by $|\Psi_{\beta_R=1}(x,y)|^2$, which in the plots has been normalized according to

$$\int_0^W \mathrm{d}y\, \Psi_1^\dagger(x=-\frac{L}{2},y)\Psi_1(x=-\frac{L}{2},y) = 1. \tag{5.11}$$

Let us first concentrate on the Figs. 5.4a, 5.4c and 5.4d, for which $L \neq L_{\mathrm{max}}$. Due to the large doping mismatch C, a strong reflection occurs at the left interface, which causes standing waves in the left lead, see, e.g., Fig. 5.4d. The local DOS peaks inside the tunneling junction. The incoming modes from the left lead are purely metallic bulk states without any admixture of edge states. In the short tunneling junctions (see Fig. 5.4a), these metallic states are not able to adjust to the shape of the edge states, so that they keep their form and tunnel directly through the QSH insulating region. Therefore, the conductance signals from HBC and PBC should coincide for short L, as indeed found in Fig. 5.3a. When the length of the QSHI is comparable

[6] The conductance maximum can be restored by increasing $|C|$ even further.

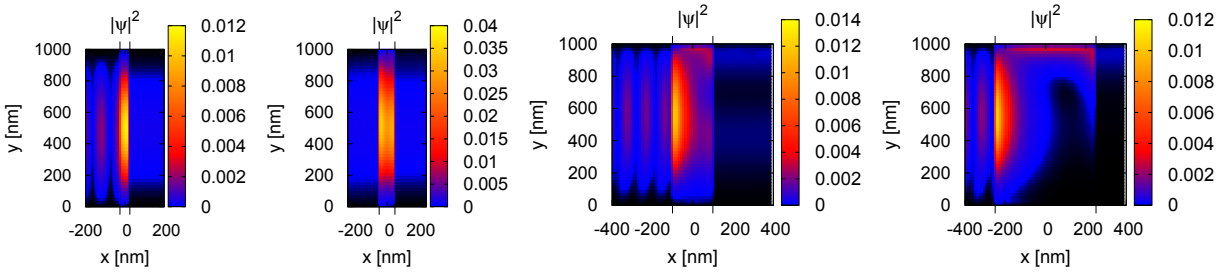

(a) $L = 50$ nm (b) $L \approx L_{\max}$ (c) $L = 200$ nm (d) $L = 500$ nm

Figure 5.4.: The local DOS in a metal-QSHI-metal junction for fixed width $W = 1000$ nm and different sample lengths L. The DOS was calculated as the response to the first incoming mode from the left lead. The color code ranges from white for high DOS to black (vanishing DOS). The interfaces at $\pm L/2$ are indicated by two black lines. In the plot, only one edge state at the upper edge is present, because the calculations have been restricted to one Kramers' partner block. Adapted from [Reinthaler12].

to the decay length of the evanescent modes, (see Fig. 5.4c), electrons are more likely to scatter from the bulk into the edge states, until the transport is driven exclusively by the edge states in long QSHIs, cf. Fig. 5.4d.
It is interesting to compare Figs. 5.4a, 5.4c and 5.4d with Fig. 5.4b, where we choose the length of the tunneling junction to correspond to the peak in conductance, i.e., $L = 100$ nm $\approx L_{\max}$. Here, one finds the local DOS of the QSHI to be strongly enhanced in comparison with the cases where $L \neq L_{\max}$. Additionally, we do not observe standing waves in the left lead, which indicates a weak reflection from the interfaces. Further, the edge states are not yet populated, causing the coincidence of conductance signals for PBC and HBC.
In conclusion, we observe coherent tunneling with suppressed backscattering around the sample length $L \approx L_{\max}$. Moreover, the edge states cannot form in short tunneling junctions.

Detection of the conductance maximum as a function of the gate voltage

So far, we have established, that the topologically trivial and non-trivial regime can be distinguished by a distinct conductance maximum which originates purely from the evanescent bulk modes. This effect does not depend on the applied boundary conditions, as long as the sample is wide enough. Before we discuss the underlying mechanism in more detail in the next section, let us describe an experimentally realizable detection scheme which does not rely on the possibility of changing the sample length L.
This can be achieved by analyzing the conductance for a fixed length as a function of the Fermi energy E_{F}, which can be varied by a top or back gate. For PBC, the two topological regimes show indistinguishable conductance signals as long as the Fermi energy lies within the conduction or the valence band of the QSHI [Novik10]. The QSHI can be distinguished from the normal insulator by a non-monotonic conductance peak for energies within the bulk gap. To analyze this, we plot the conductance as a function of L and E_{F} in Fig. 5.5. The calculations have been performed within PBC for a 1000 nm wide tunneling barrier. Around $L \approx L_{\max}$, the conductance peak is found at zero doping. If the length of the tunneling barrier does not match $L_{\max}$,

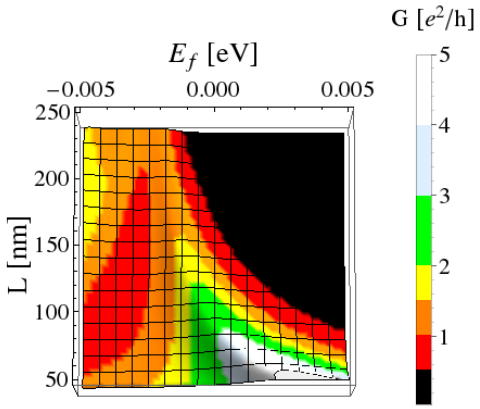

Figure 5.5.: The conductance as a function of the E_F and L of the QSHI. The doping $C = -2.5$ meV of the leads is kept constant. We used a tunneling barrier in the topologically non-trivial regime ($M < 0$) of width $W = 1000$ nm as well as PBC. The conductance maximum is shifted away from $E_\mathrm{F} = 0$, when the length of the sample does not match L_max.

the conductance peak is shifted to finite energies within the bulk gap.
In wide and short tunneling junctions where the bulk states dominate the transport, we find the same behavior for HBC and PBC. When we increase the length of the QSHI above the decay length of the evanescent modes, the conductance is governed by the edge state contribution. In this limit, the signal for PBC drops to zero, while for HBC, the conductance is $2e^2/h$, if the width is large enough to suppress Fabry-Pérot oscillations. In narrow and short tunneling junctions, however, the transport is mediated by a mixture of edge and bulk states. Exactly this latter limit is shown in Fig. 5.6, which presents the conductance as a function of the Fermi energy in the QSHI tunneling junction. In contrast, the doping inside the metallic leads has been kept constant at $C = -2.5$ eV. The bulk gap of the QSHI is indicated by two black vertical lines in Fig. 5.6. It is enhanced above $2|M|$ due to quantum confinement. Additionally, the blue vertical lines present the energy range, in which the overlap of the edge states opens the mini-gap in the system, cf. [Zhou08] and section 2.3.3. Outside of the bulk gap, the signals of the normal and the inverted regime behave similar, like it was predicted for large widths in [Novik10, Recher10]. Within the gap, however, the signal depends on the boundary conditions: for PBC, (black lines) a clear conductance peak is found in the topologically non-trivial regime ($M < 0$, solid lines) around $E_\mathrm{F} = 0$, because of $L \approx L_\mathrm{max}$. In contrast, the transport is almost completely suppressed in the topologically trivial regime (dotted lines). For HBC (red lines), one observes a similar behavior for the normal regime, but the existence of the edge states changes the signal drastically for $M < 0$. Within the gap and for energies smaller than zero, we find the quantized conductance of the edge states. Around zero and for positive energies, the signal is strongly reduced and resembles that of the bulk modes. This behavior can be understood by looking at the local DOS in an infinitely long QSHI, which we present in the inset to Fig. 5.6 as a function of the y-coordinate and of E_F. It has been obtained within HBC by summing over all incoming modes $\sum_{\beta_R} |\Psi_{\beta_R}(y)|^2$. As before, we consider just one of the Kramers' partner blocks, so that only one edge state is present. The mini-gap can be identified in the local DOS by the lack of propagating solutions. Around the mini-gap, the edge state spreads over

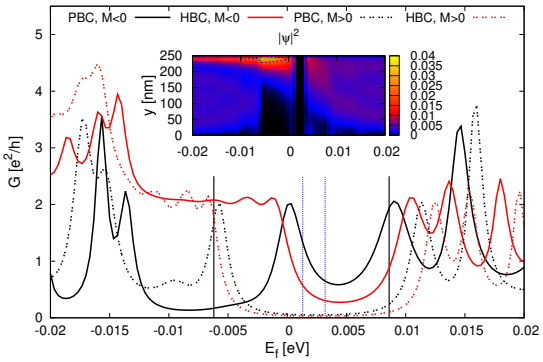

Figure 5.6.: The conductance as a function of the Fermi energy in the QSHI. We compare PBC (black lines) with HBC (red lines) for $M > 0$ (dotted lines) and $M < 0$ (solid lines). The doping $C = -2.5$ meV of the leads is kept constant. The sample is 250 nm wide and 100 nm long. The vertical lines indicate the bulk gap (black), which is larger than $2|M|$ due to quantum confinement, and the mini-gap (blue). The inset shows the total DOS of a single Kramers' partner as a function of E_F and y, which has been calculated for an infinitely long QSHI wire within HBC. The mini-gap can be identified by a zero DOS over the whole sample width. Adapted from [Reinthaler12].

the whole width of the QSHI, leading to an overlap of the counter propagating edge states which crucially influences the transport in narrow metal-QSHI-metal junctions. The overlap of the edge states is in general a function of the energy [Zhou08, Krueckl11, Lu12], which is also confirmed by the inset to Fig. 5.6. This behavior is asymmetric around the charge neutrality point $E_\mathrm{F} = 0$, because a finite D parameter breaks the symmetry of the E1 and H1 bands. For negative energies, the edge state is strongly localized at the upper edge ($y = W$). The small decay length leads to the existence of the edge state even at energies inside the valence band. For our parameters, it merges to the valence band at energies around $E_\mathrm{F} = -80$ meV. Up to this energy, the strong localization ensures the quantization of the conductance, which can be verified in Fig. 5.6. In contrast, at energies above the mini-gap ($E_\mathrm{F} > 3$ meV) the edge state is delocalized, so that a strong backscattering occurs. Moreover, it merges quickly to the bulk states around $E_\mathrm{F} = 10$ meV. Therefore, we conclude that at these energies the transport is dominated by evanescent bulk states and the conductance signals of PBC and HBC coincide qualitatively.

To summarize this section, the conductance maximum can be observed as a function of E_F in short and wide tunneling barriers. In narrow samples, the edge states can contribute to transport at Fermi energies where they are most localized.

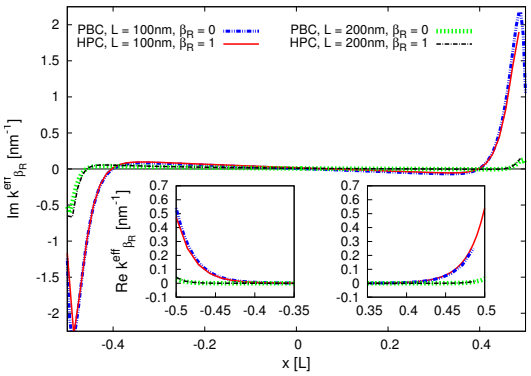

(a) $\mathrm{Im}\, k^{\mathrm{eff}}_{\beta_R}$ and $\mathrm{Re}\, k^{\mathrm{eff}}_{\beta_R}$ (inset) as a function of L for different modes β_R and boundary conditions.

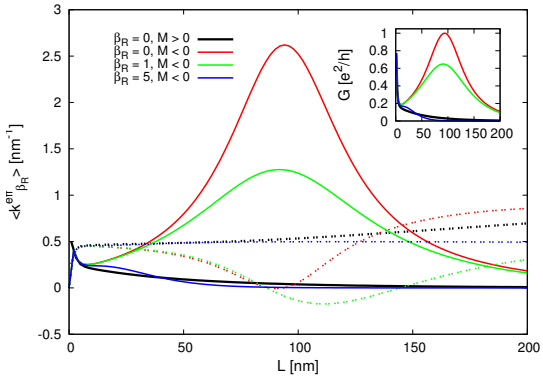

(b) $\mathrm{Re}\langle k^{\mathrm{eff}}_{\beta_R}\rangle$ (solid lines), $\mathrm{Im}\langle k^{\mathrm{eff}}_{\beta_R}\rangle$ (dotted lines) and G (inset) calculated for different β_R within PBC. For comparison, we show the topologically trivial regime ($M > 0$) for $\beta_R = 0$.

Figure 5.7.: The effective wave vector $k^{\mathrm{eff}}_{\beta_R}$ for tunneling junctions in the topologically non-trivial ($M < 0$) regime. The conductance maximum is $L_{\max} \approx 100$ nm. The calculation was done for $W = 1000$ nm. Adapted from [Reinthaler12].

5.3.3. Effectively propagating solution

To further investigate the origin of the conductance maximum when bulk states dominate transport, we analyze the effective wave vector in the direction of propagation for the QSHI

$$k^{\mathrm{eff}}_{\beta_R}(x) = \int_0^W \mathrm{d}y\, \Psi^{\dagger}_{\beta_R}(x,y)\,(-\mathrm{i}\partial_x)\,\Psi_{\beta_R}(x,y), \quad x \in \left[-\frac{L}{2}, \frac{L}{2}\right], \tag{5.12}$$

where $\Psi_{\beta_R}(x,y)$ is the full scattering solution in Eq. (4.39). Our analysis will focus on the lowest incoming modes β_R in PBC and HBC, which give the largest contribution to the signal[7]. In Fig. 5.7a, we present the imaginary as well as the real (inset) part of $k^{\mathrm{eff}}_{\beta_R}(x)$ for different lengths and boundary conditions. In general, $k^{\mathrm{eff}}_{\beta_R}$ can exhibit a finite real part even for PBC, i.e., in absence of edge states, due to the combination of evanescent solutions with complex amplitudes in $\Psi_{\beta_R}(x,y)$. Indeed, Fig. 5.7a confirms that the real part of $k^{\mathrm{eff}}_{\beta_R}$ is non-zero and decays exponentially away from the two interfaces. The imaginary part instead has a more sophisticated behavior with several crossings of zero. In particular, $\mathrm{Im}\, k^{\mathrm{eff}}_{\beta_R}(x)$ shows an antisymmetric behavior with respect to the middle of the tunneling barrier at $x = 0$, when the length corresponds to the conductance maximum, i.e., $L = 100$ nm $\approx L_{\max}$. This behavior is observed for PBC and HBC, which are shown as blue dashed and red solid lines, respectively. This resembles a mode, which enters and decays in the QSH region equivalently from both interfaces, albeit the presented $k^{\mathrm{eff}}_{\beta_R}$ is the response of an incoming mode only from the left. This suggests that the lowest mode coherently traverses the tunneling barrier and that the imaginary part of $k^{\mathrm{eff}}_{\beta_R}$

[7]For PBC, the lowest incoming mode is $k_y = 0$, which is represented by the index $\beta_R = 0$ in Eq. (4.26). In the case of HBC, we label it, like in Fig. 5.3b, with $\beta_R = 1$.

vanishes after averaging over the x-coordinate. We define the averaged $k^{\text{eff}}_{\beta_R}$ as:

$$\langle k^{\text{eff}}_{\beta_R} \rangle := \int_{-L/2}^{L/2} \mathrm{d}x \, k^{\text{eff}}_{\beta_R}(x) \tag{5.13}$$

Fig. 5.7b shows $\langle k^{\text{eff}}_{\beta_R} \rangle$ as a function of L for PBC. The dotted red curve in Fig. 5.7b demonstrates that $\mathrm{Im}\langle k^{\text{eff}}_{\beta_R} \rangle$ indeed vanishes at $L_{\max}$ for the zero mode. The vanishing evanescent part of the effective wave vector coincides with a maximum of the real part of $\langle k^{\text{eff}}_{\beta_R} \rangle$ (solid red line), which gives the impression of an effectively propagating state, which causes the conductance maximum. Away from $L_{\max}$, $\mathrm{Re}\langle k^{\text{eff}}_{\beta_R} \rangle$ decreases while $\mathrm{Im}\langle k^{\text{eff}}_{\beta_R} \rangle$ becomes finite, even for $\beta_R = 0$. Indeed, Fig. 5.7a shows that the signal for $\mathrm{Im}\, k^{\text{eff}}_{\beta_R}$ and $L = 200$ nm $\approx 2L_{\max}$ is not antisymmetric. The inset to Fig. 5.7b shows $G(L)$ for different modes β_R and for PBC. Although higher modes contribute less to the conductance maximum, the mode with $\beta_R = 1$ still exhibits a maximum of $\mathrm{Re}\langle k^{\text{eff}}_{\beta_R} \rangle$ around $L_{\max}$ (solid green line in Fig. 5.7b). The maximum for $\beta_R = 1$ is smaller in comparison to $\beta_R = 0$ and is shifted in the same way as the respective conductance maximum in the inset to Fig. 5.7b. $\mathrm{Im}\langle k^{\text{eff}}_{\beta_R} \rangle$ for $\beta_R = 1$ has a zero value at $L_{\max}$ as well. In contrary, for $\beta_R = 5$, which does not contribute to the maximum, $\mathrm{Im}\langle k^{\text{eff}}_{\beta_R} \rangle$ (blue dotted line) is constant and $\mathrm{Re}\langle k^{\text{eff}}_{\beta_R} \rangle$ (blue solid line) drops to zero. For our parameters, the modes with $\beta_R > 4$ thus behave like modes in the topologically trivial regime and have evanescent character. This can exemplary be verified by comparing the black ($\beta_R = 0$ for $M > 0$) with the blue ($\beta_R = 5$ for $M < 0$) lines.
In principle, one could use the parameter limits of section 5.3.1 to derive an analytical condition for $\mathrm{Im}\langle k^{\text{eff}}_{\beta_R} \rangle = 0$. However, one of the key assumptions was to set $\exp[\mathrm{i}k_4 L]$ to zero. Since this adds to the effective wave vector $k^{\text{eff}}_{\beta_R}$, this simplification drastically influences the shape of $\langle k^{\text{eff}}_{\beta_R} \rangle$, i.e., it will not go to zero at $L_{\max}$.
In short, we found that the lowest modes of the topologically non-trivial regime, which carry the conductance maximum, form effectively propagating modes, while the higher modes are indistinguishable from trivial bulk modes.

5.3.4. Robustness against scalar disorder

One of the Hallmarks of topologically protected states is their robustness against elastic backscattering by scalar disorder. Here, we want to check, if this protection, which is normally associated with the spatially separated edge states, is also found for the effectively propagating bulk mode which carries the conductance maximum. Disorder breaks the translational symmetry along the x-direction, rendering the application of wave matching of asymptotic states impossible. As described in appendices B and C, spatially varying disorder potentials can be most conveniently implemented using tight binding (TB) calculations within the equilibrium Green's function formalism, which naturally implements the HBC. In principle, we could have performed the whole analysis, which we reported in this chapter, using TB calculations. However, to check the validity of the conclusions for experimentally relevant setups, one needs to simulate large structures. Further, a good approximation within the TB formalism, requires a small lattice constant a, because many fast decaying evanescent modes have to be taken into account. In consequence, we would have to use large matrix implementations with dimensions up to $(2000 \cdot 200 \cdot 2) \times (2000 \cdot 200 \cdot 2)$ (width $\cdot$ length $\cdot$ degrees of freedom), which demand an extraordinary amount of memory and CPU time.

One might wonder, if it is possible to rescale the parameters in a way, that the same signal of a tunneling junction of width W and length L is reproduced by a smaller system with dimension $W' \times L'$. The rescaling can be done by choosing one parameter to be constant and by expressing the rest of the parameters in terms of the constant one. Setting C as the constant reference leads to the dimensionless parameters

$$\tilde{C} = \frac{C}{C} = 1, \quad \tilde{M} = \frac{M}{C}, \quad \tilde{A} = \frac{A}{CW}, \quad \tilde{B} = \frac{B}{CW^2}, \quad \tilde{D} = \frac{D}{CW^2}, \quad \tilde{L} = \frac{L}{W}. \tag{5.14}$$

Rescaling to width W' and length L' gives

$$C' = C, \quad M' = M, \quad A' = A\frac{W'}{W}, \quad B' = B\frac{W'^2}{W^2}, \quad D' = D\frac{W'^2}{W^2}, \quad L' = L\frac{W'}{W}. \tag{5.15}$$

While the new set of parameters leads to an equivalent conductance signal in wave matching approaches, its application to the TB formalism cannot reduce the dimensionality of the matrix implementations. The reason is that the TB bands are cosine like, while the continuum dispersion is of leading order k^2. For a good approximation of the continuum results, the bandwidth of the TB model has to be wide enough, so that the Fermi energy, which is determined by $-C$, is positioned in a low energy regime, for which $\cos x \approx 1 - x^2/2$ is still valid. For this to be true, we need $-C$ to be a small fraction of the bandwidth, which for the E1 band is around eight times the hopping parameter t, cf. appendix B. This is also important to fix the number of incoming modes. For the hopping parameter of the E1 band $t_{\mathrm{E1}} = (-B - D)/a^2$ however, the rescaling

$$t'_{\mathrm{E1}} = (-B - D)\frac{W'^2}{a^2 W^2} = \frac{W'^2}{W^2} t_{E1}, \tag{5.16}$$

changes all energy scales, except one simultaneously readjusts the lattice constant by

$$a' = a\frac{W'}{W}. \tag{5.17}$$

In other words: a bisection of the width (and of the length), should be accompanied by a bisection of the lattice constant, in order to keep the energy scale, band width and number of propagating modes unchanged. Therefore, the number of grid points cannot be decreased by rescaling.

A convenient work around can be found by the functional dependencies of the hybridization of edge states in Eq. (2.75) as well as of the position of the conductance maximum in Eq. (5.10) on the bulk gap M. According to these equations, increasing M has two benefits: Firstly, the overlap of counter-propagating edge states decreases. This diminishes the interplay of bulk and edge states, which dominates the conductance in narrow QSHIs in Fig. 5.3a. Secondly, $L_{\max}$ is considerably decreased, allowing to test our predictions in shorter tunneling barriers. In this spirit, we choose a ten times larger bulk gap of $M = -31$ meV, for which $L_{\max} \approx 10$ nm is expected. This parameter choice has the drawback of departing by a considerable margin from the parameters describing the experimental realizations of HgTe/CdTe QWs. Looking at the sub-band dispersion of HgTe/CdTe QWs in Fig. 2.5, one finds that $M := E_{\mathrm{E1}} - E_{\mathrm{H1}} = -31$ meV could in principle be found around $d_{\mathrm{QW}} \approx 10$ nm. However, the principle gap at this QW thickness is built by H2 and H1 bands, undermining the validity of the BHZ model. Consequently, the following results have to be seen as conceptual ones rather than as exact predictions for experiments.

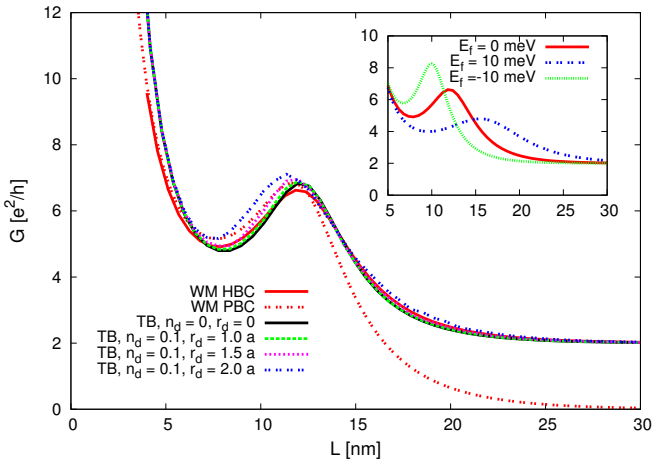

Figure 5.8.: The charge conductance G as a function of the sample length L. We compare the wave matching (WM) approach for PBC (dotted red line) and for HBC (solid red line) with the TB calculations (solid black line) and find good coincidence. Adding scalar disorder with Gaussian correlations influences the signal slightly but does not destroy the conductance peak. We used $W = 150$ nm, $C = -2.5$ eV, $M = -31$ meV and $W_d = 0.06$ eV. The inset shows the influence of the Fermi energy E_f inside the tunneling barrier. Adapted from [Reinthaler12].

We choose $N_y = 250$ grid points along the y-axis. This fixes the lattice constant to $a = 150\text{ nm}/251$, so that the number of lattice points in x-direction varies with L. In order to check the applicability of this model, we compare the TB calculations in the absence of disorder (black solid line in Fig. 5.8) with the signal computed in the wave matching formalism (WM, red solid line). The signals of the two models coincide very well, showing that the above procedure does indeed not change the results qualitatively but shifts the position of the conductance maximum to system sizes which can be easily calculated within the TB model. Further, the conductance for PBC (red dotted line) coincides with the TB signal, indicating that the overlap between the edge states is negligible.

We include scalar disorder by introducing an on-site energy V_d which varies randomly in the range $[-W_\mathrm{d}, W_\mathrm{d}]$ and is characterized by $\langle V_\mathrm{d}(\boldsymbol{r})\rangle \approx 0$. The maximal disorder strength, which can be applied without coupling the valence to the conduction band, is $W_\mathrm{d} = 2|M|$. Instead of applying a different potential at each lattice point (Anderson disorder)[8], we choose isolated scatterers on a fraction $N_\mathrm{d} = n_\mathrm{d}(N_x \cdot N_y)$ of lattice points, where we fix $n_\mathrm{d} = 0.1$ in the following. The impurities are assumed to be isometric and to spread Gaussian-like over the neighboring lattice points, with a decay length r_d, which is given in units of the lattice constant a. The results for finite disorder strength V_d have been averaged over 100 different disorder configurations.

After having established the robustness of the conductance maximum using PBC [Recher10], we focus on HBC in Fig. 5.8, where we apply the constant disorder strength $W_d = 0.06$ eV and vary r_d from a (green dashed line) to $2a$ (dotted blue line). For long sample lengths L, the disorder has no influence on the quantized conductance of the edge states, which are protected against scattering from scalar disorder. At smaller L, however, the disorder has a visible influence on

[8] For more details on the characterizations of different types of disorder, the reader is referred to [Akkermans07].

the evanescent modes. The effect of the disorder on G increases for larger r_d. It shifts and, surprisingly, increases the conductance maximum slightly. This can be understood taking into account the evanescent character of the populated modes. In this regime, the extension of the impurities can be comparable with L, which causes large fluctuations in energy over a relatively large part of the tunneling junction. A change in Fermi energy of the QSHI shifts the position of the conductance maximum, as shown in Fig. 5.5 for PBC as well as in the inset to Fig. 5.8 for HBC. Despite these small changes in the transport signal, we can conclude that the conductance signal is robust against scalar disorder in HBC.

5.4. Conclusion

We have explicitly demonstrated that the evanescent bulk modes of a QSHI carry information about the topology of the system. This is particularly interesting, because the topology, albeit being a bulk property, is usually characterized by the presence or absence of protected helical edge states in experiments, cf. section 2.2.3. Unlike previous publications [Novik10, Recher10], we included the helical edge states in our analysis by choosing HBC.
In long and wide tunneling junctions in the topologically non-trivial regime, the transport is dominated by the edge states. However, when L becomes shorter, the edge states are no longer populated due to the mismatch with the incoming bulk modes. In this regime, we have found that the bulk states of the topologically non-trivial regime form effectively propagating solutions, which carry the conductance maximum around $L = L_\mathrm{max}$. Surprisingly, the effectively propagating modes are robust against scalar disorder. Further, we have analyzed narrow tunneling junctions, where finite size effects lead to an interplay of edge and bulk states. The latter regime is characterized by Fabry-Pérot oscillations as well as a change of the position of the conductance peak.
In our analysis, the leads have been modeled by highly doped QSHIs. These behave almost like purely metallic leads at high doping, where the dispersion is dominated by terms of quadratic order in $\boldsymbol{k}$. In principle, we could have also chosen metallic leads, like for example in [Yokoyama09], and would have qualitatively obtained the same conductance maximum, because the latter is formed by the low energetic modes of the QSHI alone.
In section 5.2, we found that the edge state is not reflected from a metallic interface in a wide parameter range. This auxiliary result considerably helped to understand the tunneling junctions with two interfaces. It will also prove to be very useful, when we carry it over to chapter 6, where we analyze the injection of helical edge states into a highly doped SC.

6. Crossed Andreev reflection in helical edge states

In the last chapter, we have found that finite size effects can significantly enrich the physical phenomena in tunneling junctions. Driven by this experience, we generalize our numerical description to superconducting systems within the BdG formalism. To be specific, we analyze the fate of helical edge states, which are injected into a superconducting tunneling junction. When this tunneling junction is wide enough to prevent backscattering, its Andreev reflection (AR) probability becomes unity, providing a tool to characterize transport in protected edge states [Adroguer10]. As anticipated, finite size effects introduce a richer variety of transport channels, including a finite crossed Andreev reflection (CAR). Surprisingly, the modes associated with CAR can be spatially separated from the electron tunneling contribution, when only one Kramers' partner block is considered. Based on this, we propose an all-electrical meter for CAR processes in QSHI-SC-QSHI tunneling junctions. We will motivate the usefulness of these results in section 6.1.1. The principle mechanism how to separate CAR from electron tunneling is presented in section 6.1.2. In section 6.2, we support our argumentation by numerically calculating the transport through finitely sized tunneling junctions in the generalized wave matching approach. We explicitly show how the CAR can be tuned by the parameters of the system up to about 50% of the non-local transport. This chapter is based on [Reinthaler13][1].

6.1. All-electrical measurement scheme for crossed Andreev reflection

6.1.1. Crossed Andreev reflection as a source of spin entangled electrons

Many applications of quantum information, like quantum encryption or the error correction by CSS codes, named after Calderbank, Shor and Steane, require the entanglement of quantum states [Einstein35, Bennett00, Nielsen05]. While entanglement was achieved using the circular polarization of photons [Aspect82, Zeilinger99], it is an ongoing challenge to create entangled electrons in solid state devices. Promising candidates are found in s-wave SCs, which couple spin-$\uparrow$ and spin-$\downarrow$ electrons to Cooper pairs, as we have discussed in section 3.1. Splitting the Cooper pairs into two spatially separate electrons should provide a natural source of spin entangled electrons [Recher01, Lesovik01]. Since this is exactly the inverse process to CAR, it is interesting to study the properties of CAR and how its magnitude can be controlled. CAR was introduced in section 3.3 as a transport process in N-SC-N junctions, i.e., a SC connected to two normally conducting leads. In these setups, the splitting of Cooper pairs is driven by a finite bias difference between the left and right lead. A straightforward way to observe CAR, is by non-local conductance measurements [Beckmann04, Russo05]. However, this method has the drawback that CAR is disguised by electron tunneling [Falci01], which does not involve Cooper pairs and, therefore, is a parasitic process. More involved experimental setups could recently detect Cooper

[1]

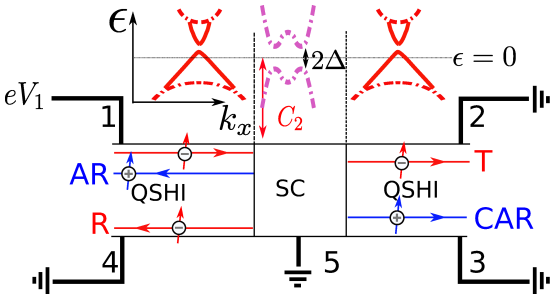

(a) 5-terminal setup. We show the corresponding excitation energy spectrum schematically above each region. Solid lines indicate edge states, dashed lines are bulk solutions. For simplicity, only electronic states are shown in the leads.

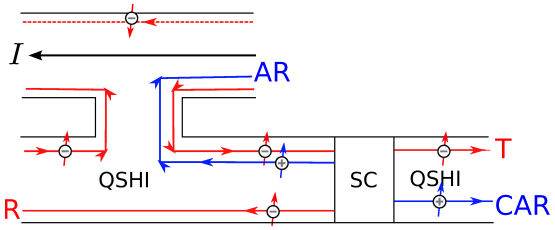

(b) Spin selection via an H-bar structure of a QSHI. Driving a current I in the upper leg of the structure leads to spin-↑ injection to the QSHI-SC-QSHI junction in the lower leg.

Figure 6.1.: We consider a QSHI-SC-QSHI junction. Electron and hole edge states are indicated by red and blue lines as well as + and − signs, respectively. The SC is doped with energy C_2 and grounded, as explicitly shown by contact 5 in (a). Taken from [Reinthaler13].

pair splitting circumventing the electron tunneling processes by including additional quantum dots [Hofstetter09, Herrmann10] or by current noise [Wei10] measurements.
In this chapter, we make use of the helicity conservation of the edge states in QSHIs to achieve a spatial separation of the CAR from all other transport channels. Unlike previous works on QSHI-SC-QSHI interfaces [Sato10, Adroguer10, Chen11], we do not restrict ourselves to a phenomenological model of the edge states, but are interested in the full solution including both edge and bulk transport.

6.1.2. Working principle of the all-electrical cross Andreev reflection meter

The basic setup is shown in Fig. 6.1a. It consist of a QSHI-SC-QSHI junction, in which the SC acts as tunneling barrier. Here, we assume that the SC consist of the hybrid system of a QSHI proximity coupled to an s-wave SC. This can be realized by growing a SC thin film of, e.g., Niobium on top of a QSHI slab. In this case, the normally- and superconducting parts of the setup are based on the same material, avoiding the difficulty to engineer a conducting contact between a SC and a QSHI. In order to avoid charging effects due to the creation of Cooper pairs, the SC is always set to ground by contact 5. The rest of the contacts will be important for the spin selection. On top of all three parts of the junction, the excitation energy spectrum is schematically presented. In the QSHI leads, transport can only take place in the edge states (solid lines). In contrast, we assume that the Fermi energy of the superconducting part is shifted by the energy C_2. In section 3.2.3, this doping was shown to occur as a byproduct of the proximity effect, if the interface in the hybrid structure of Fig. 3.1 is sufficiently clean. We assume that the doping shifts the Fermi energy of the superconducting part deep into the conduction band. This assumption is essential for the physics discussed in the following, because the evanescent bulk states stretch over the whole sample, which facilitates the coupling of the edge states at opposite edges and aids the generation of a large CAR signal.
To be specific, let us consider a spin-↑ electron to be injected from the left lead, like shown in

Fig. 6.1a. There are four possible scattering mechanisms which conserve the spin[2]. Conserving the particle character of the incoming electron, this can be either electron reflection (R) or electron tunneling (T). To enter the superconducting condensate, the electron needs a partner of opposite spin, which ejects a spin-↑ hole[3] either in the left or right lead by AR or CAR, respectively. Due to the helicity of the edge states, AR and T can only take place on the edge of the incoming electron, while R and CAR are restricted to the opposite edge. This is the basic idea of the spatial separation of the cross Andreev reflected holes from the tunneled electrons: Occupying locally separated edges of the system, both can be detected all-electrically by contacting these edges independently, cf. contacts 2 and 3 in Fig. 6.1a.
Neglecting the doping due to the superconductor, i.e., $C_2 = 0$, Adroguer et al. [Adroguer10] found that in such superconducting tunneling junctions helicity conservation enforces perfect AR, when the width (W) and length (L) of the SC become large. However, CAR and T are not conceptually forbidden in structures of finite size. In section 6.2, we will provide a numerical solution, demonstrating how CAR can be tuned up to 50% of the non-local signal by varying the geometry or the doping of the tunneling junction. For the following discussion about the working principle of the all-electrical CAR meter, it is sufficient to assume CAR to be finite.
The key requirement to obtain the spatial separation of non-local electron- and hole-like modes is to restrict transport to one spin polarization, here spin-↑. Indeed, injecting a spin-↓ electron leads to an analogous distribution of scattering channels upon mirroring the QSHI slab about $y = W/2$. In consequence, the spin-↓ CAR mode overlaps with the electron tunneling contribution of the spin-↑ electron and vice versa. In this case, all spatial resolution of electron and hole signals is lost. Here, we propose two different ways to select one spin polarization: It is possible to contact the edges independently in a 5-terminal setup [Roth09], like it is shown in Fig. 6.1a. Grounding all but contact 1, where a voltage V_1, is applied, drives only spin-↑ electrons towards the junction. Non-local conductance measurements, explicitly $\partial I_2/\partial V_1$ and $\partial I_3/\partial V_1$, then serve as a direct electrical measurement of T and CAR, respectively. In Fig. 6.1b, we propose to use the non-equilibrium QSH effect in an H-bar structure for spin selection. Applying a current I in the upper leg drives electrons from right to left in the upper leg. Due to helicity, only spin-↑ electrons propagate along the lower edge of the upper leg. These spin-↑ electrons are transmitted through the bridge to the lower leg, where they are injected to the QSHI-SC-QSHI junction.
Note that the measurement scheme, which we propose to experimentally detect CAR, relies on restricting the transport to a single spin polarization. This spin filtering destroys the spin entanglement of the underlying Cooper pair. However, spin-entangled electrons could be produced by the inverse CAR in similar setups, when both spin polarizations are present. This could, for example, be achieved by coupling both edges to the same reservoirs in Fig. 6.1a.

6.2. Spatial separation of the non-local transport signals

For a concrete numerical treatment, we concentrate on HgTe/CdTe QWs. Nevertheless, our proposal relies on finite size effects as well as the helicity of the edge states of a general QSHI. Therefore, it should be equally relevant to other 2D topological insulators, like graphene [Kane05a], inverted type-II semiconductors [Liu08] and thin films of 3D TIs [Shan10, Lu10, Liu10b].

[2]In this chapter, we use the term spin polarization or simply spin for the Kramers' partner quantum number. This is only a matter of wording, because the Kramers' partners can always be mapped onto two orthogonal (pseudo-)spin states in the system, although these do not have to be pure spin-z states, cf. section 2.1.2.
[3]Throughout this chapter, we will always refer to the hole picture introduced in appendix D. In this sense an incoming spin-↑ electron is Andreev reflected as a spin-↑ hole.

6.2.1. Numerical model

A HgTe/CdTe QW into which superconductivity is induced is described by the BdG Hamiltonian (3.85). Here, we focus on a single spin polarization, so that we can reduce the Hamiltonian to

$$H^{\uparrow}_{\mathrm{BdG}}(\boldsymbol{k}) = \begin{pmatrix} \epsilon(\boldsymbol{k}) + d_i(\boldsymbol{k})\tau_i & \tilde{\Delta} \\ \tilde{\Delta}^* & -\epsilon(-\boldsymbol{k}) - d_i(\boldsymbol{k})\tau_i \end{pmatrix}, \tag{6.1}$$

where $\epsilon(\boldsymbol{k})$ and $d_i(\boldsymbol{k})$ are defined in Eq. (2.61) and the inversion asymmetric terms of Eqs. (2.63) and (2.64) are neglected. The τ_i are the Pauli matrices in sub-band space. For convenience of notation, we did not write the 2×2 unit matrix τ_0 explicitly. The N-SC-N junction is shown in Fig. 6.1. The non-superconducting QSHI leads are modeled by $H^{\uparrow}_{\mathrm{BdG}}(\boldsymbol{k})$ with $\tilde{\Delta} = 0$ and $C = 0$, i.e., zero Fermi energy, while in the SC region, we choose the doping $C_2 = -50$ meV and $\tilde{\Delta} = 0.5$ meV, which is a realistic value for the induced superconductivity by an s-wave SC, like, e.g., bulk Niobium with $\Delta(\mathrm{Nb}) \approx 1.45$ meV at zero temperature [Chrestin97]. The rest of the parameters has been adjusted according to [Rothe10] and are given in Tab. 2.1.
Since we are interested in the edge mode transport of a QSHI, we apply HBC and the generalized wave matching approach of section 4.3.2 to solve for the asymptotic modes in the three regions of the QSHI-SC-QSHI junction. The full scattering state is found according to the matching procedure described in section 4.3.3. Since the evanescent states in the leads do not enter the S-matrix (4.6), the transport is purely determined by the scattering amplitudes of the edge states. Let β_e^R label the right (R) propagating electronic edge mode, which is injected towards the junction from the left lead. The outgoing modes are indicated by $\alpha^{e/h}_{R/L}$, where e and h indicate electrons and holes, respectively. Describing outgoing states, the modes, which propagate to the right ($\alpha_R^{e/h}$) or left ($\alpha_L^{e/h}$) are always located in the right or left lead. Eq. (4.42) determines the different transport coefficients

$$\mathrm{T} = \left|S_{\alpha^e_R,\beta^e_R}\right|^2, \quad \mathrm{R} = \left|S_{\alpha^e_L,\beta^e_R}\right|^2, \quad \mathrm{CAR} = \left|S_{\alpha^h_R,\beta^e_R}\right|^2, \quad \mathrm{AR} = \left|S_{\alpha^h_L,\beta^e_R}\right|^2, \tag{6.2}$$

where we identify the name of the transport process with its probability for simplicity of notation. Using these transport coefficients, we can express the local and non-local conductances $G_{ij}(\epsilon) = \mathrm{d}I_i/\mathrm{d}V_j$, i.e., the conductance from contact j to i, where $i, j = 1, \ldots, 4$ correspond to the contacts in Fig. 6.1a. $\epsilon = eV_1$ is the voltage applied at contact 1. Assuming spatially well separated transport signals, the conductance at zero temperature can be approximated by using the BTK formalism. From Eqs. (4.21) and (4.24), we find

$$G_{11}(\epsilon) = \frac{e^2}{h}(1 + \mathrm{AR}(\epsilon)), \quad G_{21}(\epsilon) = \frac{e^2}{h}\mathrm{T}(\epsilon), \quad G_{31}(\epsilon) = -\frac{e^2}{h}\mathrm{CAR}(\epsilon). \tag{6.3}$$

The full scattering state $\Psi(x, y)$, which is defined in Eq. (4.39), is the response to an incoming mode $\psi_{\beta^e_R,1}(x, y)$ from the left lead. Therefore, it allows us to calculate the local non-equilibrium charge density

$$n(x, y) = \Psi^\dagger(x, y)\Lambda\Psi(x, y), \quad \Lambda = \mathrm{diag}[1, 1, -1, -1]. \tag{6.4}$$

Here positive (negative) values of $n(x, y)$ indicate electron-like (hole-like) charge. For plotting the charge density, we use Eq. (5.11) to normalize $\Psi(x, y)$ at the left interface.

The influence of bulk inversion asymmetry

The general form of the BHZ Hamiltonian contains couplings between the Kramers' partner blocks stemming from structure inversion asymmetry (SIA), Eq. (2.64), and bulk inversion asymmetry (BIA), Eq. (2.63). These effects can in general compromise the spin selection proposed in Fig. 6.1, endangering the proposed measurement scheme. Here, we focus on the effects of BIA, because SIA can in principal be adjusted by the interplay of QW growth and gate voltage, cf. the discussion of Eq. (2.64).
The strength of the BIA terms, Δ_{BIA}, has been estimated to be around 1 meV.[4] Up to this coupling strength, the BIA terms only slightly influence the probabilities of the individual scattering processes. Although the energy splitting which is generated in the edge state by BIA shows energy dependence, it is generally much smaller than the coupling parameter itself [Michetti12].
However, there are two ways in which BIA terms could influence the spatially separated measurement of electrons and holes. Firstly, BIA couples and hybridizes the degenerate edge states, leading to states which exist simultaneously on both edges. One option to circumvent this problem is to inject electrons with a given spin polarization. This is not an eigenstate of the system but the equilibration process should take longer than the actual transport event due to the small influence of BIA on the edge states [Michetti12]. Another solution is to lift the degeneracy of the states at opposite edges, which suppresses the hybridization of the corresponding edge states. Since the energy shift generated by BIA is very small, already small fluctuations in experimentally relevant samples should overcome the hybridization. For example, random variations in the thickness of the QW can cause small fluctuations of the bulk gap M, which has been observed in [Tkachov11].
The second effect is based on the energy dependence of the spin rotation due to the BIA terms. This causes a more subtle problem, because the spin quantization axis in the leads and the SC may differ due to the large doping mismatch C_2. In this sense, the coupling of different spins in the leads due to the SC is no longer conceptually prohibited, because the spin precesses within the SC on a length scale which is inversely proportional to the coupling parameter. In order to calculate the spin precession length semi-analytically, we first determine the spin-$\uparrow$ and spin-$\downarrow$ eigenstates of a doped QSHI in the absence of BIA in an infinite plane. Then, we calculate the time-dependent overlap of the spin-$\downarrow$ state with the spin-$\uparrow$ state, which undergoes a time evolution in the presence of BIA. The time-dependent overlap is shown in Fig. 6.2a. From the periodicity, we extract the spin precession time t_{BIA}, which is proportional to the spin precession length. In Figs. 6.2b and 6.2c we plot t_{BIA} as a function of the BIA coupling strength and as a function of the doping C_2, respectively. We find that the spin precession time decreases with Δ_{BIA} and increases with the doping. To decrease the influence from the spin rotation, which leads to different spin quantization axes in the leads and in the SC, the spin precession length should be as large as possible in comparison with the extension of the sample. One can estimate the spin precession length, by assuming the Fermi velocity of the states to match that of the incoming electron edge state $v_{\mathrm{F}} \approx A/\hbar$, where $A = 0.365$ nm eV [Rothe10]. At $C_2 = -50$ meV and $\Delta_{\mathrm{BIA}} = 1$ meV, where $t_{\mathrm{BIA}} \approx 2$ ps, the precession lenght is about 1100 nm, exceeding the dimensions of the tunneling junction, which we propose for the all-electrical CAR meter ($L = 100$ nm and $W = 200$ nm), see below. Therefore, we conclude to neglect the BIA terms and restrict our calculations to a single Kramers' partner block.

[4] So far, experiments, in particular on Shubnikov-de Haas oscillations, do not reveal BIA characteristic signatures, suggesting that the real value might be much smaller than the current estimate (L. W. Molenkamp, private communication).

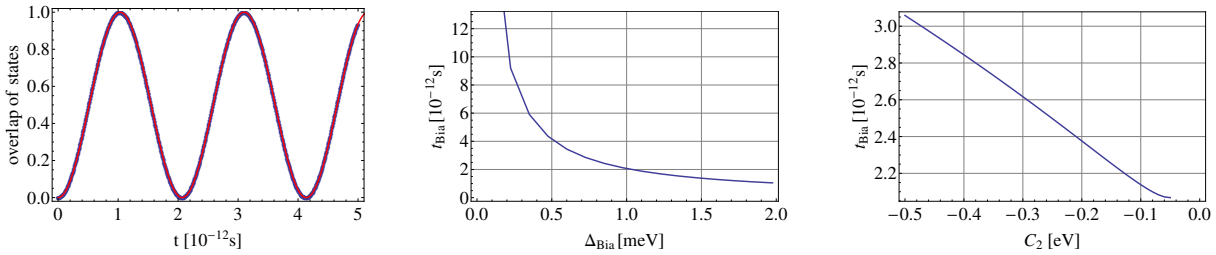

(a) Time dependent spin precession calculated from the overlap of spin-↑ and spin-↓ states in the presence of BIA. From the fit (red line) one can extract t_{BIA}.

(b) Δ_{BIA} dependence of t_{BIA} at $C_2 = -50$ meV

(c) C_2 dependence of t_{BIA} at $\Delta_{\mathrm{BIA}} = 1$ meV

Figure 6.2.: Semi-analytical estimate of the spin precession time t_{BIA} caused by BIA. We used an infinite QSHI, whose Fermi energy is shifted into the conduction band by C_2.

The influence of inter-edge Coulomb coupling

Another way to couple the edge states at opposite sides of the sample would be the inter-edge Coulomb interaction, which might play a significant role in narrow samples. Indeed, Tanaka and Nagaosa [Tanaka09] found that 2D TIs allow for the formation of an inter-edge correlated liquid. The therefor relevant process, the inter-edge pseudo-spin-flip backward scattering, opens a gap, which was estimated to be $\sim M \exp[-\epsilon'/0.7]$ for HgTe QWs with a width of the order of 100 nm, where ϵ' is the dielectric constant of the substrate. Using $\epsilon' \sim 2-3$ Tanaka and Nagaosa found an interaction induced gap of ~ 0.5 meV, which is comparable to the induced superconducting gap, which we assume. However, their estimate of ϵ' is about a factor 5 too small for HgTe/CdTe QWs. Applying the same reasoning as [Tanaka09] and using a more realistic estimate of the dielectric constant of CdTe [Strzalkowski76], decreases the gap by interaction effects drastically, so that the inter-edge Coulomb interaction should not influence the transport effects significantly.

6.2.2. Tuning the crossed Andreev reflection

In Fig. 6.3, we show the transport coefficients as a function of the width W for the constant length $L = 100$ nm. We find that R and CAR approach zero for $W \gtrsim 600$ nm, which is in agreement with Adroguer et al. [Adroguer10], although $C_2 = -50$ meV dopes the system far outside the bulk gap in our setup. We do not find quantized AR, since L was chosen relatively small and electrons can tunnel through the junction. Increasing L restores perfect AR. In contrast to [Adroguer10], we are interested in finite size effects which dominate at $W < 600$ nm. In particular, we observe large fluctuations in the signal as well as finite R and CAR. The latter reaches its maxima at points, where T is relatively small. Therefore, it is possible that CAR and T have the same probability of about 10% of the total signal in this configuration. At these points, the total charge current in the right lead, which is the sum of the currents measured in contacts 2 and 3 in Fig. 6.1a, becomes minimal, because the electron- and hole-like contributions cancel. The total signal in the right lead can thus be tuned to pure spin currents, similarly to proposals for quasi-1D wires [Das08].

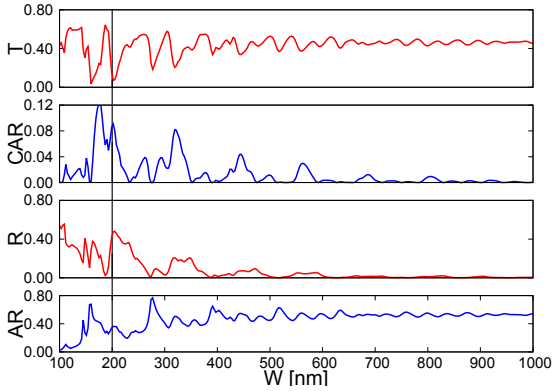

Figure 6.3.: The transport coefficients as a function of the width W at constant $L = 100$ nm and $C_2 = -50$ meV. Taken from [Reinthaler13].

Fig. 6.4 shows the non-equilibrium charge density $n(x, y)$ of Eq. (6.4). The geometrical dimension of the junction, which is fixed to $W = 200$ nm and length $L = 100$ nm, has been adjusted to support a large CAR contribution. The corresponding transport coefficients are indicated by a black vertical line in Fig. 6.3. Warm colors show electron-like charge density, cold colors symbolize an excess of holes. The two interfaces at $-L/2$ and $L/2$ are indicated by vertical black lines. Inside the leads, the charge density is only distributed along the edges, supporting the main result of this chapter: the spatial separation of the contributions of T on the upper edge and of CAR on the lower edge in the right lead, which is enforced by helicity conservation. This separation works, as long as the edge states, which according to Eq. (2.76) decay like $\exp[-\lambda y]$ away from the edges, do not overlap. This is fulfilled for our setup, where we read $1/\lambda \approx 20\text{ nm} \ll W$ from Fig. 6.4.
In the left lead, we have the incoming electron, which overlaps with a locally reflected hole at the upper edge. In section 5.2, we found that the direct electron reflection R is strongly suppressed at the left interface, again because the edge modes do not overlap. Thus, the incoming electron is either directly Andreev reflected as a hole or enters the SC. Inside the SC, the tunneling solution is reflected several times between the two interfaces, which explains the resonant behavior at small width. Since all superconducting solutions are evanescent for $0 = \epsilon < \tilde{\Delta}$, the resonant behavior due to multiple reflections decays with increasing W. A rough estimate for the length scale, up to which the resonant behavior can be observed, is obtained by $W \lesssim \xi_0$, where ξ_0 is the SC's coherence length defined in Eq. (3.46). For small energies, quadratic terms in the BdG Hamiltonian (6.1) play a minor role [Schmidt09], allowing the approximation $\xi_0 \approx A/\tilde{\Delta} = 729$ nm. In Fig. 6.3, R and CAR are suppressed earlier, which can be understood in the way that the tunneling solution does not take the direct way, but bounces back and forward between the interfaces and traverses the SC several times.
In Fig. 6.5a, we plot the transport coefficients as a function of the SC's length L at fixed $W = 200$ nm. For long L, the unit probability of AR is restored [Adroguer10], because the other transport coefficients decay due to the evanescent nature of the particles. From comparison with an exponentially decaying envelope function, we find the decay lengths ξ_0 for T, $\xi_0/2$ for R and $\xi_0/3$ for CAR. The different decay lengths directly indicate that the tunneling particle needs to traverse the sample several times in order to be scattered to the lower edge. Since the direct overlap of the edge states is suppressed, the transition between the edges is mainly mediated

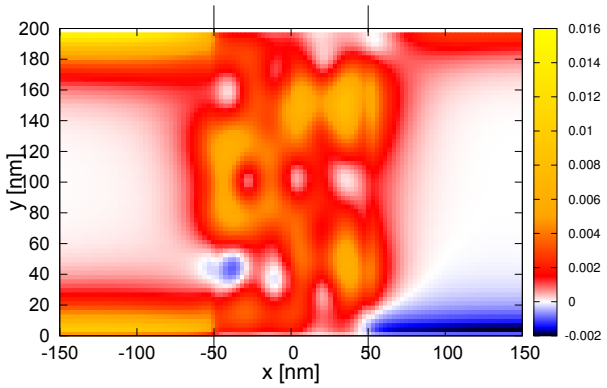

Figure 6.4.: The local charge density $n(x, y)$ as response to the incoming electronic mode at the upper edge in the left lead. $L = 100$ nm and $W = 200$ nm were chosen to meet large CAR and have been indicated by a black line in Fig. 6.3. Warm (cold) colors and positive (negative) values correspond to electron (hole) densities. The interfaces at $x = -L/2$ and $x = L/2$ are marked by black lines. In the right lead, we observe a strict separation of the charge densities of electrons and holes. Taken from [Reinthaler13].

by the existence of evanescent bulk modes, which span over the whole sample. In contrast, the absence of weakly decaying bulk modes at $C_2 = 0$ prohibits transitions between the different edges. In this case, only the direct overlap of edge states in very narrow QSHI junctions can couple the upper edge to the lower one. However, the direct overlap of edge states destroys the spatial separation of electrons and holes in the right lead. Therefore, the large doping C_2 is a key ingredient of our setup, because it generates finite R and CAR.
On top of the evanescent decay, we find resonant oscillations of the signal. The latter can be understood in the context of Fabry-Pérot oscillations. As long as $L \ll \xi_0$ is fulfilled, the signal oscillates on length scales of $L = \pi / \mathrm{Re}(k_x^\alpha)$. Although the bulk modes α are evanescent, the corresponding wave vectors k_x^α may have a finite real part, analogously to the discussion in section 5.3.3. The periodicity of the Fabry-Pérot oscillations can in general not be quantified uniquely, because many different bulk modes contribute to the resonant behavior. Nevertheless, instead of changing the geometry, which is experimentally difficult, the Fabry-Pérot condition can be fulfilled for a fixed L by varying $\mathrm{Re}(k_x^\alpha)$. Since the wave vector explicitly depends on the Fermi energy E_F, it is possible to maximize the CAR contribution by using gates as experimentally realizable knobs. Since the SC screens the system, gating can be realized most efficiently by back gates. In Fig. 6.5b, we present the behavior when the back gate changes the Fermi energy by ΔC in the SC as well as in the leads. For the E_F range, which is shown, the leads are not doped outside of the bulk gap, ensuring edge state transport and spatial separation of T and CAR channels. The transport coefficients oscillate in a similar manner, like when L is varied, demonstrating the tunability of CAR as a function of the gate voltage. The breakdown of the conductance around $\Delta C \approx -7.5$ meV is caused by the opening of the mini-gap (2.75) in the leads [Zhou08]. In the inset to Fig. 5.6, we have already observed that the edge states become delocalized around the mini-gap. This couples the opposite edges and generates a peak in the

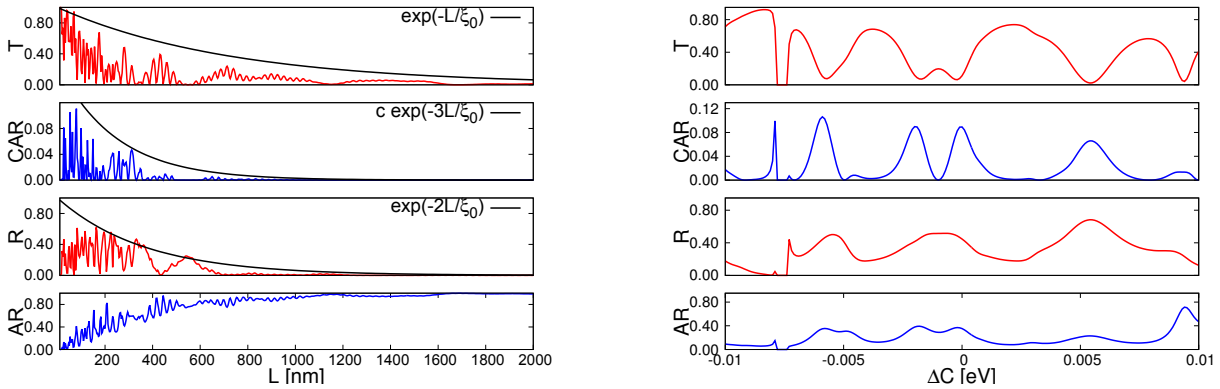

(a) The transport coefficients as a function of L for $W = 200$ nm. In addition to the resonant behavior, we observe an exponential decay of the envelope function of T, R and CAR on a length scale proportional to ξ_0. The constant $c = 0.18$ is chosen to fit the CAR signal better.

(b) The transport coefficients as a function of the global change in doping ΔC at fixed geometry $W = 200$ nm and $L = 100$ nm.

Figure 6.5.: Analysis of the transport coefficients to tune the CAR in experimental setups. Adopted from [Reinthaler13]. ©2013 American Physical Society. All rights reserved.

CAR. As discussed above, these delocalized edge states do not allow for a spatially separate measurement of electron and hole solutions.

6.3. Conclusions

In this chapter, we have used the helicity conservation of the edge states of a QSHI to propose an all-electrical measurement scheme for the CAR based on QSHI-SC-QSHI junctions. Our proposal relies on the selection of a single spin polarization. The latter can be achieved by choosing appropriate contact voltages in a 5-terminal setup or, more interestingly, by exploiting the transport properties of the helical edge states in an H-bar structure.
At the same time, the helicity conservation of the edge states also suppresses the CAR, rendering the realization of the proposal impossible in large samples. Using numerical calculations, we demonstrated that finite size effects can generate significant CAR. Our analysis revealed that a gate voltage can be used as experimental knob to tune the non-local conductance signals.
In order to obtain a finite and all-electrically measurable CAR, the SC has to couple the edge states associated with the opposite edges of the sample. In our setup, this is achieved by inducing the superconductivity into the metallic bulk modes. The latter has been modeled by a SC-QSHI hybrid system, in which the SC induces superconductivity and, at the same time, a high doping into the QSHI. The induced doping relies on a clean interface between the SC and the QSHI and might cause considerable experimental effort. For example, first measurements on proximity coupled 2D TIs did not reveal high dopings in the hybrid systems [Knez12, Hart14, Pribiag15]. A possible work around would be to use other mechanisms to couple the edge states at opposite boundaries. In HgTe/CdTe QWs one could locally decrease the thickness of the QW beneath the SC in the tunneling region. Around the critical thickness, $d_c \approx 6.4$ nm, the system is in a semimetallic phase, for which already a small doping leads to metallic states. Another way, which

does not rely on doping the system, would be to directly couple the edge states by changing the geometry of the tunneling junction. For example, edging a constriction into the superconducting region introduces a local overlap of the edge states [Krueckl11], which does not compromise the spatial separation of the edge states in the leads.

In the next chapter, we will induce the superconducting condensate directly in the QSHI edge states, which will lead to the formation of the novel superconducting quantum spin Hall effect.

7. Superconducting quantum spin Hall effect

The combination of known physical systems often paved the way to construct new states and exotic physical effects. For example, the combination of SCs with normally conducting tunneling junctions form Josephson junctions [Josephson62] which nowadays are used as highly sensitive flux meters [Jaklevic64]. More recently, Fu and Kane [Fu08] opened the field of engineered topological SCs by predicting p-wave pairing in hybrid systems of helical states and conventional SCs.
In this chapter, which is based on [Reinthaler15], we induce superconductivity in the edge states of a QSHI. Adding the orbital effect of an in-plane magnetic field, we find the novel *superconducting quantum spin Hall effect*. The latter is characterized by edge states, which remain helical and protected against scalar disorder in finite in-plane magnetic fields. The system's giant orbital g-factor, which is a non-trivial consequence of the $U(1)$-symmetry breaking, makes the edge states tunable by magnetic fields well below the critical field of the SC. The resulting gapless superconductivity and strong spin polarization can be used to detect the superconducting QSH effect by its density of states (DOS) or by its unique transport properties: a non-monotonic excess current and a zero-bias conductance peak splitting.
The magnetic field and the QSHI, which is realized in a 3D TI thin film, are described in section 7.1. The excitation spectrum and the edge states on the semi-infinite half plane are discussed in section 7.2. First, sections 7.2.1 and 7.2.2 provide a detailed description of the chosen boundary conditions and of the analytical solution of the problem. The main results of these calculations are then highlighted in sections 7.2.3, where we discuss the giant g-factor and gap closing, and 7.2.4, which links the protection of the edge states to symmetry. Finally, in section 7.3, we propose feasible experiments to test our predictions.

7.1. Specification of the quantum spin Hall insulator-superconductor hybrid structure

7.1.1. In-plane magnetic field in the hybrid structure

In this section, we determine the vector potential A_x associated with an external in-plane magnetic field, taking into account its screening by a diamagnetic current in the SC. Like in section 3.2.2, we introduce a hybrid system of a QSHI and a SC, the interface of which is lying in the $z = 0$ plane. The profile of this system is sketched in Fig. 7.1. We assume the in-plane magnetic field B_y to be constant and to point in y-direction, which can be most conveniently formulated in the London gauge (3.41)

$$\boldsymbol{A} = A_x(z)\hat{x}. \tag{7.1}$$

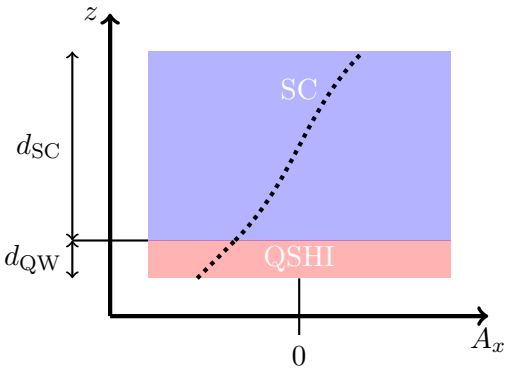

Figure 7.1.: Geometry of SC-QSHI hybrid structure. The dashed curve shows the z-dependence of the vector potential in Eq. (7.4). Adapted from the supplementary material of [Reinthaler15].

This ensures a real pair potential, so that the screening current density can be described by the London equation (3.48). Ampère's law then yields for our geometry

$$\partial_z^2 A_x(z) = \mu_0 \frac{e^2 n_{\mathrm{SC}}}{m^*} A_x(z) = \frac{1}{\lambda_{\mathrm{L}}^2} A_x(z), \tag{7.2}$$

where the London length λ_{L} is defined by Eq. (3.51) in terms of the vacuum permeability μ_0, the effective electron mass m^* and the density of the Cooper pairs in the SC n_{SC}. The boundary conditions to Eq. (7.2) are symmetric with respect to the applied field

$$\partial_z A_x(z=0) = B_y, \qquad \partial_z A_x(z=d_{\mathrm{SC}}) = B_y. \tag{7.3}$$

Here, d_{SC} is the thickness of the SC in z-direction. Consequently, the solution of this boundary problem is anti-symmetric with respect to the middle of the SC:

$$A_x(z) = B_y \lambda_{\mathrm{L}} \frac{\sinh\left[\frac{1}{\lambda_{\mathrm{L}}}\left(z - \frac{d_{\mathrm{SC}}}{2}\right)\right]}{\cosh\left[\frac{d_{\mathrm{SC}}}{2\lambda_{\mathrm{L}}}\right]}, \qquad 0 \le z \le d_{\mathrm{SC}}. \tag{7.4}$$

By continuity, the vector potential in the QSHI is

$$A_x(z) = B_y z + A_x(0^+) = B_y z - B_y \lambda_{\mathrm{L}} \tanh \frac{d_{\mathrm{SC}}}{2\lambda_{\mathrm{L}}}, \qquad -d_{\mathrm{QW}} \le z \le 0, \tag{7.5}$$

where the first term is the vector potential of the external field and $A_x(0^+)$ is the solution (7.4) at the surface $z = 0$. Since, for typical SC-QSHI structures, the thickness of the QSHI $d_{\mathrm{QW}} \ll \lambda_{\mathrm{L}} \tanh\left(d_{\mathrm{SC}}/2\lambda_{\mathrm{L}}\right)$, we can approximate Eq. (7.5) by a constant

$$A_x(z) \approx A_x(0^+) = -B_y \lambda_{\mathrm{L}} \tanh \frac{d_{\mathrm{SC}}}{2\lambda_{\mathrm{L}}}, \qquad -d_{\mathrm{QW}} \le z \le 0. \tag{7.6}$$

The vector potential inside the QSHI can thus be tuned by the parameters of the SC, particularly by its geometry. We will rely on our choice of a real pair potential in the following calculations.

In this sense, the solutions (7.4) to (7.6) are unique and may not be changed by an arbitrary gauge potential.

7.1.2. 3D to 2D crossover

The physics we discuss in the following relies on the combination of superconductivity with the helical edge states of a QSHI. Our results should therefore be applicable for any realization of the QSH phase, like, e.g., HgTe/CdTe QWs [Bernevig06] or inverted type-II semiconductors [Liu08]. For an explicit model, we choose thin films of 3D TIs [Shan10, Lu10, Liu10b].
To motivate this, let us have a short look at the tight binding (TB) dispersion in a 3D TI thin film in the ribbon geometry. To be specific, we assume the 3D TI to be described by the Hamiltonian for Bi_2X_3 (X = Se or Te) in the orbital basis $(|P1_z^+,\uparrow\rangle, |P2_z^-,\uparrow\rangle, |P1_z^+,\downarrow\rangle, |P2_z^-,\downarrow\rangle)$ [Zhang09, Liu10a]

$$\begin{aligned}
\mathcal{H}_{\mathrm{3DTI}} &= \begin{pmatrix} \epsilon(\boldsymbol{k})+\mathcal{M}(\boldsymbol{k}) & \mathcal{B}(k_z) & 0 & \mathcal{A}(k_x,k_y)(k_x-\mathrm{i}k_y) \\ \mathcal{B}(k_z) & \epsilon(\boldsymbol{k})-\mathcal{M}(\boldsymbol{k}) & \mathcal{A}(k_x,k_y)(k_x-\mathrm{i}k_y) & 0 \\ 0 & \mathcal{A}(k_x,k_y)(k_x+\mathrm{i}k_y) & \epsilon(\boldsymbol{k})+\mathcal{M}(\boldsymbol{k}) & -\mathcal{B}(k_z) \\ \mathcal{A}(k_x,k_y)(k_x+\mathrm{i}k_y) & 0 & -\mathcal{B}(k_z) & \epsilon(\boldsymbol{k})-\mathcal{M}(\boldsymbol{k}) \end{pmatrix}, \\
\epsilon(\boldsymbol{k}) &= C_0 + C_1 k_z^2 + C_2(k_x^2+k_y^2) \\
\mathcal{M}(\boldsymbol{k}) &= M_0 + M_1 k_z^2 + M_2(k_x^2+k_y^2) \\
\mathcal{A}(k_x,k_y) &= A_0 + A_2(k_x^2+k_y^2) \\
\mathcal{B}(k_z) &= B_0 + B_1 k_z.
\end{aligned} \tag{7.7}$$

We discretize the Hamiltonian on a square lattice according to appendix B. The ribbon is infinite in x-direction. N_y and N_z give the number of lattice points in y- and z-direction, respectively. While N_y is large, N_z gives the thickness of the thin film. To identify the qualitative behavior, we choose the unit-less toy parameters

$$A_0 = B_0 = M_1 = M_2 = 1, \quad M_0 = -1, \quad C_0 = A_2 = B_1 = C_1 = C_2 = 0, \quad a = 1 \tag{7.8}$$

where a is the lattice constant of the TB discretization. Further, the Fermi energy is at the charge neutrality point ($C_0 = 0$), the valence and the conduction band are symmetric ($C_1 = C_2 = 0$) and terms of the order of $\boldsymbol{k}^3$ and k_z are disregarded. The formation of edge states out of the surface states is presented in Fig. 7.2, where the TB dispersion is plotted for $N_y = 40$ and varying N_z. The color code symbolizes the weight of the state on the first and last 10% of lattice sites in y-direction. For $N_z = 10$ in Fig. 7.2a, the quadratic bulk states are connected by linearly dispersing surface states. The gap in the surface states is caused by hybridization of the states at the top ($z = N_z$) and bottom ($z = 1$) surface, in analogy to the mini-gap in the edge state spectrum in section 2.3.3. When the film thickness becomes thinner in Figs. 7.2b and 7.2c, the surface states gap out and a pair of strongly localized edge states appears.
The low energetic behavior of 3D TIs can be described in an effective model for the linearly dispersing surface states [Fu07b, Liu10a]

$$H_{t,b} \approx \pm v_{\mathrm{F}}(p_x\sigma_x + p_y\sigma_y), \tag{7.9}$$

where the top (t) and bottom (b) surface have opposite helicity. v_{F} is the Fermi velocity and σ_i are the Pauli matrices in spin basis. The Peierls' substitution $\boldsymbol{p} \to \hbar\boldsymbol{k} + e\boldsymbol{A}$ includes the magnetic vector potential. For the in-plane magnetic field of section 7.1.1, this specifically

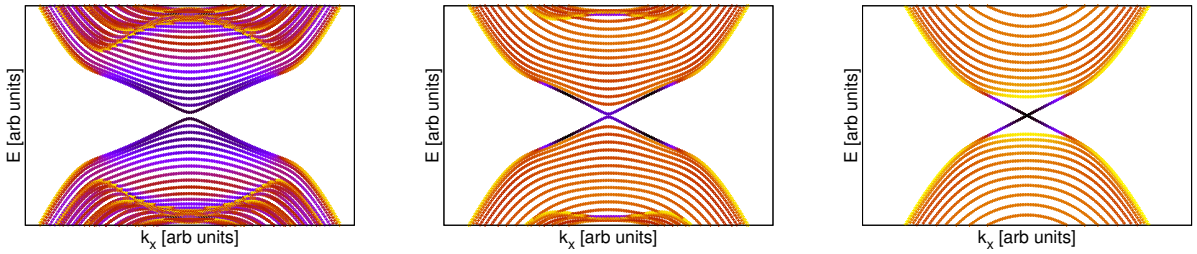

(a) $N_z = 10$ (b) $N_z = 5$ (c) $N_z = 3$

Figure 7.2.: The TB dispersions of Hamiltonian (7.7) show a 3D to 2D crossover when N_z is decreased. The color code gives the localization in y-direction: the darker the color the stronger localized are the states to the edges at $y = 1$ and $y = N_y$. $N_y = 40$ and the rest of the parameters has been chosen according to Eq. (7.8).

results in $\boldsymbol{p} \to (\hbar k_x + eA_x, \hbar k_y)^T$. The hybridization of the surface states can be introduced by the coupling strength Γ, so that the effective Hamiltonian for the QSHI takes the form

$$\begin{aligned} H_{\text{QSHI}} &= \begin{pmatrix} -\mu\sigma_0 + H_t & \Gamma\sigma_0 \\ \Gamma\sigma_0 & -\mu\sigma_0 + H_b \end{pmatrix} \\ &= -\mu\tau_0\sigma_0 + v_{\text{F}} p_x \tau_z \sigma_x + v_{\text{F}} p_y \tau_z \sigma_y + \Gamma\tau_x\sigma_0. \end{aligned} \tag{7.10}$$

The Pauli matrices τ_i refer to the top and bottom surface. The latter can be interpreted as a pseudo-spin degree of freedom and is treated like the sub-bands in the basis of the BHZ model (2.58). In Eq. (7.10) we assume that the chemical potential μ is the same for both surfaces. H_{QSHI} coincides, up to a unitary transformation, with the Hamiltonian derived by projecting Eq. (7.7) onto the low energetic states in [Lu10]. Since we are interested in the vicinity of the $\boldsymbol{p} = 0$ point, we only keep the terms which are constant or linear in $\boldsymbol{p}$.
The low energy behavior of HgTe/CdTe QWs can be similarly described by only considering the constant and linear in k terms in the BHZ Hamiltonian (2.59) [Schmidt09], resulting in a Hamiltonian which is closely related to Eq. (7.10). In H_{QSHI}, the coupling energy Γ takes the role of the bulk gap M. In contrast to the thin film Hamiltonian (7.10), the terms of the BHZ model that are linear in k do not couple the real spin (σ_i) but the pseudo-spin in form of the sub-bands (τ_i). Nevertheless, we have explicitly calculated in section 3.2.4 that both models lead to triplet pairing terms, making our results for the 3D TI thin film applicable to general superconducting QSHIs.

7.1.3. Bogoliubov-de Gennes Hamiltonian and symmetries

When the SC of Fig. 7.1 induces the pair potential $\tilde{\Delta}$, the system can be described in the Nambu basis

$$\left(b_{\boldsymbol{k}t\uparrow}, b_{\boldsymbol{k}t\downarrow}, b_{\boldsymbol{k}b\uparrow}, b_{\boldsymbol{k}b\downarrow}, b^\dagger_{-\boldsymbol{k}t\uparrow}, b^\dagger_{-\boldsymbol{k}t\downarrow}, b^\dagger_{-\boldsymbol{k}b\uparrow}, b^\dagger_{-\boldsymbol{k}b\downarrow} \right), \tag{7.11}$$

where the operators $b_{\boldsymbol{k}\tau\sigma}$ are defined in Eq. (3.53). The additional pseudo spin τ again refers to the top (t) and bottom (b) surface state. The BdG Hamiltonian reads

$$\begin{aligned} H_{\mathrm{BdG}}(\boldsymbol{k}) &= \begin{pmatrix} H_{\mathrm{QSHI}}(\boldsymbol{k}) & \mathrm{i}\tilde{\Delta}\tau_0\sigma_y \\ -\mathrm{i}\tilde{\Delta}\tau_0\sigma_y & -H^*_{\mathrm{QSHI}}(-\boldsymbol{k}) \end{pmatrix} \\ &= \hbar v_{\mathrm{F}} k_x \pi_0 \tau_z \sigma_x + v_{\mathrm{F}} e A_x \pi_z \tau_z \sigma_x + \hbar v_{\mathrm{F}} k_y \pi_z \tau_z \sigma_y \\ &\quad - \mu \pi_z \tau_0 \sigma_0 + \Gamma \pi_z \tau_x \sigma_0 - \tilde{\Delta} \pi_y \tau_0 \sigma_y, \end{aligned} \tag{7.12}$$

where we introduced the Pauli matrices in particle-hole space (π_i). Here and in the following, we restrict our discussion to real $\tilde{\Delta}$, in accordance with the gauge (7.1). Since the thickness of the QSHI is much smaller than the coherence length of the superconductor (3.46), we assume $\tilde{\Delta}$ to be the same for the top and bottom surface, in accordance with the discussion in section 3.2.2. Further, we assume that the induced superconductivity does not notably dope the QSHI, which coincides with the case of a dirty interface between the QSHI and the SC, as discussed in section 3.2.3. Although the explicit form of the induced pair potential is purely s-wave, we found in section 3.2.4 that the combination with spin-momentum locking induces effective triplet pairing contributions.

Note that the term proportional to the magnetic vector potential A_x has a different structure in particle-hole space than that proportional to k_x. The reason can be understood from the BdG formalism. The latter describes the superconductor as a system composed of electron- and hole-like excitations[1]. The charge q of the electron- and hole-like excitations is opposite, resulting in a qualitatively different influence of the magnetic vector potential on the two sub-systems. This difference between the superconducting and normal QSHI has striking consequences in the response to the in-plane magnetic field, as will be shown in section 7.2.3.

The relevant symmetry operations for our system are time-reversal symmetry (TRS), particle-hole symmetry (PHS) and the combination of time-reversal and particle-hole symmetry (TPS). TRS has been introduced in section 2.1. In the Nambu basis (7.11), the time-reversal operator acts according to

$$\hat{\Theta} = -\mathrm{i}\pi_0\tau_0\sigma_y\hat{K}, \quad \text{with} \quad \hat{\Theta} H_{\mathrm{BdG}}(\boldsymbol{A})\hat{\Theta}^{-1} = H_{\mathrm{BdG}}(-\boldsymbol{A}). \tag{7.13}$$

As expected, a finite magnetic vector potential breaks TRS[2]. In the same way, one finds for the PHS, which has been discussed in the context of the BdG formalism in section 3.1.3,

$$\hat{C} = -\pi_x\tau_0\sigma_0\hat{K}, \quad \text{with} \quad \hat{C} H_{\mathrm{BdG}}(\boldsymbol{A})\hat{C}^{-1} = -H_{\mathrm{BdG}}(\boldsymbol{A}). \tag{7.14}$$

[1] Throughout this chapter, when we talk about hole-like excitations, we will always refer to the missing electron picture introduced in appendix D. In this sense, an incoming spin-↑ electron is Andreev reflected as an empty electronic state with spin-↓.

[2] Note that also an imaginary pair potential apparently breaks TRS. In this case, the Hamiltonian contains the term

$$-|\tilde{\Delta}| \sin\phi \pi_x\tau_0\sigma_y \xrightarrow{\hat{\Theta}} +|\tilde{\Delta}| \sin\phi \pi_x\tau_0\sigma_y.$$

This can be understood by Eq. (3.40), which connects the phase of the pair potential to the gauge of the magnetic vector potential. In the case that the gauge corresponds to a zero magnetic field, the TRS breaking is an artifact and can be cured by a redefinition of $\hat{\Theta}$. Anyway, throughout this chapter, we work in the London gauge (3.41), which ensures real $\tilde{\Delta}$.

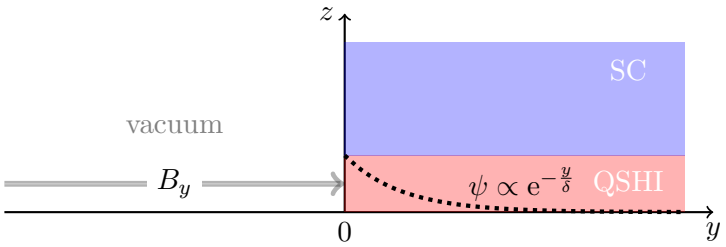

Figure 7.3.: Sketch of the semi-infinite superconducting QSHI as cut in the $y-z$-plane. The system is assumed to be infinitely long in x-direction and covers the half space $y \geq 0$, leading to localized edge states ψ (dotted line), see Eq. (7.21).

The operator and action of TPS can be inferred from the above to be

$$\hat{X} := \hat{\Theta}\hat{C} = \mathrm{i}\pi_x\tau_0\sigma_y, \quad \text{with} \quad \hat{X}H_{\mathrm{BdG}}(\boldsymbol{A})\hat{X}^{-1} = -H_{\mathrm{BdG}}(-\boldsymbol{A}). \tag{7.15}$$

7.2. The edge states in the semi-infinite geometry

In this section, we solve H_{BdG} (7.12) on the semi-infinite half plane $y \geq 0$, which is depicted in Fig. 7.3. This geometry breaks translational invariance in y-direction and $k_y = -\mathrm{i}\partial_y$ is not conserved. In contrast, the system stretches infinitely in x-direction, so that k_x remains the only good momentum quantum number in the gauge (7.1). In the following, we will refer to k_x by k for simplicity of notation.

7.2.1. Boundary conditions

In order to confine the wave function at $y = 0$, we have to impose the correct boundary conditions. Simply setting the wave function to zero, $\psi|_{y=0} = 0$, does not work, because of the Dirac-like nature of the BdG Hamiltonian (7.12). Instead, imposing that the boundary conditions define the Hamiltonian as a hermitian operator within its domain, which here is the half plane, it was shown [Berry87, McCann04], that the most general boundary condition is given by the matrix equation

$$\psi|_{y=0} = M\psi|_{y=0}. \tag{7.16}$$

In the Nambu basis Eq. (7.11), the wave function ψ has 8 components:

$$\psi = \left(\psi_{\boldsymbol{p}t\uparrow}, \psi_{\boldsymbol{p}t\downarrow}, \psi_{\boldsymbol{p}b\uparrow}, \psi_{\boldsymbol{p}b\downarrow}, \psi^*_{-\boldsymbol{p}t\uparrow}, \psi^*_{-\boldsymbol{p}t\downarrow}, \psi^*_{-\boldsymbol{p}b\uparrow}, \psi^*_{-\boldsymbol{p}b\downarrow}\right)^T. \tag{7.17}$$

Consequently, M is given by an 8×8 unitary matrix, which meets the requirement $M^2 = 1$ and $\left[M, \hat{j}_y\right]_+ = 0$. The anti-commutation relation with the current operator in y-direction is equivalent to the condition that the current through the boundary vanishes

$$j_{y=0} = \langle\psi|\,\hat{j}_y\,|\psi\rangle\Big|_{y=0} = 0. \tag{7.18}$$

The confinement of the states can in general be enforced by opening an energy gap in the spectrum, which is assumed to rise to infinity at the boundary of the system. In a purely

2D Dirac system, the gap is induced by a magnetic term $\propto m_z\sigma_z$ [Berry87], which by itself breaks TRS. In the case of two hybridizing surface states, the gap opening can by achieved by the coupling terms $\propto \Gamma\sigma_0$. The latter conserve TRS, which is a fundamental symmetry of the underlying QSHI. One can understand this confinement by considering the physical nature of the surface states at the boundary: cutting the sample will leave a new surface, which connects the top and bottom surface states, leading to a strong hybridization and the opening of a gap. From Heisenberg's equation of motion, we find the current operator $\hat{j}_y = v_\mathrm{F}\pi_z\tau_z\sigma_y$ and write Eq. (7.18) explicitly as

$$\begin{aligned} j_{y=0} = \mathrm{i}v_\mathrm{F}\big(&-\psi^*_{\boldsymbol{p}t\uparrow}\psi_{\boldsymbol{p}t\downarrow} + \psi^*_{\boldsymbol{p}t\downarrow}\psi_{\boldsymbol{p}t\uparrow} + \psi^*_{\boldsymbol{p}b\uparrow}\psi_{\boldsymbol{p}b\downarrow} - \psi^*_{\boldsymbol{p}b\downarrow}\psi_{\boldsymbol{p}b\uparrow} \\ &+\psi_{-\boldsymbol{p}t\uparrow}\psi^*_{-\boldsymbol{p}t\downarrow} - \psi_{-\boldsymbol{p}t\downarrow}\psi^*_{-\boldsymbol{p}t\uparrow} - \psi_{-\boldsymbol{p}b\uparrow}\psi^*_{-\boldsymbol{p}b\downarrow} + \psi_{-\boldsymbol{p}b\downarrow}\psi^*_{-\boldsymbol{p}b\uparrow}\big) \overset{!}{=} 0, \end{aligned} \tag{7.19}$$

which can be solved by

$$\begin{aligned} \psi_{\boldsymbol{p}b\uparrow} = \psi_{\boldsymbol{p}t\downarrow}, \quad \psi_{\boldsymbol{p}b\downarrow} = -\psi_{\boldsymbol{p}t\uparrow}, \quad \psi^*_{-\boldsymbol{p}b\uparrow} = \psi^*_{-\boldsymbol{p}t\downarrow}, \quad \psi^*_{-\boldsymbol{p}b\downarrow} = -\psi^*_{-\boldsymbol{p}t\uparrow} \\ \Leftrightarrow \quad \psi = \pi_0\tau_y\sigma_y\psi \quad \Rightarrow \quad M = \pi_0\tau_y\sigma_y. \end{aligned} \tag{7.20}$$

As expected this boundary condition couples the top and bottom surface states and preserves TRS. Using the confinement (7.20) ensures that the applied magnetic field is the only term in our model, which breaks TRS.

7.2.2. Dispersion and spinors

Here, we present a detailed analytical calculation of the eigenstates for the interested reader. The main results, the giant orbital g-factor and the protection of the edge states are then recapitulated and discussed in sections 7.2.3 and 7.2.4, respectively.
To solve for the edge states in the bulk gap, we choose an ansatz, which decays exponentially away from the boundary for $y \geq 0$

$$\psi = \Phi_k \exp\left[\mathrm{i}kx - \frac{y}{\delta}\right]. \tag{7.21}$$

Plugging it into the stationary Schrödinger equation, $H_\mathrm{BHZ}\psi = E\psi$, we arrive at

$$\left[v_\mathrm{F}\hbar k\pi_0\tau_z\sigma_x + v_\mathrm{F}eA_x\pi_z\tau_z\sigma_x + \frac{\mathrm{i}\hbar v_\mathrm{F}}{\delta}\pi_z\tau_z\sigma_y - \mu\pi_z\tau_0\sigma_0 + \Gamma\pi_z\tau_x\sigma_0 - \tilde{\Delta}\pi_y\tau_0\sigma_y\right]\Phi_k = E\Phi_k. \tag{7.22}$$

At $y = 0$, where Eq. (7.20) holds, we use

$$\pi_z\tau_x\sigma_0\Phi_k = \pi_z\tau_x\sigma_0(\pi_0\tau_y\sigma_y)\Phi_k = \pi_z(\mathrm{i}\tau_z)\sigma_y\Phi_k \tag{7.23}$$

to cast the sum $(\mathrm{i}\hbar v_\mathrm{F}/\delta)\pi_z\tau_z\sigma_y + \Gamma\pi_z\tau_x\sigma_0$ into $(\Gamma + \hbar v_\mathrm{F}/\delta)\pi_z\tau_x\sigma_0$. Equating this term to zero, we find the decay length

$$\delta = -\frac{\hbar v_\mathrm{F}}{\Gamma} = \frac{\hbar v_\mathrm{F}}{|\Gamma|}. \tag{7.24}$$

The edge solution exists only for the inverted band structure with $\Gamma < 0$. Since the boundary condition (7.20) relates the top and bottom surface, the spinor Φ_k simplifies to

$$\Phi_k = (\chi_k, \mathrm{i}\sigma_y\chi_k, \xi_k, \mathrm{i}\sigma_y\xi_k)^T . \tag{7.25}$$

Now, we can reformulate the problem as a system of coupled linear equations

$$0 = [v_\mathrm{F}(\hbar k + eA_x)\sigma_x - (\mu + E)\sigma_0]\,\chi_k + \tilde{\Delta}\mathrm{i}\sigma_y\xi_k \tag{7.26a}$$
$$0 = [-v_\mathrm{F}(\hbar k + eA_x)\sigma_x - (\mu + E)\sigma_0]\,\mathrm{i}\sigma_y\chi_k + \tilde{\Delta}\mathrm{i}\sigma_y(\mathrm{i}\sigma_y)\xi_k \tag{7.26b}$$
$$0 = -\tilde{\Delta}\mathrm{i}\sigma_y\chi_k + [v_\mathrm{F}(\hbar k - eA_x)\sigma_x + (\mu - E)\sigma_0]\,\xi_k \tag{7.26c}$$
$$0 = -\tilde{\Delta}\mathrm{i}\sigma_y(\mathrm{i}\sigma_y)\chi_k + [-v_\mathrm{F}(\hbar k - eA_x)\sigma_x + (\mu - E)\sigma_0]\,\mathrm{i}\sigma_y\xi_k. \tag{7.26d}$$

Upon multiplication by $-\mathrm{i}\sigma_y$, Eqs. (7.26b) and (7.26d) correspond to Eqs. (7.26a) and (7.26c), respectively. We hence solve Eqs. (7.26a) and (7.26c) independently. From Eq. (7.26a), we find

$$\xi_k = \frac{1}{\tilde{\Delta}}\,[v_\mathrm{F}(\hbar k + eA_x)\sigma_z - \mathrm{i}(\mu + E)\sigma_y]\,\chi_k. \tag{7.27}$$

Plugging this into Eq. (7.26c), we arrive at

$$\begin{aligned} 0 &= \left[(2v_\mathrm{F}\hbar k\mu - 2v_\mathrm{F}eA_xE)\,\sigma_z - \left(v_\mathrm{F}^2(\hbar^2k^2 - e^2A_x^2) + \mu^2 - E^2 + \tilde{\Delta}^2\right)\mathrm{i}\sigma_y\right]\chi_k \quad |\cdot\,\mathrm{i}\sigma_y \\ 0 &= -\,(2v_\mathrm{F}\hbar k\mu - 2v_\mathrm{F}eA_xE)\,\sigma_x\chi_k + \left(v_\mathrm{F}^2(\hbar^2k^2 - e^2A_x^2) + \mu^2 - E^2 + \tilde{\Delta}^2\right)\sigma_0\chi_k \end{aligned} \tag{7.28}$$

so that χ_k must be an eigenstate to σ_x:

$$\chi_{ks} = (s, 1)^T , \quad s = \pm 1. \tag{7.29}$$

Finally, we can solve the excitation energy spectrum at the interface

$$E_\alpha^s = sv_\mathrm{F}eA_x + \alpha\sqrt{\tilde{\Delta}^2 + (\mu - sv_\mathrm{F}\hbar k)^2}, \tag{7.30}$$

where $\alpha = \pm 1$ designates conduction or valence bands. We will discuss the dispersion in detail in section 7.2.3.
The normalized solutions can be found from Eq. (7.21) together with (7.25), (7.27) and (7.29) to be

$$\psi_{ks}^\alpha(y) = \frac{\exp\left[\mathrm{i}kx - y\frac{|\Gamma|}{\hbar v_\mathrm{F}}\right]}{N}\begin{pmatrix} u_{ks}^\alpha\phi_s \\ v_{ks}^\alpha\phi_{-s}\end{pmatrix} \tag{7.31}$$

The solution decouples in a part which comes from the particle solution $\exp\left[\mathrm{i}kx - y\frac{|\Gamma|}{\hbar v_\mathrm{F}}\right]\phi_s$ with the spinor

$$\phi_s = (s, 1, 1, -s)^T \tag{7.32}$$

and a part containing the superconducting coherence factors:

$$u_{ks}^{\alpha} = \frac{1}{\tilde{N}(\alpha,k,s)} = \frac{1}{\sqrt{2}} \frac{|\tilde{\Delta}|}{\sqrt{\tilde{\Delta}^2 + (\mu - sv_{\mathrm{F}}\hbar k)^2 + \alpha(\mu - sv_{\mathrm{F}}\hbar k)\sqrt{\tilde{\Delta}^2 + (\mu - sv_{\mathrm{F}}\hbar k)^2}}} \tag{7.33a}$$

$$\begin{aligned} v_{ks}^{\alpha} &= \frac{1}{\tilde{\Delta}\tilde{N}(\alpha,k,s)} \left(-v_{\mathrm{F}}\hbar k + s\mu + \alpha s\sqrt{\tilde{\Delta}^2 + (\mu - sv_{\mathrm{F}}\hbar k)^2} \right) \\ &= \frac{1}{\sqrt{2}} \frac{s\alpha|\tilde{\Delta}|}{\sqrt{\tilde{\Delta}^2 + (\mu - sv_{\mathrm{F}}\hbar k)^2 - \alpha(\mu - sv_{\mathrm{F}}\hbar k)\sqrt{\tilde{\Delta}^2 + (\mu - sv_{\mathrm{F}}\hbar k)^2}}}. \end{aligned} \tag{7.33b}$$

The coherence factors are normalized according to $|u_{ks}^{\alpha}|^2 + |v_{ks}^{\alpha}|^2 = 1$ by setting

$$\tilde{N}^2(\alpha,k,s) = \frac{2}{\tilde{\Delta}^2} \left[\tilde{\Delta}^2 + (\mu - sv_{\mathrm{F}}\hbar k)^2 + \alpha(\mu - sv_{\mathrm{F}}\hbar k)\sqrt{\tilde{\Delta}^2 + (\mu - sv_{\mathrm{F}}\hbar k)^2} \right]. \tag{7.34}$$

Further, the normalization over the half space $y > 0$ and over the dimensions of the spinor takes the form

$$N^2 = \int_0^{\infty} \mathrm{d}y \, \exp\left[-2y \frac{|\Gamma|}{\hbar v_{\mathrm{F}}} \right] (\phi_s^* \cdot \phi_s) = (2 + 2s^2) \frac{\hbar v_{\mathrm{F}}}{2|\Gamma|} = 2\frac{\hbar v_{\mathrm{F}}}{|\Gamma|}. \tag{7.35}$$

In the following, we will analyze how the eigenstates behave under the symmetry operations of section 7.1.3. For this, it is useful to reformulate the eigenstates in an energy dependent form and to identify the quasi-particle character of the states:

Excitation energy representation of the states

We solve the dispersion (7.30) for

$$k_s^{\beta}(E) = \frac{1}{v_{\mathrm{F}}\hbar} \left(s\mu + \beta\sqrt{(E - sev_{\mathrm{F}}A_x)^2 - \tilde{\Delta}^2} \right), \quad \beta = \pm 1. \tag{7.36}$$

By squaring the dispersion one looses the information about the sign of α, so that β is not in one-to-one correspondence to α.[3] The correct relation can be found by checking the consistency of the equation

$$E_s^{\alpha} = sv_{\mathrm{F}}eA_x + \alpha\sqrt{\tilde{\Delta}^2 + (\mu - sv_{\mathrm{F}}\hbar k_s^{\beta}(E))^2} \stackrel{!}{=} E, \tag{7.37}$$

where we fix E and β. The result is independent of β:

$$E_s^{\alpha} = sv_{\mathrm{F}}eA_x + \alpha|E - sev_{\mathrm{F}}A_x| \quad \Rightarrow \quad \alpha = \begin{cases} 1, & E > sev_{\mathrm{F}}A_x \\ -1, & E < sev_{\mathrm{F}}A_x \end{cases} \tag{7.38}$$

[3] Although α and β are not in one-to-one correspondence, both are related to the quasi-particle character of the solution, as we will find later in Eq. (7.42). Throughout this chapter, we will always use α (β) when we refer to the momentum (energy) representation.

and α is fixed by energetic constraints. In total, the energy dependent formulation takes the form

$$\psi^{\beta}_{Es}(y) = \frac{\exp\left[\mathrm{i}k^{\beta}_{Es}x - y\frac{|\Gamma|}{\hbar v_{\mathrm{F}}}\right]}{N}\begin{pmatrix} u^{\beta}_{Es}\phi_s \\ v^{\beta}_{Es}\phi_{-s}\end{pmatrix}. \tag{7.39}$$

The coherent factors in the excitation energy representation

$$u^{\beta}_{Es} = \frac{1}{\sqrt{2}}\frac{\tilde{\Delta}}{\sqrt{(E-sev_{\mathrm{F}}A_x)^2 - s\beta(E-sev_{\mathrm{F}}A_x)\sqrt{(E-sev_{\mathrm{F}}A_x)^2-\tilde{\Delta}^2}}} \tag{7.40a}$$

$$v^{\beta}_{Es} = \frac{1}{\sqrt{2}}\frac{s\tilde{\Delta}\,\mathrm{sign}\left[E-sev_{\mathrm{F}}A_x\right]}{\sqrt{(E-sev_{\mathrm{F}}A_x)^2 + s\beta(E-sev_{\mathrm{F}}A_x)\sqrt{(E-sev_{\mathrm{F}}A_x)^2-\tilde{\Delta}^2}}}. \tag{7.40b}$$

are related by

$$v^{\beta}_{Es} = s\ \mathrm{sign}\left[E-sev_{\mathrm{F}}A_x\right]u^{-\beta}_{Es}, \tag{7.41}$$

indicating that the sign of β determines the carrier as electron- or hole-like.

Quasi-particle character of the states

A full estimate of the quasi-particle character P can be obtained by the expectation value of the operator $\pi_z\tau_0\sigma_0$:

$$\begin{aligned} P^{\beta}_{Es} &= \left\langle \psi^{\beta}_{Es}\right| \pi_z\tau_0\sigma_0 \left|\psi^{\beta}_{Es}\right\rangle = \left(u^{\beta}_{Es}\right)^* u^{\beta}_{Es} - \left(v^{\beta}_{Es}\right)^* v^{\beta}_{Es} = s\beta\frac{\sqrt{(E-sev_{\mathrm{F}}A_x)^2-\tilde{\Delta}^2}}{E-sev_{\mathrm{F}}A_x} \\ P^{\alpha}_{ks} &= \langle\psi^{\alpha}_{ks}|\,\pi_z\tau_0\sigma_0\,|\psi^{\alpha}_{ks}\rangle \quad = (u^{\alpha}_{ks})^*\,u^{\alpha}_{ks} - (v^{\alpha}_{ks})^*\,v^{\alpha}_{ks} = -\alpha\frac{\mu - s\hbar v_{\mathrm{F}}k}{\sqrt{\tilde{\Delta}^2+(\mu-s\hbar v_{\mathrm{F}}k)^2}}, \end{aligned} \tag{7.42}$$

showing how the quasi-particle character depends on α (β), s and k (E). At the Fermi points, $k_{\mathrm{F}} = \frac{s\mu}{\hbar v_{\mathrm{F}}}$ ($E_{\mathrm{F}} = E^s_{\alpha}(k_{\mathrm{F}}) = sv_{\mathrm{F}}eA_x + \alpha\tilde{\Delta}$), one finds

$$P^{\beta}_{E_{\mathrm{F}}s} = P^{\alpha}_{k_{\mathrm{F}}s} = 0, \tag{7.43}$$

i.e., electron- and hole-like states are perfectly mixed at the band edges. Far away from the quasi-particle gap, we get ($k=\kappa|k|,\ E=\epsilon|E|$, where $\kappa=\epsilon=\pm1$)

$$\lim_{|E|\to\infty} P^{\beta}_{Es} = \epsilon s\beta, \quad \lim_{|k|\to\infty} P^{\alpha}_{ks} = \kappa s\alpha, \tag{7.44}$$

where $P\to 1$ ($P\to -1$) indicates electrons (holes). Especially, we find that, for fixed energy E, magnetic vector potential A_x and spin s, the quasi-particle character is determined by α (β) in the momentum (energy) representation.

Symmetry relations for the edge states

Here, we finally analyze, how TRS (7.13), PHS (7.14) and TPS (7.15) act on the edge state (7.39). This knowledge will help us to understand the edge states' protection against backscattering in section 7.2.4. Since the spinors are real, the complex conjugation simply inverts the propagation in x-direction:

$$\exp\left[\mathrm{i}k^{\beta}_{Es}(A_x)x\right] \xrightarrow{\hat{K}} \exp\left[-\mathrm{i}k^{\beta}_{Es}(A_x)x\right] = \exp\left[\mathrm{i}k^{-\beta}_{E-s}(-A_x)x\right] = \exp\left[\mathrm{i}k^{-\beta}_{-E-s}(A_x)x\right], \quad (7.45)$$

where the last two equalities are obtained by comparison with Eq. (7.36). The last equality especially holds, because the excitation energy E and the vector potential A_x enter the solution in a symmetric way. The coherence factors (7.40a) and (7.40b) show an analogous behavior

$$u^{\beta}_{Es}(A_x) = u^{-\beta}_{E-s}(-A_x) = u^{-\beta}_{-E-s}(A_x), \quad v^{\beta}_{Es}(A_x) = -v^{-\beta}_{E-s}(-A_x) = -v^{-\beta}_{-E-s}(A_x). \quad (7.46)$$

Considering TRS, the particle spinor transform as

$$\phi_s = (s,1,1,-s)^T \xrightarrow{\hat{\Theta}} -\mathrm{i}\tau_0\sigma_y(s,1,1,-s)^T = (-1,s,s,1)^T = s\phi_{-s} \quad (7.47)$$

and with Eqs. (7.45) and (7.46) one obtains

$$\psi^{\beta}_{Es}(A_x) \xrightarrow{\hat{\Theta}} s\psi^{-\beta}_{E-s}(-A_x). \quad (7.48)$$

For preserved TRS at $A_x = 0$, this resembles the Kramer's partner relation (2.19). Similarly, one obtains the relations for PHS and TPS

$$\psi^{\beta}_{Es} \xrightarrow{\hat{C}} -s\,\mathrm{sign}\left[E - sv_{\mathrm{F}}eA_x\right]\psi^{-\beta}_{-E-s} \quad (7.49)$$

$$\psi^{\beta}_{Es} \xrightarrow{\hat{X}} \mathrm{sign}\left[E - sv_{\mathrm{F}}eA_x\right]\exp\left[\mathrm{i}(k^{\beta}_{Es} - k^{-\beta}_{Es})x\right]\pi_z\tau_0\sigma_0\psi^{-\beta}_{Es}. \quad (7.50)$$

The prefactor in Eq. (7.50)

$$\exp\left[\mathrm{i}(k^{\beta}_{Es} - k^{-\beta}_{Es})x\right] = \exp\left[\mathrm{i}\frac{2\beta\sqrt{(E - sev_{\mathrm{F}}A_x)^2 - \tilde{\Delta}^2}}{\hbar v_{\mathrm{F}}}x\right] \quad (7.51)$$

simplifies to a phase factor for propagating solutions, for which $(E - sv_{\mathrm{F}}eA_x)^2 > \tilde{\Delta}^2$. In contrast to Eqs. (7.48) and (7.49), the relation for TPS is not broken by a finite vector potential and connects states at the same energy. The price is the x-dependent phase and a transformation in particle-hole space. It is interesting to note that both, $\hat{C}$ and $\hat{X}$, invert the quasi-particle character (7.42) of the states.

7.2.3. Giant orbital g-factor

In Eq. (7.30), we found the excitation energy spectrum of the edge states

$$\begin{aligned} E^s_\alpha &= sv_{\mathrm{F}}eA_x + \alpha\sqrt{\tilde{\Delta}^2 + (\mu - sv_{\mathrm{F}}\hbar k)^2} \\ &= -sg_*\mu_{\mathrm{B}}B_y + \alpha\sqrt{\tilde{\Delta}^2 + (\mu - s\hbar v_{\mathrm{F}}k)^2}. \end{aligned} \quad (7.52)$$

In section 3.1.5 and especially in Eq. (3.48), we discussed that a magnetic vector potential generates the momentum of the superconducting condensate. Hence, the term $\propto sA_x$ is to be interpreted as the locking of the spin to the momentum of the superconducting condensate. In consequence, the SC restores and stabilizes the helicity of the edge states and the eigenenergies are characterized by the conserved spin s, even in finite in-plane magnetic fields. We will therefore refer to these edge states as the *superconducting quantum spin Hall effect*.
In the second line of Eq. (7.52), we used the dependence of the vector potential in the QSHI in Eq. (7.6) and introduced the effective g-factor

$$g_* = \frac{2mv_\mathrm{F}}{\hbar}\lambda_\mathrm{L}\tanh\frac{d_\mathrm{SC}}{2\lambda_\mathrm{L}} \tag{7.53}$$

as well as the Bohr magneton μ_B. Eq. (7.52) shows that the orbital effect takes the form similar to the Zeeman spin splitting in thin superconducting films [Meservey70]. However, in the superconducting QSH effect the effective g-factor can be tuned and engineered by an appropriate choice of the material and structure parameters, i.e., the edge state velocity v_F, the thickness of the SC d_SC and the London length λ_L. Let us estimate g_* for Bi_2X_3 (where X=Se, Te) and HgTe-based structures which typically have $\hbar v_\mathrm{F} \approx 300$ meV nm [Liu10a, Brüne11] and, consequently, $g_* \approx 7.9\ \mathrm{nm}^{-1} \times \lambda_\mathrm{L}\tanh(d_\mathrm{SC}/2\lambda_\mathrm{L})$. For the commonly used SC Nb with $\lambda_\mathrm{L} \approx 50$ nm [Maxfield65] and nanoscale thicknesses ranging from $d_\mathrm{SC} = 50$ nm up to 250 nm, we obtain $g_* \approx 200 - 400$, which exceeds the electron spin g-factor by at least two orders of magnitude.
Note, that the giant g-factor is not a trivial consequence of the helical edge states of the non-superconducting QSHI. The orbital effect of A_x enters via the Peierls substitution and gauges the wave function by a complex phase factor. In a non-superconducting QSH system, this phase factor cannot have any physical consequences due to Noether's theorem. In terms of the energy dispersion, the orbital effect of A_x only causes a shift of the band structure in the magnetic Brillouin zone ($\tilde{p}_x = p_x + qA_x$) and can be taken out of the calculations by a simple redefinition of the lattice momentum ($\tilde{p}_x - qA_x$). This is not possible in superconducting systems, which break $U(1)$-gauge symmetry. In this case, the vector potential A_x couples differently to electron- and hole-like states, due to their opposite charge q, allowing for non-trivial effects, which can be measured.
In conclusion, this novel effect is non-trivial and fundamentally relies on the interplay of the helical edge states with the superconducting condensate, which breaks $U(1)$-symmetry. As a direct consequence, we find that the orbital g-factor depends on λ_L and d_SC, i.e., on the parameters of the SC.

Gap closing

Exhibiting a giant orbital g-factor, the superconducting QSH effect does not require high magnetic fields to generate spin splitting, which we analyze in Fig. 7.4. At $\mu = A_x = \tilde{\Delta} = 0$, Eq. (7.52) describes a Dirac cone, which is double degenerate due to the redundancy of the BdG formalism. A finite chemical potential shifts the electron- and hole-like branches relatively to each other, so that the pair potential $\tilde{\Delta}$ opens a gap at the two Fermi points $\pm k_\mathrm{F} = \pm\mu/(\hbar v_\mathrm{F})$, cf. Fig. 7.4a for $A_x = B_y = 0$. Note that the Fermi points $\pm k_\mathrm{F}$ correspond to the opposite-spin states with $s = \pm 1$. Therefore, the magnetic field splits the states at different Fermi points, shifting them relatively to each other in energy, as depicted in Fig. 7.4b. The excitation gap vanishes in Fig. 7.4c, when the orbital energy scale matches the induced gap at $|A_x| = \tilde{\Delta}/(ev_\mathrm{F})$.

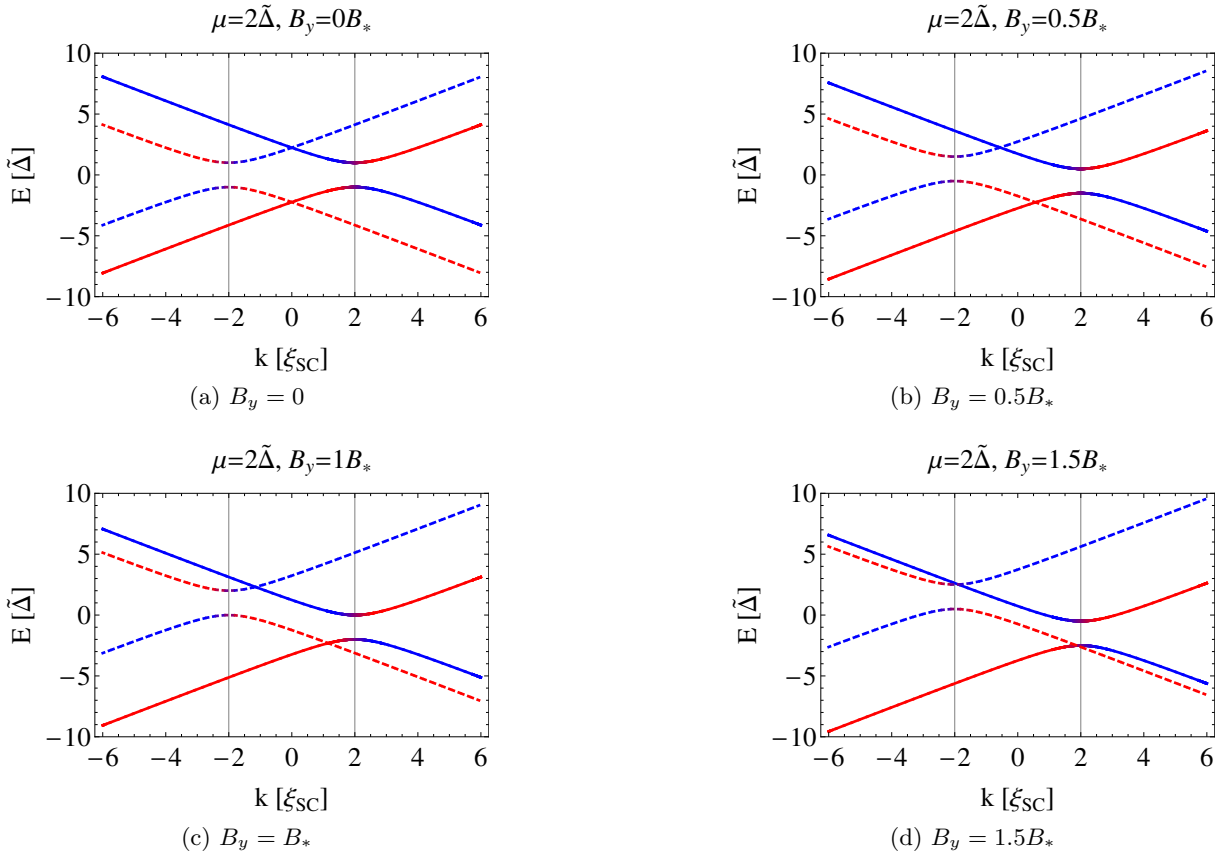

(a) $B_y = 0$ (b) $B_y = 0.5B_*$

(c) $B_y = B_*$ (d) $B_y = 1.5B_*$

Figure 7.4.: Excitation energy spectrum of the superconducting QSH effect for different in-plane magnetic fields. Solid and dashed curves correspond to the opposite spin states with $s = \pm 1$, respectively. Red and blue colors schematically indicate electron- and hole-like branches corresponding to those in the normal system. For $B_y = 0$, there is an excitation gap at the two Fermi points $\pm k_\mathrm{F}$ indicated by the vertical lines. For $B_y \neq 0$, the gap is reduced (b) and vanishes completely for $|B_y| = B_*$ (c). For $|B_y| > B_*$ (d) the spectrum remains gapless, albeit each spin branch separately has a gap at finite energies. Adapted from [Reinthaler15].

The magnetic field, at which the superconducting gap closes, takes the form

$$B_* = \frac{\tilde{\Delta}}{e v_\mathrm{F} \lambda_\mathrm{L} \tanh(d_\mathrm{SC}/2\lambda_\mathrm{L})} = \frac{\hbar}{e \xi_\mathrm{SC} \lambda_\mathrm{L} \tanh(d_\mathrm{SC}/2\lambda_\mathrm{L})}, \tag{7.54}$$

where ξ_SC is the coherence length introduced in Eq. (3.46). For the induced gap $\tilde{\Delta} \lessapprox 0.1$ meV [Maier12] and the Nb-structure parameters used above, $B_* \lessapprox 5.5$ mT is much smaller than the critical field of Nb. For $|B_y| > B_*$, the spectrum remains gapless, as can be observed in Fig. 7.4d. The branches for each spin polarization, however, remain gapped between the spin-dependent

band edges

$$E_{\pm} = sev_{\mathrm{F}}A_x \pm \tilde{\Delta}. \tag{7.55}$$

Zero energy modes

For $|B_y| > B_*$, see Eq. (7.54), there are always four states at zero excitation energy[4]. At the transition $|B_y| = B_*$, their number is reduced to two:

$$\psi_s^0(y) = \frac{\exp\left[\mathrm{i}sk_Fx - y\frac{|\Gamma|}{\hbar v_{\mathrm{F}}}\right]}{N}\begin{pmatrix}\phi_s\\ -\mathrm{sign}A_x\phi_{-s}\end{pmatrix}. \tag{7.56}$$

These states are equivalent to two Majorana zero modes, which are proposed to occur in p-wave superconductors [Kitaev01, Alicea12]. Indeed, defining $\eta = (1+\mathrm{sign}A_x)/2$, one can construct new states $\gamma_1 = \exp[\mathrm{i}\eta\pi/2](\psi_s^0 + \psi_{-s}^0)$ and $\gamma_2 = -\mathrm{i}\exp[\mathrm{i}\eta\pi/2](\psi_s^0 - \psi_{-s}^0)$ with the self-adjoint properties of emergent Majorana zero modes.

7.2.4. Protection against backscattering

In the following, we show that the superconducting edge states are protected against elastic scattering even in finite in-plane magnetic fields. To this end, we introduce the non-magnetic disorder potential $H_{\mathrm{dis}} = \mathcal{U}(x)\pi_z\tau_0\sigma_0$ and calculate the matrix element of H_{dis} between states with the same energy E:

$$\begin{aligned}\left\langle \psi_{Es_1}^{\beta_1}\right| H_{\mathrm{dis}} \left|\psi_{Es_2}^{\beta_2}\right\rangle =& \frac{\mathcal{U}(x)}{2}\exp\left[\mathrm{i}(k_{Es_2}^{\beta_2} - k_{Es_1}^{\beta_1})x\right]\\ &\cdot(1+s_1s_2)\left(\left(u_{Es_1}^{\beta_1}\right)^* u_{Es_2}^{\beta_2} - \left(v_{Es_1}^{\beta_1}\right)^* v_{Es_2}^{\beta_2}\right).\end{aligned} \tag{7.57}$$

The matrix element vanishes for the states with opposite spin projections $s_1 = -s_2$. This means the absence of backscattering that couples different Fermi points $k_{\mathrm{F}}^{\pm} = \pm\mu/\hbar v_{\mathrm{F}}$. This is true irrespective of the presence or absence of the magnetic field. Furthermore, there is no scattering between the states belonging to the same spin branch. For such states $s_1 = s_2 = s$, $\beta_1 = -\beta_2 = \beta$, and $(u_{Es}^{\beta})^* u_{Es}^{-\beta} = (v_{Es}^{\beta})^* v_{Es}^{-\beta}$, also yielding a vanishing matrix element (7.57). This can be interpreted as protection by the TPS, whose operator $\hat{X}$ has the same matrix structure as H_{dis}, leading to a generalized Kramers' theorem

$$\left\langle \psi_{Es}^{\beta}\right| \hat{X} \left|\psi_{Es}^{\beta}\right\rangle \propto \left\langle \psi_{Es}^{\beta}\right| \pi_z\tau_0\sigma_0 \left|\psi_{Es}^{-\beta}\right\rangle = 0. \tag{7.58}$$

However, TPS is not a rigorous symmetry of the underlying system in finite magnetic fields, for which H_{BdG} does not respect TPS, cf. Eq. (7.15). To better understand the protection against scalar disorder, note that the states at finite A_x can always be mapped to a system with an effectively vanishing vector potential but with a finite phase of the superconducting pair potential ϕ, cf. Eq. (3.40) and its discussion. In the approximation (7.6), the effect of the magnetic field is equivalent to a linearly varying phase $\phi(x) = (2e/\hbar)A_x\,x$, whose gradient generates a condensate flow with the momentum $2eA_x$. As we have mentioned in section 7.1.3, the full H_{BdG} does not conserve TRS for $\phi \neq 0$. Nevertheless, the gauge transformation shifts the TRS breaking terms from the single-particle part H_{QSHI} to the superconducting condensate.

[4] Note that two of the solutions are redundant because of the PHS in the BdG formalism.

In consequence, all single-particle processes, like electron reflection, cannot depend on A_x and are protected exactly as in the zero field situation. In contrast, all processes, which rely on the superconducting condensate, are influenced by the magnetic field.

Andreev reflection

Physically, the TPS protection means that the states with opposite β, i.e., opposite particle character cannot be converted into each other without being Andreev reflected, see, e.g., [Blonder82] and section 3.3.
In order to allow for Andreev reflection (AR) processes, we need to introduce a barrier between two regions of different induced pair potentials. Imagine a sharp interface between $\tilde{\Delta}_1$ at $x \leq 0$ and $\tilde{\Delta}_2$ at $x > 0$. For a state incoming from the left, the scattering problem can be written as

$$\psi^{\beta}_{Es}(\tilde{\Delta}_1) + {R_h}^s \psi^{-\beta}_{Es}(\tilde{\Delta}_1) + R^s_e \psi^{-\beta}_{E-s}(\tilde{\Delta}_1) = T^s_e \psi^{\beta}_{Es}(\tilde{\Delta}_2) + {T_h}^s \psi^{\beta}_{E-s}(\tilde{\Delta}_2), \tag{7.59}$$

where R^s_e and T^s_e are the amplitudes of electron reflection and electron tunneling processes with spin s. Analogously, ${R_h}^s$ and ${T_h}^s$ describe AR and crossed Andreev reflection (CAR). The barrier cannot couple branches with different s eigenvalue due to the orthogonality of the eigenstates. The solutions

$$\begin{aligned}
{T_h}^s &= R^s_e = 0 \\
{R_h}^s &= \frac{u^{\beta}_{Es}(\tilde{\Delta}_2) v^{\beta}_{Es}(\tilde{\Delta}_1) - u^{\beta}_{Es}(\tilde{\Delta}_1) v^{\beta}_{Es}(\tilde{\Delta}_2)}{u^{-\beta}_{Es}(\tilde{\Delta}_1) v^{\beta}_{Es}(\tilde{\Delta}_2) - u^{\beta}_{Es}(\tilde{\Delta}_2) v^{-\beta}_{Es}(\tilde{\Delta}_1)} \\
T^s_e &= \frac{u^{-\beta}_{Es}(\tilde{\Delta}_1) v^{\beta}_{Es}(\tilde{\Delta}_1) - u^{\beta}_{Es}(\tilde{\Delta}_1) v^{-\beta}_{Es}(\tilde{\Delta}_1)}{u^{-\beta}_{Es}(\tilde{\Delta}_1) v^{\beta}_{Es}(\tilde{\Delta}_2) - u^{\beta}_{Es}(\tilde{\Delta}_2) v^{-\beta}_{Es}(\tilde{\Delta}_1)},
\end{aligned} \tag{7.60}$$

show finite AR, while CAR and electron reflection are suppressed for a single pair of helical edge states [Adroguer10]. By virtue of Eq. (7.41), the solutions fulfill

$$T^s_e \overset{\tilde{\Delta}_1 = \tilde{\Delta}_2}{=} 1, \quad {R_h}^s \overset{\tilde{\Delta}_1 = \tilde{\Delta}_2}{=} 0. \tag{7.61}$$

N-SC junction

In the special case of a N-SC junction, the normal part of the junction is described by H_{BdG} with $\tilde{\Delta}_1 \to 0$. Defining $D_{Es} = E - s e v_{\mathrm{F}} A_x$ and using

$$\sqrt{D^2_{Es} + \tilde{\Delta}^2} \overset{\tilde{\Delta} \ll D_{Es}}{\approx} |D_{Es}| \left(1 - \frac{\tilde{\Delta}^2}{2 D^2_{Es}}\right), \tag{7.62}$$

we perform the limits

$$\begin{aligned}
\lim_{\tilde{\Delta}\to 0} u_{Es}^{\beta} &= \frac{1}{\sqrt{2}} \frac{\tilde{\Delta}}{\sqrt{D_{Es}^2(1 - s\beta\mathrm{sign}[D_{Es}]) + s\beta\mathrm{sign}[D_{Es}]\frac{\tilde{\Delta}^2}{2}}} \\
&= \begin{cases} 0, & \mathrm{sign}[D_{Es}]s\beta < 0 \\ 1, & \mathrm{sign}[D_{Es}]s\beta > 0 \end{cases} \\
\lim_{\tilde{\Delta}\to 0} v_{Es}^{\beta} &= \frac{s\ \mathrm{sign}[D_{Es}]}{\sqrt{2}} \frac{\tilde{\Delta}}{\sqrt{D_{Es}^2(1 + s\beta\mathrm{sign}[D_{Es}]) - s\beta\mathrm{sign}[D_{Es}]\frac{\tilde{\Delta}^2}{2}}} \\
&= \begin{cases} 0, & \mathrm{sign}[D_{Es}]s\beta > 0 \\ s\ \mathrm{sign}[D_{Es}], & \mathrm{sign}[D_{Es}]s\beta < 0 \end{cases}.
\end{aligned} \tag{7.63}$$

The solutions in the normal regime take the form

$$\begin{aligned}
\text{electrons:} \quad \psi_{Es}^{\beta(e^-)}(y) &= \frac{\exp\left[\mathrm{i}k_{Es}^{\beta(e^-)}x - y\frac{|\Gamma|}{\hbar v_\mathrm{F}}\right]}{2} \begin{pmatrix} \phi_s \\ 0 \end{pmatrix} \\
\text{holes:} \quad \psi_{Es}^{\beta(h^+)}(y) &= \frac{\exp\left[\mathrm{i}k_{Es}^{\beta(h^+)}x - y\frac{|\Gamma|}{\hbar v_\mathrm{F}}\right]}{2} \begin{pmatrix} 0 \\ \phi_{-s} \end{pmatrix},
\end{aligned} \tag{7.64}$$

where β no longer is a degree of freedom, but fixed by Eq. (7.63). In order to describe incoming electrons,

$$\beta(e^-) = s\ \mathrm{sign}[D_{Es}] \tag{7.65}$$

has to be chosen. With this, the spin-dependent Andreev reflection coefficient (7.60) becomes

$$R_h{}^s = s\ \mathrm{sign}[D_{Es}] \frac{v_{Es}^{\beta}}{u_{Es}^{\beta}}, \tag{7.66}$$

meaning that the Andreev reflection is given by the ratio of the weight of electron- and hole-like components in the SC's solution, as we have already anticipated in Eq. (3.99).

7.3. Proposal to measure the superconducting quantum spin Hall effect

The superconducting QSH effect is characterized by a giant g-factor. Here, we propose to experimentally verify our predictions by the tunability of the edge states and their excitation spectra in rather weak external magnetic fields. Especially, we demonstrate, how the closure of the quasi-particle gap and the resulting spin polarization can be detected in the spin-dependent density of states (DOS). Further, we analyze transport through N-SC junctions in section 7.3.2. We find that the gap closure translates into unusual magnetotransport signals. To be specific, we predict a non-monotonic excess current as well as a peak splitting in the $\mathrm{d}I/\mathrm{d}V$ characteristics.

7.3.1. Density of states and spin polarization

The spin splitting in the superconducting QSHI can be characterized by the spin-dependent DOS, which, in the interval $[E, E + \mathrm{d}E]$ and at position y, is defined by [Datta07]

$$\rho_s(y, E) = -\frac{1}{\pi}\mathrm{Tr}\ \mathrm{Im}\left[G_s^R(y, y)\right]_{11}. \tag{7.67}$$

The retarded Green's function $G_s^R(y, y)$ can be evaluated in the eigenfunction expansion or Lehmann representation

$$G_s^R(y, y') = \sum_{k,\alpha=\pm} \frac{\psi_{ks}^\alpha(y) \otimes (\psi_{ks}^\alpha(y'))^\dagger}{E - E_\alpha^s(k) + \mathrm{i}0^+} \tag{7.68}$$

$$= \sum_{k,\alpha=\pm} \frac{\psi_{ks}^\alpha(y) \otimes (\psi_{ks}^\alpha(y'))^\dagger}{(E - E_\alpha^s(k))^2 + (0^+)^2} \left[E - E_\alpha^s(k) - \mathrm{i}0^+\right]. \tag{7.69}$$

The (11) component $\left[G_s^R(y, y')\right]_{11}$ corresponds to the electron block of the Green's function. The diagonal parts of $\psi_{ks}^\alpha(y) \otimes (\psi_{ks}^\alpha(y'))^\dagger$ are purely real, because the y-dependence is an exponential decay instead of a plain wave. Using the Lorentz representation of the Dirac delta-distribution

$$\delta(x) = \lim_{\epsilon\to 0^+} \delta_\epsilon(x) = \lim_{\epsilon\to 0^+} \frac{1}{\pi}\frac{\epsilon}{x^2 + \epsilon^2}, \tag{7.70}$$

we find that the diagonal elements of the imaginary part of the Green's function can be written as

$$\begin{aligned}\mathrm{Im}\left(G_s^R(y, y')\right)_{m,m} &= -\sum_{k,\alpha=\pm} 0^+ \frac{\left(\psi_{ks}^\alpha(y) \otimes (\psi_{ks}^\alpha(y'))^\dagger\right)_{m,m}}{(E - E_\alpha^s(k))^2 + (0^+)^2} \\ &= -\pi \sum_{k,\alpha=\pm} \left(\psi_{ks}^\alpha(y) \otimes \left(\psi_{ks}^\alpha(y')\right)^\dagger\right)_{m,m} \delta\left(E - E_\alpha^s(k)\right).\end{aligned} \tag{7.71}$$

Evaluating the trace, we arrive at the simple form ($D_{Es} = E - sev_\mathrm{F}A_x$)

$$\rho_s(y, E) = \sum_{k,\alpha=\pm} \left\|\left[\psi_{ks}^\alpha(y)\right]_{e^-}\right\|^2 \delta\left(E - E_\alpha^s(k)\right) \tag{7.72}$$

$$= \sum_{k,\alpha=\pm} \sum_{\{k_0 | E_\alpha^s(k_0) = E\}} \left\|\left[\psi_{ks}^\alpha(y)\right]_{e^-}\right\|^2 \delta(k - k_0) \left|\frac{\mathrm{d}E_\alpha^s(k')}{\mathrm{d}k'}\right|^{-1}_{k'=k_0}$$

$$= \sum_{\beta=\pm} \left\|\left[\psi_{Es}^\beta(y)\right]_{e^-}\right\|^2 \frac{1}{\hbar v_\mathrm{F}} \frac{|E - sev_\mathrm{F}A_x|}{\sqrt{(E - sev_\mathrm{F}A_x)^2 - \tilde{\Delta}^2}} \left(\Theta[-D_{Es} - \tilde{\Delta}] + \Theta[D_{Es} - \tilde{\Delta}]\right).$$

where only the electron-like components of the solution (7.39) have to be taken into account. In effect, $\rho_s(y, E)$ is the summation over the propagating modes with energy E and spin s weighted with the slope of the corresponding excitation energy spectrum. To arrive at the last line, we

have evaluated the derivative of the excitation energy spectrum

$$\left|\frac{\mathrm{d}E^s_\alpha(k')}{\mathrm{d}k'}\right|^{-1}_{k'=k^\beta_s} = \frac{1}{\hbar v_\mathrm{F}} \frac{|E - sev_\mathrm{F}A_x|}{\sqrt{(E - sev_\mathrm{F}A_x)^2 - \tilde{\Delta}^2}}, \tag{7.73}$$

which neither depends on α nor β. Further, we switched to the energy representation of the eigenstates, which naturally respects the restrictions imposed by the δ-distribution. Additionally, we have introduced the Heavyside-Θ functions to restrict the evaluation of $\rho_s(y, E)$ to propagating solutions outside the spin-dependent quasi-particle gap. Summing over the electron-like components of Eq. (7.39) leads to the closed form

$$\begin{aligned}\rho_s(y, E) =& \frac{2|\Gamma|}{\hbar v_\mathrm{F}} \exp\left[-2y\frac{|\Gamma|}{\hbar v_\mathrm{F}}\right] \frac{1}{\hbar v_\mathrm{F}} \frac{|E - sev_\mathrm{F}A_x|}{\sqrt{(E - sev_\mathrm{F}A_x)^2 - \tilde{\Delta}^2}} \\ & \Big(\Theta[sev_\mathrm{F}A_x - \tilde{\Delta} - E] + \Theta[E - (sev_\mathrm{F}A_x + \tilde{\Delta})]\Big). \end{aligned} \tag{7.74}$$

Further, the full signal can be obtained by integration over the half space $y > 0$:

$$\rho_s(E) = \frac{1}{\hbar v_\mathrm{F}} \frac{|E - sev_\mathrm{F}A_x|}{\sqrt{(E - sev_\mathrm{F}A_x)^2 - \tilde{\Delta}^2}} \Big(\Theta[sev_\mathrm{F}A_x - \tilde{\Delta} - E] + \Theta[E - (sev_\mathrm{F}A_x + \tilde{\Delta})]\Big). \tag{7.75}$$

Its main contribution comes from the inverted band curvature (7.73), which shows poles at the band edges (7.55) and goes to $(\hbar v_\mathrm{F})^{-1}$ far above the superconducting gap. The sum $\rho_\uparrow(E)+\rho_\downarrow(E)$ yields the DOS, while the difference $\rho_\uparrow(E) - \rho_\downarrow(E)$ characterizes the spectral spin polarization. Clearly, the spin polarization vanishes for $A_x = 0$, because all s dependence vanishes. But also for $\tilde{\Delta} = 0$, we find zero spin polarization, because of

$$\left.\frac{1}{\hbar v_\mathrm{F}} \frac{|E - sev_\mathrm{F}A_x|}{\sqrt{(E - sev_\mathrm{F}A_x)^2 - \tilde{\Delta}^2}}\right|_{\tilde{\Delta}=0} = \frac{1}{\hbar v_\mathrm{F}} = \text{const.} \tag{7.76}$$

together with $\Theta[E - sev_\mathrm{F}A_x] + \Theta[sev_\mathrm{F}A_x - E] \equiv 1$, which is expected for a gapless system. Again $\rho_\uparrow$ and $\rho_\downarrow$ are equivalent and the spin polarization vanishes.
The DOS and spectral spin polarization are plotted as a function of E and B_y in Fig. 7.5. The gray shaded planes indicate $B_y/B_* = 0$, 1 and 1.5 used in Fig. 7.4. At zero magnetic field, the DOS shows a quasi-particle gap between $E = \pm\tilde{\Delta}$. Within the bands, the DOS is constant and spin degenerate. Hence, the spin polarization vanishes. A finite B_y shifts the energy of the spin branches by $-sg_*\mu_\mathrm{B}B_y$. This is reflected by a splitting of the peaks in Fig. 7.5a. At gap closing, cf. Eq. (7.54), the two peaks cross and the gaps for the different spin branches separate in energy. In the energy range, where only one s-branch is gaped, a finite spin polarization arises, which can be seen from comparing Figs. 7.5a and 7.5b.
Although the spin s, which characterizes the states, is derived from a σ_x eigenstate χ_s, the structure of the solution (7.25) always combines parts with opposite σ_x expectation values. The reason is that the eigenstates of the thin film Hamiltonian (7.10) consist of a perfect mixture of the two surface states with opposite helicity. Hence, s is to be understood as a pseudo-spin and the spin polarization does not result in a spin signal, which is directly measurable by a magnetic tip. This might be seen as a disadvantage of the realization of the QSHI, which we have chosen in section 7.1.2, whereas in HgTe/CdTe QWs, the eigenstates would show polarization in the

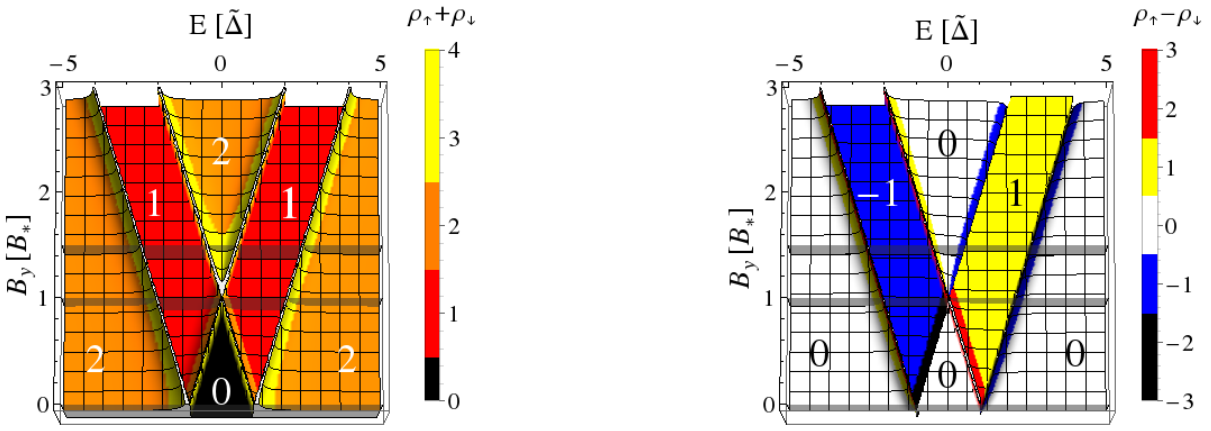

(a) charge DOS

(b) spin polarization

Figure 7.5.: The DOS and spectral spin polarization as a function of B_y and E. The gap closing is clearly visible at $B_y = B_*$. The shaded planes indicate the B_y values used in Figs. 7.4a, 7.4c and 7.4d, respectively. Adapted from [Reinthaler15].

real spin [Brüne12]. However, comparing Figs. 7.5a and 7.5b, we see that the spectral spin polarization is identically mapped on the regions with unit DOS, which therefore is an indirect measure of the spin polarization for general QSHIs. Moreover, in the next section, we will explore magnetotransport signals, which serve as a direct measure of the spin polarization of the edge states.

Scanning tunneling spectroscopy

The DOS can be measured by the scanning tunneling microscope technique. This can be done in two different measurement setups: the usual out-of-plane geometry and in-plane one. The first can be achieved, when the principle setup in Fig. 7.1 is inverted by growing the QSHI on top of the SC, which then serves as the substrate. In this case the the QSHI layer becomes accessible from above. The in-plane geometry requires to adjust the tunneling junction in the plane of the QSHI [Kashiwaya11], i.e., from the left in Fig. 7.3.

7.3.2. Signatures in transport

A direct measurement of the spin polarization can be realized in transport experiments. To this end, we propose the Y-forked 3 terminal N-SC junction, sketched in Fig. 7.6. In this realization, the SC is the superconducting QSHI described by H_{BdG} (7.12). The normal conductor (N) is the non-superconducting QSHI, which has been introduced in section 7.1.2 and is described by H_{BdG} with $\tilde{\Delta} \to 0$. This has the advantage, that the 3 terminal N-SC junction can be etched out of a single QSHI slab, onto which an s-wave SC is grown for $x > 0$. The slab has a finite width W in y-direction. When W is large enough, that the edge states, which are localized at $y = 0$ and $y = W$, have a sufficiently small overlap, we can treat the edges independently. In this sense, the edge channels, for which the local DOS is sketched for spin-↑ (green line) and spin-↓ (red line) in Fig. 7.6, correspond to independent realizations of the edge state in the half

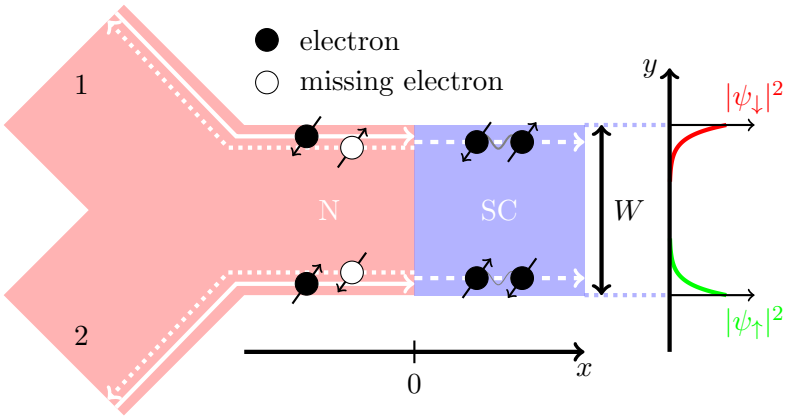

Figure 7.6.: Y-shaped N-SC junction between a normally conducting (indicated by N) and a superconducting QSHI (indicated by SC). The incoming spin branches ↑ and ↓ (solid lines) are in one-to-one correspondence with the physical edges of the system. The width W in y direction is assumed to be large enough, so that the states with different s do not overlap, as shown in the sketch of the edge states' local DOS on the right. In this case, the states with opposite spin polarization can be measured independently in the leads 1 or 2. The total charge transport is obtained by summing up the contributions of both leads. Adapted from [Reinthaler15].

plane, cf. Fig. 7.3. Therefore, we can apply the results of the semi-infinite system. Especially, we can calculate the transport through the N-SC junction using the transport coefficients, which we obtained in section 7.2.4. Since the spin orientations are in one-to-one correspondence to the geometrical edges, the two spin branches can be detected directly by measuring transport in contacts 1 and 2 independently.
We assume a voltage V to be applied across the junction. The transport at $\mu = 2\tilde{\Delta}$ and finite temperature $k_\mathrm{B}T = 0.1\tilde{\Delta}$ is calculated within the BTK formalism, which has been introduced in section 4.2.4. In Fig. 7.7a we plot the excess current I_ex (4.22) as a function of B_y. While the total current (blue dotted line) is symmetric, the individual spin branches (black dashed and solid red lines) are odd and show a distinct, spin-dependent maximum at finite $B_y = B_s^\mathrm{max}$. To determine B_s^max, we write the excess current per spin I_ex^s at zero temperature

$$I_\mathrm{ex}^s = \frac{e}{h}\int_0^{eV} \mathrm{d}E\, |{R_h}^s|^2 = \frac{e}{h}\int_{+sg_*\mu_\mathrm{B}B_y}^{eV+sg_*\mu_\mathrm{B}B_y} \mathrm{d}D_{Es}\, |{R_h}^s|^2, \tag{7.77}$$

where in the last step we used, that E and B_y only enter the AR amplitude ${R_h}^s$ via $D_{Es} = E + sg_*\mu_\mathrm{B}B_y$ in Eq. (7.66). The maximum in B_y is obtained by setting

$$\partial_{B_y} I_\mathrm{ex}^s \propto |{R_h}^s(eV + sg_*\mu_\mathrm{B}B_y)|^2 - |{R_h}^s(+sg_*\mu_\mathrm{B}B_y)|^2 \stackrel{!}{=} 0. \tag{7.78}$$

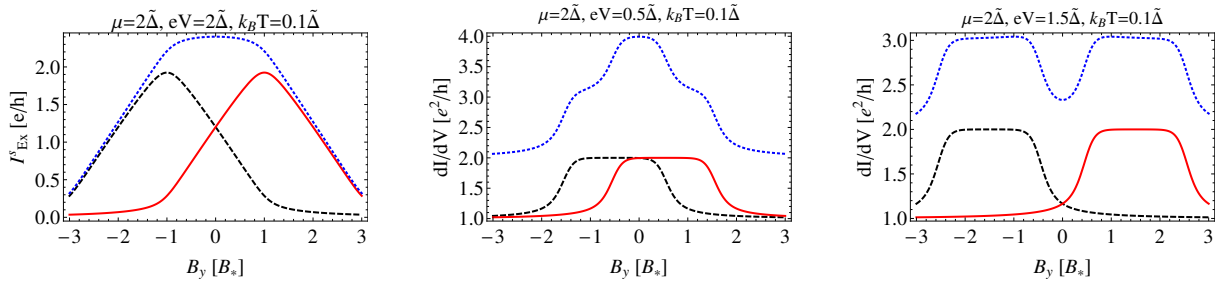

(a) I_{ex} at $eV = 2\tilde{\Delta}$ (b) $\mathrm{d}I/\mathrm{d}V$ at $eV = 0.5\tilde{\Delta}$ (c) $\mathrm{d}I/\mathrm{d}V$ at $eV = 1.5\tilde{\Delta}$

Figure 7.7.: Transport through the 3 terminal N-SC junction of Fig. 7.6 as a function of B_y at temperature $k_{\mathrm{B}}T = 0.1\tilde{\Delta}$ and chemical potential $\mu = 2\tilde{\Delta}$. The different spin branches, depicted as black, dashed (s=1, ↑) and red, solid (s=-1, ↓) lines, can be measured independently in the leads 2 or 1 and sum up to the total signal (blue, dotted). We show the excess current I_{ex} (a) and the $\mathrm{d}I/\mathrm{d}V$ characteristics (b,c). Adapted from [Reinthaler15].

With

$$|{R_h}^s(D_{Es})|^2 := \left|\frac{D_{Es} - s\beta(e^-)\sqrt{D_{Es}^2 - \tilde{\Delta}^2}}{D_{Es} + s\beta(e^-)\sqrt{D_{Es}^2 - \tilde{\Delta}^2}}\right| = \left|\frac{D_{Es} - \mathrm{sign}D_{Es}\sqrt{D_{Es}^2 - \tilde{\Delta}^2}}{D_{Es} + \mathrm{sign}D_{Es}\sqrt{D_{Es}^2 - \tilde{\Delta}^2}}\right|$$
$$= |{R_h}^s(-D_{Es})|^2 \tag{7.79}$$

we arrive at the solution

$$B_s^{\max} = -s\frac{eV}{2g_*\mu_{\mathrm{B}}} = -s\frac{eV}{2\tilde{\Delta}}B_*, \tag{7.80}$$

where B_* is the magnetic field at which the SC becomes gapless, as defined in Eq. (7.54) and shown in Fig. 7.4c.
Further, we show the $\mathrm{d}I/\mathrm{d}V$ characteristics, cf. Eq. (4.23), as a function of B_y in Figs. 7.7b and 7.7c. The quasi-particle gap of each spin polarization corresponds to a conductance plateau of $2e^2/h$ and can be detected directly by measuring the non-local conductances in lead 1 and 2 separately. The peak in the total conductance at zero field splits, when eV exceeds the superconducting gap, i.e., when the quasi-particle gap is closed at $B_y = B_*$. This is a rather general signature of spin-split superconducting states [Tkachov05]. Since excitation energy and magnetic field enter the solutions (7.39) in the same way, an analogous signal can be obtained by varying V for fixed B_y.
The non-monotonic excess current and the split conductance peak are both hallmarks of the spin polarization in a superconducting quantum spin Hall insulator. This kind of experiments is realizable and has been used to explore the spin polarization of ferromagnetic contacts [Meservey70].

7.4. Conclusion

We have described the hybrid system of a QSHI in proximity to an ordinary SC in magnetic fields. Surprisingly, the edge states of this system remain spin polarized and protected against elastic backscattering even in finite in-plane magnetic fields, opening the new area of the superconducting quantum spin Hall effect. We have traced the protection of the edge states to a combination of time-reversal and particle-hole symmetry, which map the system in presence of a magnetic field to the zero field problem. This novel effect is characterized by a giant g-factor, which cannot be found in the absence of superconductivity. Therefore, this system allows a strong tuning of the edge states in weak in-plane magnetic fields with possible applications in the generation of spin currents.
We further have demonstrated that the helical nature of the states causes a non-monotonic excess current and a split conductance peak. On the one hand, this provides a measurement scheme of this new phenomenon. On the other hand, this addresses the problem of measuring the spin polarization of helical edge states in general. The main difficulty of measuring the spin polarization of edge states is that normally both counter-propagating modes are simultaneously probed, canceling any net spin polarization. Therefore, the only successful experiment so far had to rely on an indirect and non-local measurement of the spin polarization of the edge states [Brüne12]. The giant g-factor allows to split the edge states in small magnetic fields, without breaking the helicity of the edge states. The resulting unique $\mathrm{d}I/\mathrm{d}V$ and I_{ex} characteristics pave the way for a direct detection of the spin polarization of the underlying QSH system.

8. Conclusion and outlook

The field of topological insulators offers promising prospectives for future information processing. Their helical edge states turn topological insulators into prime candidates to generate ballistic spin currents for high fidelity spintronics. Moreover, hybrid systems of topological insulators and superconductors are believed to host Majorana bound states, which are at the center of interest for topological quantum computing. A large research community is working on bringing these fascinating concepts to life in functional devices. This thesis contributes to the understanding of heterostructures based on topological insulators in contact to metals or superconductors. In particular, we demonstrate how bulk and edge contributions compete in finite size heterostructures. We describe how these effects can be applied in measurement schemes for topologically non-trivial bulk transport signals and crossed Andreev reflection. Moreover, we predict a superconducting quantum spin Hall effect, which remains robust in finite magnetic fields. To conclude this thesis, we want to wrap up our results and point out interesting aspects for future research.
Part I has introduced the theory and methods needed to describe heterojunctions of topological insulators. The latter have been discussed in chapter 2, where topological indices have been connected to the geometrical phase. As an explicit example we have derived the TKNN invariant in appendix A. Chapter 3 has focused on superconducting topological insulators. We have demonstrated how triplet pairing is induced in topological insulators upon combination with an ordinary s-wave superconductor. The introduction of superconductivity has been completed by pointing out subtle differences between missing electrons and holes in appendix D. Chapter 4 has linked the transport through mesoscopic structures to elastic scattering theory. The scattering problem for bulk and edge states has been simultaneously solved in the generalized wave matching approach, which we have described in section 4.3.2. Additionally, transport calculations within the tight binding formalism have been reviewed in appendices B and C.
In chapter 5, we have presented a numerical study of finite size tunneling junctions of two-dimensional topological insulators in between two metallic leads. In narrow conductors, the finite size effects are twofold: Firstly, the overlap of two edge states, which are associated with the same Kramers' partner polarization but different boundaries, introduces backscattering, even when time-reversal symmetry is unbroken. Secondly, bulk and edge contributions to the conductance are mixed in a ratio which depends on the width of the sample. In contrast, when the system is wide enough, transport is determined entirely by the edge or bulk states for long and short tunneling junctions, respectively. The latter regime is particularly interesting, because it confirms and strengthens the prediction [Novik10, Recher10] of a non-monotonic tunneling conductance, which identifies the topologically non-trivial regime. In section 5.3.3, we have linked the emerging conductance maximum to an effectively propagating bulk solution. This allows a direct classification of different topological regimes by transport measurements, without relying on the bulk-boundary correspondence. For future research, it would thus be very interesting to look for similar conductance properties in a wider range of topologically non-trivial phases. This might be of importance especially for transport measurements of the topological regime in materials, where surface or edge transport is obscured by a residual bulk contribution, like in three-dimensional topological insulators [Xia09, Chen09] and in gapless two-dimensional topological insulators [Baum15a, Baum15b]. On the experimental side, topological insulator structures

in the sub-micrometer domain have been realized [Brüne12, Pribiag15]. Nevertheless, the verification of the predicted conductance maximum requires further efforts in nanolithography to decrease the length of the tunneling junction to the order of 100 nm. Since the measurement of the conductance maximum needs short but not narrow tunneling junctions, it would also be possible to grow a large topological insulator slab and to create a short tunneling junction by attaching metallic leads from the top. This procedure has, for example, been used to realize superconductor - topological insulator - superconductor junctions in [Hart14].
The finite size effects in superconducting tunneling junctions in between leads of two-dimensional topological insulators have been analyzed in chapter 6. For the helical edge states, crossed Andreev reflection is spatially separated from the electron tunneling and becomes significant, when the system is narrow enough so that the evanescent bulk states in the superconductor couple both edges. We have studied the effectiveness of this separation as a function of the system geometry and the doping of the superconductor. Moreover, based on the spatial separation we have proposed an all-electrical measurement of crossed Andreev reflection in multi-terminal setups, in which one spin polarization can be selected by choosing appropriate contact voltages or by using the quantum spin Hall effect in an H-bar structure. Our setup couples the opposite edges of the sample via the highly doped superconductor, which relies on very clean interfaces between the topological insulator and the superconductor and which to achieve might need considerable experimental effort. Indeed, although superconductivity has been successfully induced into two-dimensional topological insulators [Knez12, Hart14, Pribiag15], the associated doping into the bulk regime has not been observed so far. Therefore, it would be desirable that the experimental realization of the all-electrical measurement of crossed Andreev reflection is supported by the theoretical exploration of other mechanisms to couple the edge states at opposite boundaries. For example, one could directly couple the edge states without endangering the spatial separation by etching local restrictions in the superconducting part [Krueckl11]. Further, the topological properties of HgTe/CdTe quantum wells can be tuned by the well width. Decreasing the latter to the critical thickness of about 6.4 nm causes a topological phase transition [Bernevig06], which is characterized by a semi-metallic phase. A local variation of the quantum well width could allow the coupling of the edge states via the semi-metallic phase. Another possibility would be to implement the tunneling setup in gapless two-dimensional topological insulators, which can be realized in HgTe/CdTe double quantum wells [Baum15b]. The latter materials allow to control the coupling of the coexisting bulk and edge states by applying a small gate voltage.
In chapter 7, we have described the superconducting quantum spin Hall effect. The latter arises in a hybrid system of helical edge states and ordinary superconductors. We have demonstrated that the helicity of the system's edge states as well as their protection against scalar disorder is immune to the presence of an in-plane magnetic field, because the system can be mapped to the zero field case. However, the magnetic field has a strong effect on the dispersion and the magnetotransport signals due the giant g-factor, which characterizes the superconducting quantum spin Hall effect. Especially, we have predicted a non-monotonic excess current and a peak splitting in the $\mathrm{d}I/\mathrm{d}V$ characteristics. Both are Hallmarks for this novel effect as well as for the spin polarization of helical edge states in general. Since it has already been achieved to induce superconductivity into helical edge states [Knez12, Hart14, Pribiag15], we can be confident, that our predictions can be experimentally tested in the near future. On the theoretical side, the immunity of the edge states should be tested for arbitrary orientations of the magnetic field. Moreover, in section 7.2.3, we have discussed the emergence of Majorana bound states at gap closing in the systems. The latter can be controlled by a weak in-plane magnetic field, which

should allow to use these exotic states in measurement and braiding proposals similar to [Mi13].

We have already discussed some prospects for further research, which might extend the results of this thesis. The general field of topological states of matter has been growing at rapid speed with new candidate materials being proposed and found [Ando13]. Current developments are at the stage where the conducting properties of a device can be designed to accomplish certain tasks [Fiete11]. In order to fulfill this goal, further scientific progress in understanding the fundamental physical properties of these materials has to be achieved: the theoretical analysis and experimental realization of topological insulators with sufficiently large band gaps is essential to realize functional components, which operate at room temperature. Further experimental advances in sample fabrication might, for example, lead to the reduction of residual bulk conductance, the minimization of aging problems of samples and the growth of cleaner contacts as well as interfaces. On the theoretical side, a generalization of the classification scheme of topological insulators [Schnyder08] would help to predict new kinds of topological materials, whose protection does not rely on time-reversal symmetry, like crystalline topological insulators [Fu11, Hsieh12, Tanaka12]. The understanding of strong interactions might enrich the field with new kinds of topological phase transitions, like predicted for topological Mott insulator [Raghu08]. In the field of topological quantum computation, the experimental verification of Majorana bound states in InAs quantum wires [Mourik12, Das12, Deng12] is still on debate [Pikulin12]. Therefore, it would be desirable to experimentally test the formation of Majorana bound states in the helical edge states of topological insulators [Mi13, Crépin14]. In the mean time, theorists can search for ways to scale and braid these states, analogously to proposals for InAs quantum wires [Alicea11, Sau11, Hyart13].

A. The TKNN invariant

In order to give an example how the Berry phase (2.31) is connected with physical observables, we calculate the topological invariant defined for the integer QH effect (TKNN invariant), named after Thouless, Kohmoto, Nightingale, and den Nijs [Thouless82]. Let us assume a 2D system of size $L \times L$ in the $x-y$-plane. We apply a magnetic field $\mathcal{B}_z$ in z-direction and an electric field $\mathcal{E}_y$, which drives a current along the y-axis. We will find that in linear response, the Hall conductance is proportional to the Berry phase.
To start, we write the Hamiltonian in two parts

$$H = H_0 - e\mathcal{E}_y\hat{y}, \tag{A.1}$$

where the non-degenerate spectrum $H_0 |\alpha\rangle = E_\alpha |\alpha\rangle$ is known and we perturb the system with the potential $\mathcal{U} = -e\mathcal{E}_y\hat{y}$. In lowest order, the new eigenstates are [Schwabl07]

$$|\alpha\rangle_\mathcal{E} = |\alpha\rangle + \sum_{\beta(\beta\neq\alpha)} \frac{\langle\beta| - e\mathcal{E}_y\hat{y}\,|\alpha\rangle}{E_\alpha - E_\beta}. \tag{A.2}$$

With this, the current density in x-direction becomes

$$\begin{aligned}\langle j_x\rangle &= \sum_\alpha f_{E_\alpha} \langle\alpha|_\mathcal{E} \frac{e\hat{v}_x}{L^2} |\alpha\rangle_\mathcal{E} = \qquad (A.3)\\ &= \langle j_x\rangle_{\mathcal{E}_y=0} - \underbrace{\frac{e^2}{L^2}\sum_\alpha \sum_{\beta(\beta\neq\alpha)} f_{E_\alpha}\left(\frac{\langle\alpha|\,\hat{v}_x\,|\beta\rangle\langle\beta|\,\mathcal{E}_y\hat{y}\,|\alpha\rangle}{E_\alpha - E_\beta} - \frac{\langle\alpha|\,\mathcal{E}_y\hat{y}\,|\beta\rangle\langle\beta|\,\hat{v}_x\,|\alpha\rangle}{E_\alpha - E_\beta}\right)}_{=\langle j_x\rangle_\mathcal{E}} + \mathcal{O}(\mathcal{E}_y^2).\end{aligned}$$

Since we assume zero temperature, the Fermi distribution function f_{E_α} is 1 for occupied states and 0 else. We can therefore restrict the sum to occupied states. For the further analysis, we will work in the Bloch basis: $|\alpha\rangle = |u_\kappa(\boldsymbol{k})\rangle$, where the index α splits in a band index κ and a conserved lattice momentum $\boldsymbol{k}$. In this basis the canonical commutation relations tell us that $\hat{y} = \mathrm{i}\partial_{k_y}$. Using the Heisenberg equation $\dot{\hat{y}} = \hat{v}_y = -\mathrm{i}/\hbar\,[\hat{y}, H]$ one finds

$$\langle\beta|\,\hat{v}_i\,|\alpha\rangle = \frac{1}{\mathrm{i}\hbar}(E_\alpha - E_\beta)\langle\beta|\,\hat{i}\,|\alpha\rangle = \frac{1}{\hbar}(E_\kappa(\boldsymbol{k}) - E_{\kappa'}(\boldsymbol{k}))\langle u_\kappa(\boldsymbol{k})|\,\partial_{k_i}\,|u_{\kappa'}(\boldsymbol{k})\rangle\,, \quad i = x, y. \tag{A.4}$$

The Hall conductance is defined by (we stick to the composite indices α and β here)

$$\sigma_{xy} := \frac{\langle j_x\rangle_\mathcal{E}}{\mathcal{E}_y} = -\mathrm{i}\frac{e^2}{\hbar L^2}\sum_{\alpha,\mathrm{occ}}\sum_{\beta,\mathrm{occ},\beta\neq\alpha}\left(\langle\alpha|\,\partial_{k_y}\,|\beta\rangle\langle\beta|\,\partial_{k_x}\,|\alpha\rangle - \langle\alpha|\,\partial_{k_x}\,|\beta\rangle\langle\beta|\,\partial_{k_y}\,|\alpha\rangle\right). \tag{A.5}$$

Now, we follow the steps

1. Note that for $\alpha = \beta$ the two summands cancel $\Rightarrow$ sum over all β

2. Use the completeness relation: $\sum_\beta |\beta\rangle \langle\beta| = \mathbb{I}$.

3. Use $0 = \partial_{k_i} \underbrace{\langle\alpha|\beta\rangle}_{=\delta_{\alpha\beta}} = (\partial_{k_i} \langle\alpha|)|\beta\rangle + \langle\alpha| \partial_{k_i} |\beta\rangle$ to write $\langle\alpha| \partial_{k_i} |\beta\rangle = -(\partial_{k_i} \langle\alpha|)|\beta\rangle$.

4. Replace $(\partial_{k_i} \langle\alpha|)\partial_{k_j} |\beta\rangle$ with $\partial_{k_i} \langle\alpha| \partial_{k_j} |\beta\rangle$, because the mixed terms $\langle\alpha| \partial_{k_i}\partial_{k_j} |\beta\rangle$ cancel due to $\left[\partial_{k_i}, \partial_{k_j}\right] = 0$.

5. Do the continuum limit $\sum_\alpha = \sum_{\boldsymbol{k}} \sum_\kappa = \frac{1}{\Delta k} \sum_{\boldsymbol{k}} \Delta k \sum_\kappa \longrightarrow \left(\frac{L}{2\pi}\right)^2 \sum_\kappa \int_{\mathrm{BZ_{mag}}} \mathrm{d}^2k$ in order to integrate over the whole magnetic Brillouin zone $\mathrm{BZ_{mag}}$[1].

6. Identify $-\mathrm{i}\langle\alpha| \partial_{k_j} |\beta\rangle$ with the Berry connection $[\boldsymbol{A}_\kappa(\boldsymbol{k})]_j$ in Eq. (2.32) .

to find

$$\begin{aligned}\sigma_{xy} &= \frac{e^2}{h} \sum_{\kappa,\mathrm{occ}} \int_{\mathrm{BZ_{mag}}} \frac{\mathrm{d}^2k}{2\pi} \left(\partial_{k_x}[\boldsymbol{A}_\kappa(\boldsymbol{k})]_y - \partial_{k_y}[\boldsymbol{A}_\kappa(\boldsymbol{k})]_x\right) \\ &= \frac{e^2}{h} \sum_{\kappa,\mathrm{occ}} \int_{\mathrm{BZ_{mag}}} \frac{\mathrm{d}^2k}{2\pi} \left[\nabla_{\boldsymbol{k}} \times \boldsymbol{A}_\kappa(\boldsymbol{k})\right]_z = \frac{e^2}{h} \sum_{\kappa,\mathrm{occ}} n_\kappa. \end{aligned} \tag{A.6}$$

For each occupied band, we defined the TKNN invariant

$$n_\kappa = \int_{\mathrm{BZ_{mag}}} \frac{\mathrm{d}^2k}{2\pi} \left[\nabla_{\boldsymbol{k}} \times \boldsymbol{A}_\kappa(\boldsymbol{k})\right]_z \tag{A.7}$$

as an integral of the Berry curvature (2.34) over the magnetic BZ. To show that this is a quantized number, we follow the argumentation of [Shen12]. Let $\tilde{a}$ ($\tilde{b}$) be the lattice constants of the magnetic unit cell in x (y)-direction. With this we can rewrite Eq. (A.7) to

$$\begin{aligned} n_\kappa = &\frac{1}{2\pi} \int_0^{\frac{2\pi}{\tilde{a}}} \mathrm{d}k_x \int_0^{\frac{2\pi}{\tilde{b}}} \mathrm{d}k_y \left(\partial_{k_x}[\boldsymbol{A}_\kappa(\boldsymbol{k})]_y - \partial_{k_y}[\boldsymbol{A}_\kappa(\boldsymbol{k})]_x\right) \\ = &\frac{1}{2\pi} \int_0^{\frac{2\pi}{\tilde{b}}} \mathrm{d}k_y \left([\boldsymbol{A}_\kappa(2\pi/\tilde{a},\ k_y)]_y - [\boldsymbol{A}_\kappa(0, k_y)]_y\right) \\ &-\frac{1}{2\pi} \int_0^{\frac{2\pi}{\tilde{a}}} \mathrm{d}k_x \left([\boldsymbol{A}_\kappa(k_x,\ 2\pi/\tilde{b})]_x - [\boldsymbol{A}_\kappa(k_x, 0)]_x\right). \end{aligned} \tag{A.8}$$

Due to the periodicity of the system, the BZ can be identified with a torus T^2. Hence, the states at the boundaries of the BZ are equivalent up to a phase:

$$\begin{aligned} \left|u_\kappa(k_x,\ 2\pi/\tilde{b})\right\rangle &= \exp\left[\mathrm{i}\theta_x(k_x)\right] |u_\kappa(k_x, 0)\rangle\,, \\ |u_\kappa\left(2\pi/\tilde{a},\ k_y\right)\rangle &= \exp\left[\mathrm{i}\theta_y(k_y)\right] |u_\kappa(0, k_y)\rangle\,. \end{aligned} \tag{A.9}$$

[1] The magnetic unit cell contains an integer multiple of the magnetic flux quantum and will be introduced in detail below. For the calculations here, it is sufficient to interpret it as a conventional unit cell of a lattice periodic system.

In terms of the Berry connection, this resembles the gauge transformation

$$\begin{aligned}\left[\boldsymbol{A}_\kappa(k_x,\ 2\pi/\tilde{b})\right]_x &= -\partial_{k_x}\theta_x(k_x) + \left[\boldsymbol{A}_\kappa(k_x,0)\right]_x\,,\\ \left[\boldsymbol{A}_\kappa\left(2\pi/\tilde{a},\ k_y\right)\right]_y &= -\partial_{k_y}\theta_y(k_y) + \left[\boldsymbol{A}_\kappa(0,k_y)\right]_y\,.\end{aligned} \tag{A.10}$$

This simplifies Eq. (A.8) further to

$$\begin{aligned}n_\kappa &= \frac{1}{2\pi}\left(-\int_0^{\frac{2\pi}{\tilde{b}}}\mathrm{d}k_y\,\partial_{k_y}\theta_y(k_y) + \int_0^{\frac{2\pi}{\tilde{a}}}\mathrm{d}k_x\,\partial_{k_x}\theta_x(k_x)\right)\\ &= \frac{1}{2\pi}\left(\theta_y(0) - \theta_y(2\pi/\tilde{b}) + \theta_x(2\pi/\tilde{a}) - \theta_x(0)\right).\end{aligned} \tag{A.11}$$

Since the states at the four corners of the BZ are physically indistinguishable, we can identify them with one another via Eq. (A.9)

$$\begin{aligned}|u_\kappa(0,0)\rangle &= e^{-\mathrm{i}\theta_y(0)}\left|u_\kappa\left(\frac{2\pi}{\tilde{a}},0\right)\right\rangle = e^{-\mathrm{i}\left(\theta_y(0)+\theta_x\left(\frac{2\pi}{\tilde{a}}\right)\right)}\left|u_\kappa\left(\frac{2\pi}{\tilde{a}},\frac{2\pi}{\tilde{b}}\right)\right\rangle\\ &= e^{-\mathrm{i}\left(\theta_y(0)+\theta_x\left(\frac{2\pi}{\tilde{a}}\right)-\theta_y\left(\frac{2\pi}{\tilde{b}}\right)\right)}\left|u_\kappa\left(0,\frac{2\pi}{\tilde{b}}\right)\right\rangle\\ &= e^{-\mathrm{i}\left(\theta_y(0)+\theta_x\left(\frac{2\pi}{\tilde{a}}\right)-\theta_y\left(\frac{2\pi}{\tilde{b}}\right)-\theta_x(0)\right)}\left|u_\kappa\left(0,0\right)\right\rangle.\end{aligned} \tag{A.12}$$

In order to ensure a single valued $|u_\kappa(0,0)\rangle$, the condition

$$\theta_y\left(0\right) + \theta_x\left(\frac{2\pi}{\tilde{a}}\right) - \theta_y\left(\frac{2\pi}{\tilde{b}}\right) - \theta_x\left(0\right) = 2\pi\nu, \quad \nu\in\mathbb{Z} \tag{A.13}$$

has to hold. Consequently, the TKNN invariant (A.7) must be an integer and the Hall conductance (A.6) is quantized in units of e^2/h in the so-called integer QH effect [Klitzing80].
In the remainder of this section, we will present an instructive picture of how the TKNN invariant is connected with the number of flux quanta in the magnetic unit cell [Kohmoto85]. Therefore, we return to the unperturbed system

$$H_0\left|\alpha\right\rangle = \left[\frac{\hbar^2}{2m}(\boldsymbol{k}+e\boldsymbol{\mathcal{A}})^2 + U(x,y)\right]\left|\alpha\right\rangle = E\left|\alpha\right\rangle. \tag{A.14}$$

Here, we used the symmetric gauge $\boldsymbol{\mathcal{A}} = \boldsymbol{\mathcal{B}}\times\boldsymbol{r}/2$ and the periodic lattice potential

$$U(\boldsymbol{r}) = U(\boldsymbol{r}+\boldsymbol{R}). \tag{A.15}$$

The Bravais vector is defined by $\boldsymbol{R} = la\hat{e}_x + mb\hat{e}_y$ with $l,m\in\mathbb{Z}$ and lattice constants a and b along the x and y-axis, respectively. Since generally $\boldsymbol{\mathcal{A}}(\boldsymbol{r}) \neq \boldsymbol{\mathcal{A}}(\boldsymbol{r}+\boldsymbol{R})$, the usual translation operator

$$\hat{T}_{\boldsymbol{R}} f(\boldsymbol{r}) = f(\boldsymbol{r}+\boldsymbol{R}), \quad \hat{T}_{\boldsymbol{R}} = \exp[\mathrm{i}\boldsymbol{k}\cdot\boldsymbol{R}] \tag{A.16}$$

does not commute with the Hamiltonian. Redefining the translation by

$$\tilde{T}_{\boldsymbol{R}} = \exp\left[\mathrm{i}\boldsymbol{R}\cdot(\boldsymbol{k}-e\boldsymbol{\mathcal{A}})\right] = \exp\left[\mathrm{i}\boldsymbol{R}\cdot\left(\boldsymbol{k}+e\frac{\boldsymbol{r}\times\boldsymbol{\mathcal{B}}}{2}\right)\right] = \hat{T}_{\boldsymbol{R}}\exp\left[\mathrm{i}\frac{e}{2}(\boldsymbol{\mathcal{B}}\times\boldsymbol{R})\cdot\boldsymbol{r}\right] \tag{A.17}$$

ensures $[\tilde{T}_{\boldsymbol{R}}, H_0] = 0$. However, the $\boldsymbol{r}$ dependence causes ($\boldsymbol{a} = a\hat{e}_x$, $\boldsymbol{b} = b\hat{e}_y$)

$$\tilde{T}_{\boldsymbol{a}}\tilde{T}_{\boldsymbol{b}} = \exp[\mathrm{i}2\pi\phi]\tilde{T}_{\boldsymbol{b}}\tilde{T}_{\boldsymbol{a}}, \tag{A.18}$$

where we defined the magnetic flux through the unit cell to be

$$\phi = \frac{eB}{h}ab. \tag{A.19}$$

This means that the newly defined translation operators do not commute unless the magnetic flux takes integer values. Imagine the flux to be a rational number $\phi = p/q$, $p, q \in \mathbb{Z}$. The Bravais lattice with lattice constants $\tilde{a} = qa$ and $\tilde{b} = b$

$$\tilde{\boldsymbol{R}} = lq\boldsymbol{a} + m\boldsymbol{b} \tag{A.20}$$

defines the so-called magnetic unit cell which contains an integral flux $\tilde{\phi} = p$. All translations by the new Bravais lattice vectors commute and we can define magnetic Bloch wave functions

$$\begin{aligned}\psi^{\kappa}_{k_xk_y}(x,y) &= \exp[\mathrm{i}k_x x + \mathrm{i}k_y y]u^{\kappa}_{k_xk_y}(x,y),\\ \tilde{T}_{\tilde{\boldsymbol{R}}}\psi^{\kappa}_{k_xk_y}(x,y) &= \exp[\mathrm{i}k_x l\tilde{a} + \mathrm{i}k_y m\tilde{b}]\psi^{\kappa}_{k_xk_y}(x,y),\end{aligned} \tag{A.21}$$

which obey the generalized Bloch conditions

$$u^{\kappa}_{k_xk_y}(x+\tilde{a},y) = \exp\left[-\frac{\mathrm{i}\pi py}{\tilde{b}}\right]u^{\kappa}_{k_xk_y}(x,y), \quad u^{\kappa}_{k_xk_y}(x,y+\tilde{b}) = \exp\left[\frac{\mathrm{i}\pi px}{\tilde{a}}\right]u^{\kappa}_{k_xk_y}(x,y). \tag{A.22}$$

Since a $U(1)$ gauge transformation

$$\boldsymbol{\mathcal{A}}' = \boldsymbol{\mathcal{A}} + \boldsymbol{\nabla}f(x,y) \Rightarrow {\psi^{\kappa}_{k_xk_y}}'(x,y) = \exp\left[-\frac{\mathrm{i}e}{\hbar}f(x,y)\right]\psi^{\kappa}_{k_xk_y}(x,y) \tag{A.23}$$

must not influence the physical observables, we look for gauge independent quantities. From Eq. (A.22), we find that the accumulated phase along the boundary of the magnetic unit cell is gauge invariant and yields $2\pi p$, which is proportional to the enclosed magnetic flux p. This number is a topological invariant, because it corresponds to the number of magnetic vortices in the magnetic unit cell [Kohmoto85]. The transition to momentum space shows that the phase accumulated around the boundary of the magnetic BZ in Eq. (A.12) is equally determined by the number of flux quanta per magnetic unit cell.

B. Tight binding formalism

The thorough description of a solid state system requires a full quantum mechanical treatment. Often, it is impossible to find an analytical solution to these problems. Hence, one searches for appropriate approximations and/or numerical solutions. For example, the highly mobile conduction band electrons in metals can be modeled as free electrons, where the structure of the underlying crystal is disregarded.
The tight binding (TB) method considers the atomic structure of the solid (or molecule) explicitly. Electrons can move on the atomic lattice by tunneling from one atomic site i to another site j. The likeliness of this so-called hopping is determined by the overlap of the wave function of the electron at i with the atom j. The approximation now lies in neglecting all hopping processes where i and j are far from each other. The strictest approximation in this sense is to take only nearest neighbor hoppings into account. This is a good approximation when the electrons are *tightly bound* to the atoms and their wave functions decay exponentially on the length scale of the atomic lattice. Higher corrections can be considered by taking into account the hopping to next-nearest neighbors and so on. The nearest neighbor and the next-nearest neighbor hoppings in a square lattice are exemplarily depicted in Fig. B.1.
A convenient way to write down this approximation is to use second quantization. Let $\hat{\psi}^\dagger_{i\alpha}$ ($\hat{\psi}_{i\alpha}$) be field operators which create (annihilate) an electron at atom i in state α, where α may be a spin or an orbital degree of freedom. In this language, the TB Hamiltonian takes the form

$$H_{\mathrm{TB}} = \sum_i \sum_{\alpha,\alpha'} \epsilon_{i,\alpha\alpha'} \hat{\psi}^\dagger_{i\alpha} \hat{\psi}_{i\alpha'} - \sum_{\langle i,j\rangle} \sum_{\alpha,\alpha'} t_{i\alpha,j\alpha'} \hat{\psi}^\dagger_{i\alpha} \hat{\psi}_{j\alpha'}. \tag{B.1}$$

Here, $\epsilon_{i,\alpha\alpha'}$ is an on-site energy, like, e.g., an electrostatic potential. The sum $\langle i,j\rangle$ runs over nearest neighbors and the hopping term $t_{i\alpha,j\alpha'}$ is determined by the overlap of the electronic wave functions $\psi_{i\alpha}(\boldsymbol{r})$ and $\psi_{j\alpha'}(\boldsymbol{r})$. If the hopping is independent of the position on the lattice,

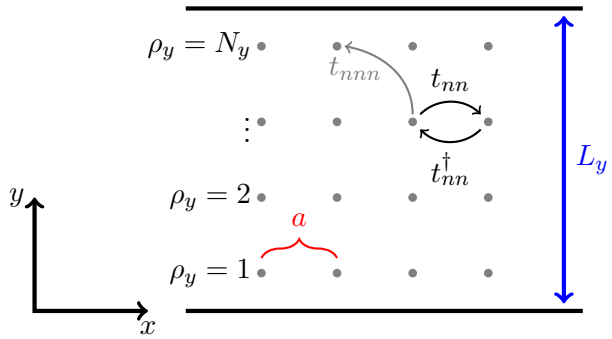

Figure B.1.: The TB method is visualized for a square lattice with lattice constant a. The sample has a finite width in y-direction: $L_y = (N_y+1)a$. Exemplary nearest neighbor (t_{nn}) and next-nearest neighbor (t_{nnn}) hoppings are indicated by black and gray arrows.

it can be written as a constant matrix t_{nn} which acts on the different quantum numbers α. In order to ensure that H_{TB} is hermitian, the hoppings in forward ($i \to i+1$) and backward ($i+1 \to i$) direction have to be connected by hermitian conjugation, cf. Fig. B.1.
So far, we have considered a real atomic lattice, but in the following we will use the TB formalism to find the numerical solutions to continuum Hamiltonians. To do so, we discretize the system on an artificial square lattice with lattice constant a. An explicit example of a discretized sample is shown in Fig. B.1. The lattice points are labeled by the collective index $\rho = \{\rho_x, \rho_y\}$. Explicitly, we assume a quasi one-dimensional nano-ribbon, which is infinitely extended along the x-axis. The number of lattice points in y-direction N_y is connected to the ribbon's width by $L_y = (N_y + 1)a$.
We assume a continuous, single-particle Hamiltonian which depends on position $\boldsymbol{r}$ and momentum $\boldsymbol{p}$

$$\mathcal{H}_{\alpha\alpha'}(\boldsymbol{r}, \hat{\boldsymbol{p}}) = H^0_{\alpha\alpha'}(\boldsymbol{r}) + \sum_i H^{1,i}_{\alpha\alpha'}(\boldsymbol{r})\hat{p}_i + \sum_i H^{2,i}_{\alpha\alpha'}(\boldsymbol{r})\hat{p}_i^2 + \mathcal{O}(\hat{\boldsymbol{p}}^3). \tag{B.2}$$

For N_α different degrees of freedom α, the continuous Hamiltonian is a matrix of dimension $N_\alpha \times N_\alpha$ and, consequently, its eigenvectors $\psi_\alpha(\boldsymbol{r})$ are N_α-dimensional wave functions. In the TB formalism, the Hamiltonian is only evaluated on the discrete points of the lattice. The discretized wave functions can be written as vectors with components

$$\Psi_{\alpha\rho=\{\rho_x,\rho_y,\ldots\}} = \psi_\alpha\left(\boldsymbol{r}(\rho) = \rho_x a\hat{e}_x + \rho_y a\hat{e}_y + \ldots\right), \quad \rho_x, \rho_y, \ldots \in \mathbb{Z}. \tag{B.3}$$

In the real space representation, the momentum operator is $\hat{\boldsymbol{p}} = -\mathrm{i}\hbar\boldsymbol{\nabla}$. Its j^{th} component acts on a discretized wave functions according to

$$\hat{p}_j\Psi_{\alpha\rho} = -\mathrm{i}\hbar\partial_j\Psi_{\alpha\rho} = -\frac{\mathrm{i}\hbar}{2a}\left(\Psi_{\alpha\{\ldots,\rho_j+1,\ldots\}} - \Psi_{\alpha\{\ldots,\rho_j-1,\ldots\}}\right) \tag{B.4}$$

$$\hat{p}_j^2\Psi_{\alpha\rho} = -\hbar^2\partial_j^2\Psi_{\alpha\rho} = -\frac{\hbar^2}{a^2}\left(\Psi_{\alpha\{\ldots,\rho_j+1,\ldots\}} + \Psi_{\alpha\{\ldots,\rho_j-1,\ldots\}} - 2\Psi_{\alpha\{\ldots,\rho_j,\ldots\}}\right). \tag{B.5}$$

Up to second order in momentum, only nearest neighbor sites are connected[1]. Higher derivatives will require additional next-nearest neighbor, next-next-nearest neighbor, ... hopping terms. Being associated with the momentum operator, the hopping terms are to be interpreted as

[1] To ensure this, we had to use a different discretization of the first derivative in Eq. (B.5):

$$-\hbar^2\partial_j^2\Psi^\alpha_\rho = -\mathrm{i}\hbar\partial_j\left[-\frac{\mathrm{i}\hbar}{a}\left(\Psi_{\{\alpha\ldots,\rho_j+0.5,\ldots\}} - \Psi_{\alpha\{\ldots,\rho_j-0.5,\ldots\}}\right)\right].$$

This is consistent with Eq. (B.4), because both definitions yield the exact derivative in the continuum limit $a \to 0$.

moving electrons. With this, the Schrödinger equation can be rewritten in matrix form

$$\sum_{\alpha'\rho'} H_{\alpha\rho,\alpha'\rho'}\Psi_{\alpha'\rho'} = E^{\alpha}\Psi_{\alpha\rho} \tag{B.6}$$

$$\text{with: } H_{\alpha\rho,\alpha'\rho'} = \begin{cases} H^0_{\alpha\alpha'} - 2\frac{\hbar^2}{a^2}\sum_i H^{2,i}_{\alpha\alpha'}(\rho) & ,\rho = \rho' \\ -\frac{\mathrm{i}\hbar}{2a}H^{1,j}_{\alpha\alpha'}(\rho) + \frac{\hbar^2}{a^2}H^{2,j}_{\alpha\alpha'}(\rho) & ,\rho_j = \rho'_j + 1 \\ \left[-\frac{\mathrm{i}\hbar}{2a}H^{1,j}_{\alpha\alpha'}(\rho)\right]^\dagger + \frac{\hbar^2}{a^2}\left[H^{2,j}_{\alpha\alpha'}(\rho)\right]^\dagger & ,\rho_j = \rho'_j - 1 \\ 0 & ,\text{ else} \end{cases}. \tag{B.7}$$

The dependence of Eq. (B.7) on ρ offers the possibility to directly implement spatially dependent potentials, like, e.g., scalar disorder or gate potentials. Including a magnetic field via the Peierls substitution $\hat{\boldsymbol{p}} - q\boldsymbol{A}(\boldsymbol{r})$ has a more subtle effect. It can be shown from gauge invariance that in this case the matrix elements obtain a space dependent phase [Datta07, Rothe09]

$$H_{\alpha\rho,\alpha'\rho'} \longrightarrow H_{\alpha\rho,\alpha'\rho'}\exp\left[\frac{\mathrm{i}q}{\hbar}\int_{\boldsymbol{r}(\rho)}^{\boldsymbol{r}(\rho')}\mathrm{d}\boldsymbol{r}\cdot\boldsymbol{A}(\boldsymbol{r})\right]. \tag{B.8}$$

Since the momentum $\hat{p}_j$ generates translation in j-direction, we can connect the wave functions at different lattice points by the translation operator ($\hat{T}$) [Sakurai94]

$$\hat{T}[a\hat{e}_j]\Psi_{\alpha\{\ldots,\rho_j,\ldots\}} = \exp\left[\frac{\mathrm{i}}{\hbar}\hat{p}_j a\right]\Psi_{\alpha\{\ldots,\rho_j,\ldots\}} = \Psi_{\alpha\{\ldots,\rho_j+1,\ldots\}}. \tag{B.9}$$

From comparison to Eqs. (B.4) and (B.5), we find the lattice regularization

$$\hat{p}_j \to \frac{\hbar}{a}\sin\left[\frac{\hat{p}_j a}{\hbar}\right], \quad \hat{p}_j^2 \to \frac{2\hbar^2}{a^2}\left(1 - \cos\left[\frac{\hat{p}_j a}{\hbar}\right]\right). \tag{B.10}$$

An easy example

Consider a quadratic, one-dimensional system

$$\mathcal{H}(x,p) = \epsilon(x) + \frac{\hat{p}^2}{2m^*}. \tag{B.11}$$

This is a spinless one-band model with an x-dependent band off-set ϵ and an effective mass m^*. Its discretized version reads

$$H_{\rho_x,\rho'_x} = \delta_{\rho_x\rho'_x}\left(2t + \epsilon(\rho_x\hat{e}_x)\right) - t\left(\delta_{\rho'_x\rho_x+1} + \delta_{\rho'_x\rho_x-1}\right), \quad t = \frac{\hbar^2}{2m^*a^2}. \tag{B.12}$$

The translational symmetry is preserved, when the lattice is infinitely extended and $\epsilon = \text{const}$. In this case, we can replace the momentum operator by its eigenvalue $p = \hbar k$, which labels the solutions with eigenenergies

$$E(k) = \epsilon + 2t\left(1 - \cos\left[ka\right]\right). \tag{B.13}$$

Boundary conditions and numerical solution

The TB formalism is a very apt tool to describe edge- and finite size effects in topological insulators. For example, the lattice in Fig. B.1 has a finite number of lattice points in y-direction, meaning that the system is cut at the lattice points $\rho_y = 1,\ N_y$ due to the lack of additional hopping terms. This resembles hard-wall boundary conditions. On the contrary, periodic boundary conditions can be implemented by adding an additional hopping term, which connects the lattice points $\rho_y = 1$ and $\rho_y = N_y$. Doing so, all edge related effects are lost and the result reflects the pure bulk properties of the system. This technique has, for example, been used in [Recher10].
Having reformulated the system in matrix form allows to find the numerical solutions by diagonalization. The energy spectrum is given by the matrix' eigenvalues. Further information, like the DOS or the spin polarization, can be extracted from its eigenstates.
The simulation of realistically sized systems often requires large lattices, the matrix implementations of which demand high memory and CPU time consumption. In general, it is possible to decrease the number of necessary lattice points by increasing a in the TB model. Being an artificial parameter, the exact value of a should not influence the outcome of the calculations. However, to ensure comparability with the continuum model ($a \to 0$), the lattice constant has to be chosen small enough, so that the outcome converges.
Since the TB approximation couples only neighboring lattice sites, Eq. (B.7) takes the form of a band matrix. Hence, it is possible to use sparse matrix solvers, when one is only interested in a small subset of the solutions. This reduces memory consumption and CPU time significantly. In this thesis, the implementation and diagonalization of the TB matrices was implemented in *Mathematica 9.0* [Wolfram Research12] and *Mathematica 10.0* [Wolfram Research14], which provide dense and sparse matrix solvers.

C. Transport in the tight binding formalism

The technique of equilibrium transport in TB is only used shortly in section 5.3.4. It, however, has been the main tool in the author's master thesis [Reinthaler10], from which we adopt a shortened description of the formalism. The interested reader is referred to [Wimmer08, Rothe09, Reinthaler10] for details.

Equilibrium Green's function formalism

We are interested in the transport through a conductor which is attached to leads, like, for example, the quantum wire depicted in Fig. 4.3. We formulate the problem at energy E in terms of the Green's function

$$G := [E - H]^{-1} = \begin{pmatrix} E - H_p & H_{Cp} \\ H_{Cp}^\dagger & E - H_C \end{pmatrix}^{-1} = \begin{pmatrix} G_p & G_{pC} \\ G_{Cp} & G_p \end{pmatrix}, \tag{C.1}$$

where H_C and H_p are the Hamiltonians for the conductor and lead p, respectively. H_{Cp} describes the coupling of the lead p to the conductor. The sub-matrix structure of G reflects the different sub-systems of the total Hamiltonian H. In the TB formulation (cf. appendix B), the Green's function has a discrete matrix structure. H_C is of finite dimension $(N_x N_y F) \times (N_x N_y F)$, where N_x (N_y) is the number of lattice points along x (y) direction and F the number of degrees of freedom per lattice site. However, the semi-infinite leads transform in matrices of infinite dimension, rendering a direct numerical implementation of G impossible. Following the steps which led to an effective description of the superconducting TI layer in section 3.2.3, we find

$$G_C = [E - H_C - \Sigma]^{-1}, \tag{C.2}$$

which is of finite dimension. The self energy Σ describes the coupling to the leads effectively. It is given by the sum over all leads p

$$\Sigma = \sum_p \Sigma_p = \sum_p H_{Cp}^\dagger \, [E - H_p]^{-1} \, H_{Cp}, \tag{C.3}$$

which still contains the multiplication of infinitely dimensional matrices, which will be solved below. The imaginary part of the self energy, $\Gamma_p = \mathrm{i}(\Sigma_p - \Sigma_p^\dagger)$, gives the finite lifetime of the carriers, which exit the conductor and vanish into the leads. The transmission function, cf. Eq. (4.8), from lead q to lead p can be calculated by the Fisher-Lee relation [Datta07]

$$\bar{T}_{pq} = \begin{cases} \mathrm{Tr}\left[\Gamma_p G_C \Gamma_q G_C^\dagger\right] & , p \neq q \\ \mathcal{M}_p - \sum_{m \neq p} \bar{T}_{mq} & , p = q \end{cases}, \tag{C.4}$$

where $\mathcal{M}_p$ is the number of propagating modes in lead p. Moreover, we made use of the sum rule (4.9). Eq. (C.4) is only valid in the absence of magnetic fields in the leads. A generalized version, which is valid for all classes of TB Hamiltonians, is discussed in [Wimmer08].

The transmission function and the Green's function have to be evaluated at a fixed energy E, corresponding to an equal chemical potential in all leads. Like in the derivation of Landauer's formula in section 4.2.3, this corresponds to an equilibrium regime, where a finite bias is only taken into account in lowest order. The description of a biased conductor in the non-equilibrium regime requires a self-consistent solution, see, e.g., [Datta05].

Self energy of the leads

We follow [Sanvito99, Rocha06, Rungger08] and give a short recipe how to calculate the self energy of a semi-infinitely long lead. For a start, imagine the lead to be infinitely extended in x-direction, which corresponds to the schematic in Fig. B.1. We can imagine the system as consisting of slices at points $\ldots, x-a, x, x+a, \ldots$, which contain N_y lattice points in y-direction. Let H_0 be the on-site Hamiltonian for a slice x. When only nearest neighbor processes are considered, H_1 and $H_{-1} = H_1^\dagger$ are the hopping terms which connect the slice x to $x+a$ and $x-a$, respectively. H_0 and H_1 are matrices of dimension $(N_yF)\times(N_yF)$, which have to be independent of x to ensure translational invariance along the x-axis inside the leads. The periodicity of the infinite lead allows to write the systems eigenstates in Bloch form, $\Psi_x \propto \exp[\mathrm{i}k_x x]\phi_{k_x}$, and the system's Schrödinger equation becomes

$$\left[H_0 - E + H_1 e^{\mathrm{i}k_x a} + H_{-1} e^{-\mathrm{i}k_x a}\right] \phi_{k_x} = 0. \tag{C.5}$$

A transformation analogously to that of Eq. (4.36) leads to the matrix

$$\begin{pmatrix} -H_1^{-1}(H_0 - E) & -H_1^{-1}H_{-1} \\ \mathbb{I} & 0 \end{pmatrix}, \tag{C.6}$$

which has the eigenvalues $e^{\mathrm{i}k_\alpha a}$ and $e^{\mathrm{i}\bar{k}_\alpha a}$. Here, k_α and $\bar{k}_\alpha$ characterize the right- and left moving solutions, respectively. The corresponding eigenvectors contain ϕ_{k_α} and $\phi_{\bar{k}_\alpha}$ in their upper (N_yF) components, where α denotes the (N_yF) different modes. These solutions can be combined to the right- and left going *transfer matrices*

$$T^x = \sum_\alpha \phi_{k_\alpha} e^{\mathrm{i}k_\alpha x} \tilde{\phi}_{k_\alpha}^\dagger \quad \text{and} \quad \bar{T}^x = \sum_\alpha \phi_{\bar{k}_\alpha} e^{\mathrm{i}\bar{k}_\alpha x} \tilde{\phi}_{\bar{k}_\alpha}^\dagger. \tag{C.7}$$

Here, we introduced the dual vectors $\tilde{\phi}_{k_\alpha}$ as the columns of the matrix

$$\left[\left(\phi_{k_1}, \phi_{k_2}, \ldots, \phi_{k_{(N_yF)}}\right)^\dagger\right]^{-1}, \tag{C.8}$$

and the dual vectors $\tilde{\phi}_{\bar{k}_\alpha}$ are equivalently defined. Truncating the infinitely long lead results in the self energies of lead 1 and 2 in Fig. 4.3 [Rungger08]:

$$\Sigma_1 = H_{-1}\bar{T}^a \quad \text{and} \quad \Sigma_2 = H_1 T^a. \tag{C.9}$$

Since the system (C.6) does not need to be hermitian, its eigenvectors might become linear dependent, rendering the matrix inversion (C.8) numerically unstable. A possible solution is provided in form of a Schur decomposition and is discussed in detail in [Wimmer08].

Implementation

For the numerical solution of the transport problem in section 5.3.4, we have adapted a highly efficient code by Dietrich Rothe [Rothe09], which was written in functional Fortran 95.

D. From the missing electron to the hole picture

The pairing Hamiltonian for superconductivity (3.13) contains the pairwise creation and annihilation of electrons, describing the formation of Cooper pairs. The system can be conveniently solved in the BdG formalism by rewriting it in the Nambu basis (3.23), in which the pairing of electrons is incorporated by a doubling of the Hilbert space into sub-spaces connected with the creation and annihilation of an electron. Here, we elaborate the description of the second sub-space as hole-like excitations and point out a subtle difference between its interpretation as a missing electron or as a hole, which is often neglected in literature.

In Fig. D.1a, we show the annihilation of an electron from the Fermi sea, which describes the filled electronic states up to the Fermi energy E_F and is indicated by a blue shading. The main idea of the BdG formalism is to describe the annihilation of an electron at energy $-\epsilon$, which is measured relatively to E_F, analogously to the creation of an electron at ϵ above the Fermi sea. To this end, one mirrors the band structure $\xi_{\boldsymbol{k}}$ around the Fermi energy and around $\boldsymbol{k} = 0$, creating an inverted band structure $-\xi_{-\boldsymbol{k}}$. The inverted band structure allows to describe all operations at positive ϵ, making the interpretation of ϵ as an excitation energy above the ground state energy obvious. In Fig. D.1b, we present the original dispersion $\xi_{\boldsymbol{k}}$ (solid line) together with the inverted one (dashed line). The states at $\epsilon < 0$ are redundant and can be neglected in the following, cf. section 3.1.3. In this picture, the annihilation of an electron in Fig. D.1a is represented by the creation of an electron in the inverted band at $-\boldsymbol{k}$ and excitation energy ϵ.

Since the inverted band has a negative curvature, its effective mass $m \propto \partial^2\xi/\partial k^2$ is negative. Electronic states with negative effective mass respond to an electric field in the same way as states with positive effective mass and positive charge. Therefore, the inverted bands are often referred to as hole-like states [Ashcroft76].

In Fig. D.2b, we depict a current, which is created by a right-moving spin-↑ electron. Imagine a fully occupied, spin-degenerate Fermi sea[1]. It consists of right- and left-moving electrons for

[1]One might think that the situation changes for helical states, for which the spin polarization is coupled to the direction of motion. However, the main arguments remain valid. To see this, imagine a single edge of a

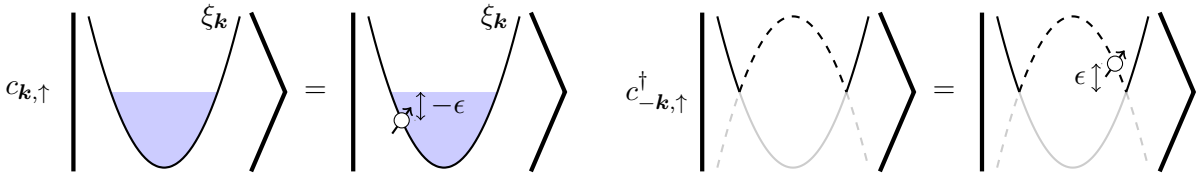

(a) electron annihilation (b) creation of an electron in the inverted band

Figure D.1.: The BdG formalism treats the annihilation of an electron from the Fermi sea at $-\epsilon$ (a) like the creation of an electron at ϵ in a band with inverted band structure (dashed curve) (b).

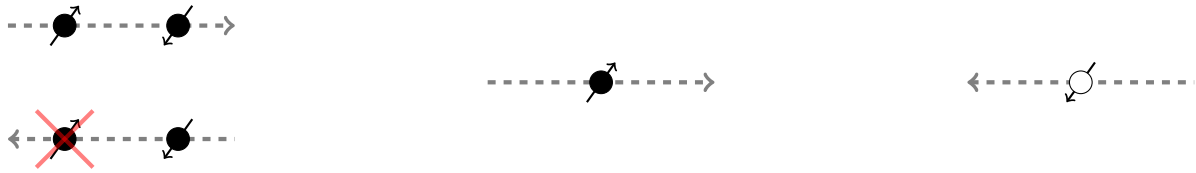

(a) missing electron with spin-↑ (b) effective charge and spin current (c) hole with spin-↓

Figure D.2.: The annihilation of a left-moving spin-↑ electron (a) causes a charge current, which is equivalent to a right-moving spin-↑ electron (b). This can be described as a left-moving hole with spin-↓ (c).

both spin polarizations. The annihilation of a left-moving spin-↑ electron in Fig. D.2a causes an imbalance of left- and right-moving carriers and results in the current of Fig. D.2b. This is the *missing electron picture*, in which we interpret the annihilation of the electron as a spin-↑ excitation, like in Fig. D.1b. When we want to describe the same physical situation with a single positively charged particle in Fig. D.2c, it has to be a left-moving spin-↓ hole. In this so-called *hole picture* the same physical excitation is associated with the opposite spin.
Both pictures are different interpretations of the same physical situation. As long as the spin is not important, we do not explicitly distinguish between both interpretations and simply call it a hole-like excitation. However, when we deal with Andreev reflection of a spin-↑ electron we will either talk about an empty electronic state with spin-↓ in chapter 7 or about a spin-↑ hole in chapter 6.

2D TI, where a spin-↓ (spin-↑) electron moves to the right (left). While the charge current vanishes, there is a spin current flowing to the right, which corresponds to two neutral spin-↓ particles moving rightwards. Removing the left-going particle, causes a finite charge current and decreases the spin current by half, i.e., a spin-↑ current to the right has been generated, analogously to Fig. D.2b.

Acronyms and Symbols

R_h	Andreev reflection amplitude.
T_h	crossed Andreev reflection amplitude.
$\hat{C}$	charge conjugation operator.
$\hat{K}$	complex conjugation operator.
$\hat{T}$	translation operator.
$\hat{X}$	operator for combined time-reversal and particle-hole symmetry.
$\hat{\Pi}$	parity operator.
$\hat{\Theta}$	time-reversal operator.
$\mathbb{I}$	identity operation.
π_i	Pauli matrices in particle-hole space.
σ_i	Pauli matrices in spin space.
τ_i	Pauli matrices in sub-band space.
2D	two-dimensional.
2DEG	two-dimensional electron gas.
3D	three-dimensional.
AR	Andreev reflection.
BCS	Bardeen, Cooper, and Schriefer.
BdG	Bogoliubov-de Gennes.
BHZ	Bernevig, Hughes, and Zhang.
BIA	bulk inversion asymmetry.
BTK	Blonder, Tinkham, and Klapwijk.
BZ	Brillouin zone.
CAR	crossed Andreev reflection.
DOS	density of states.
HBC	hard-wall boundary conditions.
N-SC junction	junction between a normal conductor and a superconductor.
N-SC-N junction	normal - superconducting - normal junction.
PBC	periodic boundary conditions.
PHS	particle-hole symmetry.
QH	quantum Hall.

QSH	quantum spin Hall.
QSHI	quantum spin Hall insulator.
QW	quantum well.
R	electron reflection.
SC	superconductor.
SIA	structure inversion asymmetry.
SOI	spin-orbit interaction.
T	electron tunneling.
TB	tight binding.
TI	topological insulator.
TKNN invariant	topological invariant defined for the integer QH effect.
TPS	combination of time-reversal and particle-hole symmetry.
TR	time-reversal.
TRIM	time-reversal invariant momenta.
TRS	time-reversal symmetry.
Z_2 invariant	topological invariant which is defined as an integer modulo 2.

Bibliography

[Abrahams79] E. Abrahams, P. W. Anderson, D. C. Licciardello, and T. V. Ramakrishnan. Scaling theory of localization: Absence of quantum diffusion in two dimensions. *Phys. Rev. Lett.* **42**(10):673 (1979).

[Adroguer10] P. Adroguer, C. Grenier, D. Carpentier, J. Cayssol, P. Degiovanni, and E. Orignac. Probing the helical edge states of a topological insulator by Cooper-pair injection. *Phys. Rev. B* **82**(8):081303 (2010).

[Aharonov59] Y. Aharonov and D. Bohm. Significance of electromagnetic potentials in the quantum theory. *Phys. Rev.* **115**(3):485 (1959).

[Akkermans07] E. Akkermans and G. Montambaux. *Mesoscopic Physics of Electrons and Photons*. Cambridge University Press (2007).

[Alicea11] J. Alicea, Y. Oreg, G. Refael, F. von Oppen, and M. P. A. Fisher. Non-abelian statistics and topological quantum information processing in 1D wire networks. *Nat. Phys.* **7**:412 (2011).

[Alicea12] J. Alicea. New directions in the pursuit of Majorana fermions in solid state systems. *Reports on Progress in Physics* **75**(7):076501 (2012).

[Anderson99] E. Anderson, Z. Bai, C. Bischof, S. Blackford, J. Demmel, J. Dongarra, J. Du Croz, A. Greenbaum, S. Hammarling, A. McKenney, and D. Sorensen. *LAPACK Users' Guide*. Society for Industrial and Applied Mathematics, Philadelphia, PA, 3rd edn. (1999).

[Ando13] Y. Ando. Topological insulator materials. *Journal of the Physical Society of Japan* **82**(10):102001 (2013).

[Andreev64] A. F. Andreev. The thermal conductivity of the intermediate state in superconductors. *JETP* **19**:1228 (1964).

[Ashcroft76] N. W. Ashcroft and N. D. Mermin. *Solid State Physics*. Holt, Rinehart and Winston (1976).

[Aspect82] A. Aspect, J. Dalibard, and G. Roger. Experimental test of Bell's inequalities using time-varying analyzers. *Phys. Rev. Lett.* **49**:1804 (1982).

[Awschalom07] D. D. Awschalom and M. E. Flatte. Challenges for semiconductor spintronics. *Nat. Phys.* **3**:153 (2007).

[Bardeen48] J. Bardeen and W. H. Brattain. The transistor, a semi-conductor triode. *Phys. Rev.* **74**(2):230 (1948).

[Bardeen57] J. Bardeen, L. N. Cooper, and J. R. Schrieffer. Theory of superconductivity. *Phys. Rev.* **108**:1175 (1957).

[Baum15a] Y. Baum, T. Posske, I. C. Fulga, B. Trauzettel, and A. Stern. Coexisting edge states and gapless bulk in topological states of matter. *Phys. Rev. Lett.* **114**:136801 (2015).

[Baum15b] Y. Baum, T. Posske, I. C. Fulga, B. Trauzettel, and A. Stern. Gapless topological superconductors: Model Hamiltonian and realization. *Phys. Rev. B* **92**:045128 (2015).

[Beckmann04] D. Beckmann, H. B. Weber, and H. v. Löhneysen. Evidence for crossed Andreev reflection in superconductor-ferromagnet hybrid structures. *Phys. Rev. Lett.* **93**:197003 (2004).

[Bennett00] C. H. Bennett and D. P. DiVincenzo. Quantum information and computation. *Nature* **404**:247 (2000).

[Bernevig06] B. A. Bernevig, T. L. Hughes, and S.-C. Zhang. Quantum spin Hall effect and topological phase transition in HgTe quantum wells. *Science* **314**(5806):1757 (2006).

[Berry84] M. V. Berry. Quantal phase factors accompanying adiabatic changes. *Proceedings of the Royal Society of London. A. Mathematical and Physical Sciences* **392**(1802):45 (1984).

[Berry87] M. V. Berry and R. J. Mondragon. Neutrino billiards: Time-reversal symmetry-breaking without magnetic fields. *Proceedings of the Royal Society of London. A. Mathematical and Physical Sciences* **412**(1842):53 (1987).

[Blonder82] G. E. Blonder, M. Tinkham, and T. M. Klapwijk. Transition from metallic to tunneling regimes in superconducting microconstrictions: Excess current, charge imbalance, and supercurrent conversion. *Phys. Rev. B* **25**:4515 (1982).

[Bohm03] A. Bohm, A. Mostafazadeh, H. Koizumi, Q. Niu, and J. Zwanziger. *The Geometric Phase in Quantum Systems*. Springer-Verlag Berlin Heidelberg (2003).

[Born28] M. Born and V. Fock. Beweis des Adiabatensatzes. *Zeitschrift für Physik* **51**(3-4):165 (1928).

[Brüne11] C. Brüne, C. X. Liu, E. G. Novik, E. M. Hankiewicz, H. Buhmann, Y. L. Chen, X. L. Qi, Z. X. Shen, S. C. Zhang, and L. W. Molenkamp. Quantum Hall effect from the topological surface states of strained bulk HgTe. *Phys. Rev. Lett.* **106**:126803 (2011).

[Brüne12] C. Brüne, A. Roth, H. Buhmann, E. M. Hankiewicz, L. W. Molenkamp, J. Maciejko, X.-L. Qi, and S.-C. Zhang. Spin polarization of the quantum spin Hall edge states. *Nat. Phys.* **8**:486 (2012).

[Brüne13] C. Brüne, H. Buhmann, and L. Molenkamp. Chapter 5 - Quantum Spin Hall State in HgTe . In M. Franz and L. Molenkamp (editors), *Topological Insulators*, vol. 6 of *Contemporary Concepts of Condensed Matter Science*, pp. 125 – 142. Elsevier (2013).

[Brüne14] C. Brüne, C. Thienel, M. Stuiber, J. Böttcher, H. Buhmann, E. G. Novik, C.-X. Liu, E. M. Hankiewicz, and L. W. Molenkamp. Dirac-screening stabilized surface-state transport in a topological insulator. *Phys. Rev. X* **4**:041045 (2014).

[Budich12a] J. Budich and B. Trauzettel. Local topological phase transitions in periodic condensed matter systems. *Eur. Phys. J. B* **85**(3):94 (2012).

[Budich12b] J. C. Budich, F. Dolcini, P. Recher, and B. Trauzettel. Phonon-induced backscattering in helical edge states. *Phys. Rev. Lett.* **108**:086602 (2012).

[Büttiker85] M. Büttiker, Y. Imry, R. Landauer, and S. Pinhas. Generalized many-channel conductance formula with application to small rings. *Phys. Rev. B* **31**(10):6207 (1985).

[Büttiker86] M. Büttiker. Four-terminal phase-coherent conductance. *Phys. Rev. Lett.* **57**:1761 (1986).

[Büttiker88] M. Büttiker. Symmetry of electrical conduction. *IBM J. Res. Dev.* **32**:317 (1988).

[Castro Neto09] A. H. Castro Neto, F. Guinea, N. M. R. Peres, K. S. Novoselov, and A. K. Geim. The electronic properties of graphene. *Rev. Mod. Phys.* **81**(1):109 (2009).

[Chen09] Y. L. Chen, J. G. Analytis, J.-H. Chu, Z. K. Liu, S.-K. Mo, X. L. Qi, H. J. Zhang, D. H. Lu, X. Dai, Z. Fang, S. C. Zhang, I. R. Fisher, Z. Hussain, and Z.-X. Shen. Experimental realization of a three-dimensional topological insulator, Bi_2Te_3. *Science* **325**(5937):178 (2009).

[Chen11] W. Chen, R. Shen, L. Sheng, B. G. Wang, and D. Y. Xing. Resonant nonlocal Andreev reflection in a narrow quantum spin Hall system. *Phys. Rev. B* **84**:115420 (2011).

[Chrestin97] A. Chrestin, T. Matsuyama, and U. Merkt. Evidence for a proximity-induced energy gap in Nb/InAs/Nb junctions. *Phys. Rev. B* **55**:8457 (1997).

[Cooper56] L. N. Cooper. Bound electron pairs in a degenerate Fermi gas. *Phys. Rev.* **104**:1189 (1956).

[Crépin12] F. Crépin, J. C. Budich, F. Dolcini, P. Recher, and B. Trauzettel. Renormalization group approach for the scattering off a single Rashba impurity in a helical liquid. *Phys. Rev. B* **86**:121106 (2012).

[Crépin14] F. Crépin, B. Trauzettel, and F. Dolcini. Signatures of Majorana bound states in transport properties of hybrid structures based on helical liquids. *Phys. Rev. B* **89**:205115 (2014).

[Das08] S. Das, S. Rao, and A. Saha. Spintronics with NSN junction of one-dimensional quantum wires: A study of pure spin current and magnetoresistance. *Europhysics Letters* **81**(6):67001 (2008).

[Das12] A. Das, Y. Ronen, Y. Most, Y. Oreg, M. Heiblum, and H. Shtrikman. Zero-bias peaks and splitting in an Al-InAs nanowire topological superconductor as a signature of Majorana fermions. *Nat. Phys.* **8**(12):887 (2012).

[Datta05] S. Datta. *Quantum Transport: Atom to Transistor.* Cambridge University Press (2005).

[Datta07] S. Datta. *Electronic Transport in Mesoscopic Systems.* Cambridge University Press (2007).

[Deng12] M. T. Deng, C. L. Yu, G. Y. Huang, M. Larsson, P. Caroff, and H. Q. Xu. Anomalous zero-bias conductance peak in a Nb-InSb nanowire-Nb hybrid device. *Nano Letters* **12**(12):6414 (2012).

[DiVincenzo00] D. P. DiVincenzo. The physical implementation of quantum computation. *Fortschritte der Physik* **48**(9-11):771 (2000).

[Dzero10] M. Dzero, K. Sun, V. Galitski, and P. Coleman. Topological Kondo insulators. *Phys. Rev. Lett.* **104**:106408 (2010).

[Einstein35] A. Einstein, B. Podolsky, and N. Rosen. Can quantum-mechanical description of physical reality be considered complete? *Phys. Rev.* **47**:777 (1935).

[Falci01] G. Falci, D. Feinberg, and F. W. J. Hekking. Correlated tunneling into a superconductor in a multiprobe hybrid structure. *Europhysics Letters* **54**(2):255 (2001).

[Fiete11] G. A. Fiete. How do you want that insulator? *Science* **332**:546 (2011).

[Franklin12] A. D. Franklin, M. Luisier, S.-J. Han, G. Tulevski, C. M. Breslin, L. Gignac, M. S. Lundstrom, and W. Haensch. Sub-10 nm carbon nanotube transistor. *Nano Letters* **12**(2):758 (2012).

[Fu06] L. Fu and C. L. Kane. Time reversal polarization and a Z_2 adiabatic spin pump. *Phys. Rev. B* **74**:195312 (2006).

[Fu07a] L. Fu and C. L. Kane. Topological insulators with inversion symmetry. *Phys. Rev. B* **76**:045302 (2007).

[Fu07b] L. Fu, C. L. Kane, and E. J. Mele. Topological insulators in three dimensions. *Phys. Rev. Lett.* **98**(10):106803 (2007).

[Fu08] L. Fu and C. L. Kane. Superconducting proximity effect and Majorana fermions at the surface of a topological insulator. *Phys. Rev. Lett.* **100**:096407 (2008).

[Fu09] L. Fu and C. L. Kane. Josephson current and noise at a superconductor/quantum-spin-Hall-insulator/superconductor junction. *Phys. Rev. B* **79**:161408 (2009).

[Fu11] L. Fu. Topological crystalline insulators. *Phys. Rev. Lett.* **106**:106802 (2011).

[Gennes99] P. G. de Gennes. *Superconductivity of Metals and Alloys*. Perseus Books (1999).

[Gor'kov79] L. P. Gor'kov, A. I. Larkin, and D. E. Khmel'Nitskiĭ. Particle conductivity in a two-dimensional random potential. *Soviet Journal of Experimental and Theoretical Physics Letters* **30**:228 (1979).

[Guennebaud10] G. Guennebaud, B. Jacob *et al.* Eigen v3. http://eigen.tuxfamily.org (2010).

[Halperin82] B. I. Halperin. Quantized Hall conductance, current-carrying edge states, and the existence of extended states in a two-dimensional disordered potential. *Phys. Rev. B* **25**:2185 (1982).

[Han14] S.-J. Han, A. V. Garcia, S. Oida, K. A. Jenkins, and W. Haensch. Graphene radio frequency receiver integrated circuit. *Nat. Commun.* **5**: (2014).

[Hart14] S. Hart, H. Ren, T. Wagner, P. Leubner, M. Mühlbauer, C. Brüne, H. Buhmann, L. W. Molenkamp, and A. Yacoby. Induced superconductivity in the quantum spin Hall edge. *Nat. Phys.* **10**(9):638 (2014).

[Hasan10] M. Z. Hasan and C. L. Kane. Colloquium: Topological insulators. *Rev. Mod. Phys.* **82**(4):3045 (2010).

[Herrmann10] L. G. Herrmann, F. Portier, P. Roche, A. L. Yeyati, T. Kontos, and C. Strunk. Carbon nanotubes as Cooper-pair beam splitters. *Phys. Rev. Lett.* **104**:026801 (2010).

[Hofstetter09] L. Hofstetter, S. Csonka, J. Nygård, and C. Schönenberger. Cooper pair splitter realized in a two-quantum-dot y-junction. *Nature* **461**:960 (2009).

[Houzet13] M. Houzet, J. S. Meyer, D. M. Badiane, and L. I. Glazman. Dynamics of Majorana states in a topological Josephson junction. *Phys. Rev. Lett.* **111**:046401 (2013).

[Hsieh08] D. Hsieh, D. Qian, L. Wray, Y. Xia, Y. S. Hor, R. J. Cava, and M. Z. Hasan. A topological Dirac insulator in a quantum spin Hall phase. *Nature* **452**(7190):970 (2008).

[Hsieh12] T. H. Hsieh, H. Lin, J. Liu, W. Duan, A. Bansil, and L. Fu. Topological crystalline insulators in the SnTe material class. *Nat. Commun.* **3**:982 (2012).

[Hu12] J. Hu, J. Alicea, R. Wu, and M. Franz. Giant topological insulator gap in graphene with 5*d* adatoms. *Phys. Rev. Lett.* **109**:266801 (2012).

[Hyart13] T. Hyart, B. van Heck, I. C. Fulga, M. Burrello, A. R. Akhmerov, and C. W. J. Beenakker. Flux-controlled quantum computation with Majorana fermions. *Phys. Rev. B* **88**:035121 (2013).

[Ivanov01] D. A. Ivanov. Non-abelian statistics of half-quantum vortices in p-wave superconductors. *Phys. Rev. Lett.* **86**:268 (2001).

[Jaklevic64] R. C. Jaklevic, J. Lambe, A. H. Silver, and J. E. Mercereau. Quantum interference effects in Josephson tunneling. *Phys. Rev. Lett.* **12**:159 (1964).

[Josephson62] B. Josephson. Possible new effects in superconductive tunnelling. *Physics Letters* **1**(7):251 (1962).

[Kane05a] C. L. Kane and E. J. Mele. Quantum spin Hall effect in graphene. *Phys. Rev. Lett.* **95**(22):226801 (2005).

[Kane05b] C. L. Kane and E. J. Mele. Z_2 topological order and the quantum spin Hall effect. *Phys. Rev. Lett.* **95**:146802 (2005).

[Kashiwaya11] S. Kashiwaya, H. Kashiwaya, H. Kambara, T. Furuta, H. Yaguchi, Y. Tanaka, and Y. Maeno. Edge states of Sr_2RuO_4 detected by in-plane tunneling spectroscopy. *Phys. Rev. Lett.* **107**:077003 (2011).

[Kato50] T. Kato. On the adiabatic theorem of quantum mechanics. *Journal of the Physical Society of Japan* **5**(6):435 (1950).

[Khaymovich11] I. M. Khaymovich, N. M. Chtchelkatchev, and V. M. Vinokur. Instability of topological order and localization of edge states in HgTe quantum wells coupled to s-wave superconductor. *Phys. Rev. B* **84**:075142 (2011).

[King-Smith93] R. D. King-Smith and D. Vanderbilt. Theory of polarization of crystalline solids. *Phys. Rev. B* **47**:1651 (1993).

[Kish02] L. B. Kish. End of Moore's law: Thermal (noise) death of integration in micro and nano electronics. *Physics Letters A* **305**(3-4):144 (2002).

[Kitaev01] A. Y. Kitaev. Unpaired Majorana fermions in quantum wires. *Physics-Uspekhi* **44**(10S):131 (2001).

[Kitaev03] A. Kitaev. Fault-tolerant quantum computation by anyons. *Annals of Physics* **303**(1):2 (2003).

[Kittel96] C. Kittel. *Introduction to Solid State Physics*. Wiley, 7th edn. (1996).

[Klitzing80] K. v. Klitzing, G. Dorda, and M. Pepper. New method for high-accuracy determination of the fine-structure constant based on quantized Hall resistance. *Phys. Rev. Lett.* **45**(6):494 (1980).

[Knez11] I. Knez, R.-R. Du, and G. Sullivan. Evidence for helical edge modes in inverted InAs/GaSb quantum wells. *Phys. Rev. Lett.* **107**:136603 (2011).

[Knez12] I. Knez, R.-R. Du, and G. Sullivan. Andreev reflection of helical edge modes in InAs/GaSb quantum spin Hall insulator. *Phys. Rev. Lett.* **109**:186603 (2012).

[Kohmoto85] M. Kohmoto. Topological invariant and the quantization of the Hall conductance. *Annals of Physics* **160**(2):343 (1985).

[König07] M. König, S. Wiedmann, C. Brüne, A. Roth, H. Buhmann, L. W. Molenkamp, X.-L. Qi, and S.-C. Zhang. Quantum spin Hall insulator state in HgTe quantum wells. *Science* **318**(5851):766 (2007).

[König08] M. König, H. Buhmann, L. W. Molenkamp, T. Hughes, C.-X. Liu, X.-L. Qi, and S.-C. Zhang. The quantum spin Hall effect: Theory and experiment. *Journal of the Physical Society of Japan* **77**(3):031007 (2008).

[Krueckl11] V. Krueckl and K. Richter. Switching spin and charge between edge states in topological insulator constrictions. *Phys. Rev. Lett.* **107**:086803 (2011).

[Laughlin81] R. B. Laughlin. Quantized Hall conductivity in two dimensions. *Phys. Rev. B* **23**:5632 (1981).

[Lesovik01] G. B. Lesovik, T. Martin, and G. Blatter. Electronic entanglement in the vicinity of a superconductor. *Eur. Phys. J. B* **24**(3):287 (2001).

[Liu08] C. Liu, T. L. Hughes, X.-L. Qi, K. Wang, and S.-C. Zhang. Quantum spin Hall effect in inverted type-II semiconductors. *Phys. Rev. Lett.* **100**(23):236601 (2008).

[Liu10a] C.-X. Liu, X.-L. Qi, H. J. Zhang, X. Dai, Z. Fang, and S.-C. Zhang. Model Hamiltonian for topological insulators. *Phys. Rev. B* **82**:045122 (2010).

[Liu10b] C.-X. Liu, H. Zhang, B. Yan, X.-L. Qi, T. Frauenheim, X. Dai, Z. Fang, and S.-C. Zhang. Oscillatory crossover from two-dimensional to three-dimensional topological insulators. *Phys. Rev. B* **81**:041307 (2010).

[Lloyd00] S. Lloyd. Ultimate physical limits to computation. *Nature* **406**(6799):1047 (2000).

[London35] F. London and H. London. The electromagnetic equations of the supraconductor. *Proceedings of the Royal Society of London A: Mathematical, Physical and Engineering Sciences* **149**(866):71 (1935).

[Loth12] S. Loth, S. Baumann, C. P. Lutz, D. M. Eigler, and A. J. Heinrich. Bistability in atomic-scale antiferromagnets. *Science* **335**(6065):196 (2012).

[Lu10] H.-Z. Lu, W.-Y. Shan, W. Yao, Q. Niu, and S.-Q. Shen. Massive Dirac fermions and spin physics in an ultrathin film of topological insulator. *Phys. Rev. B* **81**:115407 (2010).

[Lu12] F. Lu, Y. Zhou, J. An, and C.-D. Gong. Transversal propagation of helical edge states in quantum spin Hall systems. *Europhysics Letters* **98**(1):17004 (2012).

[Maier12] L. Maier, J. Oostinga, D. Knott, C. Brüne, P. Virtanen, G. Tkachov, E. Hankiewicz, C. Gould, H. Buhmann, and L. Molenkamp. Induced superconductivity in the three-dimensional topological insulator HgTe. *Phys. Rev. Lett.* **109**:186806 (2012).

[Matsuura13] S. Matsuura, P.-Y. Chang, A. P. Schnyder, and S. Ryu. Protected boundary states in gapless topological phases. *New Journal of Physics* **15**(6):065001 (2013).

[Maxfield65] B. W. Maxfield and W. L. McLean. Superconducting penetration depth of niobium. *Phys. Rev.* **139**:A1515 (1965).

[McCann04] E. McCann and V. I. Fal'ko. Symmetry of boundary conditions of the Dirac equation for electrons in carbon nanotubes. *Journal of Physics: Condensed Matter* **16**(13):2371 (2004).

[McMillan68] W. L. McMillan. Tunneling model of the superconducting proximity effect. *Phys. Rev.* **175**:537 (1968).

[Meissner58] H. Meissner. Measurements on superconducting contacts. *Phys. Rev.* **109**:686 (1958).

[Meissner60] H. Meissner. Superconductivity of contacts with interposed barriers. *Phys. Rev.* **117**:672 (1960).

[Meservey70] R. Meservey, P. M. Tedrow, and P. Fulde. Magnetic field splitting of the quasiparticle states in superconducting aluminum films. *Phys. Rev. Lett.* **25**:1270 (1970).

[Mi13] S. Mi, D. I. Pikulin, M. Wimmer, and C. W. J. Beenakker. Proposal for the detection and braiding of Majorana fermions in a quantum spin Hall insulator. *Phys. Rev. B* **87**:241405 (2013).

[Michetti12] P. Michetti, P. H. Penteado, J. C. Egues, and P. Recher. Helical edge states in multiple topological mass domains. *Semiconductor Science and Technology* **27**(12):124007 (2012).

[Min06] H. Min, J. E. Hill, N. A. Sinitsyn, B. R. Sahu, L. Kleinman, and A. H. MacDonald. Intrinsic and Rashba spin-orbit interactions in graphene sheets. *Phys. Rev. B* **74**:165310 (2006).

[Moore65] G. E. Moore. Cramming more components onto integrated circuits. *Electronics* **38**(8):114 (1965).

[Mourik12] V. Mourik, K. Zuo, S. M. Frolov, S. R. Plissard, E. P. A. M. Bakkers, and L. P. Kouwenhoven. Signatures of Majorana fermions in hybrid superconductor-semiconductor nanowire devices. *Science* **336**(6084):1003 (2012).

[Murakami06] S. Murakami. Quantum spin Hall effect and enhanced magnetic response by spin-orbit coupling. *Phys. Rev. Lett.* **97**:236805 (2006).

[Murakami07] S. Murakami. Phase transition between the quantum spin Hall and insulator phases in 3D: Emergence of a topological gapless phase. *New Journal of Physics* **9**(9):356 (2007).

[Nakahara03] M. Nakahara. *Geometry, Topology and Physics*. Taylor & Francis, 2nd edn. (2003).

[Nayak08] C. Nayak, S. H. Simon, A. Stern, M. Freedman, and S. Das Sarma. Non-abelian anyons and topological quantum computation. *Rev. Mod. Phys.* **80**:1083 (2008).

[Nielsen05] M. A. Nielsen and I. L. Chuang. *Quantum Computation and Quantum Information* . Cambridge University Press, 1st edn. (2005).

[Norman11] M. R. Norman. The challenge of unconventional superconductivity. *Science* **332**(6026):196 (2011).

[Novik05] E. G. Novik, A. Pfeuffer-Jeschke, T. Jungwirth, V. Latussek, C. R. Becker, G. Landwehr, H. Buhmann, and L. W. Molenkamp. Band structure of semimagnetic $Hg_{1-y}Mn_yTe$ quantum wells. *Phys. Rev. B* **72**(3):035321 (2005).

[Novik10] E. G. Novik, P. Recher, E. M. Hankiewicz, and B. Trauzettel. Signatures of topological order in ballistic bulk transport of HgTe quantum wells. *Phys. Rev. B* **81**(24):241303 (2010).

[Onnes11] H. K. Onnes. The resistance of pure mercury at helium temperatures. *Commun. Phys. Lab. Univ. Leiden* **12**:120+ (1911).

[Oreg10] Y. Oreg, G. Refael, and F. von Oppen. Helical liquids and Majorana bound states in quantum wires. *Phys. Rev. Lett.* **105**:177002 (2010).

[Pfeuffer-Jeschke00] A. Pfeuffer-Jeschke. *Bandstruktur und Landau-Niveaus quecksilberhaltiger II-IV-Heterostrukturen.* Ph.D. thesis, University of Würzburg (2000).

[Pikulin12] D. I. Pikulin, J. P. Dahlhaus, M. Wimmer, H. Schomerus, and C. W. J. Beenakker. A zero-voltage conductance peak from weak antilocalization in a Majorana nanowire. *New Journal of Physics* **14**(12):125011 (2012).

[Prada13] E. Prada and G. Metalidis. Transport through quantum spin Hall insulator/metal junctions in graphene ribbons. *Journal of Computational Electronics* **12**(2):63 (2013).

[Pribiag15] V. S. Pribiag, B. J. A., F. Qu, M. C. Cassidy, C. Charpentier, W. Wegscheider, and L. P. Kouwenhoven. Edge-mode superconductivity in a two-dimensional topological insulator. *Nat. Nano.* **10**(7):593 (2015).

[Qi09] X.-L. Qi, T. L. Hughes, S. Raghu, and S.-C. Zhang. Time-reversal-invariant topological superconductors and superfluids in two and three dimensions. *Phys. Rev. Lett.* **102**:187001 (2009).

[Qi11] X.-L. Qi and S.-C. Zhang. Topological insulators and superconductors. *Rev. Mod. Phys.* **83**:1057 (2011).

[Raghu08] S. Raghu, X.-L. Qi, C. Honerkamp, and S.-C. Zhang. Topological Mott insulators. *Phys. Rev. Lett.* **100**:156401 (2008).

[Recher01] P. Recher, E. V. Sukhorukov, and D. Loss. Andreev tunneling, Coulomb blockade, and resonant transport of nonlocal spin-entangled electrons. *Phys. Rev. B* **63**:165314 (2001).

[Recher10] P. Recher, E. G. Novik, R. W. Reinthaler, D. G. Rothe, E. M. Hankiewicz, and B. Trauzettel. Signatures of topology in ballistic bulk transport of HgTe quantum wells. In H.-J. M. Drouhin, J.-E. Wegrowe, and M. Razeghi (editors), *Proc. of SPIE*, vol. 7760, p. 776018. SPIE (2010).

[Reinthaler10] R. W. Reinthaler. *Topology Related Transport Effects in HgTe Quantum Wells*. Master's thesis, Universität Würzburg (2010).

[Reinthaler12] R. W. Reinthaler and E. M. Hankiewicz. Interplay of bulk and edge states in transport of two-dimensional topological insulators. *Phys. Rev. B* **85**:165450 (2012).

[Reinthaler13] R. W. Reinthaler, P. Recher, and E. M. Hankiewicz. Proposal for an all-electrical detection of crossed Andreev reflection in topological insulators. *Phys. Rev. Lett.* **110**:226802 (2013).

[Reinthaler15] R. W. Reinthaler, G. Tkachov, and E. M. Hankiewicz. Superconducting quantum spin Hall systems with giant orbital g factors. *Phys. Rev. B* **92**:161303 (2015).

[Rocha06] A. R. Rocha, V. M. García-Suárez, S. Bailey, C. Lambert, J. Ferrer, and S. Sanvito. Spin and molecular electronics in atomically generated orbital landscapes. *Phys. Rev. B* **73**(8):085414 (2006).

[Rokhinson12] L. P. Rokhinson, X. Liu, and J. K. Furdyna. The fractional a.c. Josephson effect in a semiconductor-superconductor nanowire as a signature of Majorana particles. *Nat Phys* **8**(11):795 (2012).

[Roth09] A. Roth, C. Brüne, H. Buhmann, L. W. Molenkamp, J. Maciejko, X.-L. Qi, and S.-C. Zhang. Nonlocal transport in the quantum spin Hall state. *Science* **325**(5938):294 (2009).

[Rothe09] D. G. Rothe. *Spin-Hall Effect in Semiconducting Quantum Wells*. Master's thesis, University of Würzburg (2009).

[Rothe10] D. G. Rothe, R. W. Reinthaler, C.-X. Liu, L. W. Molenkamp, S.-C. Zhang, and E. M. Hankiewicz. Fingerprint of different spin-orbit terms for spin transport in HgTe quantum wells. *New Journal of Physics* **12**(6):065012 (2010).

[Rungger08] I. Rungger and S. Sanvito. Algorithm for the construction of self-energies for electronic transport calculations based on singularity elimination and singular value decomposition. *Phys. Rev. B* **78**(3):035407 (2008).

[Russo05] S. Russo, M. Kroug, T. M. Klapwijk, and A. F. Morpurgo. Experimental observation of bias-dependent nonlocal Andreev reflection. *Phys. Rev. Lett.* **95**:027002 (2005).

[Sakurai94] J. J. Sakurai. *Modern Quantum Meachanics*. Addison Wesley, rev. edn. (1994).

[Sanvito99] S. Sanvito, C. J. Lambert, J. H. Jefferson, and A. M. Bratkovsky. General Green's-function formalism for transport calculations with *spd* Hamiltonians and giant magnetoresistance in Co- and Ni-based magnetic multilayers. *Phys. Rev. B* **59**(18):11936 (1999).

[Sato10] K. Sato, D. Loss, and Y. Tserkovnyak. Cooper-pair injection into quantum spin hall insulators. *Phys. Rev. Lett.* **105**:226401 (2010).

[Sau11] J. D. Sau, D. J. Clarke, and S. Tewari. Controlling non-abelian statistics of Majorana fermions in semiconductor nanowires. *Phys. Rev. B* **84**:094505 (2011).

[Schmidt09] M. J. Schmidt, E. G. Novik, M. Kindermann, and B. Trauzettel. Optical manipulation of edge-state transport in HgTe quantum wells in the quantum Hall regime. *Phys. Rev. B* **79**:241306 (2009).

[Schnyder08] A. P. Schnyder, S. Ryu, A. Furusaki, and A. W. W. Ludwig. Classification of topological insulators and superconductors in three spatial dimensions. *Phys. Rev. B* **78**:195125 (2008).

[Schwabl07] F. Schwabl. *Quantum Mechanics*. Springer-Verlag Berlin Heidelberg, 4th edn. (2007).

[Shan10] W.-Y. Shan, H.-Z. Lu, and S.-Q. Shen. Effective continuous model for surface states and thin films of three-dimensional topological insulators. *New Journal of Physics* **12**(4):043048 (2010).

[Shen12] S.-Q. Shen. *Topological Insulators: Dirac Equation in Condensed Matters*. Springer-Verlag Berlin Heidelberg (2012).

[Sochnikov15] I. Sochnikov, L. Maier, C. A. Watson, J. R. Kirtley, C. Gould, G. Tkachov, E. M. Hankiewicz, C. Brüne, H. Buhmann, L. W. Molenkamp, and K. A. Moler. Nonsinusoidal current-phase relationship in Josephson junctions from the 3D topological insulator HgTe. *Phys. Rev. Lett.* **114**:066801 (2015).

[Ström10] A. Ström, H. Johannesson, and G. I. Japaridze. Edge dynamics in a quantum spin Hall state: Effects from Rashba spin-orbit interaction. *Phys. Rev. Lett.* **104**:256804 (2010).

[Strzalkowski76] I. Strzalkowski, S. Joshi, and C. R. Crowell. Dielectric constant and its temperature dependence for GaAs, CdTe, and ZnSe. *Applied Physics Letters* **28**(6):350 (1976).

[Tan10] K. Y. Tan, K. W. Chan, M. Möttönen, A. Morello, C. Yang, J. v. Donkelaar, A. Alves, J.-M. Pirkkalainen, D. N. Jamieson, R. G. Clark, and A. S. Dzurak. Transport spectroscopy of single phosphorus donors in a silicon nanoscale transistor. *Nano Letters* **10**(1):11 (2010).

[Tanaka09] Y. Tanaka and N. Nagaosa. Two interacting helical edge modes in quantum spin Hall systems. *Phys. Rev. Lett.* **103**:166403 (2009).

[Tanaka12] Y. Tanaka, Z. Ren, T. Sato, K. Nakayama, S. Souma, T. Takahashi, K. Segawa, and Y. Ando. Experimental realization of a topological crystalline insulator in SnTe. *Nat. Phys.* **8**(11):800 (2012).

[Thouless82] D. J. Thouless, M. Kohmoto, M. P. Nightingale, and M. den Nijs. Quantized Hall conductance in a two-dimensional periodic potential. *Phys. Rev. Lett.* **49**:405 (1982).

[Tinkham04] M. Tinkham. *Introduction To Superconductivity.* Dover Publications, 2nd edn. (2004).

[Tkachov05] G. Tkachov and K. Richter. Andreev magnetotransport in low-dimensional proximity structures: Spin-dependent conductance enhancement. *Phys. Rev. B* **71**:094517 (2005).

[Tkachov11] G. Tkachov, C. Thienel, V. Pinneker, B. Büttner, C. Brüne, H. Buhmann, L. W. Molenkamp, and E. M. Hankiewicz. Backscattering of Dirac fermions in HgTe quantum wells with a finite gap. *Phys. Rev. Lett.* **106**:076802 (2011).

[Tkachov13] G. Tkachov. Suppression of surface p-wave superconductivity in disordered topological insulators. *Phys. Rev. B* **87**:245422 (2013).

[Tkachov15] G. Tkachov. *Topological Insulators: The Physics of Spin Helicity in Quantum Transport.* Pan Stanford (2015).

[Wei10] J. Wei and V. Chandrasekhar. Positive noise cross-correlation in hybrid superconducting and normal-metal three-terminal devices. *Nat. Phys.* **6**:494 (2010).

[Wiedenmann16] J. Wiedenmann, E. Bocquillon, R. S. Deacon, S. Hartinger, O. Herrmann, T. M. Klapwijk, L. Maier, C. Ames, C. Brune, C. Gould, A. Oiwa, K. Ishibashi, S. Tarucha, H. Buhmann, and L. W. Molenkamp. 4π-periodic Josephson supercurrent in HgTe-based topological Josephson junctions. *Nat Commun* **7**: (2016).

[Wimmer08] M. Wimmer. *Quantum Transport in Nanostructures: From Computational Concepts to Spintronics in Graphene and Magnetic Tunnel Junctions.* Ph.D. thesis, University of Regensburg (2008).

[Winkler03] R. Winkler. *Spin-Orbit Coupling Effects in Two-Dimensional Electron and Hole Systems.* Springer-Verlag Berlin Heidelberg (2003).

[Wolf01] S. A. Wolf, D. D. Awschalom, R. A. Buhrman, J. M. Daughton, S. von Molnár, M. L. Roukes, A. Y. Chtchelkanova, and D. M. Treger. Spintronics: A spin-based electronics vision for the future. *Science* **294**(5546):1488 (2001).

[Wolfram Research12] Wolfram Research. *Mathematica, version 9.0.* Wolfram Research Inc. (2012).

[Wolfram Research14] Wolfram Research. *Mathematica, version 10.0.* Wolfram Research Inc. (2014).

[Wu06] C. Wu, B. A. Bernevig, and S.-C. Zhang. Helical liquid and the edge of quantum spin Hall systems. *Phys. Rev. Lett.* **96**:106401 (2006).

[Xia09] Y. Xia, D. Qian, D. Hsieh, L. Wray, A. Pal, H. Lin, A. Bansil, D. Grauer, Y. S. Hor, R. J. Cava, and M. Z. Hasan. Observation of a large-gap topological-insulator class with a single Dirac cone on the surface. *Nat. Phys.* **5**(6):398 (2009).

[Xu06] C. Xu and J. E. Moore. Stability of the quantum spin Hall effect: Effects of interactions, disorder, and F_2 topology. *Phys. Rev. B* **73**:045322 (2006).

[Yao07] Y. Yao, F. Ye, X.-L. Qi, S.-C. Zhang, and Z. Fang. Spin-orbit gap of graphene: First-principles calculations. *Phys. Rev. B* **75**:041401 (2007).

[Yokoyama09] T. Yokoyama, Y. Tanaka, and N. Nagaosa. Giant spin rotation in the junction between a normal metal and a quantum spin Hall system. *Phys. Rev. Lett.* **102**(16):166801 (2009).

[Zeilinger99] A. Zeilinger. Experiment and the foundations of quantum physics. *Rev. Mod. Phys.* **71**:288 (1999).

[Zhang09] H. Zhang, C.-X. Liu, X.-L. Qi, X. Dai, Z. Fang, and S.-C. Zhang. Topological insulators in Bi_2Se_3, Bi_2Te_3 and Sb_2Te_3 with a single Dirac cone on the surface. *Nat. Phys.* **5**(6):438 (2009).

[Zhang10a] L. B. Zhang, F. Zhai, and K. Chang. Electron tunneling through a planar single barrier in HgTe quantum wells with inverted band structures. *Phys. Rev. B* **81**(23):235323 (2010).

[Zhang10b] W. Zhang, R. Yu, H.-J. Zhang, X. Dai, and Z. Fang. First-principles studies of the three-dimensional strong topological insulators Bi_2Te_3 , Bi_2Se_3 and Sb_2Te_3. *New Journal of Physics* **12**(6):065013 (2010).

[Zhou08] B. Zhou, H.-Z. Lu, R.-L. Chu, S.-Q. Shen, and Q. Niu. Finite size effects on helical edge states in a quantum spin-Hall system. *Phys. Rev. Lett.* **101**(24):246807 (2008).

Acknowledgments

This work would not have been possible without the tremendous help and support of many friends and colleagues, to whom I like to express my most sincere gratitude.
First of all, I want to acknowledge my supervisor Prof. Dr. Ewelina Hankiewicz, whose passion for science encouraged me throughout the course of my thesis. Entrusting me with the supervision of Bachelor students and exercise groups, she enabled me to train my ability to explain and describe complicated subjects. Additionally, I am very obliged to her for the opportunity to visit various schools and conferences, where I could broaden my knowledge of the field and present my own research.
I am also deeply indebted to my collaborators Prof. Dr. Patrik Recher and Dr. Grigory Tkachov, whose experience and advice nourished my advance significantly. I am also grateful to Prof. Dr. Björn Trauzettel for his friendly and professional leadership of the group and for sharing his vast knowledge of the field. Furthermore, I want to thank all present and former members of the chair Theoretische Physik IV for the amicable and inspiring working atmosphere. The policy of open doors led to many fruitful discussions, especially with Dr. François Crépin, Dr. Pablo Burset, Dr. Marine Guigou, Dr. Paolo Michetti, Dr. Niccolò Traverso, Dr. Jan Budich, Dr. Jörg Schelter, Thore Poßke, Moritz Fuchs, Lars Elster, Christian Michel and Jan Böttcher. Additionally, I want to acknowledge Thore Poßke and Moritz Fuchs for their helpful and constructive remarks regarding the text of my thesis. Special thanks go to Dietrich Rothe, with whom I shared not only the office, but also ups, downs and uncountable hilarious moments. Besides that, I could benefit from his knowledge about computing and numerics. This list would not be complete without Nelia Meyer, who kept the group running smoothly. Besides work, regular group activities turned many colleagues into friends.

Since *mens sana in corpore sano*, I was happy to share my sportive interests with many colleagues and friends. I want to mention Sonja, Thore and Martin for helping me to find my way through overcrowded swimming pools, Pablo for keeping my mood up through hours and hours of bad gym music and to Sonja, Simone, Christoph and Erwann for encouraging me to (and through) my first marathon.
During my stay in Würzburg, I was fortunate to gain Chrissi, Joyce and Martin for true and reliable friends with whom I share so many good memories. Last but not least I want to thank my parents and Marina for their love and unconditional support.

List of publications

Peer reviewed journals

- Dietrich G. Rothe, Rolf W. Reinthaler, Chaoxing Liu, Laurens W. Molenkamp, Shoucheng Zhang, and Ewelina M. Hankiewicz.
  Fingerprint of different spin-orbit terms for spin transport in HgTe quantum wells
  New J. Phys. **12**, 065012 (2010).

- Rolf W. Reinthaler and Ewelina M. Hankiewicz.
  Interplay of bulk and edge states in transport of two-dimensional topological insulators
  Phys. Rev. B **85**, 165450 (2012).

- Rolf W. Reinthaler, Patrik Recher, and Ewelina M. Hankiewicz.
  Proposal for an all-electrical detection of crossed Andreev reflection in topological insulators
  Phys. Rev. Lett. **110**, 226802 (2013).

- Rolf W. Reinthaler, Grigory Tkachov, and Ewelina M. Hankiewicz.
  Superconducting quantum spin Hall systems with giant orbital g factors
  Phys. Rev. B **92**, 161303(R) (2015).

Conference proceedings

- Patrik Recher, Alena G. Novik, Rolf W. Reinthaler, Dietrich G. Rothe, Ewelina M. Hankiewicz, and Björn Trauzettel.
  Signatures of topology in ballistic bulk transport of HgTe quantum wells
  Spintronics III, Proc. of SPIE Vol. **7760**, 776018 (2010)